# CARBON NANOTUBE POLYMER NANOCOMPOSITES

# FOR ELECTROMECHANICAL SYSTEM APPLICATIONS

A Dissertation

by

ARNAB CHAKRABARTY

Submitted to the Office of Graduate Studies of
Texas A&M University
in partial fulfillment of the requirements for the degree of

DOCTOR OF PHILOSOPHY

August 2008

Major Subject: Chemical Engineering

# CARBON NANOTUBE POLYMER NANOCOMPOSITES

# FOR ELECTROMECHANICAL SYSTEM APPLICATIONS

A Dissertation

by

ARNAB CHAKRABARTY

Submitted to the Office of Graduate Studies of
Texas A&M University
in partial fulfillment of the requirements for the degree of

DOCTOR OF PHILOSOPHY

Approved by:

| | |
|---|---|
| Chair of Committee, | Tahir Cagin |
| Committee Members, | Perla Balbuena |
| | Daniel Shantz |
| | Zoubeida Ounaies |
| Head of Department, | Michael Pishko |

August 2008

Major Subject: Chemical Engineering

# ABSTRACT

Carbon Nanotube Polymer Nanocomposites
for Electromechanical System Applications. (August 2008)
Arnab Chakrabarty, B.Tech., IIT Kharagpur;
M.S., Texas A&M University
Chair of Advisory Committee: Dr. Tahir Cagin

Polymer nanocomposites refer to a broad range of composite materials with polymer acting as the matrix and any material which has at least one dimension in the order of 1 ~ 100 nanometer acting as the filler. Due to unprecedented improvement observed in properties of the nanocomposites, research interest in this area has grown exponentially in recent years. In designing better nano-composites for advanced technological applications some of the major challenges are: understanding the structure-property relationships, interaction and integrity of the two components at the interface, the role of nanofillers in enhancing the properties of the resulting material.

In our work, we have utilized first principle calculations, atomistic simulations, coarse-grained modeling and constitutive equations to develop structure-property relationships for an amorphous aromatic piezoelectric polyimide substituted with nitrile dipole, carbon nanotubes and resulting nanocomposites. We have studied in detail structure-property relationships for carbon nanotubes and $(\beta - CN)APB/ODPA$ polyimide. We have developed chemically sound coarse-grained model based on atomic level simulations of the piezoelectric polyimide to address the larger length and time scale phenomena. The challenge of coarse grain model for these polymers is to reproduce electrical properties in addition to the structure and energetics; our model is the first to successfully achieve this goal. We have compared and analyzed atomistic scale simulation results on the nanocomposite with those predicted from micromechanics analysis. Notably, we have investigated the time dependent response of

these highly complex polymers, to our best knowledge this is the first of its kind. In particular we have studied the thermal, mechanical and dielectric properties of the polyimide, nanotube and their nanocomposites through multi-scale modeling technique. We expect the results obtained and understanding gained through modeling and simulations may be used in guiding development of new nanocomposites for various advanced future applications. In conclusion we have developed a computational paradigm to rationally develop next generation nano-materials.

# ACKNOWLEDGEMENTS

I would like to thank my committee chair, Dr. Tahir Cagin, and my committee members, Dr. Perla Balbuena, Dr. Daniel Shantz and Dr. Zoubeida Ounaies for their guidance and support throughout the course of this research. The technical discussions with Dr. Cagin have always been very insightful, and I will always be indebted to him for all the knowledge he shared with me. His prompt responses and availability despite his constantly busy schedule are truly appreciated. His encouragement and efforts led this project to successful completion in a timely fashion.

Thanks also go to my friends and colleagues and the Chemical Engineering Department faculty and staff for making my time at Texas A&M University a great experience.

Finally, I would like to thank my family for their encouragement and support throughout this time and would like to specially thank, Nivedita, my wife, for everything.

# NOMENCLATURE

| | |
|---|---|
| NCMP | Nanocomposite |
| M_N, MN Polymer | Polymer made from ‘M’ chains with N monomers per chain |
| P | Pressure |
| T | Time |
| N | Number of atoms |
| V | Volume |
| CNT | Carbon nanotube |
| MD | Molecular dynamics |
| CG | Coarse grain |
| Normal condition | Zero atmosphere pressure and 300 K temperature |
| MWNT | Multi walled nanotube |
| SWNT | Single walled nanotube |
| DFT | Density functional theory |
| Ps | Picoseconds |
| Atm | Atmospheres |

TABLE OF CONTENTS

Page

Page

Page

Page

LIST OF FIGURES

Page

Page

Page

Page

Page

Page

# LIST OF TABLES

Page

# 1. INTRODUCTION

Polymer nanocomposite refers to a broad range of composite materials with one of the components being a polymer and the other being any material (organic, inorganic or metallic and is termed as nanofiller) that has at least one dimension in the order of 1 ~ 100 nanometer. The unprecedented set of properties obtained from nanocomposites has led researchers to have growing interest in this area and find out next generation materials for advanced applications. The possibility of engineering microstructures at the atomistic level to develop materials suited for a desired application is exciting and promising. However the lack of understanding of the physics of nanocomposites at nanoscale has kept the development of such materials still largely empirical. This naturally has restricted the achievement of a finer degree of control of properties of the nanocomposite through optimum use of the combination of properties of its constituents[1]. Thus, the increased demand for novel materials with enhanced properties and along with the potential of nanocomposites to meet the same has become a major driving force for conducting research in the field of novel nanocomposites.

Though the origin of nano structures dates back to the lecture by Richard Feynman in 1959 in an APS meeting[2], most of the development has occurred recently. In designing better nano-composites for future generation materials some of the major challenges are: understanding the structure-property relationships, interaction and integrity of the two components at the interface, the role of nanofillers in enhancing the properties of the resulting material.

In the present work we have utilized first principle calculations, atomistic simulations, coarse-grained modeling and constitutive equations to develop structure-property relationships for an amorphous aromatic piezoelectric polyimide substituted with a nitrile dipole, carbon nanotube and nanocomposites made from these components. We have elucidated structure-property relationships of carbon nanotube and the polyimide sample. We have built a coarse-grained model using atomistic level simulation of the piezoelectric polyimide in an attempt to address larger length and time

---

This dissertation follows the style and format of the Journal of Computational Chemistry.

scale phenomena. We have also compared and analyzed atomistic scale simulation results of the nanocomposite with those predicted from micromechanics analysis.

Overall this work presents a computational paradigm to rationally develop next generation nano-materials. Majority of this work has been carried out through classical molecular dynamics simulation. Accordingly, in the following parts of this section we have briefly described the fundamentals of classical molecular dynamics simulation, force field, ensembles and other related concepts of molecular dynamics. Any standard book on quantum mechanics can be used to understand the fundamentals of first principle calculations including density functional theory. The subsequent sections focus on utilization of molecular dynamics, first principle calculations, molecular mechanics, coarse graining and micromechanics model to better understand the characteristics of our carbon nanotube polymer nanocomposite system.

## 1.1 Molecular Dynamics

First introduced by Alder and Wainwright [3] molecular dynamics has long been the tool for researchers to predict bulk properties and to enhance many physical understanding related to different systems including biological and polymeric systems, based on atomistic calculations. Later in 1964 Rahman[4] carried out the first simulation with Lennard-Jones potential on liquid argon as oppose to hard sphere concept which was being used till then. The need for MD arose as unlike ideal gases and metallic crystals the properties of liquids were not easy to derive owing to their non-ordered structure and non ideal behavior. Early models of liquids involved hard spheres and disks to represent molecules of a liquid system. Due to the same reason while MD emerged as one of the main tool in predicting bulk properties of molecular systems, another method based on probabilistic approach called Monte Carlo, was also developed. Monte Carlo deals systems independent of time and hence is not capable of predicting dynamic properties. Metropolis [5] laid the foundation for modern Monte Carlo.

The theoretical basis for molecular modeling is statistical thermodynamics. Knowing the structure and dynamics of a system at the atomistic level can predict the

bulk property of a system at the macroscopic level. The approach used in knowing this information is molecular dynamics. MD generates information at the atomistic level including positions and velocities of an atom.

According to classical mechanics, given initial position and velocity of a particle and the forces acting on it at any moment, one can predict its new position and velocity from Newtonian mechanics using F = ma. So a calculation of force at every step is necessary in molecular dynamics simulation. The force is calculated by estimating the first derivative of the potential energy of the particle with respect to its position at that very instant. As a consequence evaluation of the potential energy at every moment is necessary to carry out the process. When more than one particle is involved in such a system, which is usually the case, different forms of interaction between them contributes to the potential energy.

Identification and evaluation of various types of interactions between different types of particles is done with a set of rules called force field. There are many types of force fields. Most types of interactions are all covered by a force field. But depending upon the type of particle involved in an interaction the evaluation of potential energy is different from force field to force field through different values of parameters involved. Force fields used for our study are Dreiding[6] and Consistent valence force field (CVFF)[7]. Dreiding force field was chosen because property predicted for polymer systems using this force field has given good agreement with the experimental values in the past [8,9]. CVFF force field has shown similar confidence in dealing with polymer systems[10]. The general structure of any force field is same. In section 1.21 we will briefly describe the different potentials related to Dreiding force field.

A force field has different functions describing the change in potential depending upon the structure of the system. The energy of a system can be written as:

$E = E_{VAL} + E_{NB}$ where

$E_{VAL} = E_B + E_A + E_T + E_I$

$E_{NB} = E_{VDW} + E_C + E_{HB}$

where:

$E_B$ = Energy due to Bond stretching (two body)

$E_A$ = Energy due to angle bending (three body)

$E_T$ = Energy due to torsion (four body)

$E_I$ = Energy due to out of plane configuration (four body)

$E_{VDW}$ = Energy due to van-der-Waals interaction

$E_C$ = Energy due to columbic interaction

$E_{HB}$ = Energy due to hydrogen bonding

While the first four terms are due to bonded interaction the last two terms are due to non-bonded interactions. All these terms will be discussed in more detail in section 1.2.1.

The calculation of the non bonded interaction is computationally expensive and contributes significantly to the overall simulation time. As this interaction happens between any two atoms, ideally this calculation should be carried out for each atom and hence the computational time required is in the order of $N^2$, where N is the number of atoms in the system. The electrostatic interactions are also called long-range interactions as they decay inversely with the value of 'r' and hence contribute even for a large value of 'r'. Algorithms have been developed to handle the problem in a way so that the simulation time can be decreased without sacrificing the accuracy of the results.

While length of simulation is one important aspect of a MD run, time step used for the simulation is equally significant. Ideally the time step in a simulation should be such that it can capture the fastest motion in the system which is typically the vibration mode of the lightest atom. In our study time step in the order of 1 fs to 10 fs has been used depending upon the system involved in the simulation. At times the fastest parts in a simulation are treated as rigid parts enabling one to use a larger time step resulting in acceleration of the whole process.

Since force field plays a major role in MD as discussed above, in the following section we will briefly mention different types of force field available and their applicability in different systems which consequently emphasizes on the importance of choosing a reasonable force field for a given system to obtain reliable

results. Detail information and understanding of Molecular dynamics can be obtained from any well known books in this field[11,12].

## 1.2 Force Fields

As discussed earlier it is implicit that the accuracy of the energy function directly affects the reliability and stability of the concerned MD simulation run. Since the computation of energy is required at every time step in MD, in the interest of larger system it is important to keep the energy expressions as simple as possible while sacrificing as less as possible in terms of accuracy. Till date many different force fields have been developed to suit different target systems. CHARMM, AMBER, Dreiding, CFF, PCFF, Universal and CVFF are some of the most frequently used force fields. Based upon need and target system, it's a seldom practice to modify an existing force field in order to get the best values out of it. Sometimes one may also go to an extent to develop a separate force field to suit the needs of the specific systems.

Force fields are classified in different classes. There are second generation force fields developed by high parameterization (examples CFF, PCFF COMPASS etc), rule based force fields like Universal and Dreiding where parameters are decided by some rules (example hybridization), classical or first generation force field like AMBER, CHARMM and CVFF which is also based on parameterization but mostly from experimental values as oppose to that of second generation which is based on quantum input and special purpose force field.

AMBER was originally parameterized for limited number of organic systems. The atom type it uses is more specific. It has also been used for polymers though it has been mainly developed targeting proteins and nucleic acids. It uses united atom model (some small atoms are lumped into other).

Similar to AMBER developed in early 1980's CHARMM was parameterized using experimental data. Unlike amber the hydrogen bond term is not used here separately. It is implicitly considered in van der Waals and electrostatic terms.

CFF (consistent force field) was developed by Halgren and the Biosym consortium. This force field incorporates cross terms and anharmonic terms. The parameters were estimated from ab-initio calculation. It was one of the first major force field developed based on ab-initio calculation.

The increase in use of force field for predicting structure and properties of systems can easily be observed in Figure 1. The positive trend in usage of force field is not only the result of improvement in algorithms and theories for better understanding of physics of the system but also due to improved computational power.

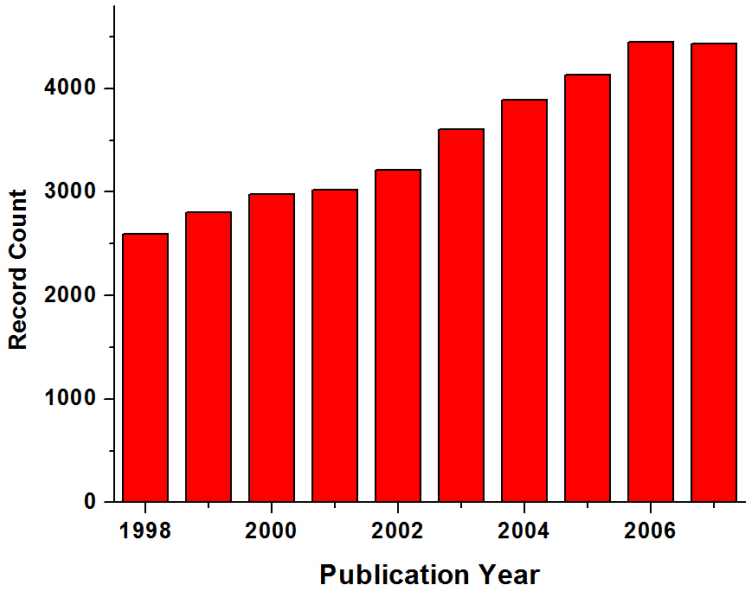


**Figure 1: Histogram analysis from ISI Web of Science with keyword 'Force Field'**

1.2.1 Dreiding Force Field

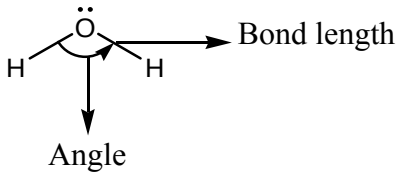


**Figure 2: Water molecule**

Figure 2 is that of a water molecule. Some of the terms mentioned below as used in the force field can also be shown in the structure of a water molecule. In the following, different forms of energy along with their functional forms in a typical force field are described.

- *Bond Stretch:* The first term in the energy expression for bonded energy describes the change in energy associated with the change in bond length Figure 3 from its equilibrium value.

**Figure 3: Bond stretching**

It is assumed that this has the same nature for molecules of same kind, e.g. C – H bond length in alkanes. The functional form is described either as in the form of simple harmonic oscillator or Morse function. The form of the energy in the harmonic oscillator is described as:

**Equation 1**

$$E = \frac{1}{2} k_e (R - R_e)^2$$

and in the morse function as:

**Equation 2**

$$E = D_e\left(e^{-\alpha(R-R_e)} - 1\right)^2$$

The value $R_e$ does not signifies the equilibrium bond distance as it might seem apparently. It is the value of the bond length in a virtual unperturbed state. For unstrained molecules however this value is close to equilibrium value. The morse function by Morse (1929) does a better job as it includes anharmonic terms near equilibrium and also gives a finite value of energy when it comes to breaking bonds as oppose to harmonic oscillator function. However if the starting structure of the system is far from equilibrium than from the energy derivative of morse function, the calculated restoring force will be very less and hence harmonic function will do a better job in quickly bringing the structure near equilibrium. The default form of bond stretching function in Dreiding is the harmonic form. The value of α in morse form can be related to harmonic form force constant by comparing the second derivative of energy. The values of these parameters are set in the force field file which is used for MD simulation.

- *Angle bending:* For describing the relation between the energy of a system with the different angle bending (Figure 4) of the same Dreiding uses two forms of equation:

**Figure 4: Angle bending**

Harmonic cosine form and harmonic angle form. The harmonic cosine form for an angle between IJK atoms, J being the center atom is described as:

**Equation 3**

$$E_{IJK} = \frac{1}{2} C_{IJK}\left[\cos\theta_{IJK} - \cos\theta_J^0\right]^2$$

where θ is the angle concerned. The equilibrium angle $\theta_J^0$ is believed to be independent of atom I and K and hence is only referred by J. The harmonic angle form is described by:

**Equation 4**

$$E_{IJK} = \frac{1}{2} K_{IJK} \left[\theta_{IJK} - \theta_J^0\right]^2$$

Harmonic cosine form is used as default functional form as the harmonic angle form does not lead to zero slope as θ approaches $180^0$. The force field file contains the values of the parameters of the equations that are used for MD.

- *Torsion:*

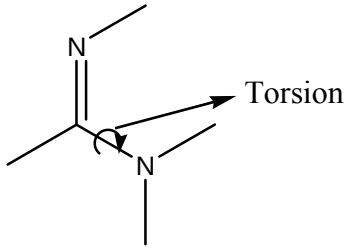


**Figure 5: Torsion**

Figure 5 shows what torsion is (as marked by the arrow). The interaction energy arising through torsional deformation between two bonds IJ and KL connected through JK is described in the form of:

**Equation 5**

$$E_{IJK} = \frac{1}{2} V_{JK} \left\{1 - \cos\left[n_{JK} (\vartheta - \vartheta_{JK}^0\right]\right\}$$

where $\vartheta$ is the dihedral or torsional angle. It is defined as the angle between IJK and JKL planes. $n_{JK}$ is the periodicity (how it is defined) and $V_{JK}$ is barrier to rotation. The parameters are taken independent of I and L. The torsional parameters are based on the type of hybridization and hence independent of the particular type of atoms involved.

The force field file contains the values of these parameters based on the type of hybridization.

- *Inversion:* This term accounts for the easiness or the difficulty of keeping all four atoms in the same plane when one single atom is bonded with the other three. Both for planar molecules and non-planar molecules this term is important to account for. Denoting the angle between the JIL and KIL plane as $\psi$ and n=2 (for planar centers) or n=3 (for tetrahedral centers) the energy due to inversion is expressed as:

**Equation 6**

$$E_{inv}(\psi) = \frac{1}{2} K_{inv} \{1 - \cos[n(\psi - \psi_0)\}$$

- *Nonbonded Interactions*: There are two expressions by which nonbonded van der Waals interactions are described. Lennard – Jones (LJ) 12 -6 forms and the exponential 6 form. The LJ form is described as:

**Equation 7**

$$E_{vdw}^{LJ} = AR^{-12} - BR^{-6}$$

And the exponential 6 form is described as:

**Equation 8**

$$E_{vdw}^{\exp 6} = Ae^{-CR} - BR^{-6}$$

As observed the difference between the two forms is the way of describing the repulsive part. For minute distance between two atoms the LJ potential gives a large repulsive force and hence throws the atoms away. Though the LJ potential requires only two parameters for the evaluation of the potential and faster to compute, the exponential 6 form shows a better agreement for short range interactions. The default form used in Dreiding is LJ. The parameter values are calculated differently if the interaction concerned is between two different types of atoms. The way it is calculated can be based on arithmetic or geometric combination of the parameters of the pure system.

- *Electrostatic interactions:* The interaction energy due to electrostatic interactions between atom ‘i’ and atom ‘j’ is calculated by:

**Equation 9**

$$E_Q = KQ_iQ_j / R_{ij}$$

where $Q_i$ and $Q_j$ are the charges on the atoms and $R_{ij}$ is the distance between them. K is a constant that takes care of the dielectric constant and unit consideration. Interactions are not calculated for atoms bonded to each other (1, 2 interaction) and those involved in angle terms (1, 2, 3 interactions) as these are taken care by bond and angle stretching interactions.

- *Hydrogen Bonding*: The center of, charges and van der Waals interaction must be in the center of the atom in order to have the position of the point charge on an atom and center of the atom to be the same. Satisfying this constraint it is difficult to parameterize a force field that correctly predicts the structure and the bond energy of $H_2O$ dimer, correctly predicts the sublimation energy and the structure of ice and correctly use van der Waals parameter for non-hydrogen bonded system. Dreiding uses a separate term to account for hydrogen bonding to describe interaction involving hydrogen atom with that of very electronegative atoms (e.g. N, O, F) associated with hydrogen bond. In that case in addition to van der Waals forces and electrostatic interactions, a hydrogen bonding potential of the following form is included.

**Equation 10**

$$E_{hb} = D_{hb}\left[5(R_{hb} / R_{DA})^{12} - 6(R_{hb} / R_{DA})^{10}\right]\cos^4(\theta_{DHA})$$

where $\theta_{DHA}$ is the bond angle between hydrogen donor (D), hydrogen (H) and hydrogen acceptor (A). $R_{DA}$ is the distance between the donor and acceptor atoms and the values of $D_{hb}$ and $R_{hb}$ depends on the convention for assigning charges.

## 1.3 Ensembles

As mentioned earlier, the success of MD simulations is primarily due to the existence of statistical thermodynamics. It acts as the bridge between microscopic structure and the macroscopic bulk properties. One of the basic concepts in statistical mechanics is that if one waits long enough he or she will observe almost all the microscopic states of the

system for which the system will have the same set of macroscopic properties. This is termed as ergodicity. In other words a set of macroscopic properties which completely defines a system has many microstates. These set of macroscopic properties by which a system is defined completely, are defined as different ensembles. There are mainly four kinds of ensembles in statistical mechanics. Ensembles are nothing but a set of configurations (microstates) of the same set of molecules (making the system) while being consistent with the constraints with which the system is characterized macroscopically. The main four kids of ensembles are namely micro-canonical (N, V, E), canonical (N, V, T), grand canonical (T, V, μ) and Isothermal-Isobaric (N, P, T) ensembles where N stands for number of particles, V stands for volume of the system, P is pressure T is temperature and μ is chemical potential. Different algorithms exist to ensure the constant property dynamics while running MD. All these ensembles are related to macroscopic property by the corresponding partition function.

- *NVE or microcanonical:* The value of macroscopic properties N, V and E are constant in this ensemble. As these three macroscopic properties are kept constant the value of Pressure, Temperature and chemical potential are determined for the equilibrated system.
- *NVT or canonical ensemble:* The value of N, V and T are constant in this ensemble.
- *NPT or Isothermal-Isobaric ensemble:* In this ensemble as the name suggests the different systems which are dealt with has the same value of N, P and T.
- *TV μ or grandcanonical ensemble:* Here the value of T, V and μ are kept constant.

Any standard book[13-15] can be referred for detailed description of these ensembles and their relation to the macroscopic property of the material.

## 1.4 Electrostatics

Though the interaction due to charges is already taken care by force field energy expressions and mentioned above, the evaluation of charges on atoms and different algorithms to handle this long range interaction is worth mentioning separately as it takes a major part of the computational usage and hence determine many limitations to

calculations. The long range nature of this interaction makes it the most expensive part of the simulation and hence even a slight improvement here helps a lot in the whole run. For a system consisting of N atoms the number of interactions needs to be evaluated each time step is ~ $N^2$. It is obvious that for larger system this becomes very expensive and hence one of the major factor. One of the traditional ways of handling is to truncate the range of interaction between charges after a certain cut-off distance. The Ewald summation technique (1921) is a better way to handle these interactions for infinite periodic systems.

### 1.4.1 Ewald Summation

In this technique instead of completely neglecting the effect of charges outside the cutoff radius of any atom, the effect is dealt in an efficient way to ensure better results. Any charge is assumed to be the sum of the charge itself, a diffuse charge surrounding the point charge in a way that the total charge is exactly equal and opposite to the point charge and a diffuse charge of the same nature but opposite in sign as the other diffuse charge to maintain the total charge. The reason for adding a diffuse charge to cancel the effect of point charge and treating its effect as a diffuse charge is that the sum $\sum_{i=1}^{\alpha}\sum_{j=1,i\neq j}^{\alpha} K\frac{q_i q_j}{r}$ is conditionally convergent. The diffuse charge however can be expressed as sum of infinite sine ad cosine series and hence the summation can be computed through Fourier transform. The CPU time scales as $N^2$ for a fixed cut off in ewald summation.

### 1.4.2 Particle Particle Particle Mesh Method

As mentioned above the convergence of the infinite sum needed to calculate coulomb energy is poor. This factor can be significantly improved if a canceling charge distribution can be added and then computed through ewald summation. But the CPU time requirement (O ( $N^2$ )) still remains expensive due to the reciprocal space part of the ewald sum. The order of computation can be made ~ NlogN with the help of

combination of a similar approach like ewald summation technique and fast Fourier transform. The function is rewritten as given below:

$$\frac{1}{r} = \frac{f(r)}{r} + \frac{1 - f(r)}{r}$$

This idea is similar to adding diffused charges in ewald summation. However careful choice of f(r) is important for efficient use of the method. This makes a significant difference in the computational efforts.

## 1.5 Speeding up Simulation

Speeding up the simulation is definitely one of the most important areas in molecular dynamics without losing much accuracy. As mentioned above the calculation of long range interaction namely the electrostatic interaction becomes expensive as system grows bigger and bigger and starts playing a major rule in the speed of the simulation. Without any approximation or tricks the time needed to calculate these interactions will be proportional to $N^2$. As discussed in the above section one way to handle these interactions approximately is to use idea of cut off. Even in techniques like ewald summation the idea of cut off is still valid as after that cut off distance the potential is calculated through ewald summation instead of just chopping it off. So the interaction with neighboring atoms is calculated in each time step those who are inside the cut off radius and the interaction potential due to rest of the particles is handles in different ways depending upon the technique used. In order to find out the atoms which lie within the cutoff radius of a specific atom, the distance with other atoms need to be calculated at each time-step for each atom. This calculation is also proportional to $N^2$ and has the potential of slowing down the whole simulation. Verlet list, linked list method and combination of verlet and linked list method are some techniques which play a significant role in making this process less expensive and yet not sacrificing the accuracy.

### 1.5.1 Verlet List

Verlet first proposed to build a neighbor list for each atom which will contain all its neighboring atoms. Just outside the cutoff radius for interactions another bigger cut off radius is drawn. The region between inner and outer radius is called the skin. The skin is built so that in some specific timeframe no atom outside the skin can travel into the region inside the (inner) cutoff radius. A list is built of all the atoms within the bigger sphere of all the atoms. These atoms in that specific timeframe can move in and out of the cutoff radius. Accordingly one does not need to calculate the distance between a specific atom of concern and the atoms outside the region of the skin at every time-step. While this seems to make the calculation in O(N), the fact is that after sometime the neighbor list need to be updated (as atoms outside the skin has the possibility of getting in inside the cutoff radius by then) after some specific time. In effect it again becomes O ($N^2$) periodically, whenever the list needs to be updated.

### 1.5.2 Linked List Method

As the system grows bigger and bigger the verlet list of keeping track of neighbor becomes inefficient. Linked list method keeps track of neighbors in a different way. The super cell containing the concerned atom is divided into small cubic cells. So each cell will have 26 neighboring such child cells. The concerned atom will interact with the atoms in its own cell and the periodic images in the neighboring atoms. Since the operation of allocation of each atom in a cell scales with N and the total number of cells that needs to be considered is independent of system size, this method scales as N.

To run faster simulation the time step becomes an important factor. The maximum size of the time step is determined by the fastest mode in the system involved. Generally the vibration modes involving the lightest atoms in the system are the fastest motion in a system. The SHAKE algorithm [16] is one of the most used algorithms which are usually applied to X – H bond types to increase the time step of the simulation. It freezes the fastest vibration modes in the system and thereby gives the ability to increase the size of the time step. Later other algorithms like RATTLE and generalization of

SHAKE like GSHAKE, QSHAKE algorithms were developed which allowed even larger time steps with better stability of the system.

Other than changing the time step of a system for faster simulation another way to deal with this is called multiple time step algorithms. Here the fast and slow motions of the system is separated assuming that the interactions involving larger distances vary slowly with time.

## 1.6 Integration Techniques

To carry out Newtonian mechanics at each time step the equation of motion needs to be integrated to find out the positions and velocities of the atoms for $t = t_0 + \tau$ where $t_0$ is the starting point. Different numerical integration techniques are available to carry out these. The chosen technique also plays a key role in the accuracy of the simulation.

To describe these different methods lets first consider a system of N atoms with co-ordinates $x_i$ , $y_i$ and $z_i$ or $\vec{r}_i$ . From Newton's equation of motion we have :

**Equation 11**

$$m_i r_i^{\cdot\cdot} = \frac{\partial U_{POT}}{\partial r_i} = F_i$$

Where:

$m_i$ is the mass of the $i^{th}$ atom

$F_i$ is the force on the $i^{th}$ atom due to the change in potential energy of the same.

### 1.6.1 Verlet

From Taylor expansion around a point we can write that:

$$r(t_o + \Delta t) = r(t_0) + \frac{\partial r(t)}{\partial t}\Delta t + \frac{1}{2!}\frac{\partial^2 r(t)}{\partial t^2}(\Delta t)^2 + \frac{1}{3!}\frac{\partial^3 r(t)}{\partial t^3}(\Delta t^3) + O(4)$$

And similarly

$$r(t_o - \Delta t) = r(t_0) - \frac{\partial r(t)}{\partial t}\Delta t + \frac{1}{2!}\frac{\partial^2 r(t)}{\partial t^2}(\Delta t)^2 - \frac{1}{3!}\frac{\partial^3 r(t)}{\partial t^3}(\Delta t^3) + O(4)$$

From the above two equation one can write:

$$r(t_o + \Delta t) = 2r(t_0) - r(t_0 - \Delta t) + \frac{\partial^2 r(t)}{\partial t^2}(\Delta t)^2 + O(4) \text{ Or}$$

$$r(t_o + \Delta t) = 2r(t_0) - r(t_0 - \Delta t) + \frac{F}{m}(\Delta t)^2 + O(4)$$

So if one has past information about the position of an atom, the position of the same can be calculated from this simple equation without even having the knowledge of the velocity of the atom. Also the error is in the order of $(\Delta t)^4$, which is remarkable. Also at any point if the velocity needs to be calculated it can be directly calculated from the following equation derived from above equations:

$$2v(t)\Delta t = r(t_o + \Delta t) - r(t_o - \Delta t) + O(2)$$

The order of error here is $(\Delta t)^2$. The verlet algorithm is one of the most widely used integration technique for its simplicity and accuracy.

### 1.6.2 Leapfrog Verlet

There are some variants of verlet algorithm. As the earlier one this one is also is based on truncated verlet algorithm. Accordingly the position of a particle can be expressed as

$$r(t + \Delta t) = r(t) + v(t)\Delta t + \frac{f(t)}{2m}\Delta t^2 + \ldots$$

Now the velocity of a particle at half integer time step can be expressed as

$$v(t - \Delta t/2) \equiv \frac{r(t) - r(t - \Delta t)}{\Delta t}$$

And

$$v(t + \Delta t/2) \equiv \frac{r(t + \Delta t) - r(t)}{\Delta t}$$ This leads to:

$r(t + \Delta t) = r(t) + \Delta t v(t + \Delta t/2)$ And from the verlet algorithm, we get the following expression for velocity updates.

$$v(t + \Delta t/2) = v(t - \Delta t/2) + \Delta t \frac{f(t)}{m}$$

However it must be noted that the velocity and position are not computed at the same time step and hence the total energy in this case is not computed at the same time.

In the present work, runs executed using Cerius[2.0] used the above-mentioned algorithm for integration.

### 1.6.3 Velocity Verlet

Another variant of verlet algorithm is velocity verlet. In this case the following equations are used to integrate the equation of motion.

$$r(t+\Delta t) = r(t) + v(t)\Delta t + \frac{f(t)}{2m}\Delta t^2 + \ldots$$

And

$$v(t+\Delta t) = v(t) + \frac{f(t+\Delta t) + f(t)}{2m}\Delta t$$

In this algorithm the new positions are calculated, based on which the new velocities and from those the new forces on atoms. LAMMPS uses this scheme as the default integrator scheme for equation of motion.

## 1.7 The System

### 1.7.1 Piezoelectric Polymer

The piezoelectric polyimide studied by us is an amorphous, aromatic polyimide substituted with nitrile dipole. Piezoelectricity refers to the electro mechanical coupling in materials. The term ‘piezo’ derives from the Greek translation of ‘pressure’ or ‘to press’ and is defined as ‘polarization in a substance resulting from application of mechanical stress’ [17] Conversely this effect also works reversibly as applying a voltage to the material results in deformation of the piezoelectric crystal.

Piezoelectric activity in polymers has been quite of interest to researchers for a while because of their numerous potential applications ranging from microelectronics to spacecraft. Thousands of years before modern world learned the concept of piezoelectricity the Uncompahgre Ute Indians from central Colorado, used the concept to generate light in special ceremonial raffles made from buffalo rawhide, filling the same with clear quartz crystals (Figure 6).

**Figure 6: An Uncompahgre Ute Buffalo rawhide ceremonial rattle filled with quartz crystals [18]**

The rattle produced flashes of light created by the piezoelectric effect of quartz crystals being subjected to mechanical stress when the rattle was shaken in darkness.

Many years later in the early 19th century, the ability of generating electrical charge when heated by some certain mineral crystals was discovered and the property was named pyroelectricity by David Brewster in 1824[18-20].Shortly after that in 1880, Pierre and Jacques Curie discovered piezoelectric property of certain crystals[19]. A year later in 1881 the reversibility of piezoelectricity was proved mathematically by Lippmann[19], which was later confirmed by Curies.

Later piezoelectric transducers replaced electric transducers in SONAR (**SO**und **N**avigation **A**nd **R**anging) technique, a technique used widely to identify under water objects[20] during World War I . The success of piezoelectric transducers in sonar created a lot of interests in developing new piezoelectric materials and applications.

The potential of piezoelectric polymers of being used as sensors, actuators, structural reinforcement, and use in micro-electro-mechanical systems or MEMS, nano-electro-mechanical systems or NEMS has made researchers to have more interest in understanding the physics behind its properties. Some of the latest research tells the possibility of building piezoelectric nano-generators [21], spacecraft applications[22], possible use in sensor and actuator applications[23] etc.

The polymer in the present work is made from (β – CN) APB/ODPA monomer (not available commercially), which is made from 19 hydrogen atoms (17 atoms and one atom at the head and another at the tail of the monomer), 35 carbon atoms, 3 Nitrogen atoms and 7 Oxygen atoms. The monomer structure is shown in Figure 7 and Figure 8 as given below. The 'CN' group attached to the benzene ring is the nitrile group as shown in Figure 7. Other than nitrile group the other part highlighted in the figure are the anhydride groups of the monomer.

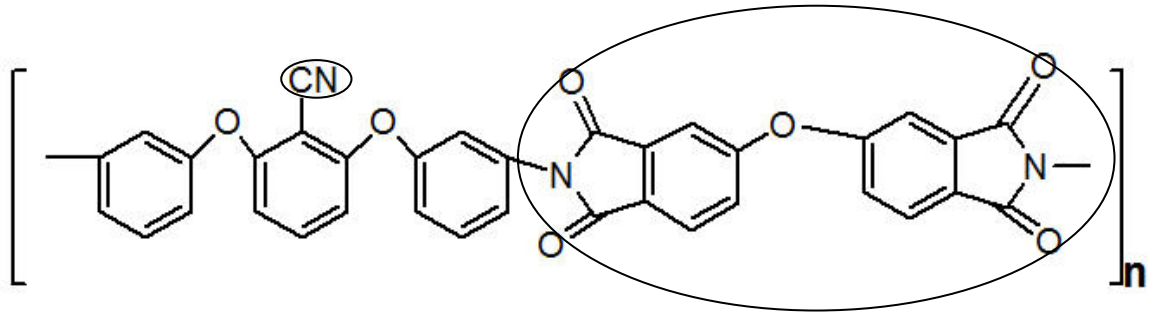


**Figure 7: Molecular structure of the monomer ($C_{35}H_{19}O_7N_3$)**

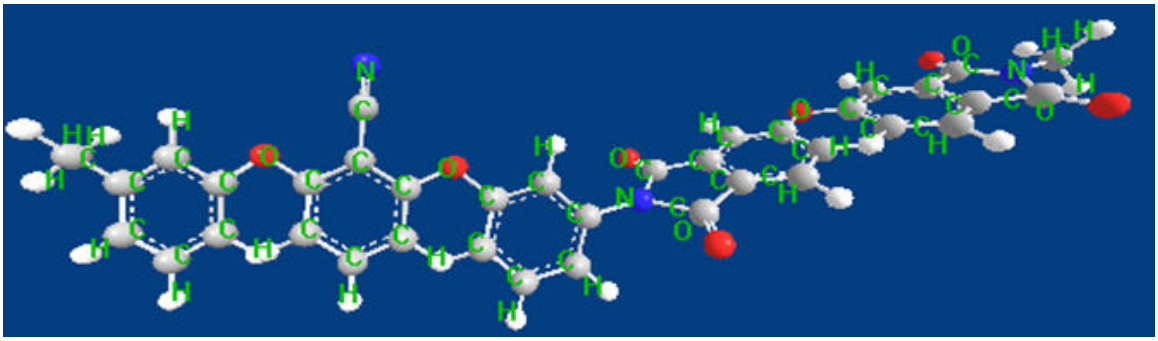

**Figure 8: Molecular structure of the monomer in a simulation window**

The nitrile and anhydride groups in the polymer mainly contribute to the polarization of the whole system. It has been shown[24] that the nitrile group contributes to 48% of the total polarization and 39% of the polarization is contributed from the di-anhydride group. A more detailed overview of data related to polarization of different piezoelectric polymers can be found in [25].

### 1.7.2 Carbon Nanotube

The second component of the nanocomposite, the nano-filler in the present study, carbon nanotube is nothing but a honeycomb lattice (graphite sheet, Figure 9) rolled into a cylindrical tube. Depending upon the direction of rolling, also defined as the chiral vector, the nanotube is given the name of (n, m) nanotube. The two extreme cases of chiral nanotubes are zigzag and armchair nanotubes (Figure 10).

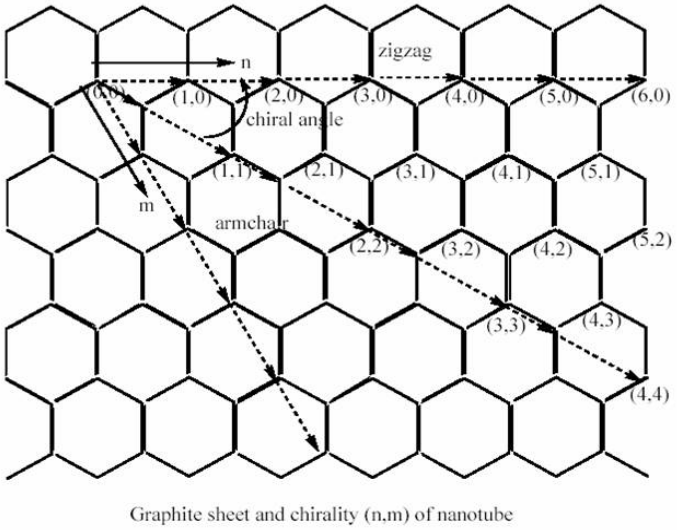


**Figure 9: Graphene sheet**

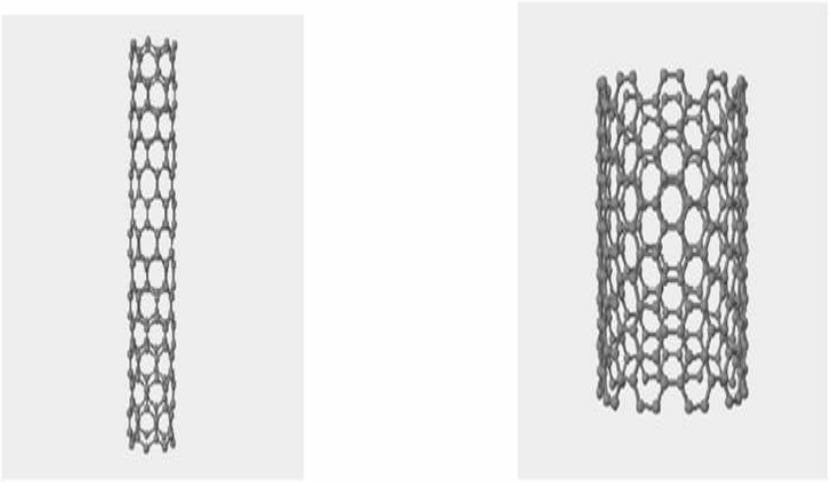

**Figure 10: Zigzag and armchair nanotube**

Member of the fullerene structural family, nanotubes having $sp^2$ bond structure, similar to that of graphite is expected to be very strong structures as the strength of C-C bond in graphite is one of the strongest bonds in nature. Held together by van der Waals forces (forces arising from polarization of molecules into dipoles) the nanotubes generally tend to align themselves in bundles and hence also termed as nanoropes.

The observed (experimentally and theoretically) exceptional mechanical properties of Carbon nanotubes (both single walled and multi walled) and its potential in enhancing properties of nanocomposites have made it the most commonly used nanofiller. However the cost of the same still remains high and research in producing nanotubes economically is one area of concern among researchers. Figure 11[26] gives an idea about the price and the direction of the price trend of carbon nanotube.

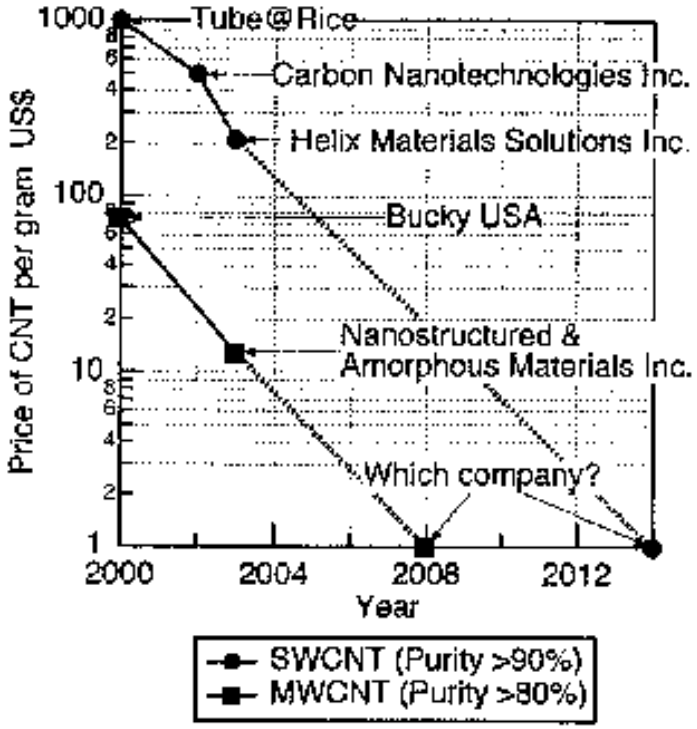


**Figure 11:Cost of producing nanotubes** [26]

1.7.3 Polymer – Nanocomposite

The concept of composite is not new. In mid 1950's 1960's, the demand for lower weight and higher rigidity material for space applications, electronics and other applications became the driving force for interest and investment in composite research. Some of the composites with fillers as carbon black and fumed silica have been used for more than a century. However the increase in research and development of polymer nanocomposite came later in late 1980's both in commercial research organizations and academia. The first company to commercialize polymer nanocomposite was Toyota in 1980's in one of its popular car model. They used Nylon-clay nanocomposite for timing belt covers developed in Toyota's central research and developmental laboratories[27]. After getting introduced commercially in market in 1980, the interest in the research of the same (polymer nanocomposite) kept on increasing as some people came up with

unprecedented combination of properties of nanocomposites. Messersmith et. al showed an increase of 58 % in Young's modulus in epoxy by adding only 0.04% of mica-type silicates or commonly known as MTS[28]. Yano et. al. showed a 50% decrease in the permeability of polyimides at only 2% loading of MTS[29]. While silicate helped nanocomposite research to take it first few steps, it next thrust after Smalley discovered fullerene in 1985 followed by S. Ijima's discovery of multi walled Carbon nanotube in 1991[30] while manufacturing fullerenes by electric arc deposition method. Though nanotube like material was first observed as early as 1960's[31] it was only in 1990's its importance was first realized after proper characterization and manufacturing. Later S. Ijima[32] and Bethune et. al[33] both came up with Single walled nanotube independently. Significant development in chemical processing of nanoparticles at the same time helped to carry on research on nanocomposites.

The primary reason for nanocomposites behaving significantly different from its composite counterparts is the nano dimensions of the nanofillers, where quantum effect plays a significant role in obtaining excellent set of properties. Due to the presence of nanoparticles many composite property changes in a different way than it would have been otherwise. As an example because of their small size it does not scatter light significantly and hence changes the mechanical and electrical property without changing the optical property. Due to their small size it does not create large stress concentration and hence does not increase the ductility of the polymer. Having a large surface area to volume ratio, the interfacial area between polymer and nanoparticle is large. This interface is of primary importance as it controls the degree of interaction between the two materials and hence plays a major role in the properties of the composite. Having control over the interface region is thus an important factor. It is defined as the region from where the property starts differing from the bulk polymer property. One example one can think about regarding relation of property and interface region is the stress transfer mechanism from the bulk polymer to the nanoparticle. More efficient the stress transfer is, stronger will be the composite.

Due to the limitation in coming up with experiments for finding out the mechanical properties of the carbon nanotube, numerical studies were conducted and exciting set of properties of carbon nanotube was found out. This gave a huge driving force in using carbon nanotube in using it as a filler material for nanocomposites which also includes polymer nanocomposite. A comparison of the number of articles published and presented from 1986 onwards till 2004 has been given in Figure 12. The rapid increase in the research of nanocomposite interest is very obvious from the figure given below. It seems that the major change in the slope of the curve came after nanotube was discovered. Before that it seems that there was not much increase in nanocomposite research from year to year. While the main reason can be attributed to nanotube discovery and its exceptional set of properties, some of the fascinating initial results obtained from silicate nanocomposite are also responsible for this change.

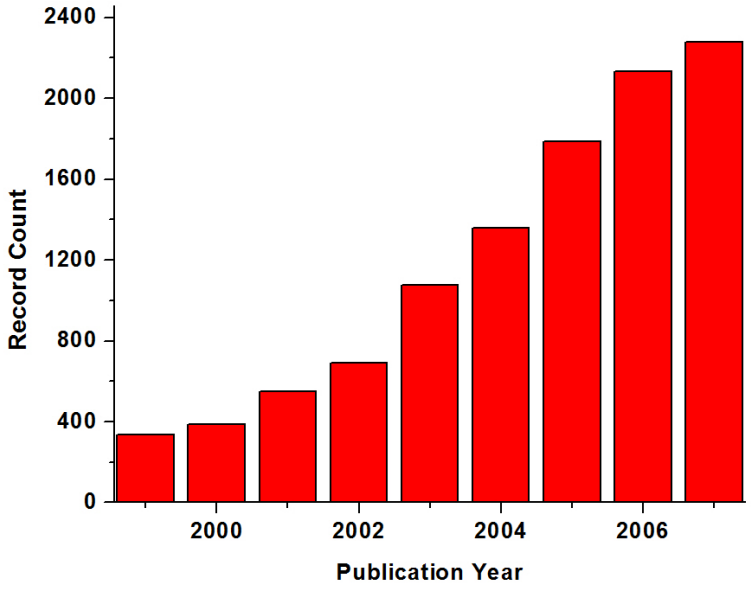


**Figure 12: Comparison of journal, conference articles on 'Nanocomposite' on yearly basis (Based on a keyword search 'Nanocomposite' in ISI Web of Science)**

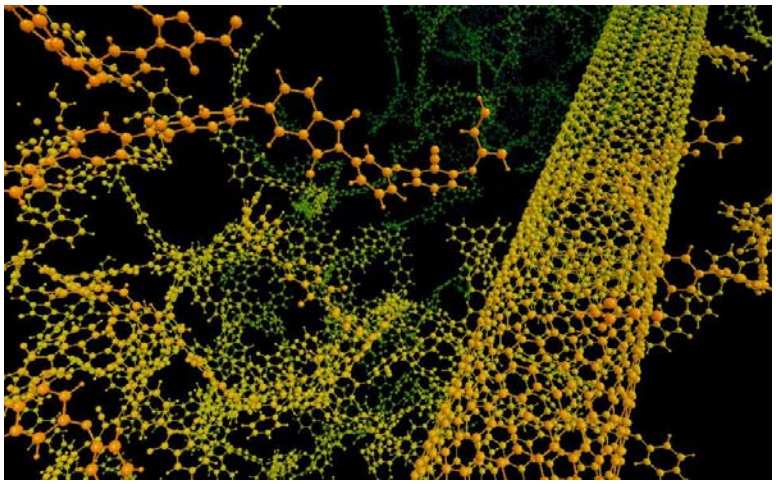

**Figure 13: Polymer - CNT nanocomposite**

Figure 13 shows a crude model of a polymer-carbon nanotube nanocomposite. It must be noted that for modeling purposes the nanotube is treated as an infinite one and hence exist along one of the direction of the unit cell.

Polyimides are widely used in applications ranging from microelectronics to spacecraft technologies. These are thermally stable polymers having good set of properties[34]. Carbon nanotubes, which are used as nanofillers (diameter is in the nanometer range); on the other hand has exceptional set of properties. It can be used as conductive filler in polyimides to achieve a certain degree of conductivity and also has the potential for improving mechanical properties and thermal properties at the same time. Here we attempt to understand the relation between structure and properties at the microscopic level for a piezoelectric (The term piezoelectric refers to the coupling between elastic and dielectric variables of a material) polyimide and its carbon nanotube based composites. This will enable one to come up with the design for next generation material which has wide range of applications in spacecraft technology, sensors, MEMS (Micro electromechanical systems), NEMS (Nano electromechanical systems) and other devices. In other words, we need to come up with nanocomposite materials based upon understanding of the structure-property relationship with desired material properties tailored to the application needs while economically permissible. In order to perform

computational experiments on the nanocomposite system we have used molecular dynamics simulation, molecular mechanics and ab-initio calculations as our main tool.

## 1.8 Objective

Here we attempt to develop a computational approach for understanding the structure and properties relationships at the microscopic level for a piezoelectric polyimide and its carbon nanotube based nanocomposites, which are stable at high temperatures. We also intend to have better understanding of the physics behind polyimide nanotube interaction which will also help design future generation nanocomposite for different applications.

Piezoelectric activity in polymers has been quite of interest to researchers for a while [35-37]. PVDF (Poly vinylidene fluoride), one of the popular piezoelectric polyimide has got a lot of attention from researchers [38-41] for it's piezoelectric activity. Evidence [42-44] of piezoelectric behavior by Nylon is also shown in literature. Though PVDF shows a large piezoelectric response it cannot be used for high temperature applications[36,45]. The amorphous polyimide made of (β – CN) APB/ODPA monomer we are interested in is a piezoelectric polyimide having a $T_g$ (glass transition temperature) approximately 493 K which gives a much higher temperature range for application. Experiments has shown it can generate piezoelectric responses at elevated temperatures[46]. One of the main challenges faced with regards to application of this particular polyimide is its low piezoelectric response than required[47] in practical utilities. To enhance this, there is a need to understand the physics behind the electromechanical coupling in the polyimide and the parameters affecting the same. In other words this relates to the understanding of the different interactions and phenomena happening at atomistic scale resulting in bulk response of the materials.

An amorphous polar polymer can be made piezoelectric by poling after applying a strong electric field at a temperature $T_p \geq T_g$ . This introduces both induced and orientational polarization through dipole alignment due to an applied electric field[35]. The temperature is then lowered below $T_g$ in the presence of the field and freeze in a polarized state. Once the applied field is taken out while the induced polarization is lost,

the orientational polarization still remains and gives remnant polarization. This remnant polarization is proportional to the piezoelectricity of the material and hence the enhancement of piezoelectricity can be achieved by maximizing remnant polarization, which is given by equation 12 [48].

**Equation 12**

$$P_r = \varepsilon_0 \Delta\varepsilon E_p$$

where $P_r$ stands for remnant polarization, $\varepsilon_0$ is the permittivity of the free space, $E_p$ is the applied electric field and $\Delta\varepsilon$ is the dielectric relaxation strength at $T_g$ (change in dielectric constant during glass transition of the material). In order to make improvements in piezoelectric response and find and suggest ways of improving the parameters affecting this property and other desirable properties, modeling of the material emulating the actual material and its properties becomes very important. Carbon nanotube which has large potential in property enhancements[26,49-53], has shown to wet the polyimide in question very well [54]. This is an encouraging fact for the interfacial interaction between the bulk polyimide and the nanotube and together with exceptional set of properties of carbon nanotube gives us hope of coming up with a material with enhanced and desired set of tailored properties meeting the need of different applications.

In short our objective is to develop a computational approach for facilitating the understanding of the structure property relationship of a specific polymer, $(\beta - CN)APB/ODPA$ polyimide, carbon nanotubes and their composites. We have applied theory and computation to characterize these materials and have explained the relations between various bulk properties with the structure of a material. In particular we have studied the thermal, mechanical and dielectric properties of the polyimide, nanotube and their nanocomposites through multi-scale modeling technique. We expect the results obtained and understanding gained through modeling and simulations may be used in guiding development of new nanocomposites for various advanced future applications.

## 1.9 Background

The polyimide in question has gotten researcher's attention because of its piezoelectric properties and thermal stability. However, due to limited chain mobility this polyimide cannot orient itself efficiently when an electric field is applied and hence the piezoelectric response is lower than desired. Ways of increasing this property has been one of the main focuses of research for this polyimide. Park et al. [23] studied the polyimide made of (β – CN) APB/ODPA monomer. 'Process control' approach was taken to maximize the dipole orientation of the amorphous polymer. The dielectric behavior, remnant polarization and piezoelectric responses were assessed as a function of temperature and frequency. Since one of the most important issues here is the response to poling procedure of the polymer and the retention of the polarization, three different form of monomer were tested in this regard. It was found that the uncured oriented monomer exhibits the largest dipole moment followed by uncured and un-oriented one and finally the fully cured form of the monomer. It was also found that if the dipole concentration is increased at the monomer level it increases the piezoelectric response even more. Orientations of the dipoles are done better in low temperature that tends to randomize at high temperature due to thermal energy. In another work [47] Simpson et al. focused on the synthesis and characterization of the same polyimide. Presence of 94% remnant polarization was observed at 150 C and some was retained till the glass transition temperature. This retention of the remnant polarization observed even near the glass transition temperature of the polyimide was certainly encouraging for high temperature applications. TSC or thermally stimulated current method was used to evaluate the value of $P_r$ or remnant polarization of the system. The values obtained were one magnitude lower than that of PVDF and also that is required for many applications. Ounaies et. al. [24] did molecular modeling and dielectric measurements on the same polyimide. Molecular modeling was done to investigate the response of the polyimide to the temperature and electric field. The polymer was poled at high temperature and then was cooled down to room temperature to yield the steady state value of remnant polarization by molecular dynamics. From the molecular dynamics result it was

observed that the nitrile group in the polyimide constitutes 48% of total polarization on average. The di-anhydride part provides 39% of the polarization. The computational and experimental results showed good agreement. Nanocomposite made of another piezoelectric polyimide CP2 (having a similar structure like (β – CN) APB/ODPA polyimide), an aromatic colorless polyimide with carbon nanotubes as filler material was investigated by Ounaies et. al.[55] . The composite was prepared by in situ polymerization under sonication. TEM (Transmission Electron microscopy) study confirmed a good dispersion of single walled nanotube (SWNT) by conducting the polymerization in this way. The aspect ratio of the carbon nanotubes were around 1000. The storage modulus was found to increase linearly with increasing SWNT concentration, reaching 65 % improvement with 1vol % SWNT. The optical transparency also remained high at that loading. It was found that the experimental conductivity obeys a percolation like power law. According to percolation theory predicts there is a critical concentration or percolation threshold at which a conductive path is formed in the composite converting the material from capacitor to conductor. The experimental data was fitted nicely with the power law expression for percolation. Park et al. [56] looked into dispersion of carbon nanotubes in CP2, an aromatic colorless polyimide. In situ polymerization of monomers in presence of sonication was carried out to obtain better dispersion of SWNT. It was observed that the polymerization reaction was retarded a little bit in presence of SWNT. The degree of dispersion of SWNT in the polymer matrix was largely influenced by their state of dispersion in the solvent prior to adding with polymer matrix. The conductivity of the composite was measured and it showed good agreement with power law like percolation theory. Increase in storage modulus of the composite was also observed which varied linearly with SWNT volume %. In [35] poling of piezoelectric polyimide ((β – CN) APB/ODPA monomer and APB/ODPA monomer) was modeled using modified CFF91 force field. The modification of the force field was done based on the results obtained for semi empirical calculations of the monomer. Molecular dynamics method was used to calculate the dielectric relaxation strength which is proportional to the remnant polarization. The radial distribution function was investigated to confirm the

amorphous nature of the sample. Using Arrhenius time temperature relationship the sample was poled at a 2000 K for 50 ps to achieve the relaxation needed during poling which is believed to happen in the microsecond range. The dielectric relaxation strength value obtained with modeling was compared with experimental values which gave good agreement. Dynamic mechanical analysis was performed on (β – CN) APB/ODPA polymer in an unpublished work[22], where the increase in storage modulus was shown with inclusion of carbon nanotubes. The Halpin-Tsai[57] model was used to predict the composite storage modulus and was found that it underestimates the same. Improved thermo-mechanical property of the composite was observed, along with reinforcement and increment of $T_g$.

# 2. CARBON NANOTUBES

The excellent set of properties of carbon nanotube and carbon nanotube-based nanostructures has been established by various studies. However the claimed property values and trends have not been unanimously agreed upon. Using state of the art molecular dynamics and ab initio methods, we have extensively studied the mechanical, thermal and structural properties of carbon nanotubes and carbon nanotube based nanostructures. Additionally this study aims to address the approaches used in various studies to assess the validity and influence of various definitions used for determining the physical properties as reported in earlier experiments and theoretical calculations. We have come up with equations, which quantitatively address the wide differences in trend and values of nanotube axial modulus available across the literature. Applying a novel bond rearrangement scheme, we have found similar values in twist modulus of zigzag and armchair nanotubes. This opposes the claim of difference that was shown to be valid only at finite limit in our study. We have shown that the contribution of van der Waals energy in a multi-wall nanotube is powerful enough to make it hexagonal in shape but negligible in affecting the axial modulus. These insights will also help in designing micromechanics model of materials made from carbon nanotube or nanotube like structures. In particular, we have calculated the mechanical properties (young modulus, bending modulus and twist modulus) of isolated and bundled nanotubes, single and multi-wall nanotubes and single and multi-wall carbon nanotube based tori. We also report studies on thermal variation of moduli and thermal expansion of nanotubes. The result obtained by first principles calculation based interatomic potential agrees well with the experimental results.

## 2.1 Introduction

The plethora of definitions, procedures, techniques, instruments, theories or the lack of these has established the superiority of nanotubes. However they also have raised questions for the values observed, claimed trends and their dependence on variation of

external parameters. For instance, the elastic modulus of carbon nanotube has been calculated and measured by various approaches, ranging from values of several hundred GPa[58-63] few (Y>=1) TPa[20,64-66] to as high as 5.5 TPa [58]. A brief inspection of Figure 14 and Table 1 gives a rough idea of the scattered nature of the data available.

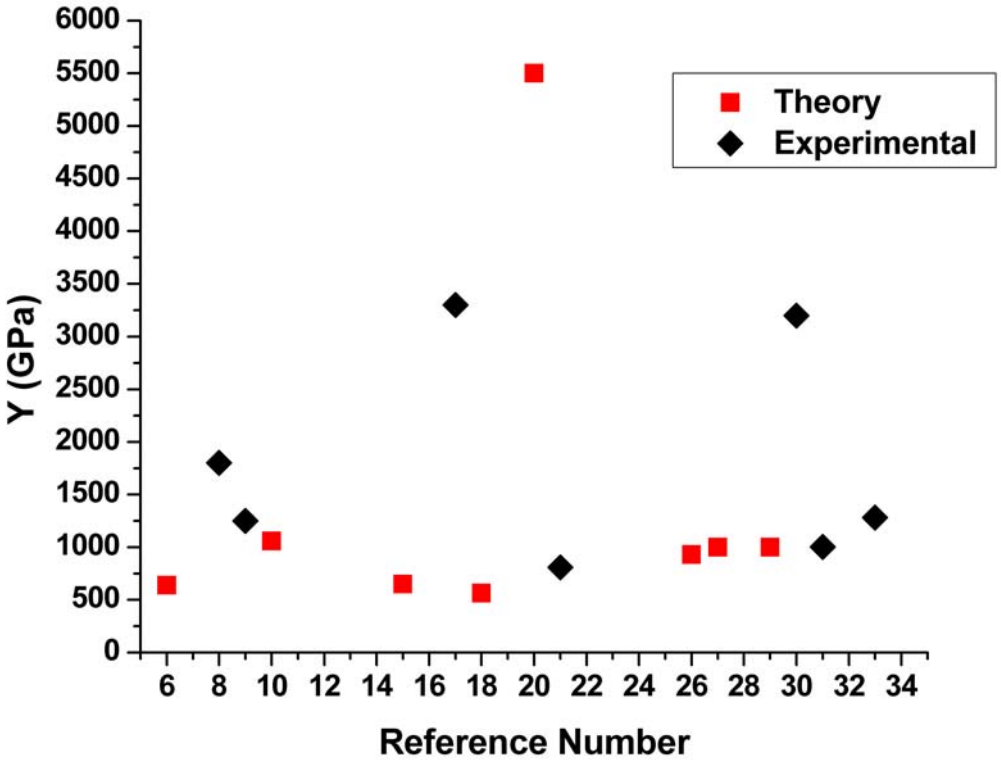


**Figure 14: The Young modulus values reported in 14 different references (theory and experiments are plotted together, to indicate the scatter mentioned in the text exists in both) for CNT. The x-axis numbering corresponds to the sequence of citation in section 2**

**Table 1: Axial elastic modulus of single-wall isolated carbon nanotubes**

| Reference | Tensile Modulus | Method |
|---|---|---|
| [59] | 650 GPa<br>(10, 10) | MD simulation using Tersoff - Brenner potential near 0 K. T < 0.005 K |
| [67] | ~ 1 TPa<br>(5, 5) and (9, 0) | *ab initio* Hartree-Fock 6-31 G basis set |
| [68] | $\frac{\partial^2 E}{\partial \varepsilon^2} = 55eV$ | Lattice dynamical model Born perturbation technique was used to derive analytical expression of sound velocities |
| [61] | 640 GPa | Molecular mechanics. Second derivative of energy with respect to strain |
| [60] | 563 GPa | Empirical force constant model. Second derivatives of energy, with respect to strain. |
| [69] | ~ 1 TPa | Analytical model based on molecular mechanics approach. Force constants obtained from experimental data of graphite. |
| [70] | $\frac{\partial^2 E}{\partial \varepsilon^2} = 52eV$<br>(10, 10) | DFT calculation with LDA approximation. |
| [71] | 930 GPa<br>(d = 14 A) | First principle calculations, using LDA in DFT. |
| [64] | 1.8 TPa (average of 11 samples) | Measuring amplitude of intrinsic thermal vibrations by Transmission electron microscope (TEM) |
| [20] | 1.06 TPa | LDA approach based on LCGTO. |
| [72] | ~ 1 TPa | Structural mechanics model for defect free model SWNT. Modified Morse potential has been used. |
| [65] | 1.25 TPa (average over 27 SWNT) | Measuring amplitude of intrinsic thermal vibrations by Transmission electron microscope (TEM) |
| [73] | 0.95 TPa<br>(5, 0) SWNT | Using Tersoff Brenner potential developed by from DFT. Second derivative of energy. |
| [58] | 5.5 TPa<br>$\frac{\partial^2 E}{\partial \varepsilon^2} = 59eV$ | Molecular mechanics using Tersoff Brenner potential |
| [62] | 0.81 TPa | Through exerting load by AFM on suspended nanotube |
| [74] | 2.8-3.6 TPa | Micro Raman Spectroscopy |

Apart from values, trends like variation of the modulus with respect to the tube diameter also shows conflicts[59,75]. In evaluations of thermal transport properties, we encounter values of thermal conductivity reported as low as ~ 30 W/cm-K[75,76] and as high as ~ 600 W/cm-K[77,78], representing a factor of 20 discrepancy. This difference is similar to the scatter observed in evaluation of mechanical properties. Results reported on the thermal

expansion of coefficients of nanotubes are not free of debate either. Promising technological application potential for carbon nanotubes, hence, has resulted in an exponentially increasing research reports (**Error! Reference source not found.**). It has also created the necessity for sifting through these inconsistencies in intrinsic property values and have a clear understanding of addressing these properties.

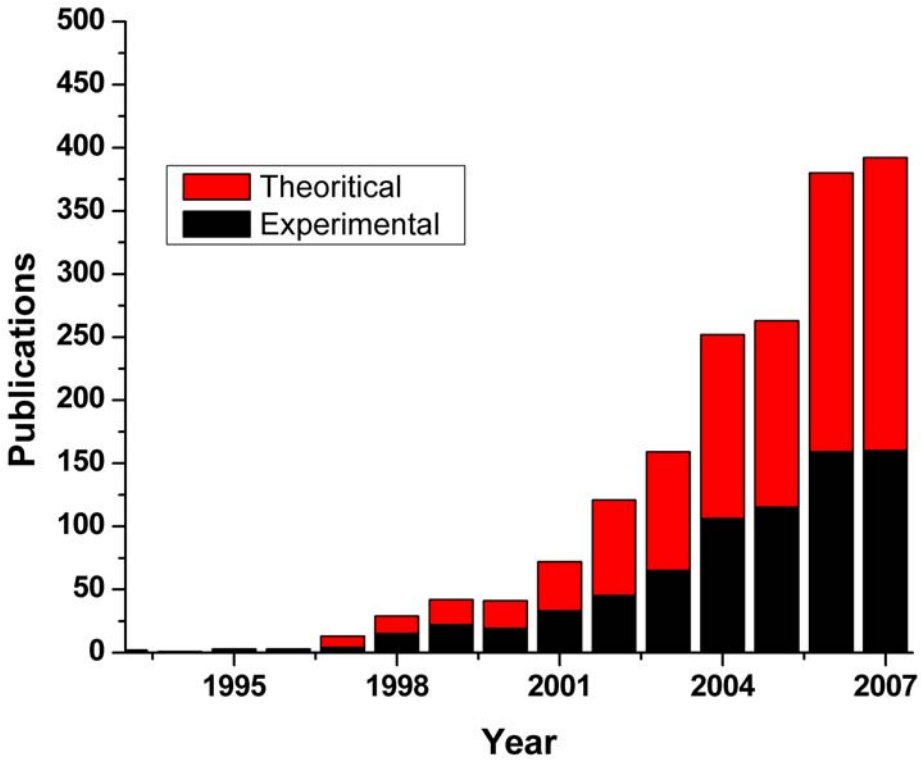


**Figure 15: Number of articles over the past decade on properties of carbon nanotubes, generated using the data from ISI Web of Science database obtained by a set of appropriate keyword search (it is not meant to be comprehensive)**

The theoretical methods[79] used to evaluate the elastic modulus of CNT include, but are not limited to, first principles[70,71] classical molecular dynamics[59], classical molecular mechanics[61], empirical force constants model[80] and structural mechanics models[72]. Multi-walled carbon nanotube has been modeled as multiple elastic cylindrical

structures to find the characteristics of wave [81]. Vibration behavior using micropolar theory has shown a decrease in fundamental frequency with increase in aspect ratio[82]. Molecular mechanics based finite element modeling has been done on carbon nanotube using semi-empirical Brenner potential [83]. The potential energy functions used to model the interactions of atoms, includes Tersoff-Brenner potentials[59,73], force fields developed from ab-initio calculations of graphite[61] or force fields developed based on the experimental results of graphite[69]. First principle calculations also come with different flavors. Most common ones are the use of methods based on Hartree Fock theory[67] or the density functional theory[70,71]. Experiments which explored the mechanical properties of nanotubes include the use of transmission electron microscope[64-66], atomic force microscope[62], micro Raman spectroscopy[74] and scanning electron microscope[84]. Furthermore, mechanical resonance method[64,65], scanning force microscopy method[85,86], nanomanipulation[84] are some of the different methods used by the researchers in experiments for nanotube property estimation. Quite a few review papers[87-92] have presented useful discussions on carbon nanotubes, their intrinsic properties, and their determination from theory and experimental characterization methods. There are suggestions that attribute the variation of properties of nanotubes to factors like purity of tubes, orientation, misalignment, etc. in experiments. In theory, one can identify the use of different definitions as a possible source of scatter in properties.

In the following section we have presented our findings on mechanical and thermal properties of carbon nanotube and nanotube like structures to get further insight and address the existing discrepancies. We assess the applicability of different definitions and show that a major part of the discrepancies have arisen from different ways of dealing with the continuum theories at the nanoscale level.

We will first present the model systems used in these simulations, followed by a description of the methods and procedures used in this study. We then present the results of our calculations on thermo mechanical properties of isolated single-wall carbon nanotubes, single-wall carbon nanotube bundles, multi-wall carbon nanotubes,

single and multi-wall carbon nanotube based tori. We finally comment and derive conclusions from these computational experiments on the properties of carbon nanotube.

## 2.2 Model Systems and Computational Methods

### 2.2.1 Model Systems

Most of our studies were conducted on single-wall carbon nanotubes both in isolated and bundled forms, either infinite or finite lengths. We have constructed model with different radii and chirality for a given (n, m)-pair. We have furthermore conducted studies on multi-wall carbon nanotubes mostly based on concentric (n, n) armchair tubes, having interlayer spacing as ~ 3.4 A, implying any double wall armchair CNT is to be made from (n, n) and (n+5, n+5) tubes. In addition to the straight nanotubes we also conducted extended study on single-wall and multi-wall carbon nanotube based tori structure as they are good structures to explore bending modulus of carbon nanotube based nanostructures.

### 2.2.2 Computational Methods

We have used three main methods in our work: ab-initio methods based molecular mechanics; classical force field based molecular mechanics and classical molecular dynamics simulation.

The *ab initio* calculations have been performed in the general framework of DFT [93-95] using projector augmented wave method (PAW) [96] with the generalized gradient approximation (GGA). To account for the exchange correlation we employed the exchange-correlation function due to Perdew-Burke-Ernzerhof (PBE)[97]. Kinetic energy cutoff of the electronic wave functions was taken as 600 eV. Integrals over the Brillouin zone were summed on a Monkhorst-Pack mesh [98] of 8x8x8 unless otherwise stated.

In molecular mechanics method we have used the force field described in section 2.3. For structural optimization (atomic positions and cell parameters) through minimization of energy we have used conjugate gradient method. We fitted the strain energy with respect to deformation and estimated the value of second derivative of

energy with respect to the strain variables. This yields the values of the elastic constants on the basis of the following Taylor series expansion of the energy E in terms of strain $\varepsilon$.

**Equation 13**

$$E(\varepsilon) = E_0 + \sum_{i=1}^{6} \left.\frac{\partial E}{\partial \varepsilon_i}\right|_0 \varepsilon_i + \frac{1}{2} \sum_{i,j=1}^{6} \left.\frac{\partial^2 E}{\partial \varepsilon_i \partial \varepsilon_j}\right|_0 \varepsilon_i \varepsilon_{j+\ldots}$$

where $E_0$ refers to the energy of the zero-strain equilibrium configuration. Hence, one can determine the value of elastic constants by calculating $\frac{\partial^2 E}{\partial \varepsilon_i \partial \varepsilon_j}$ provided that the higher order terms are negligibly small due to applied small strains.

Molecular dynamics simulations were performed under two different ensembles. For constant-strain states we have used canonical ensemble (NVT) and for constant stress simulations we have employed constant pressure and constant temperature (NPT) ensemble methods. In either case equations of motion for atoms, Nose-Hoover thermostat variable and the cell variables are iteratively solved to follow the trajectory of the model system. Hence, we trace the dynamical evolution the model systems under given constraints. By keeping track of the microscopic properties of the system with respect to time, we can evaluate different dynamic and equilibrium properties of the system. Unless otherwise specified, the time step used for all the molecular dynamics run was chosen to be 1 femto-second (fs). Leapfrog Verlet algorithm was used for the integration of equations of motion.

## 2.3 Force Field

In classical mechanics based calculations (molecular mechanics and molecular dynamics), the potential energy of a system is represented by analytical functions, namely the interaction force fields. The parameters of these functions are optimized so as to reproduce the fundamental properties, density, lattice parameters, vibrational frequencies and the like. The functional forms are based on quantum mechanical arguments (Exp-6 form for van der Waals interactions, Morse form for bond stretch and harmonic form for angle bending, periodic truncated Fourier series forms for torsion).

Hence, a force field is the mathematical expression that describes the dependence of potential energy of a molecular system to that of the atomic positions of its constituent atoms. The energy of a system can then be written as:

**Equation 14**

$$E = E_{VAL} + E_{NB}$$

**Equation 15**

$$E_{VAL} = E_B + E_A + E_T + E_I$$

**Equation 16**

$$E_{NB} = E_{VDW} + E_C$$

where :

E = Total energy of the system

$E_{VAL}$ = Energy due to bonded interaction

$E_{NB}$ = Energy due to non-bonded interaction

$E_B$ = Energy due to Bond stretching (two body)

$E_A$ = Energy due to angle bending (three body)

$E_T$ = Energy due to torsion (four body)

$E_I$ = Energy due to out of plane configuration (four body) or dihedral

$E_{VDW}$ = Energy due to van der Waals interaction

$E_C$ = Energy due to Columb interaction

In this particular work the force field used for all the molecular dynamics and molecular mechanics calculation was derived from ab-initio calculation of graphite[99]. The contribution of different components of the total energy was computed as follows:

van der Waals Interaction:

**Equation 17**

$$E_{vdw} = D_{vdw}(\rho^{-12} - \rho^{-6})$$

where $\rho = r / r_v$ , $r_v$ being the separation at minimum energy between the two atoms

Bond stretch energy:

**Equation 18**

$$E_{bond} = D_b(\chi - 1)^2$$

Where $\chi = e^{-\gamma(r-r_b)}$ with $r_b$ being the equilibrium bond distance.

Angle bending energy:

**Equation 19**

$$E_{angle} = \frac{1}{2}k_\theta(\cos\theta - \cos\theta_a)^2 + k_{1\theta}(r_1 - r_{1\theta})(\cos\theta - \cos\theta_a)$$
$$+ k_{2\theta}(r_2 - r_{2\theta})(\cos\theta - \cos\theta_a) + k_{12}(r_1 - r_{1\theta})(r_2 - r_{2\theta})$$

where k□, k□□, k□□ and k□□□are the bond stretch and stretch-bend force constants.

Dihedral energy:

**Equation 20**

$$E_{dihedral}(\phi) = V_0 + V_1\cos\phi + V_2\cos(2\phi)$$

where $V_0$, $V_1$ and $V_2$ are expansion coefficients for the truncated Fourier expansion up to second order. The details of the force field parameter values are given elsewhere[99].

## 2.4 Mechanical Properties of Carbon Nanotubes

### 2.4.1 Elastic Modulus of Carbon Nanotubes

In solid mechanics, Young's modulus or Elastic modulus gives a measure of the stiffness of a material. It is defined by

**Equation 21**

$$E = \frac{Stress}{Strain} = \frac{\sigma}{\varepsilon} = \frac{F/A_0}{\Delta l/l_0}.$$

This definition is used to find the elastic modulus from molecular dynamics simulation of a system. We can also determine the full elastic stiffness matrix by applying the formal definition in Voigt notation:

**Equation 22**

$$C_{ij} = \frac{1}{V_0}\frac{\partial^2 E}{\partial\varepsilon_i\partial\varepsilon_j}, i, j = 1,..,6,$$

*Single-wall Nanotube:* We performed molecular mechanics calculations on carbon nanotube structures, by applying strain to the model system. For each fixed strain state, the atomic positions were optimized and corresponding strain energy was evaluated. Subsequently, by using the second derivative of potential energy, we estimated the corresponding axial elastic constant. In the bundle calculations the cross sectional area was evaluated in a similar way as in reference [61]. Figure 16 shows the variation of strain energy as a function of strain and associated fitting.

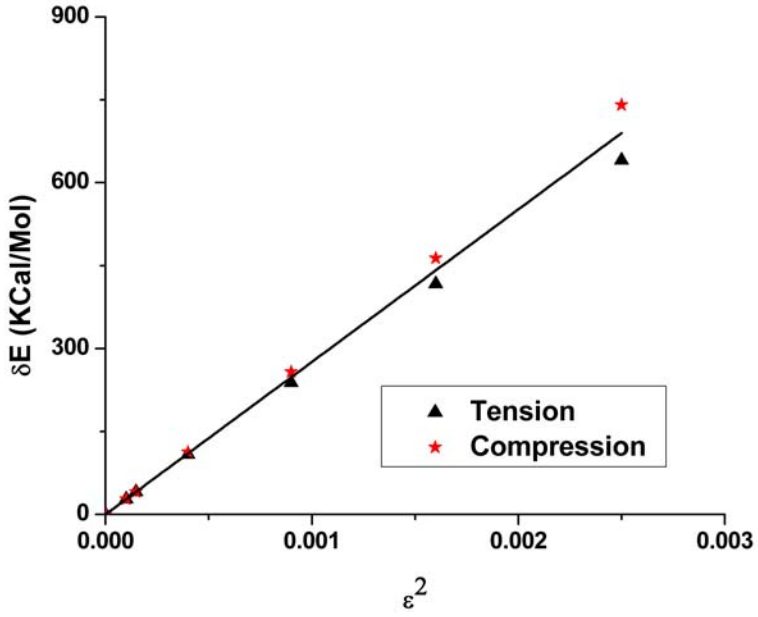


**Figure 16: Strain energy content for tensile and compressive strains obtained from molecular mechanics calculations to determine the elastic modulus**

*Validity of Force Field:* Some of the disagreement between our work and the values found in literature lead us to calculate the axial modulus through DFT and reinforce our confidence on using graphite based force fields on carbon nanotubes. These calculations were carried out with a plane wave basis set. The axial modulus of a (10, 10) SWNT bundle from the second derivative of the energy was estimated to be 605 GPa. The value of second derivative of the energy with respect to strain, $\frac{\partial^2 E}{\partial \varepsilon^2}$, was found to have a value

of 56.8 eV/atom, which compared well to values in literature[68,70,100,101]. This agreement rules out the possibility of force field being the source of any sort of discrepancy. Furthermore, it was accepted that the force field used to calculate SWNT properties through molecular mechanics is well suited to do so as the elastic modulus found is comparable to that obtained from ab-initio calculations.

### 2.4.2 Importance of Area Definition at Nanoscale

We already have pointed out that the area of the system on which the tensile and compressive force is applied, has a significant role to define the value of modulus. In order to emphasize the significance of the cross sectional area of carbon nanotube in the evaluation of axial modulus, we now look and compare few different cases. Before we proceed here are few useful facts:

- For a nanotube of a given chirality (n, m) the diameter (in angstrom) is given by:

$$D = \frac{2.46}{\pi}\sqrt{n^2 + nm + m^2}$$

- The interlayer thickness for graphite layer is 3.4 A, often used as the wall thickness for carbon nanotubes or the difference between two consecutive walls in a multi-wall nanotube. This value will be referred as‘t’.
- The mean radius $\left(\frac{r_i + r_o}{2}\right)$ of (10, 10) nanotube is 6.78 A that is approximately equals to 2t.

*Area calculation for (10,10) isolated nanotube:*

For cases where the isolated nanotube is assumed as a thin shell, the area is computed as:

$$A_1 = \pi(r_i + t)^2 - \pi r_i^2 = 46.10\pi$$

where $r_i$ represents the inner radius of the tube.

In many works this expression has further been simplified to:

$$A_2 = \pi(r_i + t)^2 - \pi r_i^2 = 2\pi r_i t \text{ [73,102]} = 34.54\pi$$

In the beam assumption, the area is taken to be:

$$A3 = \pi(r_i + t)^2 = 71.91\pi$$

Hence for the very definition of area, and the same value of $\frac{\partial^2 E}{\partial \varepsilon^2}$, the value of the reported modulus for identical cases can be widely different. We have here left aside the fact that there might even be disagreement in the value of thickness of the shell itself leading to even more diversity in reported values. While our work uses interlayer spacing of graphite (3.4 A) as shell thickness of nanotube, very different values like 0.66 A[58], 0.75 A[103] are also found in literature.

2.4.3 Predicting the Elastic Modulus

Elastic modulus of carbon nanotube is primarily dependent on its bond and angle strengths. This is mainly due to chemical bonding interactions and these do not vary across different size and shape of carbon nanotubes. Hence, the observed drastic variations in reported values from theoretical calculation are mostly because of the use of different definitions of the cross sectional area. To further emphasize the above claim a problem was formulated on the basis of the available data of isolated (10, 10) nanotube. Based on this data an attempt was made to predict the modulus of other isolated armchair nanotubes. The only assumption in deriving such an equation is that the modulus is different solely due to different area involved. Since we know that the number of bonds and angles is linearly related to the number of atoms in an infinitely long nanotube, the force required to strain the system can be related accordingly. Hence for an isolated (n, n) armchair single-wall nanotube taking the assumptions into account we can show that for beam approximation:

**Equation 23**

$$Y_{(n,n)} = \frac{\sigma}{\varepsilon} = \frac{\frac{n}{10}F_{(10,10)}}{\frac{A_{(n,n)}}{\varepsilon}} = \frac{nF_{(10,10)}}{10\varepsilon A_{(n,n)}} = \frac{nF_{(10,10)}}{10\varepsilon\pi(0.68n+1.7)^2} = \frac{nF_{(10,10)}(6.8+1.7)^2}{10\varepsilon A_{(10,10)}(0.68n+1.7)^2}$$

$$\Rightarrow Y_{(n,n)} = \frac{\sigma}{\varepsilon} = Y_{(10,10)}\frac{2.5n}{(0.4n+1)^2}$$

and similarly for thin shell approximation

**Equation 24**

$$Y_{(n,n)} = \frac{\sigma}{\varepsilon} = \frac{\dfrac{\dfrac{n}{10}F_{(10,10)}}{A_{(n,n)}}}{\varepsilon} = \frac{nF_{(10,10)}}{10\varepsilon A_{(n,n)}} = \frac{nF_{(10,10)}\left((6.8+1.7)^2-(6.8-1.7)^2\right)}{10\varepsilon A_{(10,10)}\left((0.68n+1.7)^2-(0.68n-1.7)^2\right)}$$

$$\Rightarrow Y_{(n,n)} = \frac{\sigma}{\varepsilon} = \frac{nF_{(10,10)}(13.6)(3.4)}{10\varepsilon A_{(10,10)}(1.36n)(3.4)} = Y_{(10,10)}$$

Here we have taken 6.8 A to be the mean radius of a (10, 10) nanotube. Simultaneously we calculated the effect of helicity and diameter of carbon nanotube on its mechanical properties through molecular mechanics. In the following, Figure 17 clearly shows that the drastic difference in reported mechanical property values arise from the use of different area definition. The beam choice for area definition shows substantial decrease of modulus as the diameter increases. Simple extrapolation of this assumption leads to a zero value of modulus for infinite diameter, i.e. single sheet of graphene.

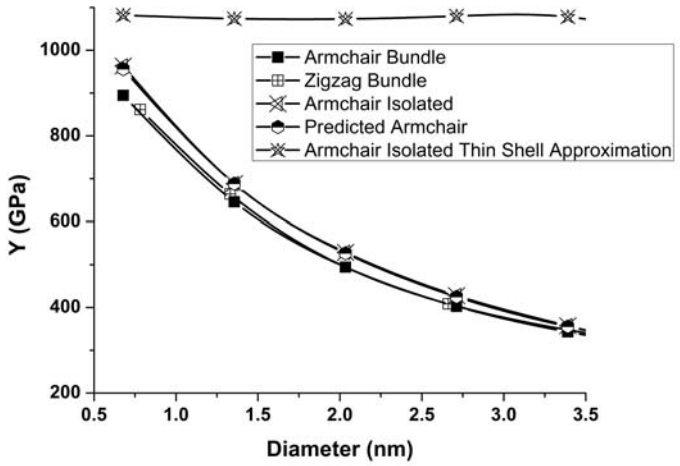


**Figure 17: Axial modulus of single-wall carbon nanotube**

From inspection of Figure 17, we observe the following:

1. Elastic modulus of carbon nanotube does not depend on helicity of the tube. This is in agreement with our expectation, as we mentioned earlier that the strength of

C—C bond and C—C—C angle are the primary factors in determining the modulus that does not vary with helicity. Since the comparison is between (almost) same diameter tubes of armchair and zigzag nanotube the area factor does not make any difference here.

2. Using beam assumption of nanotube we see a decrease in elastic modules as the tube diameter increases.
3. Using a thin shell approximation of nanotube, we see that the diameter has almost no effect on elastic modulus of nanotube.
4. Another conclusion clearly follows from the points raised in #2 and #3; Form the use of two different area definitions, one may conclude presence of two different trends on the influence of the diameter of nanotubes on their elastic modulus. This is misleading.
5. Finally, we observe that the predicted value from the equation 23 and 24 gives us good match with the value of elastic modulus calculated by molecular mechanics calculation backing the claim that the major difference in values is primarily due to the definitions and less likely due to the physical properties of the system itself.

### 2.4.4 Elastic Modulus of Multi-wall Nanotubes

Similar to the calculations of single-wall nanotubes, we carried out molecular mechanics calculations to find the young's modulus of multi-wall nanotubes bundles. We observed that the multi-wall nanotubes have a greater young's modulus than the single-wall nanotubes as found in literature [70]. We carried out these calculations on multi-wall nanotubes with different radii (inner and outermost) and different chirality. To assess the asymptotic behavior, we have also calculated the elastic modulus of graphene structures with different number of layers, i.e. the limiting case is graphite.

We have also attempted to find the Young modulus for an isolated multi-wall carbon nanotube assuming a beam with layers (10, 10), (15, 15) and so forth. This is similar to the derivation of equation 23 for the Young modulus expression with a beam approximation for an isolated single-wall carbon nanotube. If total 'm' layers are

assumed in MWNT, with the innermost being (10, 10), we can express the total force on the MWNT as the summation of all the forces on each tube. In order to calculate the cross sectional area needed to find the Young's modulus we consider the outer most tube in the 'm' layers. Accordingly we can write,

**Equation 25**

$$Y_{MWNT_{ISOLATED}}\varepsilon = \sigma = \frac{F_T}{A} = \frac{Fm(2+(m-1)0.5)}{2\pi(1.7)^2(2(1+m)+1)^2}$$

**Equation 26**

$$\Rightarrow Y_{MWNT_{ISOLATED}} = \frac{6.25m(m+3)}{(2m+3)^2} Y_{(10,10)_{ISOLATED}}$$

This simple formula does not take into account the inter layer van der Waals attraction and possible effect of the radius of curvature of different walls. However it does a good job in predicting the modulus values as evident from Figure 18. From equation 26 given above, we also find that as $m \to \infty$ the value of the modulus of a multi-wall nanotube with (10, 10) tube being the innermost tube approaches a constant value: $Y_{MWNT_{ISOLATED}} = \frac{6.25}{4} Y_{(10,10)_{ISOLATED,BeamApproximation}} \sim 1TPa$, using a value ~640 GPa for $Y_{(10,10)}$

.

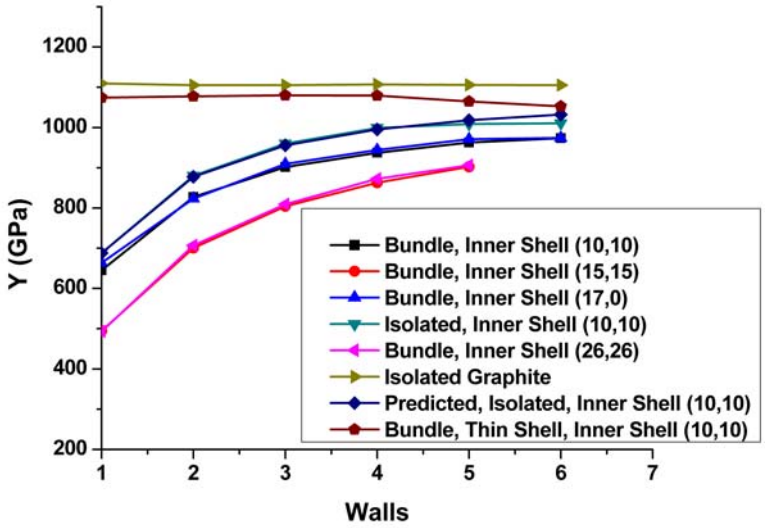


**Figure 18: Axial elastic modulus of various multi-wall carbon nanotubes**

From Figure 18, the observed points are listed as following:

1. We observe that with increased number of walls the modulus of the nanotube increases and finally approaches close to ~ 1 TPa.
2. Thin shell approximation yields a value of ~ 1 TPa independent of the number of tubes.
3. The predicted value for the isolated multi-wall nanotubes matches well with calculations from molecular mechanics method proving the validity of our assumption.
4. From #3 observation we also conclude that the van der Waals interaction among the tubes does not contribute much to the modulus as our prediction did a good job without taking that factor into account.
5. For isolated graphite sheets the modulus value does not change with increasing number of layers, in agreement with our conclusion in #4.

*Structure of Multi-wall nanotube:* We observed another interesting fact from the molecular mechanics study of carbon nanotube. We find that the minimized structure of the multi-wall nanotube in a bundle does not remain circular anymore agreeing with

experimental observations [104]. For more number of walls the outer walls tend to take a shape of hexagon. Figure 19 shows the hexagonal shape for a tube made from (15, 15), (20, 20), (25, 25), (30, 30) and (35, 35) tubes. The transition from circular to hexagonal shape, while moving from inner to outer walls, is clearly observed here.

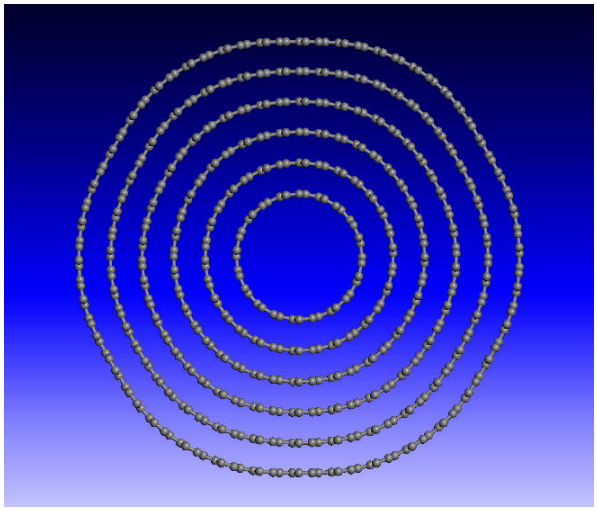

**Figure 19: Optimized structures of a MWNT looking down cylinder axis. The hexagonal shape evolves so as to minimize the strain energy due to curvature by enhancing layer-layer van der Waals interactions. Force fields without van der Waals interactions may miss this shape change**

This evolving hexagonal outer structure leads to a more efficient packing of bundles of thicker MWNT. Since nanotubes are widely used and anticipated as one the most favorable candidates as nanofillers in nanocomposites, this definitely is an interesting finding. It may result in very different surface and interface properties in nanocomposite made from multi-wall nanotube with respect to those made from single-wall nanotubes. The tendency of the outer wall tubes to form a hexagonal structure is clearly due to a delicate balance between the van der Waals forces acting between the walls and strain energy induced due to curvature. This tendency is the same tendency seen in large diameter single-wall carbon nanotube which form a collapsed stable structure as shown earlier by one of us [61].

### 2.4.5 Twist/Torsion Modulus of Carbon Nanotubes

Torsion modulus or twist modulus is another important property in assessing mechanical strength of a nanotube. In reality, the nanotube is more likely to be in a twisted form than otherwise. Torsion modulus was calculated for isolated carbon nanotube assuming it to be a thin wall hollow shaft. The strain energy in torsion in that case is given by:

**Equation 27**

$$U = \frac{GJ\theta^2}{2L}$$

Where $J = 2\pi r^3 t$

U = Strain Energy

G = Torsion modulus

$\theta$= Twist Angle in radian

r = mean radius of the shaft wall

t = thickness of the tube

L = Length of the tube

We have used two approaches in determining the twist modulus: tubes with finite length and infinite length (through the use of periodic boundary conditions in axial direction).

### 2.4.6 Twist Modulus of Single-wall Nanotubes

*Finite length:* Non-periodic system of nanotube was built. Keeping one end fixed the other end was strained in terms of twist in an increment of $2^o$. The twist was applied both in clockwise and anticlockwise direction. We fitted the strained energy calculated and different amount of twist to equation 27. This gave us the twist modulus for nanotubes. Figure 20 gives a comparison of the modulus obtained of (almost) same diameter of zigzag and armchair nanotubes of different lengths.

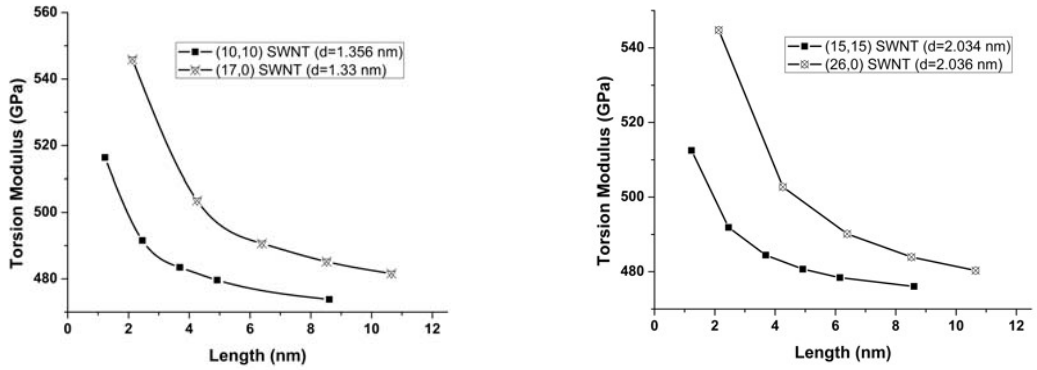


**Figure 20: Variation of twist modulus for zigzag and armchair CNTs for two different diameters (a) d=1.35 nm, (b) d=2.04 nm as a function of finite length of the tubes**

Conclusions drawn from the observation of Figure 20 are:

1. The twist modulus decreases with increasing length of the tube as expected. However the length-scale studied is significantly lesser than that of a typical length of a nanotube used in experiments. In later part of this section we have looked into twist modulus of infinite length nanotubes.
2. Zigzag nanotubes shows a higher twist modulus than armchair nanotubes agreeing with the available literature findings[20,105]
3. As the length of the tube is increased the modulus tends to take an asymptotic nature and tries to converge to a value in both types of nanotubes.
4. The difference between the modulus of two types of nanotubes with the same diameter decreases as the length of the tubes increase.

We further examined the dependence of modulus on the diameter of the tube. Figure 21 shows the diameter dependence of the torsion modulus of different lengths of nanotubes (armchair and zigzag).

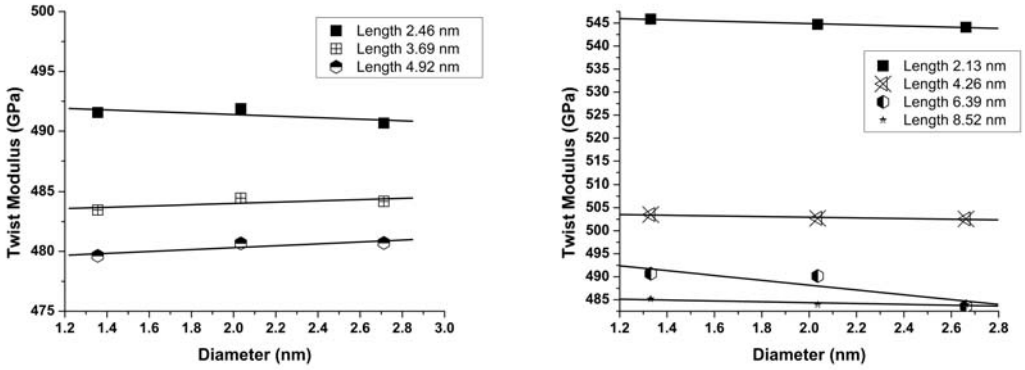


**Figure 21: Variation of twist modulus with diameter for armchair (left) and zigzag (right) nanotubes**

We observe contrary to [105] and in agreement with [20,68] that the diameter has hardly any effect on torsion modulus.

*Infinite single-wall nanotube:* We extended our study to investigate the twist modulus of an infinite isolated nanotube through the novel use of periodic boundary conditions imposed in z-direction. In a periodic model, due to presence of periodic image atoms the application of twist is entirely different than how its finite length counterpart was dealt.

The whole process of twisting an infinite isolated nanotube (m, m) and finding the torsion modulus from it consisted of the following steps:

1. Build the model
2. Select atoms on one boundary of the cell in z direction.
3. Rotate the selected atoms by $\frac{2\pi}{m}n$ (only discrete rotations, based on m)
4. Fix the rotated atoms and also fix the atoms on the other boundary of the unit cell
5. Maintaining the above constraints relaxed the structure through minimization by ab initio calculations based force fields.
6. Recalculate the bonds at the boundaries and reformed to give the desired twist to the nanotube structure.
7. A final minimization of the structure with all moveable atoms.

The final twisted nanotube, built on the above procedure is pictured in figure 22 when viewed from front and looked into the z direction.

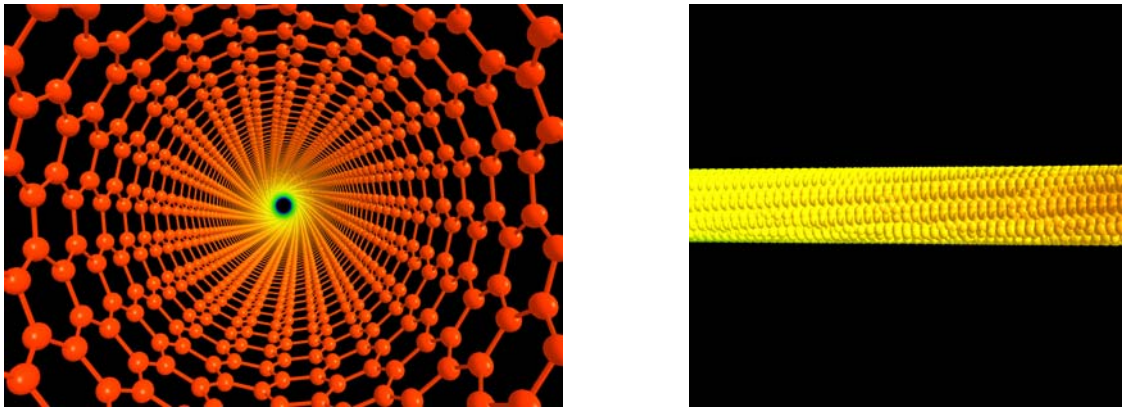

**Figure 22: Axial and lateral views of a twisted carbon nanotube**

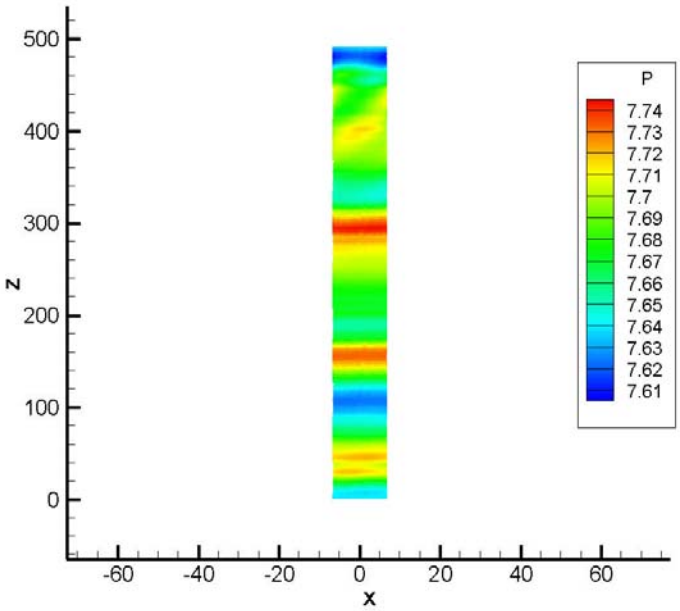


**Figure 23: Potential energy (kcal/mol) content contour plot for a twisted nanotube determined for a configuration from molecular dynamics at T=300 K. The length of the tube is 49.2 nm**

Figure 23 shows the potential energy profile obtained for a 49.2 nm long twisted tube as a contour plot. The procedure described above was repeated for different values of 'n'

and Figure 24 was obtained while plotting the energy of the strained tube with $\theta^2$. The straight line obtained was fitted to equation 27 to evaluate the twist modulus of the tube. Figure 24 shows the energy vs. torsional-strain variation obtained from the calculation.

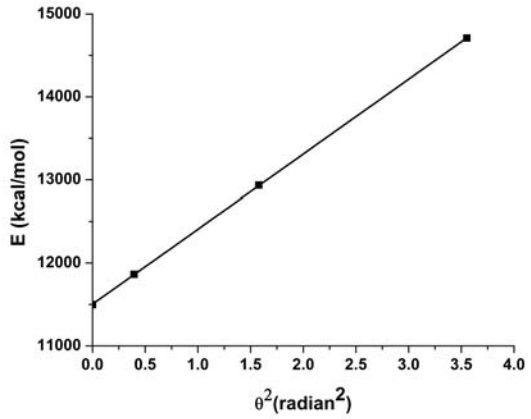


**Figure 24: Variation of energy with respect to twist angle for (10, 10) CNT**

Calculation of torsion modulus in this method is then carried out for different armchair and zigzag SWNT's with different set of c-axis values ('z' direction). The results obtained are summarized in Table 2. The modulus found agrees reasonably with the values reported in literature [20,60,72].

**Table 2: Torsion modulus of infinite single-wall nanotube**

| SWNT | Torsion Modulus (GPa) | Length of periodic cell (nm) |
|---|---|---|
| (5,5) | 452.85 | 49.2 |
| (5,5) | 462.33 | 98.4 |
| (10,10) | 463.48 | 24.6 |
| (10,10) | 466.77 | 49.2 |
| (15,15) | 465.10 | 24.6 |
| (15,15) | 437.8 | 73.8 |
| (10,0) | 464.83 | 42.61 |
| (15,0) | 462.47 | 42.61 |
| (20,0) | 460.46 | 42.61 |

Conclusions made from observation of Table 2 are listed as following:

1. As expected from the observations of the twist modulus study of finite length nanotube, the torsion modulus of an infinite long nanotube converges to a value irrespective of the chirality and diameter of the tube.
2. The claim of higher twist modulus of zigzag nanotube with respect to armchair nanotube, based on finite limit calculations is not valid in the infinite limit as twist modulus of both armchair and zigzag nanotube converges to same value
3. The converged value the twist modulus for both type of nanotube is roughly 460 GPa.

### 2.4.7 Twist Modulus of Multi-wall Carbon Nanotubes

*Finite length:* Keeping in mind that nanotubes used for practical purposes are of high aspect ratio, infinite length calculation results are more important than the finite ones. However due to the approach implemented above, not too many calculations are possible for multi-wall nanotube. Rotation by same angles of more than one tube and rearrangements of bonds at the same time at the boundary leaves us with very few choices. From the observations made for single-wall nanotube behavior with applied torque, the lengths of the multi-wall nanotube considered were higher. Higher length finite length nanotube gave results close to infinite ones. Table 3 summarizes the results obtained. The notation n_m_p MWNT stands for a MWNT with inner tube (n, n) and the outer tube (m, m) and the cell length in z-axis is p times the unit cell length (2.46 nm). It is important mentioning here that we assumed a no slip condition between the tubes. All the tubes in a multi-wall nanotube are rotated by the same angle when a torque is applied.

**Table 3: Twist modulus of finite length MWNT**

| MWNT | Length of the tube (nm) | Torsional Modulus (GPa) |
|---|---|---|
| 10_15_25 | 6.15 | 471.77 |

**Table 3: Continued**

| | | |
|---|---|---|
| 10_15_50 | 12.3 | 469.03 |
| 15_20_25 | 6.15 | 472.58 |
| 15_20_50 | 12.3 | 469.51 |
| 10_15_20_25 | 6.15 | 472.45 |
| 10_15_20_50 | 12.3 | 469.52 |

A quick comparison of these few data from Table 3 tells us that

1. Adding another wall does not affect the twist modulus and the values are close to those of infinite length single-wall nanotube twist modulus.
2. We observe no dependence of diameter and number of walls on the twist modulus. It is expected that this value should also be similar to graphite sheet shear modulus, as tubes with very big diameter and large number of walls can be approximated as layer of graphite sheet. To verify, elastic constants of graphite sheet were also evaluated by the same force field and the shear modulus was found to be 457.63 GPa, comparable to the values obtained above.

## 2.5 Carbon Nanotori

### 2.5.1 Structure, Mechanics and Stability

To understand the energetic related to nanotube bending we looked into nanotori structures made of carbon. Nanotorus is a nanotube bended into a ring. We constructed nanotori and studied its strain energies, which gave us a measure of the bending stiffness of a nanotube. One of the earliest computations on this property was conducted and presented at Foresight conference by Caltech group (Gao, Cagin, Goddard) in nineties.

Armchair carbon nanotube of different length and radius was made into a circular tube. The structure obtained was then minimized and the strain energies of the tubes were determined. Below, we have given a configuration obtained through minimization of a (10, 10) nano-torus with a mean radius = $\frac{49.2nm}{2\pi} = 7.83nm$. We observe the emergence of kinks in the minimized structure. While tension prevails in the outer wall,

the inner wall remains in compression. This leads to development of kinks in the inner wall to localize the strain energy. We will later show that heating of nanotori sometimes can help in annealing kinks to homogenize the location and number of kinks. Thermal annealing distributes the kinks more evenly throughout the structure and helps get the structure out of local minima to an energetically more favorable structure. One such kink is zoomed from the above-obtained structure (Figure 25) and given below in Figure 26.

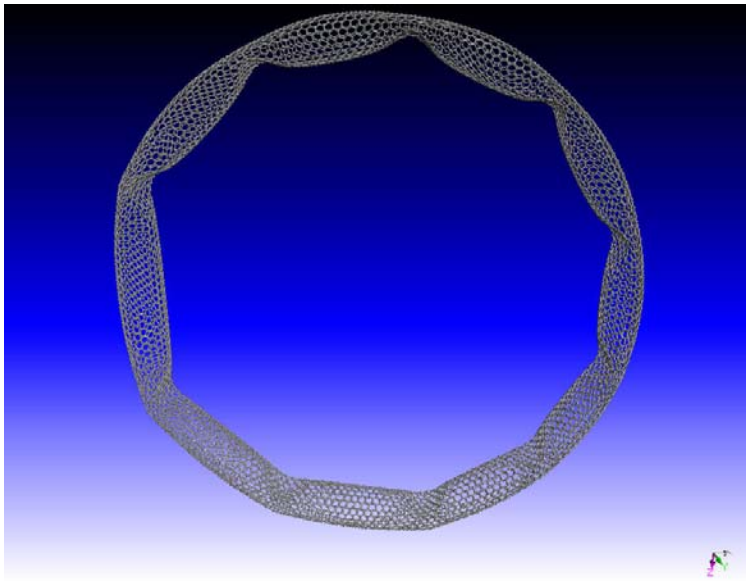

**Figure 25: Nanotori of (10, 10) nanotube**

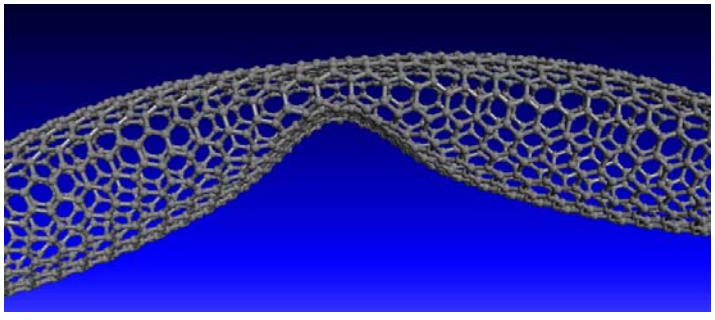

**Figure 26: Kink in nanotori**

As seen in Figure 26 the circular cross section becomes more oval sized due to brazier effect[106]. The narrowest cross section approaches close to the inter layer spacing of graphite which is 3.4 A. As observed in Figure 27, those are the regions with high energies. Kinked carbon nanotubes has also been studied using bond-order potential energy function and self-consistent tight-binding scheme [107].

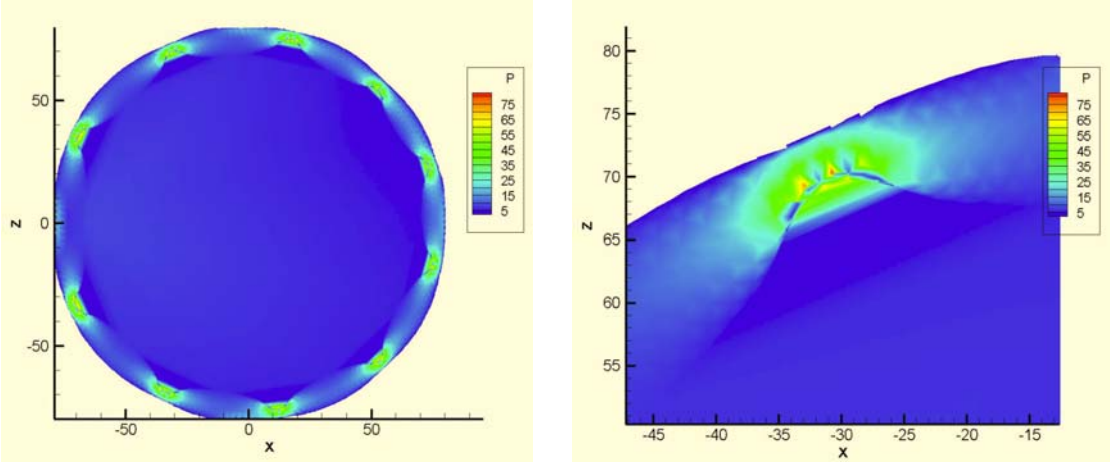


**Figure 27: Contour of potential energy (kcal/mol) of SWNT (10, 10) nanotori**

**Table 4: Strain energy of single-wall nanotori**

| Nanotube | Mean radius of Nanotori (nm) | Energy/atom (Kcal/mol) | Strain Energy ($\Delta E$) (Kcal/mol) |
|---|---|---|---|
| (10,10) | 1.9576 | 8.1676 | 5.291 |
| (10,10) | 3.9152 | 5.4987 | 2.6220 |
| (10,10) | 7.83 | 4.1936 | 1.3169 |
| (10,10) | 11.745 | 3.8910 | 1.0143 |
| (10,10) | 15.66 | 3.5031 | 0.6264 |
| (10,10) | 23.49 | 3.1873 | 0.3106 |
| (10,10) | 31.32 | 3.063 | 0.1863 |
| (10,10) | 39.15 | 3.0087 | 0.1319 |
| (10,10) | Infinite | 2.8767 | 0 |
| (15,15) | 7.83 | 3.5204 | 1.3034 |
| (15,15) | 11.745 | 3.182 | 0.9649 |
| (15,15) | 15.66 | 3.021 | 0.8039 |
| (15,15) | 23.49 | 2.7699 | 0.5528 |

**Table 4: Continued**

| | | | |
|---|---|---|---|
| (15,15) | Infinite | 2.2171 | 0 |
| (20,20) | 7.83 | 3.0076 | 1.0275 |
| (20,20) | 11.745 | 2.818 | 0.8379 |
| (20,20) | 15.66 | 2.7451 | 0.765 |
| (20,20) | Infinite | 1.98 | 0 |

Table 4 gives the strain energies of different nanotori calculated using the energy of infinite-straight nanotube as reference. Hence the energies correspond to strain energy is due to bending only. We observe from the strain energies obtained, that longer tube and hence nanotori with larger radius are more easily formed than the shorter ones as expected. Similarly we observe that nanotubes with bigger diameter are easier to bend into nanotori than their shorter diameter counterpart of same length. Given in Figure 28 are the minimized structures of (15, 15) SWNT nanotori. Diminishing number of kinks are observed as we move from lower to higher radius nanotori as expected due to reduction in strain energy.

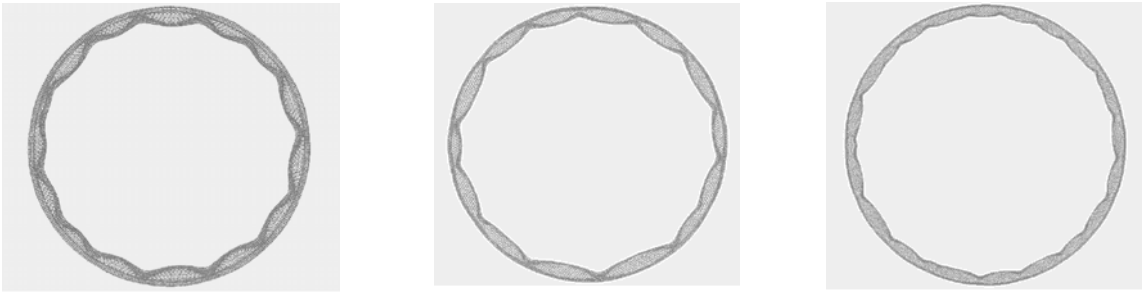

**Figure 28: Smoother structure of (15, 15) nanotori with radius from left R=7.83 nm, 11.745 nm and 15.66nm**

Figure 29 shows an exponential decay of strain energy with increasing radius of the nanotori. We see that after a certain radius, around 20 nm the curve becomes asymptotic and we expect that it is around this point onwards the appearance of kinks are almost negligible. This observation goes well with the findings in [99] where it was found

that for (10, 10) nanotori with radius more than 18.83 nm the stable structure is smooth nanotori. Fitting with an exponential function yielded the following relationship:

**Equation 28**

$$E = 7.66e^{-r/4.52}$$

where E and r are in Kcal/mol-atom and nm respectively. From equation 28, we find that the rate of change of strain energy per atom becomes negligible (less than 0.026 Kcal/mol–atom) when the torus radius becomes greater than 18.83 nm. This radius is the limiting value above which the stable structure of the nanotori becomes kink-free and smooth. However the present study does not look into the possibility of having both stable and kinked structure of nanotori that has a radius between 10.03 and 18.83 nm as pointed out in the same work.

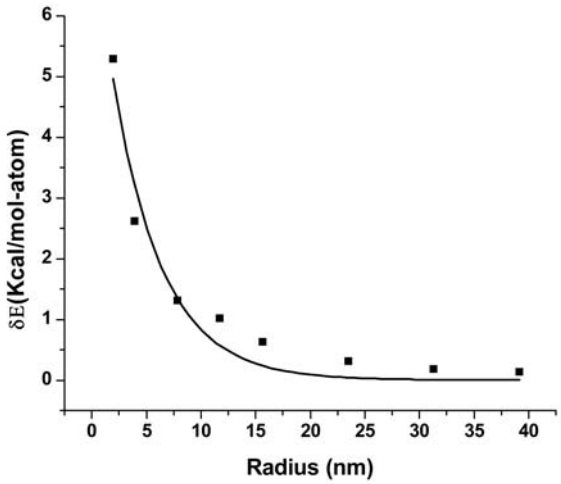


**Figure 29: Variation of strain energy with radius of (10, 10) nanotori**

Figure 29 when redrawn in a different manner as shown in Figure 30, i.e. with respect to curvature, the slope of the linear fit obtained, is then a measure of the bending modulus of a nanotube. In this manner, we have obtained the bending modulus for (10, 10) nanotube as 305 GPa. The initial points from the above figure were discarded as the

strain energy obtained at such small radii is also influenced by the presence of kinks other and hence will lead improper values for bending modulus of nanotubes.

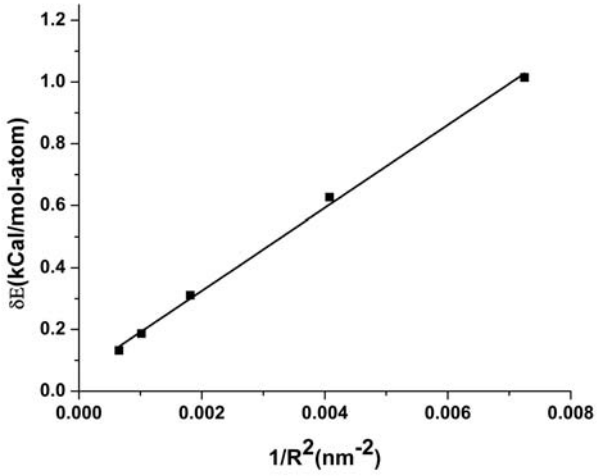


**Figure 30: Strain energy of nanotori proportional to inverse of radius squared**

In other works on nanotori, Huhtala et. al.[108,109] looked into minimum energy structure and thermal stability of large nanotori structures using Brenner potential using molecular dynamics simulation. Potential energy of the structures was monitored to determine the relation between the critical buckling diameters with that of the nanotori diameter. The strain energy of the tubes per atom basis was found to be linearly related (increasing) when the tube diameter is approximately less than that of a (10,10) tube. Cagin et al [99] have also looked into the problem of determining the critical diameter for smooth single-wall nanotorus and the bending modulus. They found that nanotori could exhibit more than one stable structure within the thermal fluctuations, which are thermally equivalent.

### 2.5.2 Multi-wall Nanotube Nanotori

With mean nanotori diameter (7.83 nm), a triple wall nanotori from (10, 10), (15, 15) and (20, 20) nanotubes and two double-wall nanotori from (10, 10), (15, 15) and (15,

15), (20, 20) nanotubes were constructed. Optimization of their energy and structures using molecular mechanics methods gave us Figure 31. We observe that the kinks in these structures emerge almost in parallel to each other on each wall. Table 5 gives the values of the strain energies obtained for the double wall nanotori made from (10, 10) and (15, 15) nanotubes.

**Table 5: Strain energy of multi-wall nanotube**

| Radius (nm) | Energy per atom (Kcal/mol) | Strain Energy per atom (Kcal/mol) |
|---|---|---|
| 7.83 | 4.01 | 2.42 |
| 11.745 | 3.15 | 1.55 |
| 15.66 | 2.89 | 1.29 |
| Infinite | 1.60 | 0.0 |

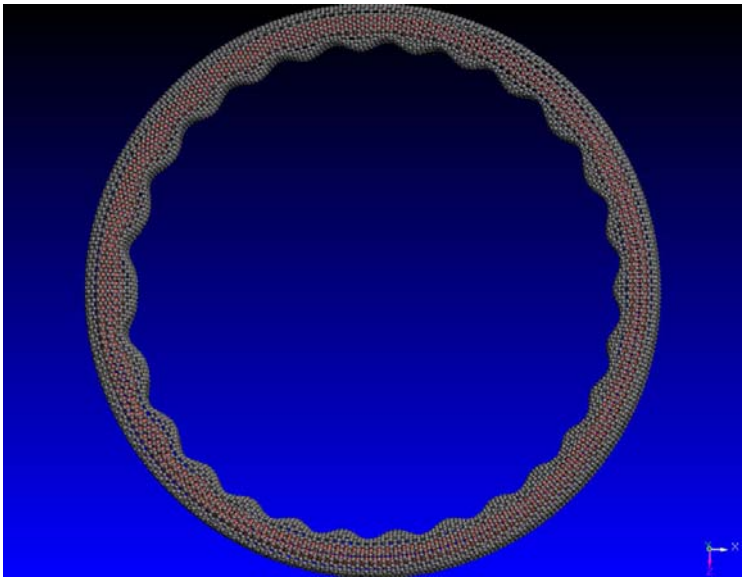

**Figure 31: MWNT nanotori**

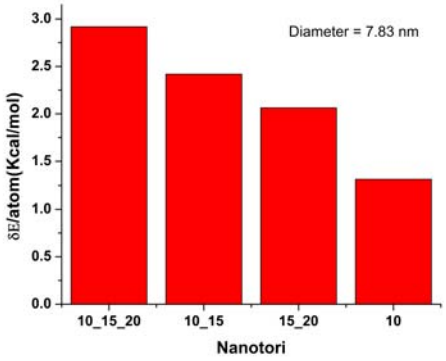


**Figure 32: Strain energy of MWNT nanotori**

The strain energies of multi-wall nanotori were found to be higher (Figure 32) than those of single-wall nanotori. This is expected, as the presence of inter wall van der Waals forces restricts the freedom of all the atoms on different walls to move and shift into a less-strained configuration. The potential energy contour plot, Figure 33, shows that the inner tube has higher energy that is expected due to the constraint put by the outer wall on its movement.

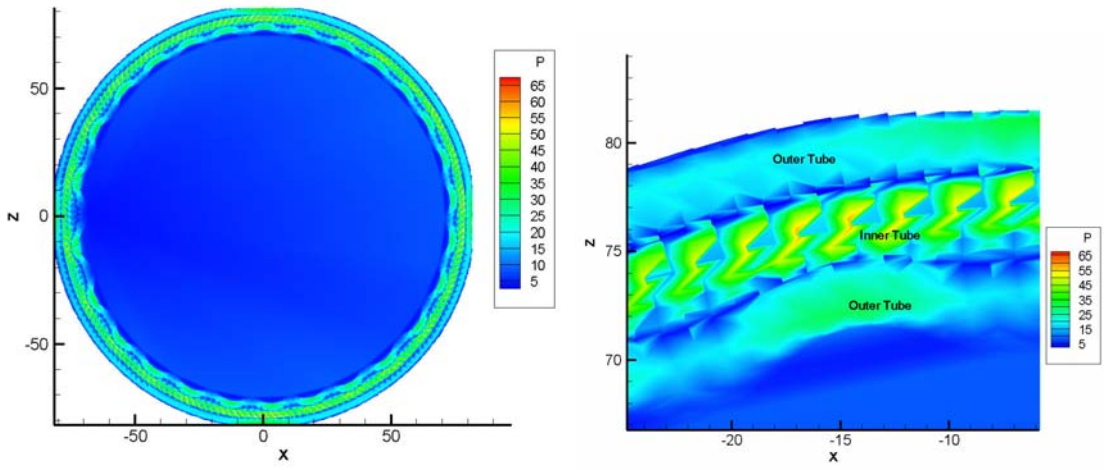


**Figure 33: Potential energy contour in MWNT nanotori**

Figure 32 shows that adding more walls increase the strain energy of nanotori. However for same number of walls, it seems that larger the outer tube diameter, lesser will the strain energy be. This is along the same lines with the result obtained for nanotori of a single-wall nanotube.

### 2.5.3 Twisted Nanotori

Liu et al. [110,111] performed atomistic simulations of defect free single and multi-wall nanotori. In their studies, they have concluded that torsion helps to reduce the strain energy of single-wall nanotori; in contrast it tends to destabilize multi-wall nanotori. The magnitudes of twists applied to the tubes were multiples of $2\pi$. These values, given the mean torus radius, are somehow larger than usual. In the present work, we also have looked into the behavior of twisted nanotori. The twist in this case was given in small increments, integer multiples of $\frac{\pi}{10}$ (least possible unit value dictated by (10, 10)-tube) as opposed to the above study. Nanotori made of (10, 10) SWNT was constructed with a nanotori diameter of 46.98 nm. Twists of different angles were given to the structure (by rearrangements of bonds as torus constructed by identifying ends). Table 6 gives the values of the strain energies obtained.

**Table 6: Strain energy of twisted nanotori**

| Nanotube | Radius (nm) | $\theta$ (Degrees) | Energy per atom (kcal/mol) | Strain Energy per atom (Bending plus torsion) (kcal/mol) | Strain Energy per atom (Torsion) (kcal/mol) |
|---|---|---|---|---|---|
| (10, 10) | 23.49 | 0 | 3.1873 | 0.3106 | 0 |
| (10, 10) | 23.49 | 36 | 3.1878 | 0.3111 | 0.0005 |
| (10, 10) | 23.49 | 72 | 3.1946 | 0.3179 | 0.0073 |
| (10, 10) | 23.49 | 108 | 3.2088 | 0.3320 | 0.0215 |
| (10, 10) | 23.49 | 144 | 3.2376 | 0.3608 | 0.0503 |

Since Table 6 is based on single nanotori, the effect of bending is same in all the cases. Hence, we expect that the strain energy would be directly proportional to the square of the angle by which it was twisted. This is clearly observed in Figure 34.

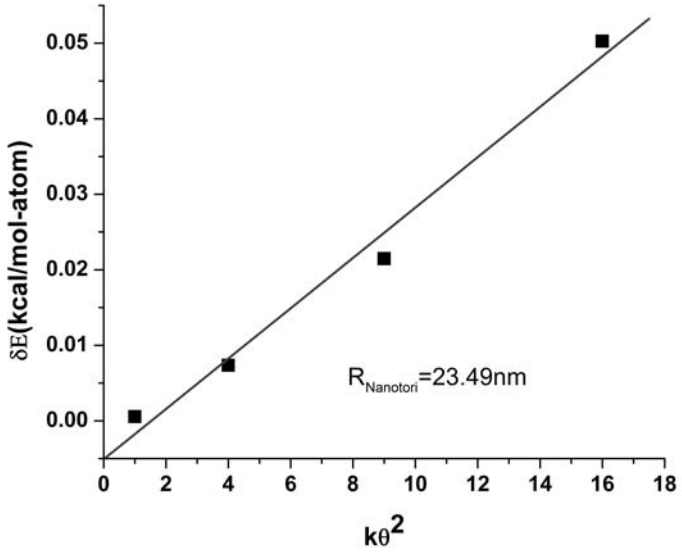


**Figure 34: Strain energy of a twisted (10, 10) nanotori for same radius and different angles**

## 2.6 Thermal Properties of Nanotubes

### 2.6.1 Effect of Temperature on Axial Modulus of Single-wall Nanotube

All molecular mechanics and density functional level of theory results in this work do not take into account the effect of temperature. However in reality it is of utmost importance to know the influence of temperature, as very rarely an application would be used at very low temperatures. Temperature effect on stress-strain behavior, and resulting axial modulus of (10, 10) nanotube was studied using molecular dynamics. Simulations were carried out from T=100 K to T=700 K in increments of 100 K. At each temperature a zero stress simulation was followed by simulations at 2, 4 6, and 8 GPa, tensile and compressive stresses along c-axis. The constant temperature constant stress (NPT) MD simulation data is collected over 400 picoseconds for calculating the

resulting compressive and tensile strain to determine the elastic modulus. The result for axial modulus vs. temperature is plotted in Figure 35. We observe almost a linear thermal softening effect in the studied temperature range, approximately with a slope of 26 MPa/K.

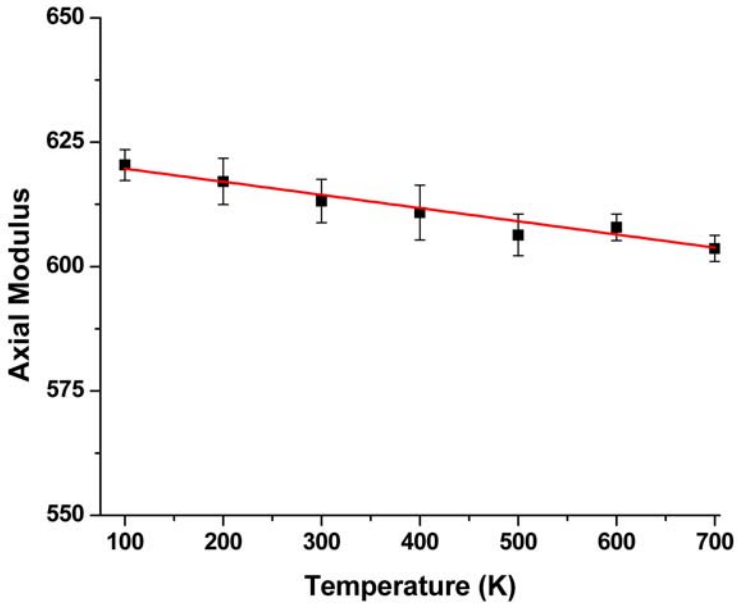


**Figure 35: Effect of temperature on axial elastic modulus**

As we have observed earlier that elastic modulus in axial direction for nanotube does not depend on the chirality, similar temperature dependence can be expected for nanotubes of other chirality. The temperature coefficient of elastic modulus 26 MPa/K implies a 2.6 GPa decrease over a 100K operation range (around 0.3% of the value), which is considerably small. Hence for all practical purposes one can safely assume the elastic modulus of nanotube as constant in presence of other more sensitive parameters, alignment, defects, impurities, etc.

### 2.6.2 Thermal Expansion of Nanotubes and Nanotube Bundles

Carbon nanotubes are deemed to show negligible expansion on heating. To validate this assessment, we have chosen a (10, 10) carbon nanotube bundle consisting 1600 atoms

and performed molecular dynamics simulation under atmospheric pressure conditions at temperatures starting T=100 K to T =700 K with increments of 100 K. Figure 36 shows the thermal expansion in axial direction. It is obvious that there is negligible expansion over 600 K range. The linear thermal expansion coefficient for (10, 10) tube, assuming constant thermal expansion was calculated to be: $\alpha = \frac{1}{L}\left(\frac{\partial L}{\partial T}\right)_P = 1.24 X 10^{-6} / K$ agreeing reasonably with literature [112,113].

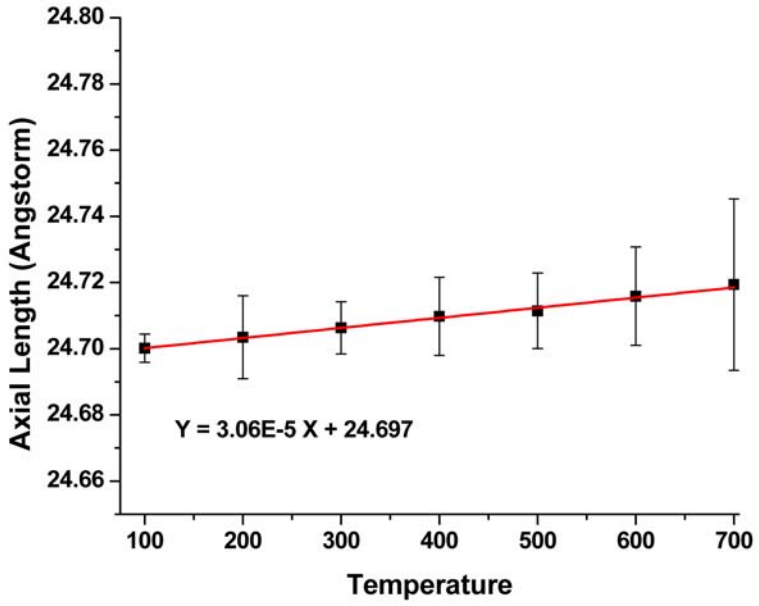


**Figure 36: Thermal expansion of nanotube in axial direction**

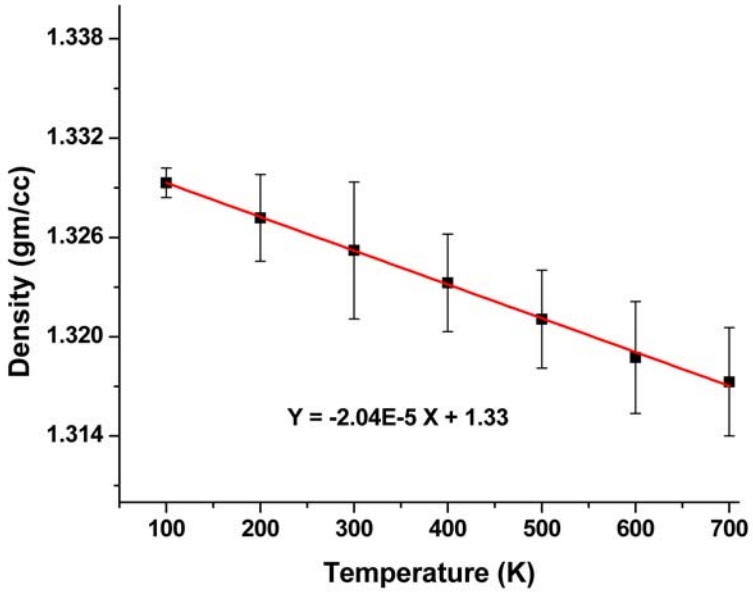


**Figure 37: Density variation of SWNT bundle with temperature**

We have determined the variation of density (Figure 37), volumetric thermal expansion and linear expansion in a- or b- axis directions. The off axis thermal coefficient expansion obtained from the relation $\beta_r = \frac{\gamma_v - \alpha}{2}$ where $\gamma_v$ is volume expansion coefficient and $\alpha$ is axial expansion coefficient, was $9.6X10^{-6}/K$. This is larger than axial linear expansion by a factor more than 7. This is understandable since it is essentially a result of the increased anharmonicity in tube-tube van der Waals interactions.

2.6.3 Kinks in Nanotori as Local Strain Energy Sinks/Sources

*Disappearance of kinks upon heating:* To study the rich configurations that result due to presence of kinks as in Cagin et al.[99], we have performed molecular dynamics simulations on a nanotori of (10, 10) nanotube with a mean radius of 7.83 nm. We performed a 50-ps constant temperature simulation at T=300 K. We observe that the structure resides in a metastable state with higher number of kinks. Thermal fluctuations

help overcoming the barriers between N and N-1 kink structures after around 40-45 ps. The sequence in Figure 38 demonstrates this process.

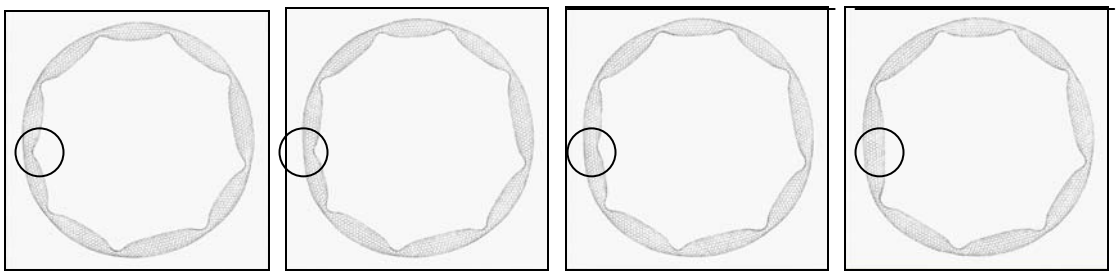

**Figure 38: Disappearance of kink upon heating**

We observe that a kink on the middle left portion of the ring as gradually disappeared as indicated in Figure 38. The time variation of the potential energy in Figure 39 apparently shows the energy drop pointing the annealing of one of the kink-defects.

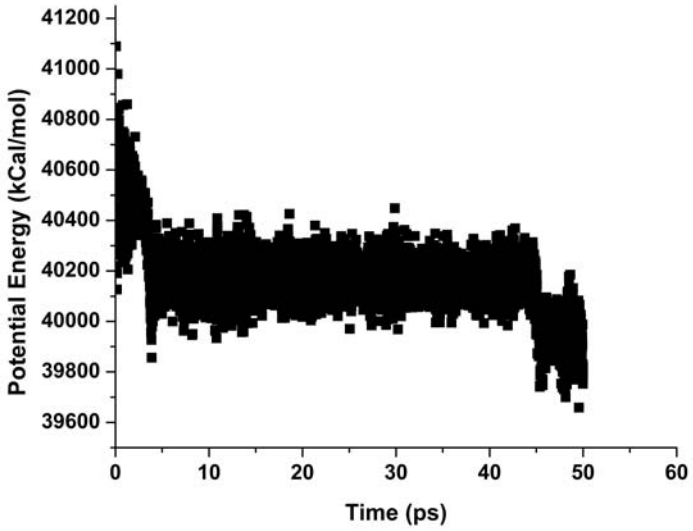


**Figure 39: Potential energy profile during kink disappearance**

The time span involved in such drop is also quite large, so the structure remains in one of the N-kink meta-stable state for almost 40 ps. We have calculated the amount of potential energy associated with this transition is ~ 200 kcal/mol. The model structure studied contains 8000 atoms. Hence, the corresponding change in potential energy per mol atoms only, $\frac{300X1000}{8000} = 37.5$ cal. If we compare this with the mean kinetic energy content of an atom at 300 K, RT ~ 600 cal/mol. Clearly, the barrier height per atom mol is within the variance of kinetic energy per atom at room temperature. Hence, we show that thermal fluctuations are strong enough to help the structure get out of metastable states local minima and move to a favorable structure with fewer kinks.

## 2.7 Dispersion of Nanotube

Dispersion of carbon nanotube in polymer matrix is one of the most frequent challenges faced by researchers[114]. The nanotubes tend to agglomerate and form bundles among themselves. It is definitely not good for the nanocomposite as it requires more weight percentage of nanotube for the desired material properties. To achieve better dispersion it is desired to have the nanotubes spread out in the matrix than agglomerate. In this regard the change in energy for different type of single walled nanotube for taking it out of the bundle was calculated. It can be assumed that, the energy required (after normalizing on per atom basis) is proportional to the ratio of surface area to volume of the individual nanotubes. Accordingly for nanotubes this ratio becomes

$$\frac{Surface\_area}{Volume} = \frac{2}{l} + \frac{2}{r}$$

For high aspect ratio which can be safely assumed to be proportional to $\frac{1}{r}$. Figure 40 and Figure 41 for armchair nanotube shows the energy dependence on the inverse of diameter of the tube.

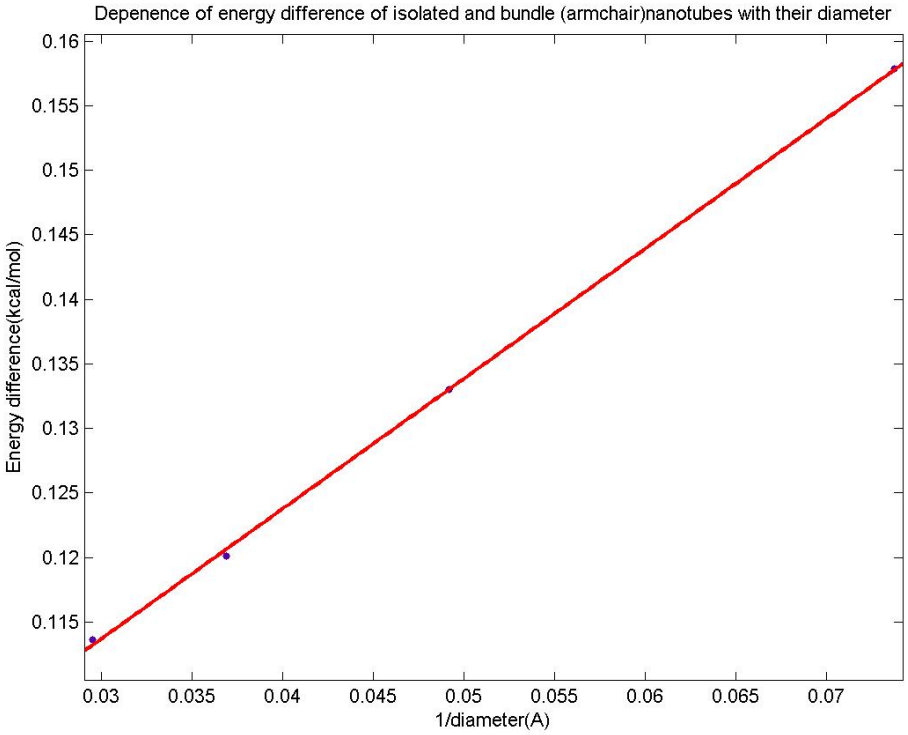


**Figure 40: Energy difference between isolated and bundle armchair SWNT for different diameter**

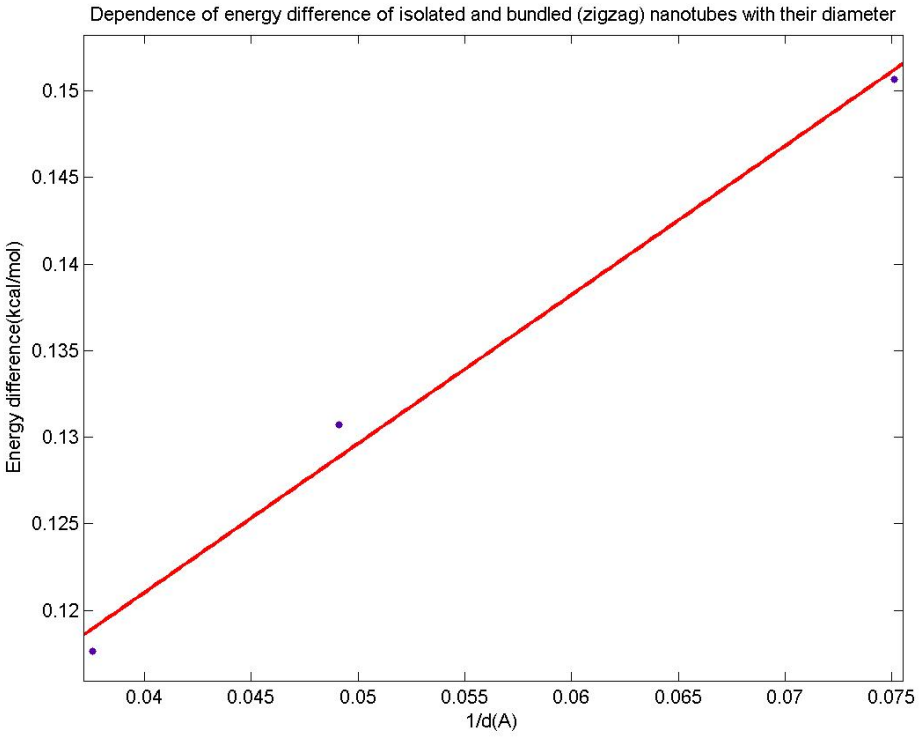


**Figure 41: Energy difference between isolated and bundle zigzag SWNT for different diameter**

In both the cases we see that the energy difference is proportional to $\frac{1}{r}$. It naturally means that it is easier to disperse larger diameter tubes than the small ones, but at the same time as observed earlier larger tube has lower modulus. This eventually brings up two opposing effects of the carbon nanotube based on their diameter.

## 2.8 Defects in Carbon nanotube

### 2.8.1 Stone Wales Defect

Strength of carbon nanotube was calculated incorporating Stone–Wales defects[115], which involves creation of one pentagon and one heptagon pair. Figure 42 shows the Stone Wales defect formation. The hashed bonds show the initial bonding in the pristine

graphene sheet, which gets broken and rearranged (basically a 90 degree rotation of a bond) in a way to give rise to a pair of heptagon and pentagon.

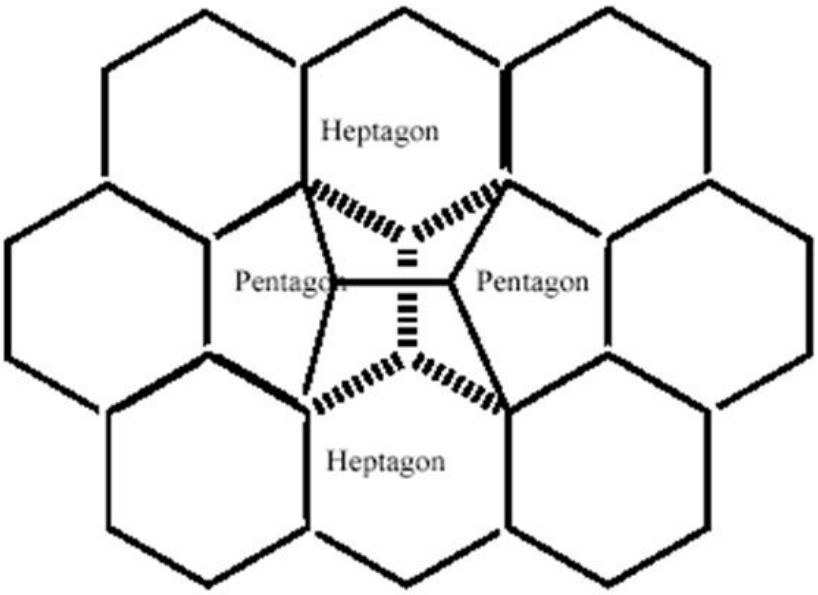


**Figure 42: Stone Wales defect**

In order to find the effect of the presence of the Stones-Wales defect on the young's modulus of single walled carbon nanotube, molecular mechanics calculation was carried on defective nanotubes of different chirality (namely zigzag and armchair) and diameters.

Figure 43 shows a (10, 10) defective nanotube having one defect per 2.47 nm. The calculation shows decrease in young's modulus for the presence of defects in the tubes.

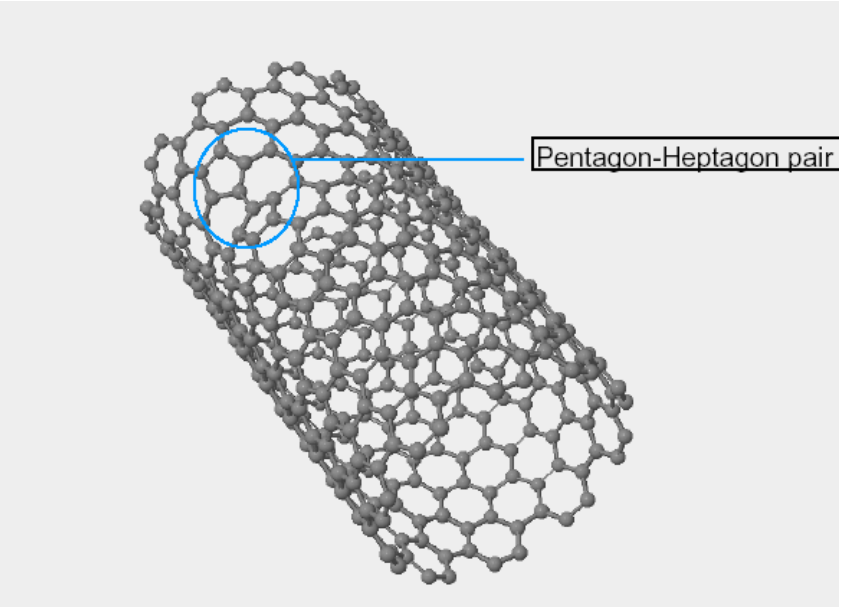


**Figure 43: Stone Wales defect in SWNT**

Figure 44 and Figure 45 give an idea about the young's modulus in highly defective nanotube obtained from molecular mechanics.

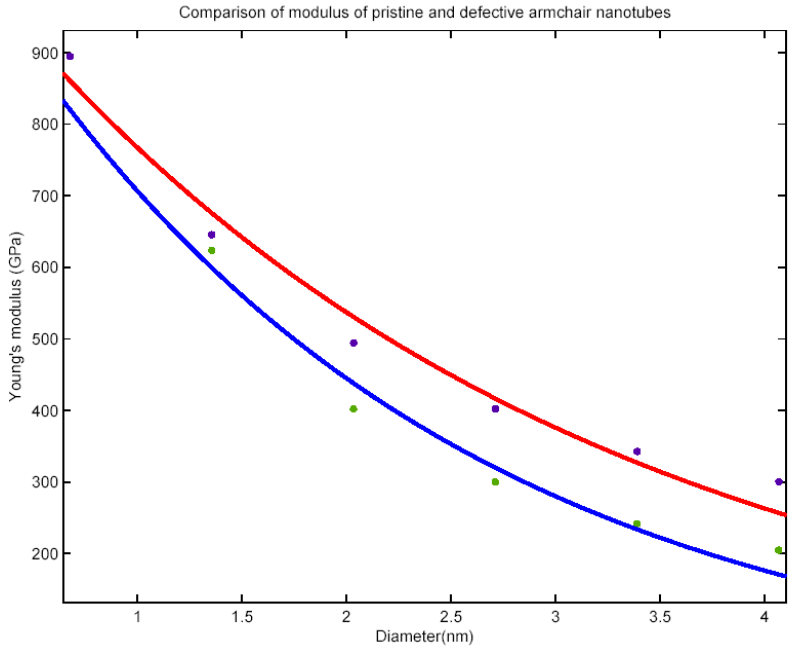


**Figure 44: Comparison of modulus for armchair SWNT for same defect concentration/ unit length**

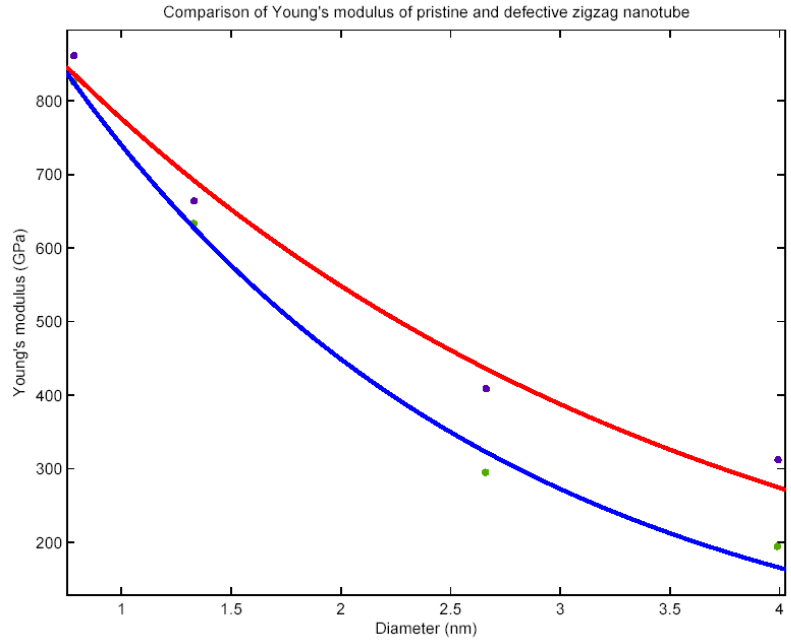


**Figure 45: Comparison of modulus for zigzag SWNT for same defect concentration/ unit length**

The interesting fact is that both for armchair and zigzag nanotubes it seems that the effect of defect also depends on the diameter of the tube and the gap becomes wider as one move to higher diameter.

A second type of defect was introduced to SWNT and the modulus was calculated. The defect was created in a way similar to the way Stone-Wales defect is created but instead of operating on the hexagonal ring structure of carbon atoms in nanotube it was operated on one of the side of a pentagonal pair (created from Stone Wales effect). This leads to creation of 4-8 rings also in addition to 5-7 rings. Figure 46 shows the same.

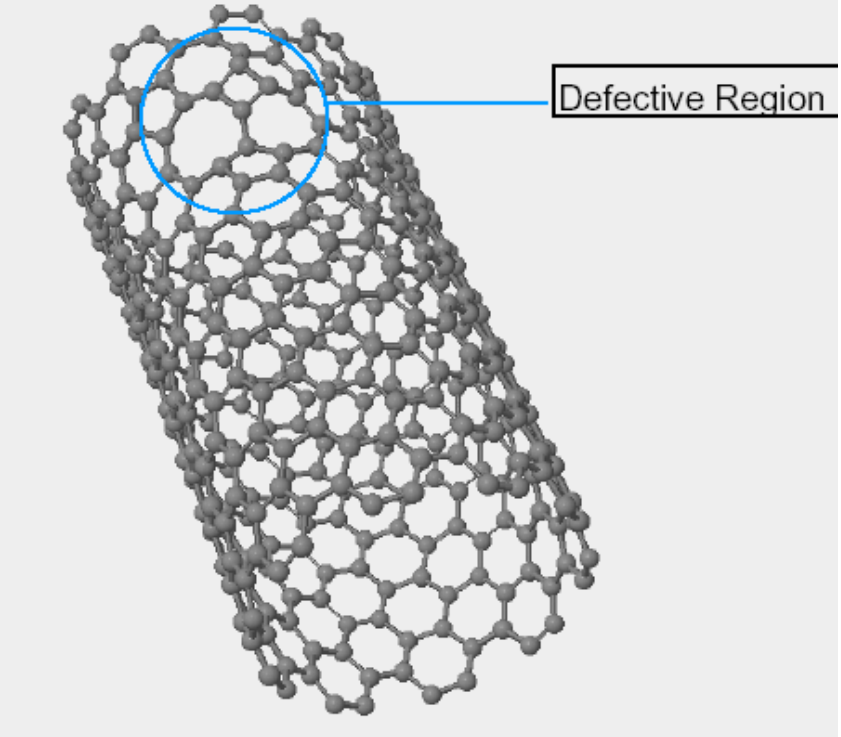


**Figure 46: Formation of (4-8) defect in SWNT**

To add variation, another calculation was carried out in SWNT bundle where only one nanotube out of four was made defective (through construction of a super cell).

Table 7 gives the value of Young's modulus for the above cases carried out for a (10, 10) tube.

**Table 7: Young modulus of defective SWNT for different cases**

| Defect type | Young's modulus (GPa) |
|---|---|
| Creation of 4-8 ring on Stone Wales defective region | 602.96 |
| One SWNT defective out of 4 in a bundle with c=2.47nm | 609.0 |

In [116] the authors looked at the effect of randomly occurring Stone Wales defect in a SWNT. They did molecular dynamics run at room temperature and found that the presence of the defects does not affect the Young's modulus significantly but it has more effect on the breaking strain of the same. However they also referred to other studies which have observed the effect of defects in SWNT. Depending upon the orientation of the defects with respect to the axial direction of nanotube Zhou et. al [117] tried to fit an equation that can predict the formation energy of those defects.

### 2.8.2 Effect of Relative Position of Defect in SWNT

In order to study the effect of relative position of defect in the young's modulus of single walled nanotube, a (10, 10) nanotube was taken with a periodic cell length of 12.3 nm. Studies were carried out with different defect concentration and different relative positions of the defect for same concentration. Table 8 briefs the findings. It seems there is a very little decrease in the modulus for tubes where the defects lie close to each other for same defect concentration.

**Table 8: Effect of relative position of defect on Young's modulus of CNT**

| SWNT | Defect Concentration (No. / Total Atoms) | Distance between two defects (nm) | Young's modulus (GPa) | Location |
|---|---|---|---|---|
| (10,10) | 2/2000 | 6.15 | 636.54 | Same wall |
| (10,10) | 2/2000 | 2.46 | 636.67 | Same wall |
| (10,10) | 2/2000 | 1.23 | 635.71 | Same wall |
| (10,10) | 4/2000 | 1.23 | 627.22 | Same wall |
| (10,10) | 5/2000 | 2.46 | 628.33 | Same wall |
| (10,10) | 4/2000 | 3.198 | 628.54 | Opposite Wall |
| (10,10) | 4/2000 | 0.738 | 627.06 | Opposite Wall |

### 2.8.3 Doping of Nitrogen in SWNT

Approximately 1% number of atoms in an SWNT was replaced by Nitrogen and young's modulus was calculated for armchair and zigzag nanotubes. Figure 47 gives an idea about the young's modulus of SWNT in such condition. The atoms were placed randomly in the structure.

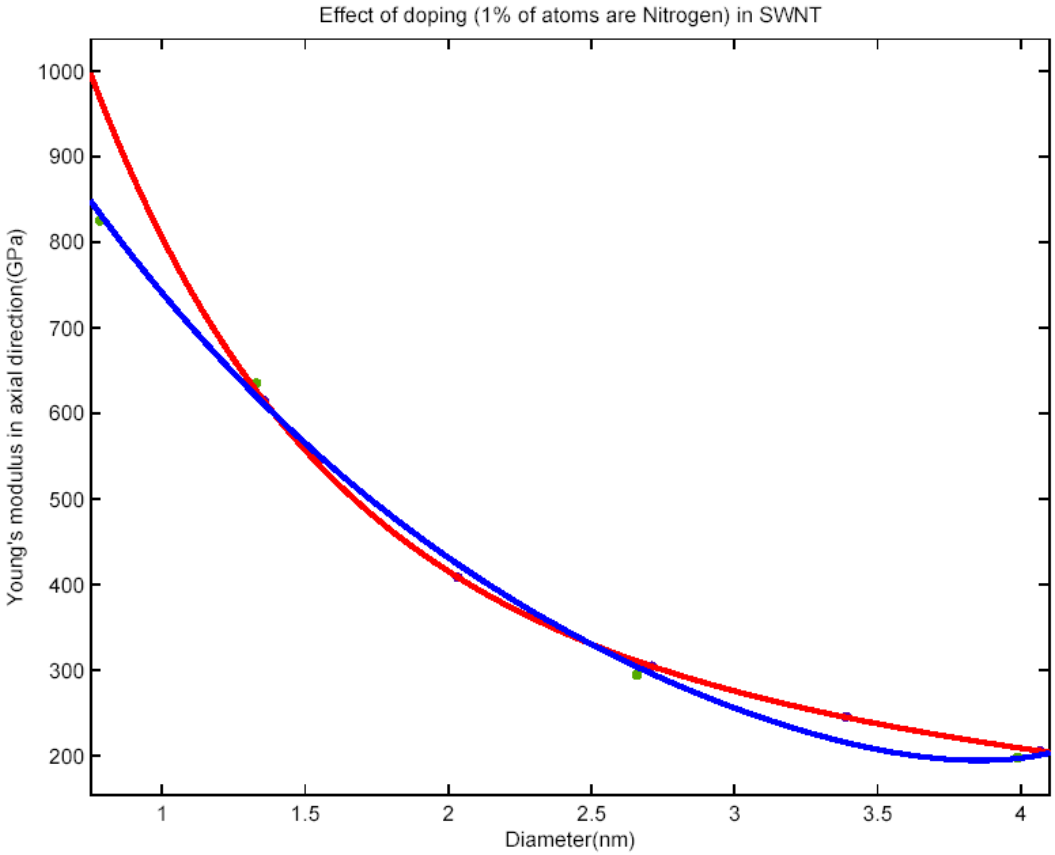


**Figure 47: Effect on Young's modulus after replacing 1% atoms by nitrogen**

From the figure it seems that it has similar effects in both armchair (blue curve) and zigzag (red curve) nanotubes. The force field used was an extended version of the graphite based force field used for calculation of pristine nanotubes by adding parameters from DREIDING to accommodate the nitrogen atoms.

In another study the modulus of SWNT was found out keeping the defect concentration same in the tubes of different diameter. One pair of pentagon-heptagon pair was introduced per 1680 atoms of a tube (except for (25, 25) for which it is per 1600 atoms). Figure 48 shows the variation of the young' modulus calculated with a graphite force field. From the figure it seems that the reduction in young's modulus is more at higher diameters than lower ones. However at lower diameters there do not seem to be

much effect for the given defect concentration. However the study can be redone after the modification of the force field based on ab-initio calculations.

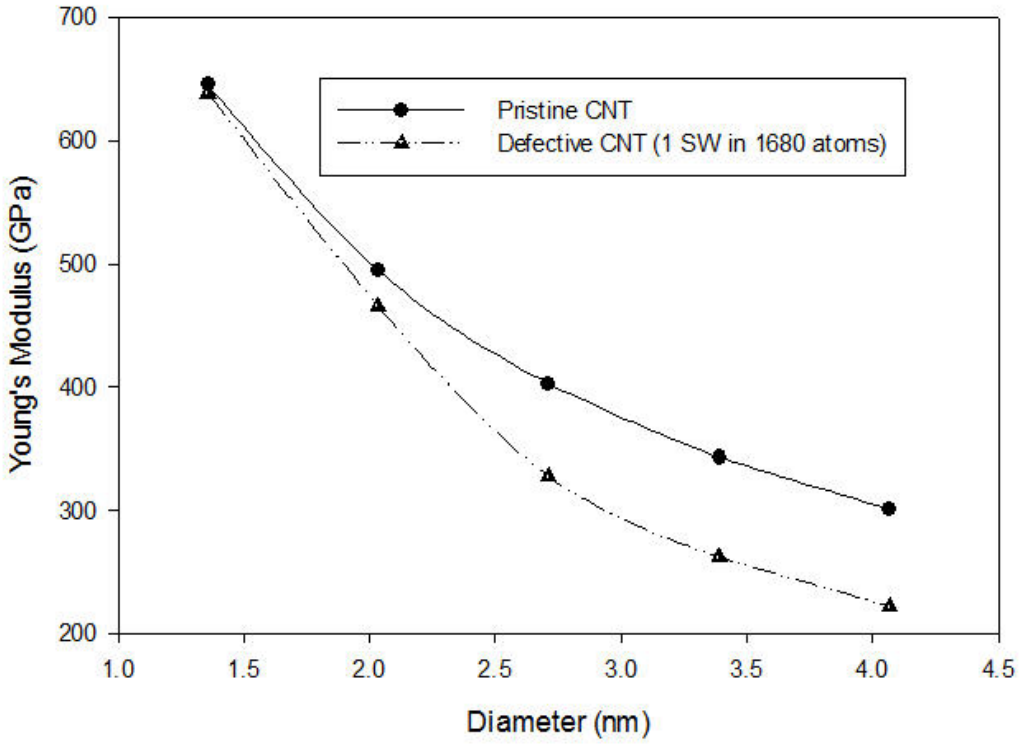


**Figure 48: Effect of Stone Wales defect on Young's modulus for same defect concentration per unit volume**

Another study was done where a (10, 10) tube was taken and two Stone Wales defect was introduced with different location to each other. The different location chosen were:

- One defect in each wall (two end points of the nanotube diameter) both located approximately at the middle (L/2 from each end) of the tube.
- Both defects in the same wall with L/3 distance between them.
- Both defects in different walls with each L/3 away from the nearest end and diagonally to each other.

Figure 49 shows a comparison of the results obtained for the above three cases along with that of a pristine tube and a defective one having one stone Wales defect. It seems that defect at same place but exactly opposite walls weakens the tube more than the other relative locations. However more studies needed to be done for a firm conclusion.

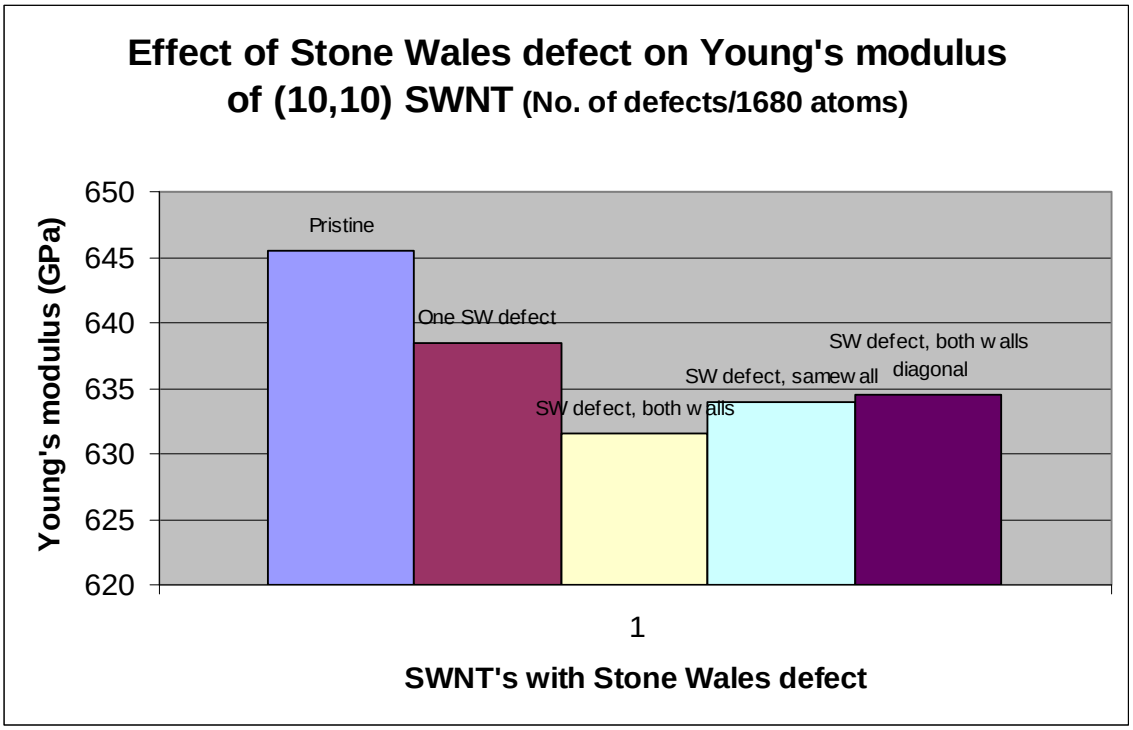


**Figure 49: Effect of the relative position on Young's modulus of (10, 10) CNT**

In another study, a (10, 10) nanotube was taken and two defects per 2000 atoms was introduced and the young's modulus of the same was calculated to see the effect of the relative distance between the two defects on the modulus. Apparently based on two studies it seems the modulus does not depend on the relative distance between the same. However more studies are being carried out presently to verify the same. In both cases the value of the young's modulus using a graphite force field was found to be ~ 636 GPa. This also goes in accordance with Figure 49 where it is shown that the modulus of

SWNT with defects in the same wall is little less than 635 GPa, as we know that the defect concentration is higher in Figure 49 than the latter case described.

2.8.4 FF issues in Defective SWNT Calculation

**Figure 50: Pure graphene sheet and a graphene sheet with Stone Wales defect**

The modulus shown in previous pages uses the graphite based force field for the calculation of the same in the presence of Stone Wales defect. In order to get better parameters, the structure and energy of a small part of graphite sheet (35 atoms, as shown above for the pure case) both pristine and having the presence of Stone Wales defect, was investigated (Figure 50) in Gaussian using density level theory (b3lyp) using a basis set 3-21g. Similar calculation was also done for doped SWNT. As one can realize there would be differences in the equilibrium distances, angles and other parameters for these defects especially for the Stone-Wales one. An obvious one is the deviation of angle values, which are approximately $120^0$ for a hexagon and $108^0$ for a pentagon structure, calculating from simple geometry. Other than angles, changes in bond lengths, torsion values should also be incorporated in the force field. Table 9 and Table 10 give an idea about the energy differences between the pristine sheet and the defective sheet.

**Table 9: Energetic of graphene sheet, pure and defective**

| Graphite sheet (35 atoms) | Energy (Hartrees) 1 Ha = 627.51 Kcal/mol |
|---|---|
| Pure | -1601.4490636 |
| With one SW defect | -1601.3272939 |

Other than calculations with defective nanotubes, ab-inito calculation was performed on a (10, 10) armchair nanotube in VASP with DFT level of theory. From the Eigen values obtained in this calculation it also shows that the difference in energies of HOMO and LUMO decreases for a defective sheet thereby indicating an increase of electrical conductivity in a defective (Stone Wales) nanotube with respect to a pristine one.

**Table 10: HOMO-LUMO calculation for pure and defective graphene sheet**

| Sheet | (LUMO – HOMO) |
|---|---|
| Pure | 0.09456 |
| Defective | 0.09435 |

2.8.5 Effect of Stone Wales Defect in Nanotori

Effect of introducing Stone Wales defect in a certain way into the nanotori structure was investigated (Table 11) for nanotori of different diameter from (10, 10) carbon nanotube. Defects were introduced at regular distance spanning the whole perimeter, and also with regular distance but mainly concentrated in one part of the nanotori.

**Table 11: Strain energy in defective nanotori**

| Radius (nm) | Energy per atom (Kcal/mol) | Strain Energy per atom (Kcal/mol) |
|---|---|---|
| 7.83 | 4.134 | 1.2095625 |
| 11.745 | 3.7985 | 0.8740625 |
| 15.66 | 3.5035 | 0.5790625 |
| 23.49 | 3.20911 | 0.2846725 |
| 31.32 | 3.091 | 0.1665625 |
| 39.15 | 3.036 | 0.1115625 |

The defect concentration was kept same (one Stone Wales defect per 8000 atoms approximately). The orientation of the defect was such that the common side of the heptagons was parallel to the nanotori perimeter. In another study the defect orientation was changed and the angle $\theta$ between the common side of the heptagons and the perimeter of the nanotori was approximately $\frac{\pi}{3}$. The comparison is given below in Table 12.

**Table 12: Effect of defect orientation on strain energy**

| Radius (nm) | Energy per atom, $\theta = 0$ (Kcal/mol) | Energy per atom, $\theta = \frac{\pi}{3}$ (Kcal/mol) |
|---|---|---|
| 7.83 | 4.134 | 4.1818 |
| 31.32 | 3.091 | 3.0946 |

In both cases the defect was introduced in the sidewalls of the non-minimized nanotori. From Table 12 it seems that the case with $\theta = 0$ is most likely to happen, as it is more favored energetically.

## 2.9 Concluding Remarks

We have evaluated mechanical and thermal properties of carbon nanotube and nanotori and in the present work to gain insight of structure property relationship of nanotube. We observed that the definition of area used for Young's modulus calculation of nanotube is non-trivial and can be the source of difference by a significant factor. It might also be responsible for the different trends reported in literature. On this basis, we have come up with equations that address discrepancies both in values and trends of axial modulus. We also find that the van der Waals forces have the least significance in the strength of multi-wall nanotube but it can govern the structure of the outer shells. This resulted in a hexagonal structure with higher packing efficiency and hence, a denser system. By applying torsion to an infinite length nanotube in a novel way, we find that the claim of higher twist modulus of zigzag nanotube relative to its armchair counterpart in the infinite limit is not valid. The effect of temperature on nanotube mechanical properties was found to be minimal and for design of nanotube-based materials the temperature effect on its intrinsic properties can be neglected if the operational range is a few hundred degrees. Importance of micromechanics modeling at interface of composites is well known[118]. Similarly the insights gained in this study can be incorporated in designing composite materials made from nanotube. Most of the nanotube structures used were defect free in this study, we expect these results to be the ideal ones and expect some deviations in reality, due to more pronounced effects of topological defects, impurities, and alignment defects in bundles[76,119]. However our study in assessing the effect of Stone Wales defects on mechanical properties on nanotube and nanotori showed non-significant effect on the modulus of the same.

# 3. POLYIMIDE

## 3.1 Introduction

### 3.1.1 Piezoelectric Polymer

As briefly mentioned in section 1.7.1, piezoelectric activity has been quite of interest to researchers[35-37] because of their numerous potential applications ranging from microelectronics to spacecraft. The addition of electromechanical coupling ability to the already existing set of exciting properties of a typical polymer makes piezoelectric polyimide very attractive in designing materials targeted to future generation applications. Within the domain of piezoelectric polymers, PVDF (Poly vinylidene fluoride) has got a lot of attention from researchers [38-41]. Due to its limitation in high temperature applications[36,45], researchers are looking for thermally stable polymers with similar properties suitable for high temperature applications. Evidence[42-44] of piezoelectric behavior by Nylon is also shown in literature.

Experiments have shown that amorphous polyimide made from (β – CN) APB/ODPA monomer can generate piezoelectric responses at elevated temperatures[46]. The glass transition temperature ($T_g$) of the polyimide is close to 500 K[47] which gives a much higher temperature range for application. However the fact that the piezoelectric response of this polyimide is lower than required[47] for practical utilities at room temperature, has become the bottle neck of promoting this polyimide further from research laboratories to commercial application.

Stimulated by its high thermal stability and piezoelectric nature along with the challenges involved in understanding the physics to help realize the viability of the polyimide to design future generation materials, in this section we will present our classical molecular dynamics simulation work to look into the polymer behavior at the atomistic level. We have estimated thermo-mechanical properties and dielectric properties of the polymer under different conditions. We have also looked into time dependent response of the polymer sample. The largest polymer sample considered has

40 chains with 40 monomers per chain. The length of a stretched chain of such polymer will be in the order of micrometer. In the following we have presented our observation and analyses from our computational experiments carried out on the piezoelectric polymer sample and have attempted to give an insight in explaining its observed behavior.

3.1.2 System

The piezoelectric polyimide studied in this work is an amorphous, aromatic polyimide substituted with nitrile dipole. For convenience Figure 7 is redrawn as Figure 51 representing $(\beta - CN)APB - ODPA$ polyimide monomer. It has been shown[24] that the nitrile group contributes to 48% of the total polarization and 39% of the polarization is contributed from the di-anhydride group.

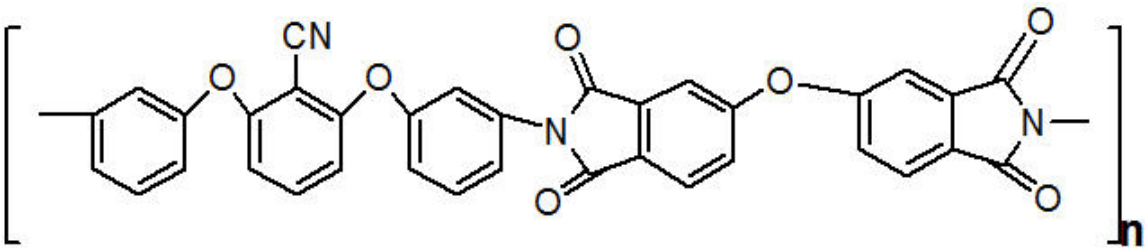


**Figure 51: Monomer**

Park et al. [23] has studied dipole orientation of the polyimide made of (β – CN) APB/ODPA monomer using 'Process control' approach. The dielectric behavior, remnant polarization and piezoelectric responses were assessed as a function of temperature and frequency. In another work [47] Simpson et al. focused on the synthesis and characterization of the same polyimide. Presence of 94% remnant polarization was observed at 150C and some were retained till the glass transition temperature. This retention of the remnant polarization observed even near the glass transition temperature of the polyimide was certainly encouraging for high temperature applications. Ounaies et. al. [24] did molecular modeling and dielectric measurements on the same polyimide to

investigate the response of the polyimide to the temperature and electric field. The polymer was poled at high temperature and then was cooled down to room temperature to estimate the steady state value of remnant polarization by molecular dynamics. In [35] poling of piezoelectric polyimide (β – CN) APB/ODPA monomer and APB/ODPA monomer) was modeled using modified CFF91 force field. Dynamic mechanical analysis were performed on (β – CN) APB/ODPA polymer in an unpublished work[22] where the increase in storage modulus was shown with inclusion of carbon nanotubes. The Halpin-Tsai[57] model was used to predict the composite storage modulus and was found that it underestimates the same. A more detailed overview of data related to polarization of different piezoelectric polymers can be found in literature[25].

### 3.1.3 Sample Building

One of the biggest challenges in atomistic simulation is to come up with the minimum energy configuration of the system concerned in a reasonable amount of time. The terms for different type of energy expressions in a force field indicates that there are many factors involved in a structure, and ideally the minimum structure should be a global minima with respect to all those parameters. For a large system, obtaining such structure often becomes challenging. Methodologies have been developed to attain an equilibrated structure of a system using reasonable computational resources. It does not however guarantee the success of the method unless validated by experimental observation. The structure of a polymer can take any form and having large number of atoms in one molecule make things more complex.

Cerius [18] , Materials Studio and LAMMPS were used for the modeling and simulation purpose of the polymer. In the following, the steps used in building the polymer through Cerius have been described. The monomer was first built using the Build module of Cerius. The homopolymer of several monomers was then built into a chain. The charges on each atom were then calculated with the help of charge equilibrium method[120]. An amorphous polymer of several chains of the polymer was built subsequently with periodicity using the amorphous builder module available in Cerius. However the target density specified while building the initial amorphous

polymer was quite low as shown in several places [8,121,122]. Figure 52 represents an amorphous sample of the polyimide in simulation window.

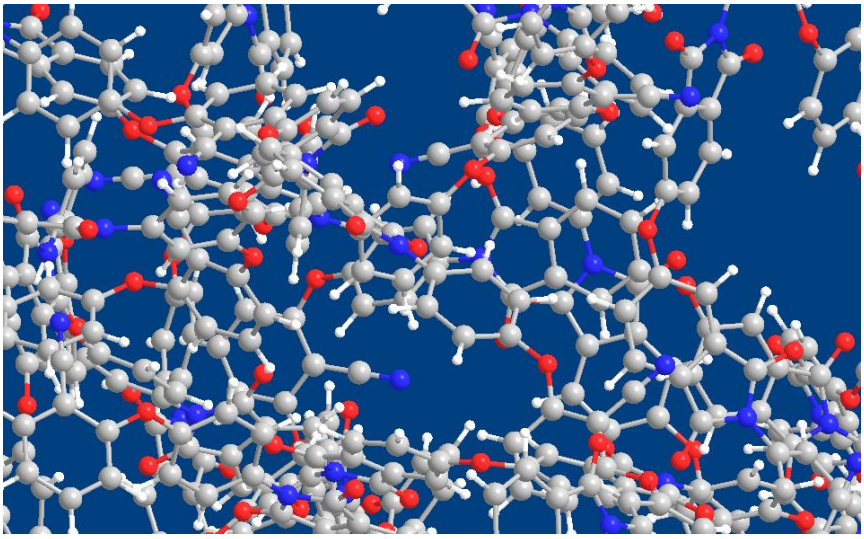

**Figure 52: Polyimide sample in simulation window**

As mentioned earlier the force field chosen for the molecular simulation run was Dreiding and CVFF. Both of these seemed to be reasonable force field for the system in hand.

The initial built was targeted with a density of 0.2 gm/cc. While the initial build was through Dreiding force field, the successive compression cycle was done using CVFF force field in LAMMPS. The structure went through cycles of minimization of energy and dynamic simulations with temperature annealing from 300K to 600K to make sure that the structure does not get trapped into a high energy local minimum. Initially the shape and volume of the unit cell was kept intact by fixing the cell parameters (a, b, c, $\alpha$, $\beta$, $\gamma$) during the process. The properties were investigated at 300K, well below glass transition temperature (~ 493K) of the polyimide as reported[24]. The density was slowly increased by reducing the lattice parameters but keeping the axis ($\alpha = \beta = \gamma = 90^0$) orthogonal to each other. Earlier experience shows [8] jumping directly to the final density as opposed to approaching it step by step might lead to jumps in sample

density while performing NPT dynamics finally for property investigation. The above cycles of minimization of energy, NVT dynamics with temperature annealing was done repeatedly until the amorphous polymer reached little over experimental density. Then first the cell parameters and then consequently the angles were given the flexibility to vary in order to reach a final reasonably equilibrated structure.

The simulated structure must show that the internal stresses of the structure have gone to (close to) zero. The time step for the simulation was chosen to be 1 fs. Generally speaking, such 600000 steps (600 ps) were used for each run for equilibrating the structure. The final run for property investigation was done for 400 ps which makes a total of 1 ns run (where 400 ps is production run) with a time step of 1 fs. In a later section, 3.2.2, we have revisited this issue with explanation of equilibration of a polymer sample with illustrative figures.

### 3.1.4 Properties from Simulation

The main purpose for doing atomistic simulation is to predict the bulk properties of the system. The understanding of the physics behind the relation of macroscopic properties and microstates is very important in this regard.

Methods have been developed to predict the mechanical properties by calculating the elastic constants by performing molecular dynamics[9,123] simulation. Young's modulus, bulk modulus and shear modulus are three main stiffness measure of a material. For an amorphous material owing to isotropic behavior these three are related. Various types of tests are available for evaluation of these properties. In here we have briefed the basic definitions of all these properties that will be used in subsequent sections to examine the material response. Young's modulus is defined by:

**Equation 29**

$$Y = \frac{\sigma}{\varepsilon}$$

Where $\sigma$ represents tensile stress and $\varepsilon$ represents tensile strain. Similarly shear modulus is defined by:

**Equation 30**

$$G = \frac{\tau}{\gamma}$$

where $\tau$ represents shear stress and $\gamma$ represents shear strain.

Bulk modulus is related to the change in volume of the material when an external force is applied uniformly in all direction. It is defined as:

**Equation 31**

$$B = -V \left.\frac{\partial P}{\partial V}\right|_T = \rho \left.\frac{\partial P}{\partial \rho}\right|_T$$

where: $\rho$ represents density.

When there is a development of tensile or compressive strain in one direction some strain is also developed in the other two directions. These strains are related by poisson ratio.

Lateral strain = - $\upsilon$ x tensile strain

where $\upsilon$ defines the poisson ratio.

In order to calculate the mechanical properties of the pure polyimide system concerned, the method in [9] was applied. To calculate the elements $C_{ij}$ of the stiffness matrix strain $\sigma_{ij}$ was applied to the system in a systematic form and molecular simulation was done in NVT ensemble and the stress $\varepsilon_{ij}$ was calculated. The stress applied was both tensile and compressive. The elastic or stiffness constant was calculated as:

**Equation 32**

$$C_{ij} = \frac{(\sigma_{i+} - \sigma_{i-})}{(\varepsilon_{j+} - \varepsilon_{j-})}.$$

Calculating the above for j = 1 to 6 for all the elements (6 X 6) allows one to estimate the stiffness matrix. However in our study we have mostly dealt with axial modulus mostly owing to limitation posed by LAMMPS current (as of 2008 April) simulation ability.

For an isotropic material the stiffness matrix has only three stiffness constants and two of which are independent, $\lambda$ and $\mu$. Ideally a stiffness matrix (Figure 53) of an isotropic material should look like [124]

$$\begin{vmatrix} \lambda+2\mu & \lambda & \lambda & 0 & 0 & 0 \\ \lambda & \lambda+2\mu & \lambda & 0 & 0 & 0 \\ \lambda & \lambda & \lambda+2\mu & 0 & 0 & 0 \\ 0 & 0 & 0 & \mu & 0 & 0 \\ 0 & 0 & 0 & 0 & \mu & 0 \\ 0 & 0 & 0 & 0 & 0 & \mu \end{vmatrix}$$

**Figure 53: Stiffness matrix for isotropic material**

The coefficients of this stiffness matrix are denoted by $c_{ij}$. So as given above for an isotropic material the following relations exist.

$c_{11} = c_{22} = c_{33} = \lambda + 2\mu$

$c_{44} = c_{55} = c_{66} = \mu$

$c_{11} - c_{12} = 2c_{44}$

The value of Young's modulus, bulk modulus and shear modulus are related to the above matrix as given below:

Shear modulus: $\mu$

Bulk modulus: $\mathrm{B} = \dfrac{Y}{3(1-2\sigma)} = \dfrac{c_{11}+2c_{12}}{3}$ where $\sigma$ is the poisson ratio.

Another important test is dynamic mechanical test[125] which reveals how the material responds under a stress which is periodic in nature unlike the ones discussed above. It is always conducted in the linear viscoelastic range. This gives an idea about how the polymer will behave during processing of the same which is of prime importance. This also gives an idea about the storage modulus and loss factor. Generally

the material is subjected to a constant load with the applied stress is given in sinusoidal form and the sample response in terms of strain is in similar fashion. For a perfectly elastic material the nature of the stress and strain curve will be in phase all the times. But for others there will be a phase lag which is defined by phase angle $\delta$. The complex modulus is defined as $E^* = E' + iE''$ where $E'$ the real part is the measure of stiffness and called as storage modulus. The imaginary part $E''$ is called the loss modulus which is understood as the measure of dissipation. The phase lag angle is defined by:

$\tan\delta = \frac{E''}{E'}$ and can be interpreted as the ratio of energy dissipated as heat to that of the maximum energy stored in the material during one cycle of oscillation. Calculation of stiffness matrix through molecular mechanics method is given in section 3.2.8.

## 3.2 Polyimide Characterization

### 3.2.1 Tools

In this classical molecular dynamics simulation work we have used CVFF as force field with 1 fs time-step. Materials Studio and Cerius[2.0 18] was used for the initial build of the amorphous structure of the polymer. Subsequent equilibration, modeling and simulation were done using LAMMPS [126,127]. Harmonic potential was used to describe the bond and angle energy. Dihedral and improper energy was described by a cosine functional. Lennard-Jones 12-6 scheme addressed the van der Waals interaction. Particle-particle particle-mesh (PPPM) method was used to incorporate the long range interaction of the columbic forces.

### 3.2.2 Equilibration

One of the biggest challenges in atomistic simulation is to come up with the minimum energy configuration of the system concerned in a reasonable amount of time. The initial amorphous structure of the polyimide was built using software mentioned above. Charge equilibrium method[120] was used to calculate the charges at the monomer level and then replicated for polymer samples. The target density of the initial build was in the order of

~ 0.2 - 0.3 gm/cc similar shown to some of the other works[8,121,122]. The initial build structure was subjected to conventional method [8] of compressing the unit cell box along with temperature annealing and finally relaxing through isothermal-isobaric ensemble to have the resultant equilibrated structure. A view of the polyimide in a molecular simulation environment is given in Figure 54.

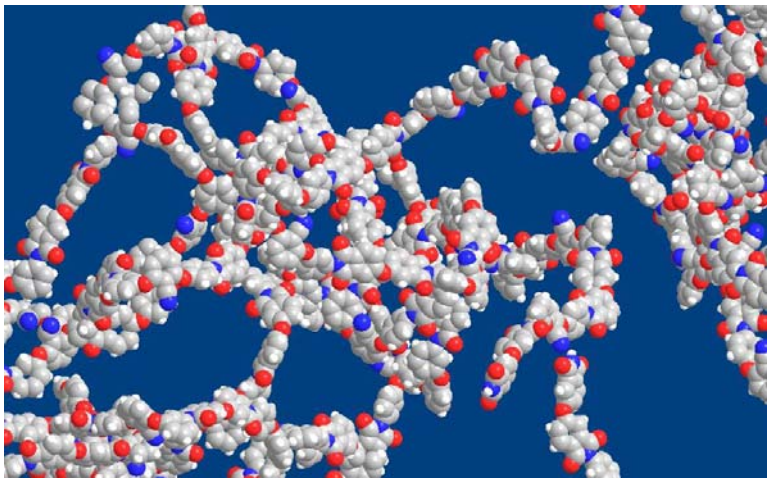

**Figure 54: Polymer sample in simulation window**

Eight different samples generated by this methodology consisted of 2244, 7460, 7760, 18620, 37230, 37240, 74460 and 99280 atoms. Referring a polymer with m chains and n-monomer per chain as m_n polymer, 6_6, 10_12, 5_25, 10_30, 15_40, 20_30, 30_40 and 40_40 polymer samples were built. The unit cell of the equilibrated sample obtained was always orthogonal. LAMMPS inability to handle non-orthogonal boxes with isothermal-isobaric ensemble[128-130] approach was the primary reason behind this.

The profile of the instantaneous values of the energy and volume were used to decide the cutoff between the equilibration and production run. Figure 55 illustrates this. Examining the trend of instantaneous values of the two properties, we observe from the above figure that the sample is equilibrated in around ~ 20 ps. In cases where the external conditions are very different from normal conditions, equilibrated structures of the samples were generated separately starting from the equilibrated structure at normal

condition through a NPT run. Normal condition refers to zero atmospheres pressure and 300 K temperature. The time required for equilibration in those cases and conditions were different accordingly. Polymer samples acting under severe stress, strain, electric field and high temperatures are examples of such cases. In all these above-mentioned cases sufficient equilibration time was given to each sample to have confidence in the properties estimated from the corresponding production run.

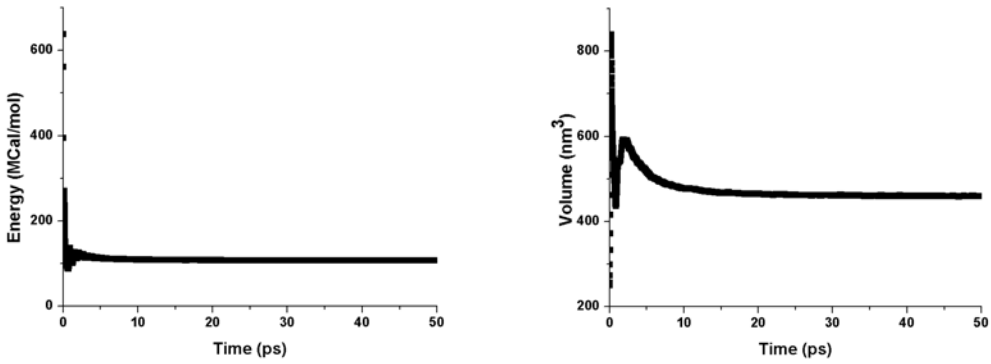


**Figure 55: Equilibration of 20_30 polyimide**

Bulk properties of polymer define the important set of properties through which a polymer is rated macroscopically. Estimation of these properties in molecular dynamics generally serves two purposes. First it tells whether the sample was properly built including the method, force field and the potential. Given the first factor is positive it helps to estimate other properties. The bulk properties of the polymer sample were estimated from the production run by performing averages on the instantaneous values. The fluctuation behavior of the sample at equilibrium was also used to estimate non-equilibrium properties by the use of fluctuation dissipation theorem.

### 3.2.3 Density

Even though straightforward in terms of estimation, it is one of the prime factors in determining the reliability of the molecular dynamics study of any material. The density

of each sample was calculated by the knowledge of the instantaneous volume of the unit cell and the molecular weight of the polymer in the unit cell. The experimental density of the polyimide being studied has been found to be 1.34 gm/cc[35]. The polyimide (β – CN) APB/ODPA was equilibrated using minimization and MD techniques as discussed in a previous section.

To compare different force field long production run was done at 300 K using Dreiding [6] and PCFF [131] or Polymer consistent force field and CVFF in Cerius. The system consisted of 7452 atoms. It was consisted of 6 chains with 20 monomers per chain. The full simulation run was for 1 nanosecond, 600 picoseconds of which was taken as equilibration run and the rest 400 ps was used as production run. The results from the production run are given in Table 13.

**Table 13: Density of pure ( $\beta$ - CN) APB/ODPA**

| Force Field | Density (gm/cc) |
|---|---|
| Dreiding (LJ) | 1.17 |
| PCFF | 1.19 |
| Dreiding (Exponential) | 1.27 |
| CVFF (modified) | 1.26 |

Upon observation of Table 13 we find that the modified CVFF and Dreiding with exponential 6 form of van der Waals interaction did better job than the other two form of force field considered.

Building more samples with different chain lengths and different number of chains in one unit cell and considering more than one samples of each of these and then estimating the properties will give more confidence in the data that is calculated by molecular simulation. In LAMMPS[17] for a smaller system which consisted of 4 chains of 5 monomer length (1304 atoms) of the same amorphous polyimide, the density was found out to be 1.26 gm/cc using a modified(all the unavailable parameter values were taken from Dreiding force field) CVFF force field. Few bond (4), angle (9), torsion (5) and inversion (5) parameters were taken from Dreiding force field. A similar polyimide

(made from APB and 6FDA) was found to have an experimental density of 1.4 gm/cc [56]. Since density is largely dependent on structure it is expected that the density of (β – CN) APB/ODPA will be in the similar range. As mentioned before Young et al. has found the density of (β – CN) APB/ODPA polyimide to be 1.34 gm/cc[35].Molecular simulation with modified CFF91 in the same paper the author could get the same density.

In our simulation changing the potential for non bond interaction from Leonard Jones (LJ) to exponential will have an effect in density of the system and might make the values more close to the experimental values. Also while simulating in Dreiding two torsion expressions were not computed (per monomer) due to non availability of force field parameters (given as a warning in Cerius 2.0). The contribution of these two torsional parameters to the potential energy of the system was found from CVFF force field and it turned out to be zero and hence has not affected the result obtained from Dreiding.

Noting the distribution of density obtained of any polymer found in literature in molecular dynamics study, a fresh set of five samples of 6-6 (6 clones of polyimide consisting of 6 monomers, 2244 atoms) was built from an initial density of 0.1 gm/cc with the Dreiding force field having van-der Waals repulsive term expressed in exponential form. The following table 14 gives the densities obtained for the five samples prepared.

**Table 14: Density of pristine polyimide of 2244 atoms**

| Samples of polyimide (2244 atoms) | Density (gm/cc) |
|---|---|
| Sample 1 | 1.34 |
| Sample 2 | 1.35 |
| Sample 3 | 1.29 |
| Sample 4 | 1.32 |
| Sample 5 | 1.34 |

From Table 14: $\rho_{avg} = 1.33 \pm 0.02$, which seems to be in good agreement with the literature value. The obtained samples were not pressure annealed. Using CVFF force field in LAMMPS pressure annealing was performed and similar to [8] it was observed that the loading (increasing pressure on sample) and unloading curve follow a different path, resulting in a higher density of the sample after unloading. Section 3.29 examines the effect of pressure annealing in the polymer sample more elaborately.

Subsequent to our force field testing on our polymer sample we have used CVFF force field to build and equilibrate polymer samples of different sizes. In section 3.2.4 we have presented the results obtained from the production runs of the various polymer samples. We observe that estimated density of the polymer sample from our simulation study is ~ 5 % different. We will later show, by using pressure annealing techniques [8] we can free out some of the trapped voids and reconcile some of the differences. However it must also be noted that larger number of samples and larger systems is expected to give more reliable and realistic estimate of the properties.

In the context of the amorphous nature of the sample the average radial distribution function of the first sample was calculated and Figure 56 gives the plot of g(r) (radial distribution function) for frame in the trajectory and was found to have a similar trend to the g(r) obtained in [35] for the same polyimide.

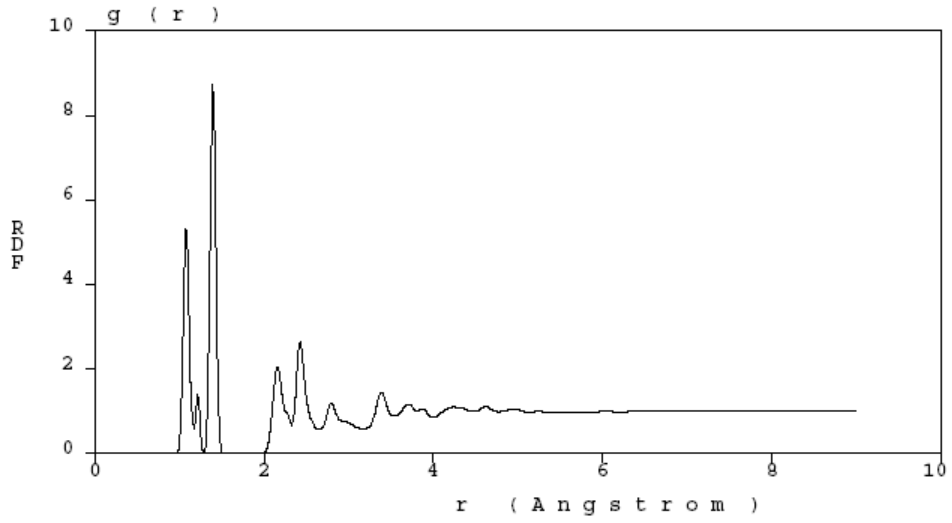


**Figure 56: Radial distribution function for polyimide sample (6-6)**

From Figure 56 we observe that after a distance of almost 5 $A^0$ there is no correlation between two atoms which is an indication of the amorphous nature of the sample[8]. The first peak is most likely that of a C – C bond of 1.39 $A^0$ found in a benzene ring.

3.2.4 Bulk Modulus

Measurement of bulk modulus of a polymer sample gives an overall stiffness measure of the same. Fluctuation dissipation theorem can be used to calculate non-equilibrium response of the sample by measuring the fluctuations at equilibrium. The unit cell volume fluctuations in the production run were used to find the bulk modulus of the system through fluctuation dissipation theorem. It can be shown that in an Isothermal-isobaric (NPT) ensemble the bulk modulus from fluctuation of volume can be calculated as:

**Equation 33**

$$\frac{1}{B} = \frac{\langle V^2 \rangle - \langle V \rangle^2}{kT\langle V \rangle}$$

where

k = Boltzmann Constant = 1.38 X $10^{-23}$ $JK^{-1}$

Table 15 summarizes the density and bulk modulus obtained from these production runs for the eight polymer samples.

### 3.2.5 Normalized Energy

The value of the total energy of the polymer sample was also calculated and was normalized per monomer basis. The normalized value can be used to compare the energetic of the different polymer samples.

### 3.2.6 Specific Heat Capacity ($C_p$)

Similar to the calculation of the bulk modulus from the fluctuation of the cell volume, the value of specific heat was calculated from the fluctuations of the internal energy in the NPT ensemble production run. The following was used to calculate the value of $C_p$:

**Equation 34**

$$\left\langle (\delta E)^2 \right\rangle = k_B T^2 C_p$$

where

$\left\langle (\delta E)^2 \right\rangle$ = Variance of Total Energy

$k_B$ = Boltzmann Constant = 1.38 X $10^{-23}$ $JK^{-1}$

T = Temperature

The following table summarizes the results obtained for the above-mentioned four properties for eight different polymer samples.

**Table 15: Density, bulk modulus, normalized energy and specific heat capacity calculation**

| Sample | Atoms | $\rho$ (gm/cc) | B (GPa) | E/ monomer (kcal/mol) | $C_p$ (KJ/ Kg-K) | Production (ns) | Equilibration (ns) |
|---|---|---|---|---|---|---|---|
| 6_6 | 2244 | 1.22 | 3.93 | 146 | 2.76 | 1.5 | 0.5 |
| 10_12 | 7460 | 1.29 | 8.81 | 142 | 3.01 | 1.5 | 0.5 |
| 5_25 | 7760 | 1.28 | 8.49 | 141 | 2.66 | 1.5 | 0.5 |

**Table 15: Continued**

| | | | | | | | |
|---|---|---|---|---|---|---|---|
| 10_30 | 18620 | 1.28 | 7.02 | 173 | 2.72 | 1.5 | 0.5 |
| 20_30 | 37240 | 1.29 | 3.97 | 234 | 2.93 | 1.5 | 0.5 |
| 15_40 | 37230 | 1.26 | 4.34 | 304 | 1.56 | 1.5 | 0.5 |
| 30_40 | 74460 | 1.26 | 2.79 | 329 | 3.87 | 1.5 | 0.5 |
| 40_40 | 99280 | 1.29 | 1.65 | 215 | 4.69 | 1.5 | 0.5 |

Our observation of Table 15 does not lead to finding of any specific trends in density or bulk modulus with respect to system size of the polymer sample. The normalized energy has a tendency to increase with bigger size of polymer. Upon investigation it was found that the primary difference was in the bond and angle energy as oppose to non-bonded energy. However there is not sufficient statistics to make a conclusion based on this. Both properties obtained from fluctuation properties, i.e specific heat capacity and bulk modulus showed wide variation across samples. The reason may be attributed to sampling and building of polymer sample. This may relate to the limited timescale simulation of the samples for study of fluctuation properties.

### 3.2.7 Dipole Moment and Dielectric Constant

Calculation of the dipole moment was important for the given polymer. Being amorphous in nature, the resultant dipole moment in each direction of the polymer is expected to be cancelled out. However to achieve such randomness in the conformations of the polymer chains a need for larger system is obvious. Simulation with larger timescale also allows a sample to visit enough microstates in order to even better estimates. The dipole moment of the system was calculated by:

**Equation 35**

$$\vec{\mu} = \sum_i q_i \vec{r}_i$$

where $\vec{\mu}$ stands for the dipole moment vector of the system, $q_i$ and $\vec{r}_i$ for charge and position vector of the $i^{th}$ atom respectively.

Dielectric constant was calculated based on fluctuations of dipole moment from Clausius-Mossotti (Equation 36) and Kirkwood-Frohlich (Equation 37) equation [132]. Clausius-Mossotti equation is suited for an isolated dielectric whereas Kirkwood-Frohlich equation is suited for a material which is embedded in its own dielectric. Although we have calculated $\varepsilon$ both of these equations, estimation of dielectric constant through equation 37 is more applicable to our study.

**Equation 36**

$$\frac{\varepsilon-1}{\varepsilon+2}=\frac{4\pi}{3}\frac{\left(\left\langle M^2\right\rangle-\left\langle M\right\rangle^2\right)}{3Vk_BT}$$

**Equation 37**

$$\frac{(2\varepsilon+1)(\varepsilon-1)}{9\varepsilon}=\frac{4\pi}{3}\frac{\left(\left\langle M^2\right\rangle-\left\langle M\right\rangle^2\right)}{3Vk_BT}$$

where $\varepsilon$ represents for dielectric constant, M represents dipole moment and the rest of the notations have their usual meanings. Both of these equations are in gaussian units. The following, Table 16, presents the dielectric properties calculated from the above-mentioned equations.

**Table 16: Dielectric properties**

| Polyimide | Dipole Moment/Monomer (Debye) | | | | Equilibration Run (ns) | Production Run (ns) | Dielectric constant (CM) Method | Dielectric constant (KF) Method |
|---|---|---|---|---|---|---|---|---|
| | $\mu_x$ | $\mu_y$ | $\mu_z$ | $\mu$ | | | | |
| 6_6 | -0.78 | 1.8 | 2.94 | 3.53 | 0.5 | 1.5 | 6.49 | 3.55 |
| 10_12 | -1.65 | 0.1 | -0.58 | 1.76 | 0.5 | 1.5 | 4.12 | 2.97 |
| 5_25 | -0.65 | 1.3 | -0.59 | 1.59 | 0.5 | 1.5 | 2.95 | 2.48 |
| 10_30 | 0.11 | 1.36 | 0.64 | 1.52 | 0.5 | 1.5 | 5.27 | 3.3 |
| 20_30 | 0.86 | -0.71 | 0.83 | 1.39 | 0.5 | 1.5 | 4.32 | 3.03 |
| 15_40 | 0.59 | 0.18 | 0.65 | 0.89 | 0.5 | 1.5 | 3.28 | 2.63 |
| 30_40 | -0.46 | 0.04 | 0.05 | 0.47 | 0.5 | 1.5 | 5.69 | 3.39 |
| 40_40 | 0.07 | 0.19 | 0.3 | 0.37 | 0.5 | 1.5 | 3.89 | 2.88 |

We observe that the normalized dipole moment per monomer reduces as the system size increases. This is expected due to the amorphous nature of the polymer. Bigger system size is likely to introduce more disorder into the system. This will effectively lead to the cancellation of dipole moments oriented in random directions. The three components of the dipole moment differ individually. This indicates that the phase space has not been sampled enough. On the contrary the dielectric constant obtained through the fluctuation property analysis does not show any specific trend with the variation of the sample size. Dielectric constant measured by KF method generated lower values than CM method. As mentioned earlier, the dielectric constant calculated by KF method is applicable for our system of study. The average dielectric constant over all the samples comes to ~ 3.0 using KF method in a zero frequency condition. Experiments have estimated the value of dielectric constant of $(\beta - CN)APB - ODPA$ polymer to be ~ 3.5 at 10Hz frequency and 300 K temperature[23].

The initial section of this work dealt with building and equilibration of the sample. Properties like density, bulk modulus, specific heat capacity, normalized energy, normalized dipole moment and dielectric constant of the eight different samples were calculated based on that. Inspection of the estimated properties from the production run forms the basis of the experiments and analysis that follows in the subsequent sections.

The structures obtained from the above mentioned production runs were subjected to molecular mechanics calculation, heating, step stress and step strain. In the following, the outcome obtained from these computational experiments carried out on these equilibrated polymer samples are presented and examined.

### 3.2.8 Molecular Mechanics

Molecular mechanics method is often used to characterize the mechanical properties of a system through second derivative method. It can be treated as a precursor of mechanical properties of a sample under normal condition. The general idea is to minimize a system under a constrained volume expanded or compressed from its equilibrium structure. The polymer sample was compressed and stretched in each axial direction and allowed to

relax without changing the cell size and shape. Expanding the potential energy of a system in Taylor series around its equilibrium structure we have:

**Equation 38**

$$E(\varepsilon) = E_0 + \frac{V_0}{1!}\frac{\partial E}{\partial \varepsilon}\varepsilon + \frac{V_0}{2!}\frac{\partial^2 E}{\partial \varepsilon^2}\varepsilon^2 + \ldots \text{ higher order terms}$$

where

E = Energy of the system

$\varepsilon$ = Strain of the system

Accordingly we can determine the elastic stiffness matrix by applying the formal definition in Voigt notation:

**Equation 39**

$$C_{ij} = \frac{1}{V_0}\frac{\partial^2 E}{\partial \varepsilon_i \partial \varepsilon_j}, i, j = 1,..,6$$

Upon compressing and expanding the system of interest and then plotting the energy vs. volume curve for the polyimide system a molecular mechanics curve as given in Figure 57 is generated. The stiffness constant is estimated by estimating the parameters of the curve fitted to equation 38.

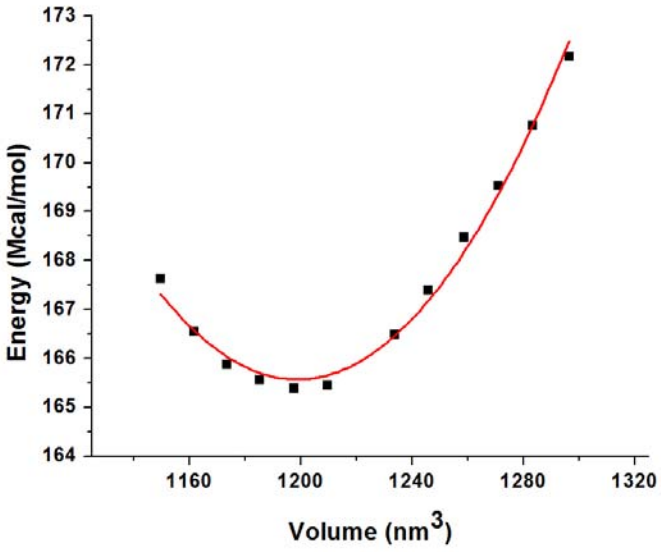


**Figure 57: Molecular mechanics curve**

Molecular mechanics does not take temperature into account. In a canonical (NVT) ensemble an equilibrated system is obtained by minimizing the Helmontz free energy. We know that:

$$dA = dU - TdS$$

Where:

A = Helmontz free energy

U = Internal energy

T = Temperature

S = Entropy

The stiffness constants are obtained by minimizing the internal energy. The entropic contribution is neglected. Hence, these constants can be regarded as stiffness constants of the material at 0 K. The softening of the material due to temperature change is not accounted for. Accordingly these calculations gave an upper estimate of the axial, shear and bulk modulus of the sample. In section 3.4 we will look into the results obtained through molecular dynamics where we have showed the softening of the material as temperature is increased.

Conjugate gradient method was used to minimize the system of interest. Hydrostatic stress was applied to calculate the bulk modulus. Pure shear could not be applied due to the limitation imposed by LAMMPS.

Shear modulus was obtained by applying tetragonal strain [133] to the sample. In tetragonal strain application, the sample is expanded in two directions by equal strains, and the third direction is compressed in a way to keep the volume of the cell intact. Since the polymer is amorphous in nature, due to its isotropic properties ideally we have:

**Equation 40**

$$C_{11} = C_{22} = C_{33}$$
$$C_{12} = C_{21} = C_{23} = C_{32} = C_{13} = C_{31}$$
$$C_{44} = C_{55} = C_{66}$$

Keeping the above equation in mind we changed the cell parameter as follows:

**Equation 41**

$$a = a_0(1+\varepsilon)$$
$$b = b_0(1+\varepsilon)$$
$$c = c_0(1-2\varepsilon)$$

So that, for small values of $\varepsilon$

**Equation 42**

$$V = a_0 b_0 c_0 (1+\varepsilon)(1+\varepsilon)(1-2\varepsilon) = V_0$$

The isotropic condition of the polymer properties due to its amorphous nature was used to find out axial modulus. Table 17 gives the values of the stiffness constants of different polymer samples obtained from molecular mechanics.

**Table 17: Molecular mechanics calculation: stiffness at 0 K**

| Polyimide | | $C_{11}$ | $C_{22}$ | $C_{33}$ | $C_{11}-C_{12}$ | $C_{22}-C_{23}$ | $C_{33}-C_{13}$ | B |
|---|---|---|---|---|---|---|---|---|
| Chains | Monomers/chain | GPa | GPa | GPa | GPa | GPa | GPa | GPa |
| 6 | 6 | 13.95 | 13.14 | 12.51 | 3.41 | 2.19 | 1.25 | 11.68 |
| 10 | 12 | 13.09 | 13.14 | 12.73 | 2.76 | 2.84 | 2.22 | 11.25 |

**Table 17: Continued**

| | | | | | | | | |
|---|---|---|---|---|---|---|---|---|
| 5 | 25 | 13.72 | 13.66 | 13.79 | 2.33 | 2.23 | 2.43 | 12.17 |
| 10 | 30 | 13.65 | 13.64 | 13.64 | 2.17 | 2.16 | 2.16 | 12.2 |
| 20 | 30 | 13.54 | 13.38 | 13.53 | 2.25 | 2.01 | 2.24 | 12.04 |
| 15 | 40 | 12.32 | 12.24 | 12.27 | 2.39 | 2.26 | 2.31 | 10.73 |
| 30 | 40 | 11.2 | 11.04 | 11.19 | 2.12 | 1.88 | 2.10 | 9.79 |
| 40 | 40 | 13.75 | 13.65 | 13.8 | 1.99 | 1.84 | 2.07 | 12.42 |

Bulk modulus found from the fluctuation properties as shown earlier in Table 15 is well below those calculated from molecular mechanics as expected. However due to large variation in values obtained from Table 15, no general conclusion can be made based on these two tables on thermal softening nature of the polymer sample.

### 3.2.9 Pressure Annealing

In building a polymer sample, one of the widely used strategies is the implementation of simulated annealing. In equilibration technique of polymer samples described earlier sometimes owing to steric hindrance and macro nature of the polymer molecules, the methods implemented may not be sufficient for exploring the phase space comprehensively with limited computational resources.

Similar to temperature annealing technique in here, a compressive hydrostatic stress is applied in steps to the polymer and then unloaded likewise. The application of the compressive stress destroys some of the high-energy local structures that were not addressed by temperature annealing. The subsequent removal of the applied stress then allows the polymer molecule to relax in a favorable way and use some of the inaccessible parts of the phase space. This is expected to result in a more favorable structure.

In our study hydrostatic pressure of compressive nature was applied to the polymer samples in steps and was allowed to relax for 200 ps in each step. The increment in pressure was given in a non-linear fashion up to ~ 1 GPa (10,000 atm). The

compressive pressure was taken off subsequently in steps similar fashion. After attaining zero atmosphere pressure it was allowed to relax for 2 ns. Similar to the non-annealed case, we have divided this run into equilibration and production run.

Table 18 presents and compares the estimated properties of different polymer samples before and after pressure annealing of few samples.

**Table 18: Comparison of non-annealed (NA) and annealed (A) samples**

| Sample | Atoms | Density (gm/cc) | | Bulk Modulus (GPa) | | Energy/ monomer (kcal/mol) | | $C_p$ (KJ/ Kg-K) | |
|---|---|---|---|---|---|---|---|---|---|
| | | NA | A | NA | A | NA | A | NA | A |
| 6_6 | 2244 | 1.22 | 1.31 | 3.93 | 9.92 | 146 | 143 | 2.76 | 2.67 |
| 10_12 | 7460 | 1.29 | 1.30 | 8.81 | 4.05 | 142 | 141 | 3.01 | 3.64 |
| 5_25 | 7760 | 1.28 | 1.30 | 8.49 | 8.83 | 141 | 141 | 2.66 | 2.54 |
| 10_30 | 18620 | 1.28 | 1.29 | 7.02 | 7.12 | 173 | 172 | 2.72 | 2.66 |

The increase in the density of the sample is clearly observed in Table 18. We observe that even after properly building the model and exploring the phase space through compressing the model in steps and temperature annealing, a net gain of ~ 1% to 7% in density of the polymer sample is achieved through pressure annealing technique. In general there is no specific trend in change of the fluctuation properties as we observe in bulk modulus and specific heat capacity.

It is also interesting to note that the normalized energy value has remained almost the similar. In other words the sample has not transformed itself to a much favorable conformation energetically through implementation of pressure annealing technique. Accordingly the nature of the fluctuation properties can entirely be different of two different states equally probable energetically. The following, Figure 58, shows the density variation with application of pressure annealing technique.

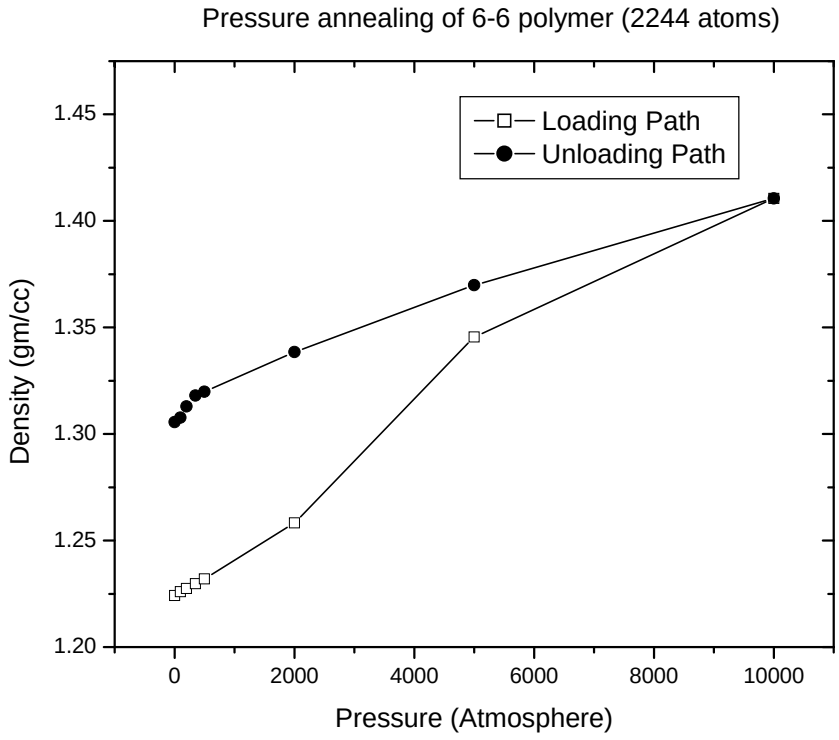


**Figure 58: Pressure annealing**

Other than clearing out the trapped spaces and increasing the density of a system in the process of pressure annealing, we also have information on compressibility of a system. The slope of the density variation with pressure near zero atmospheres gives a measure of bulk modulus at that temperature. In other words:

**Equation 43**

$$B = \rho \frac{\partial P}{\partial \rho}$$

As per the above equation we calculated the bulk modulus (Table 19) at 300 K for the eight different polymer samples. For the larger samples involved we have not performed an entire pressure annealing cycle and instead calculated the modulus from the slope obtained in the loading phase. Samples for which a full cycle of pressure

annealing was implemented, the slope during unloading was considered for calculating the bulk modulus.

**Table 19: Bulk modulus calculation from pressure annealing experiment**

| Polymer | Bulk Modulus |
|---|---|
| 6_6 | 8.87 |
| 5_25 | 10.31 |
| 10_12 | 11.91 |
| 10_30 | 9.43 |

## 3.3 Chain Properties

Estimation of the bulk properties gave us an idea about the macroscopic behavior of the polymer sample. However the exceptional set of properties offered by polymer is attributed to its interesting chain conformations, dynamics of chains and interactions among chains. Naturally one of the most interesting areas in today's research is finding the structure property relationship of a polymer sample. After the discovery of macromolecular hypothesis by Staudinger in 1920, a lot of attempt has been made to relate polymer's exceptional behavior with its underlying structure. Statistical mechanics has played a huge role since then till today to quantify the relations between polymer conformations and its properties. The works of Paul J. Flory (1974 Nobel Prize in Chemistry for Flory- Huggins theory) and Pierre G. de. Gennes (1991 Nobel Prize in Physics for Reptation model) are among the most notable works in this area of polymer physics.

The structural properties of a polymer chain are often characterized by radius of gyration, end-to-end vector, order parameter and persistence length. Correlation functions among different segmental vector, angles and torsions quantify the degree of interaction between different parts of the chain. Researchers have defined chain morphology in terms of writhing number [134], path space ratio [135] and the like. We have looked into some of these chain properties, quantified the behavior and have made an attempt to understand its physics better with the help of existing theories.

In this work we have kept track of the center of mass of each monomer with time to understand the polymer chain movement characteristics under normal condition. The center of mass of the monomer was saved every 100 fs. The vibrations at the monomer level are less frequent and hence saving data every 100 fs is a good representation of the monomer trajectory for property analysis. This data file was saved for 500 ps simulation runs for each polymer samples under normal conditions. In the following we have analyzed the chain characteristics of different polymer samples.

### 3.3.1 $R_e$ and $R_g$

Flexible polymers can take up enormous number of configurations. Due to the slow movement of the polymer chains below glass transition temperature it is difficult to visit all the conformations within a reasonable amount of simulation time. However with the use of statistical mechanics together with atomistic scale simulations, we have looked and analyzed the end-to-end vector ($R_e$) and radius of gyration ($R_g$) of different polymer samples in this section.

Table 20 gives values of the average end-to-end length and radius of gyration for each polymer samples under normal conditions.

**Table 20: Estimation of end-to-end vector and radius of gyration**

| Polymer Samples | $\langle R_e \rangle$ | $\langle R_g \rangle$ | $\frac{\langle R_e \rangle}{\langle R_g \rangle}$ |
|---|---|---|---|
| 6_6 | 23.2 | 12.1 | 1.92 |
| 10_12 | 37.9 | 16.7 | 2.27 |
| 5_25 | 41.6 | 21.2 | 1.96 |
| 10_30 | 51.8 | 23.2 | 2.23 |
| 20_30 | 58.1 | 31.7 | 1.83 |
| 15_40 | 81.6 | 43.3 | 1.88 |
| 30_40 | 83.9 | 41.5 | 2.02 |
| 40_40 | 83.3 | 40.6 | 2.05 |

Upon observation of table 20 we find that the $\frac{\langle R_e \rangle}{\langle R_g \rangle}$ value is less than expected (~ $\sqrt{6}$ ) from a freely jointed chain model describing a polymer system. This gives us a measure of the deviation of the polymer structure at the atomistic level from an ideal freely jointed chain model, which is expected. The difference can be attributed to excluded volume effect resulting in a value of radius of gyration larger than expected from a freely jointed chain model for the same end-to-end vector.

Since this section deals with chain properties, it is also appropriate to look into chain overlapping issues briefly as applicable to our model. The conformation of a chain largely depends on the concentration of a system. Fluctuations tend to decrease with increased polymer concentration. After a certain concentration, the fluctuation becomes so small that the polymer behavior can be addressed by mean field theory. The value of polymer density $\rho^*$ is taken as[136] the transition zone from dilute to semi dilute solution of a polymer is calculated as:

**Equation 44**

$$\frac{\rho^* N_A}{M}\frac{4}{3}\pi R_g^3 \approx 1$$

where the symbols have their usual meanings.

The value $\rho^*$ defines the onset of the overlapping among chains. For our smallest polymer sample the value of $\rho^*$ comes out to be 0.8 gm/cc. All our polymer samples were found to be above the dilute region and hence the effect of overlapping among chains is expected.

## 3.4 Application of Step Stress

Creep test is one of the widely performed tests on polymers to understand its mechanical behavior. The creep modulus of a viscoelastic material is a time dependent property. Below glass transition temperature the movement of polymer chains is very slow. To observe the flow characteristic of an amorphous polymer that is below its glass transition

temperature, sufficient observation time should be given. However typical molecular dynamics simulations are limited by time and length scales. The orders of magnitude difference in timescale accessible to MD and that required to observe viscoelastic nature of the polymer below glass transition then poses a problem. Theories like time temperature superposition where experiments are done at higher temperature to accelerate the process, is not of much help either. In this work we have applied extremely high stress rate for a very short amount of time on the polymer sample and have observed both elastic and plastic behavior.

In most cases the equilibrated polymer sample was subjected to stress from 0 to 2500 atmospheres in steps of 500 atmospheres. Subsequently the sample was allowed to relax for 100 ps after which the stress value was increased again. This translates to a creep rate of $5X10^{8} GPa/\sec$. In some case the time allowed for relaxation was different to inspect the time dependent response of the polymer sample. In general all the different stress rates applied in this work are in the order of $\sim 10^{8} GPa/\sec$. In other words these are huge rates.

From the creep test we have observed, as shown below that for small stress values, even for higher stress rate the polymer behaves elastically within the inspected time domain. However after a certain value of stress, the sample starts showing flow behavior that increases with higher stress, hinting the occurrence of tertiary creep behavior. In the following we have examined the response of the polymer sample on application of stress in different ways. The nature of stress applied was both tensile and compressive. Stress was also applied in continuous fashion in addition to step application. Afterwards various standard constitutive models addressing one dimensional viscoelastic response was used to fit the response of the polymer samples obtained from atomistic scale simulation. In general these models are only used to simulate macroscopic behavior. Consequently these do not provide any insight into the molecular basis for viscoelastic response. However in the following we have tried to make sense of the estimated parameters of the constitutive models and made an attempt to relate those parameters with properties estimated from the atomistic scale simulations.

Figure 59 presents the instantaneous strain in response to tensile stress from 0 to 2500 atmospheres in steps of 500 atmospheres applied to a 30_40 polyimide sample. Similar response was also obtained from the other polymer samples. We observe that the initial response of the polyimide is elastic irrespective of the stress rate. It must be kept in mind that the time given for relaxation may not be enough and the onset of plastic flow may happen at an earlier stress value. In other words this gives an upper limit of the yield stress. We also observe that somewhere between 1500 and 2000 atmosphere (~ 150 and 200 MPa) there is an onset of flow of the polymer chains. The applied stress profile is given in the inset of the figure.

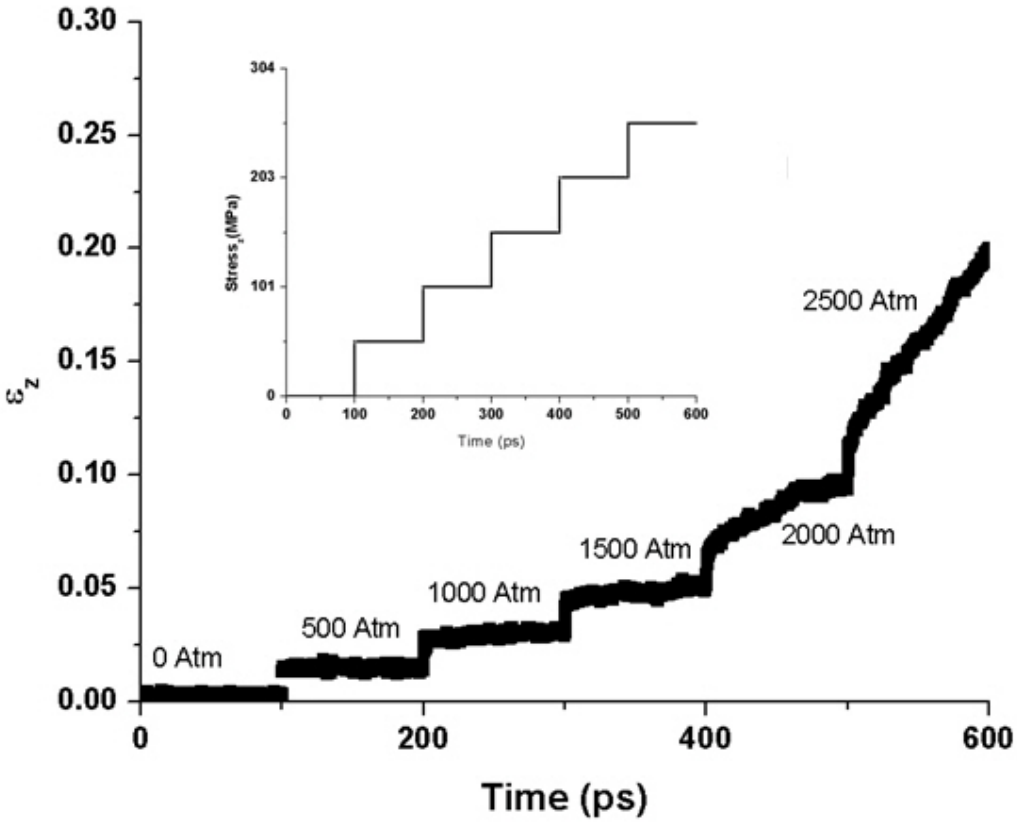


**Figure 59: Applied stress and response strain profile**

We observe from Figure 59 that there is a transition from the elastic response to plastic response of the polymer indicating the presence of viscoelastic nature. The onset

of flow that is difficult to observe under normal creep condition within atomistic scale simulation timescales was observed by accelerating the chain movement with application of high stress. The application of high stress rate can be viewed as the same way as time temperature superposition relation where higher temperature helps the chains move faster. Either way it is the presence of external energy which overcomes the slow moving nature of the polymer chains and sets the plastic flow.

Step stress of compressive nature was also applied to the above mentioned polymer sample in a similar way as described in the tensile case. This means the compressive stress was also applied at the rate of $5X10^{8} GPa/\sec$. Other than experimenting with 30_40 polyimide, stress of both natures in axial direction was also applied to other polymer samples. In addition to applying step stress we have also applied tensile and compressive stress in a continuous fashion. The stress rate in this case was identical to the step stress case. Figure 60 presents the instantaneous response of 10_30 polyimide under tensile and compressive stress. It also represents the response of the polymer under step loading and continuous loading. In order to magnify the differences, the figure was drawn by the use of block averages.

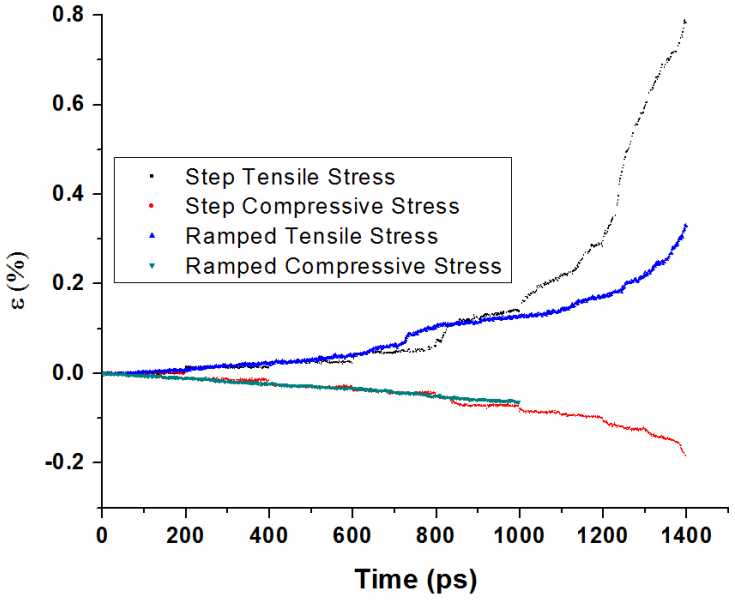


**Figure 60: Comparing polymer responses in terms of strain for various ways applied stress**

Upon observation of Figure 60 we find the following:

1. The compressive axial modulus is higher than the tensile axial modulus. This is expected. As the sample is compressed, the atoms move close to each other and repulsive van der Waals force becomes important. With less space to move under the given constraints, the polymer behaves stronger under compressive stress as oppose to tension.
2. The polymer responds to the applied stress elastically until certain stress and afterwards there is an onset of plastic behavior. This is similar to what we have observed earlier in the case of 30_40 polyimide with step stress application.
3. In the elastic region, when the value of the continuous stress becomes equal to that of the step stress, the strain in the polymer sample is identical as shown in Figure 61 that is a zoomed version of Figure 60.

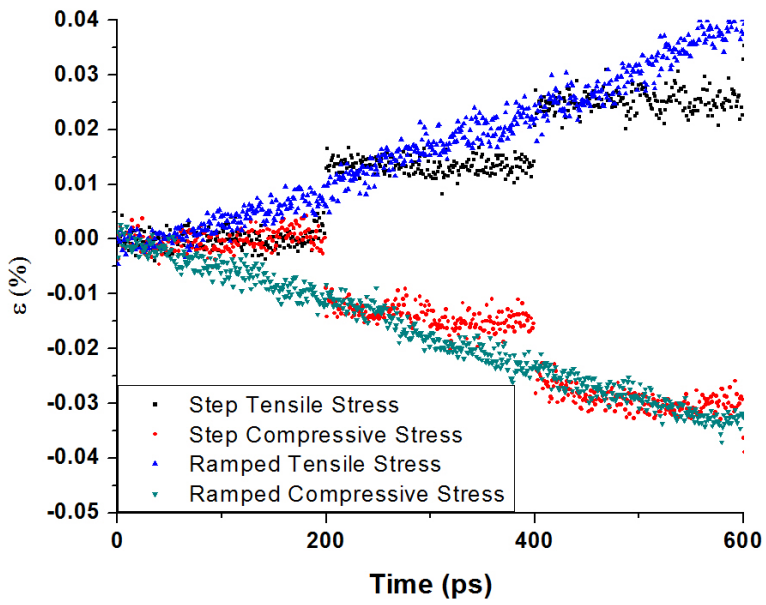


**Figure 61: End point match in polymer response for continuous and step stress application**

4. The onset of the plastic flow happens almost at similar value of stress both in tensile and compressive cases, even though the absolute strain values are quite different.
5. The onset of the plastic flow happens early in case of continuous stress loading as compared to step loading. In the ramp loading the stress value is always higher or equal to the stress in step loading owing to the nature of implementation of the same. In other words the continuous loading helped us to determine more precisely the onset point of plastic behavior in the stress-strain curve.
6. We also observe in the tensile case that, after the onset of the plastic flow in the continuous loading case, the strain in the sample does not, as oppose to the step loading cases increase significantly. It can be argued that in the step loading case after reaching close to the plastic flow region, the sudden increment in stress value acts as a shock. This application of shock after the onset of the plastic behavior generates a large amount of strain in the polymer sample.

7. We observe that after entering the plastic region, the strain rate is approximately constant. This means, the strain of the material is time dependent. Accordingly it becomes important to investigate the stress strain relationships and isochrones should be drawn to take care of the time dependent properties. Naturally the plastic region in figure 60 will look very different for different amount of time given to the polymer sample under same stress in the plastic flow region. Figure 62 shows a clear distinction of the final strain values in cases where the applied stress rates differ by four times. In the slower case the rate of applied stress was 1.25 X $10^8$ GPa/sec.

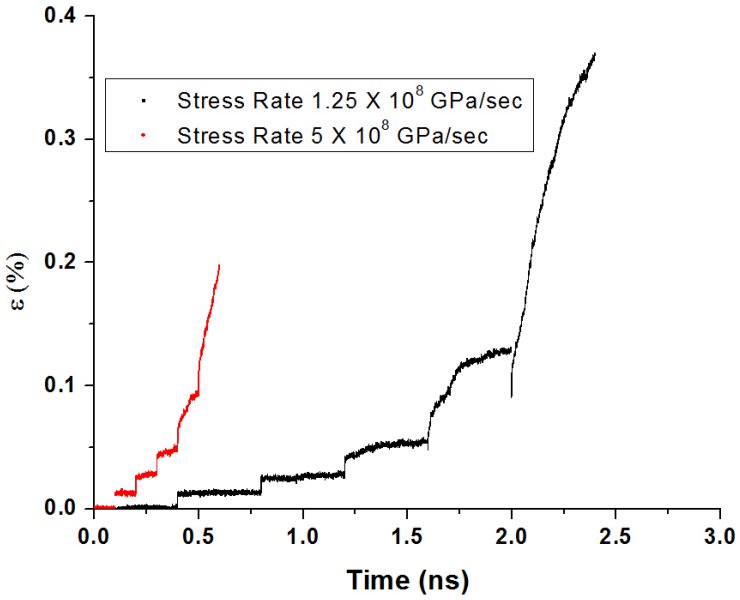


**Figure 62: Time dependent response of polymer**

8. To calculate the elastic properties of the polymer, we estimated the slope of the straight line in the elastic region incorporating response both from tensile and compressive zone. Figure 63 displays the overall polymer response around its equilibrated values at 300 K.

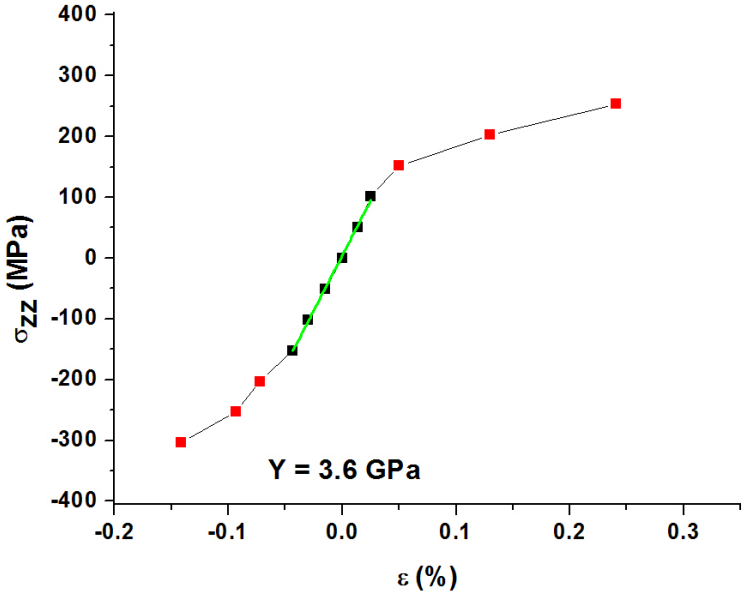


**Figure 63: Calculation of young modulus for 3040 polyimide**

The region showing the linear response is clearly identified in the above figure and is used to find the elastic modulus of the polymer sample. Figure 63 shown above is specifically for 30_40 polyimide with 200 ps run and the production run and the ultimate 140 ps was considered as production run. It must be noted that in the flow region, the concept of production run or equilibrated sample under given stress is not applicable as it appears that the sample is in steady state (with constant strain rate) than in equilibrium at higher stress. However for estimation of axial modulus, the response of the polymer sample is time independent. From the above procedure the value of axial modulus found for different polymer sample is given in Table 21:

**Table 21: Axial modulus**

| Polymer Sample | Young Modulus (GPa) |
|---|---|
| 10_30 | 4.6 |
| 15_40 | 4.53 |
| 20_30 | 3.2 |
| 30_40 | 3.61 |
| 40_40 | 4.2 |

Accordingly from table 21: $\langle Y \rangle = 3.91 GPa$

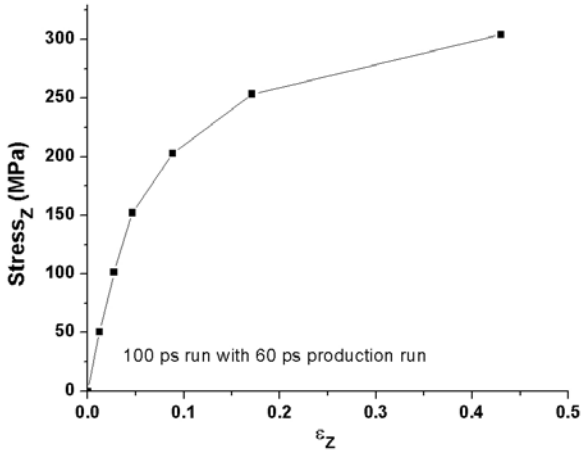


**Figure 64: Average stress-strain curve showing elastic-plastic response**

From the stress strain response (e.g. Figure 64) of the polymer in the elastic zone we also estimated the poisson ratio of the polymer sample as presented below.

**Table 22: Poisson ratio calculation from NPT runs**

| Polymer Sample | $\langle \nu \rangle$ |
|---|---|
| 10_30 | 0.41 |
| 15_40 | 0.42 |
| 20_30 | 0.43 |
| 30_40 | 0.41 |
| 40_40 | 0.41 |

From Table 22 we find $\langle \nu \rangle = 0.416$. Implementation of the isotropic condition on the amorphous polymer system yields the following well-known equations:

**Equation 45**

$$\mu = \frac{Y}{2(1+\nu)}$$

and

**Equation 46**

$$B = \frac{Y}{3(1-2\nu)}$$

Accordingly from the average values obtained for our polymer samples for Young modulus and poisson ratio we find:
$\langle \mu \rangle = 1.4 GPa$ and $\langle B \rangle = 7.76 GPa$ at normal conditions.

3.4.1 Moment of Inertia

The rate of rotation in a rigid body is directly related to moment of inertia of a system. Minimizing the moment of inertia around an axis enables one to increase the rates of rotation around it. It plays the same role in rotational dynamics as mass in basic dynamics. Moment of inertia is generally defined as a tensor made from 3 X 3 matrixes and is defined as following:

**Equation 47**

$$I_{ij} = \sum_{k=1}^{N} m_k (r_k^2 \delta_{ij} + r_{ki} r_{kj})$$

Where:

$I_{ij}$ = Moment of Inertia

$m_k$ = Mass of element k

$\delta_{ij}$ = Kronecker delta

It is hypothesized that the chains will try to get stretched in the applied stress direction and accordingly the moment of inertia around z-axis in response to applied stress along 'z' direction will tend to decrease. In the following we have examined the change in the moment of inertia values of chains of the polymer samples as stress is applied.

Figure 65 compares the normalized moment of inertia of all the chains of a 10_30 polyimide subjected to tensile step stress. The $I_{zz}$ plotted corresponds to the stress-strain experiment on 10_30 polyimide. We observe that for most of the chains there is a tendency to reduce the moment of inertia around z direction in response to $\sigma_{zz}$. The reduction in the value of $I_{zz}$ is accelerated as the polymer moves towards plastic zone. This is expected as the increase in flow behavior helps the polymer chains to straighten up faster along the applied stress direction.

We also observe that for a couple of chains the value of $I_{zz}$ does not change significantly. It appears that these chains are not able to straighten up and try to somewhat non-align themselves with z-axis and in the plastic zone aligns themselves when it is easier to flow. The reason for this anomalous behavior can be attributed to the fact that the conformations of these chains are more dictated by the alignment of the other chains than their own response to the applied stress. This increases the moment of inertia of the chains temporarily. However with increment of degree of alignment of the chains with 'z' axis, the non-aligned chains try to resist their inclination towards increasing the moment of inertia. It can probably be argued that once most of the chains have got aligned with z direction, these chains are perhaps more free to respond to the

applied stress than before. However chain entanglement restricts them from getting aligned more than a certain extent.

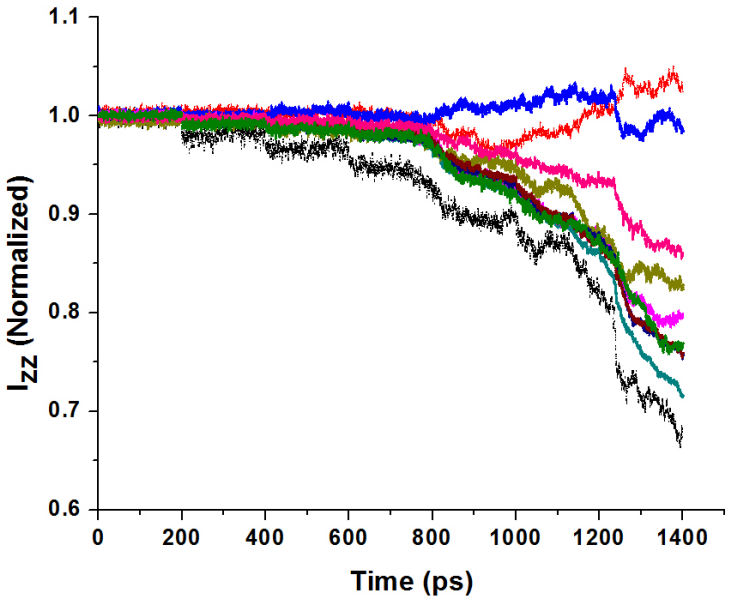


**Figure 65: Instantaneous values of moment of inertia of polymer chain along applied tensile stress direction**

Similar to the tensile experiments, we have also estimated the moment of inertia tensor for the computational compression experiment performed. It is expected that with application of tensile force the chains will try to relax and increase its contour length. However when compressive stress is applied, it is expected that the only way the chains can adjust to the applied external forces is to realign them. Owing to the nature of the force it is harder for the chains to compress its length proportional to the applied force. We observe in Figure 66 that the moment of inertia of almost all the chains has increased indicating a spread of the chains in the x and y direction. To support this we plotted the moment of inertia around y axis for the compressive stress experiment. We found as expected due to the spread in y direction the value of $I_{yy}$ has reduced for many chains as shown in Figure 67. However we also find that for some chains there is an increase of $I_{yy}$ as shown in the same figure.

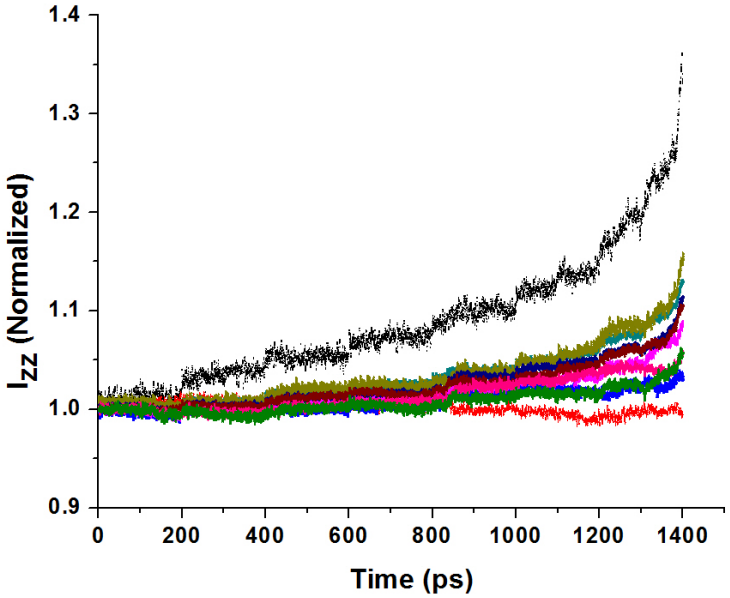


**Figure 66: Instantaneous values of moment of inertia of polymer chain along applied compressive stress direction**

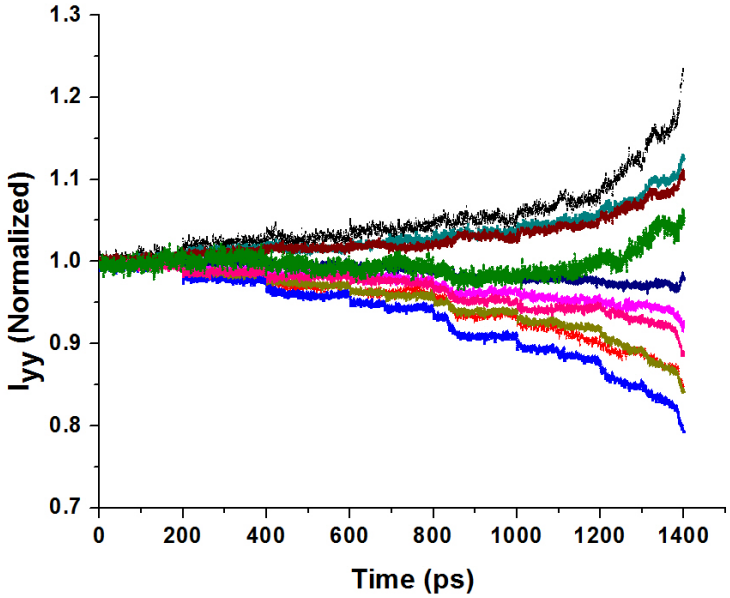


**Figure 67: Instantaneous values of moment of inertia of polymer chain perpendicular to applied compressive stress direction**

### 3.4.2 Contour Length

In order to understand what is going on during the mechanical testing of polymer we looked into the contour length distribution of the polymer chains as plotted below.

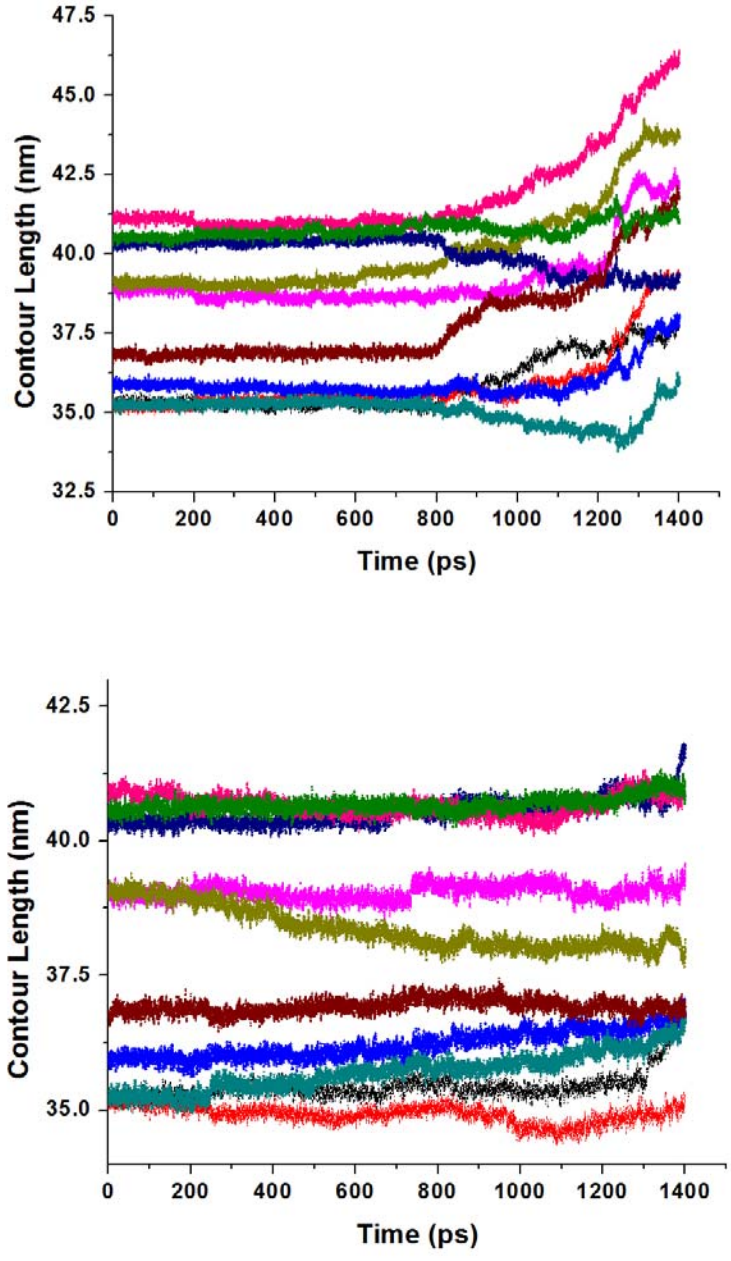


**Figure 68: Contour length changes with stress application**

From Figure 68, which shows the polymer chain contour length behavior under tension and compression test we observe the following:

1. We observe an increase in the contour length of the polymer chains when it is under tensile stress. This is expected.
2. We also observe that at higher stress the change in contour length increases. Accordingly we can say that other than the flow behavior of the polymer chains due to the increased availability of space to the chains there is also increase in contour length of the chains which contributes to the high strain values in the plastic region. On the contrary it can also be argued that in high stress region when the chains try to flow, due to the existing entanglement among the polymer chains the contour length gets stretched in the process of flowing.
3. In the compressive test however we do not see any significant change in the contour length of the chains. This also indicates unlike in the case of tensile experiment there is hardly any contribution from change in contour length in the increased value of strain at higher stress.
4. We must also mention that these high rate experiments do not take into account the chances of bond breaking. The inability of the force field to do so will perform bond stretching even when breaking it is favorable.

### 3.4.3 Viscoelastic Models

In micromechanics, polymer responses similar to these have been attempted to model through various viscoelastic models. Some of the well-known simple models are Maxwell model, Kelvin-Voigt model, three-parameter solid model, 'N' Maxwell in series model, burger model and the like. These models are made of various combinations of spring and dashpot. While the spring accounts for the elastic response of the polymer, the dashpot models the viscous nature of the same. The force deformation relation for the spring is expressed as:

**Equation 48**

$$F_S = E_S \Delta_S$$

The force deformation relation for the dashpot is expressed as:

**Equation 49**

$$F_D = \mu \dot{\Delta}_D$$

where:

$F_i$ = Force on element i ('S' refers to spring and 'D' refers to dashpot)

$E_S$= Elastic constant of the spring

$\eta$ = Viscous element of the dashpot

$\Delta_i$ = Elongation of element 'i'

The formulation of the constitutive equation of a specific model can then be constructed based upon the geometry of the model. The geometry refers to the specific combination in which the spring and dashpot has been kept to build the model. The equations conserving stress and strain across the whole model then builds the constitutive equations. There is a major difference in the application of the available viscoelastic models here. In experiments the value of stress is significantly lesser and the time given for the polymer to relax under a given stress is significantly larger than our computational experiments. In other words the experiments done here are the extreme in the opposite sense.

In our study we have found a combination of elastic and plastic response. Accordingly for small stress loading we have modeled the polymer response only through simple spring response. In other words, usage of other model will give extreme values of estimated parameters except for the spring. Once it reaches to the plastic region we have attempted to divide the resulting strain into two parts; the strain resulting from the elastic nature of the spring and the strain resulting from the constant strain rate of the dashpot. The later part of the strain source will be time dependent. To model this viscoelastic response we will fit this response to the available viscoelastic models. Figure 69 and Figure 70 represents different constitutive models that have been proved to be useful in addressing viscoelastic response of polymers. In the following we have used constitutive equations of one-dimensional response of viscoelastic materials to fit to our atomistic simulations results. We have attempted to develop model from atomistically

informed data from our computational experiments. Brief descriptions of the few models considered are given below.

### 3.4.4 Kelvin-Voigt Model

Kelvin Voigt model consist of a spring and a dashpot in parallel as indicated in Figure 69. As indicated in the diagram, the force experienced by the spring and the dashpot are different. The sum of the forces experienced by the two elements balances the external stress being applied on the material. The strain in each element however is the same from deformation analysis.

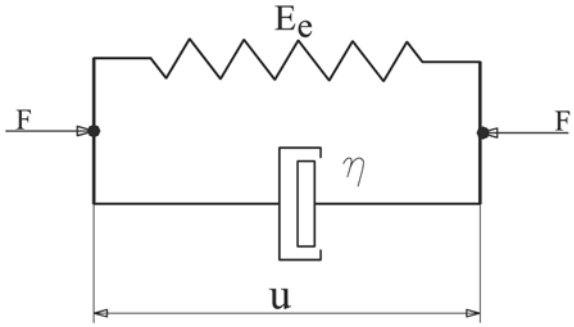


**Figure 69: Kelvin Voigt model**

After applying force deformation relationship and initial conditions we obtain for creep response of the material for a given step stress $\sigma_0$, the time dependent response of the polymer can be expressed as:

**Equation 50**

$$\varepsilon(t) = \sigma_0 \frac{1}{E_e}\left(1 - e^{-(E_e/\eta)t}\right)$$

The term $\eta / E_e$ is also termed as $\tau_c$ or the retardation time.

### 3.4.5 Three Parameter Solid Model

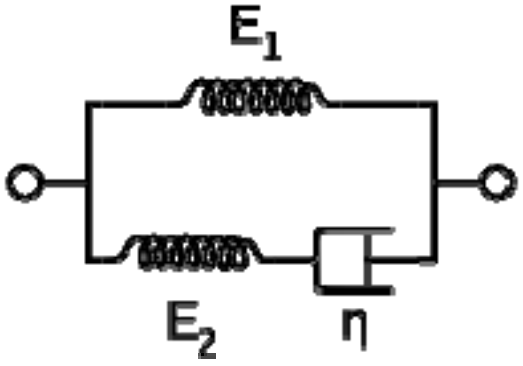


**Figure 70: Three parameter solid or standard linear solid model**

Figure 70 describes the three parameter solid model. Similar to the way described above, the force and geometry analysis of the model constructs the constitutive model. After implementing the initial conditions the creep response of the model takes the following form:

**Equation 51**

$$\varepsilon(t) = \sigma_0 \left[ \frac{1}{E_1} + \left( \frac{1}{E_1 + E_2} - \frac{1}{E_1} \right) e^{-\left[ \frac{E_1 E_2}{\eta (E_1 + E_2)} \right] t} \right]$$

Several models exist including 'N' Kelvin Voigt model in parallel, 'N' Maxwell model in series and other combinations of the basic models for simulating viscoelastic response of a polymer. The initial responses of the polymer were found to be elastic for all the polymer samples. Accordingly the first part of the modeling was just to fit the elastic part assuming only the elastic spring plays a role here. Once there the viscous part of the polymer starts appearing in the stress test, the atomistic simulation results were fitted to the available models. Naturally model with higher number of parameters fitted better. Figure 71 gives one example of fitting, where two Kelvin Voigt model in series an elastic spring has been considered.

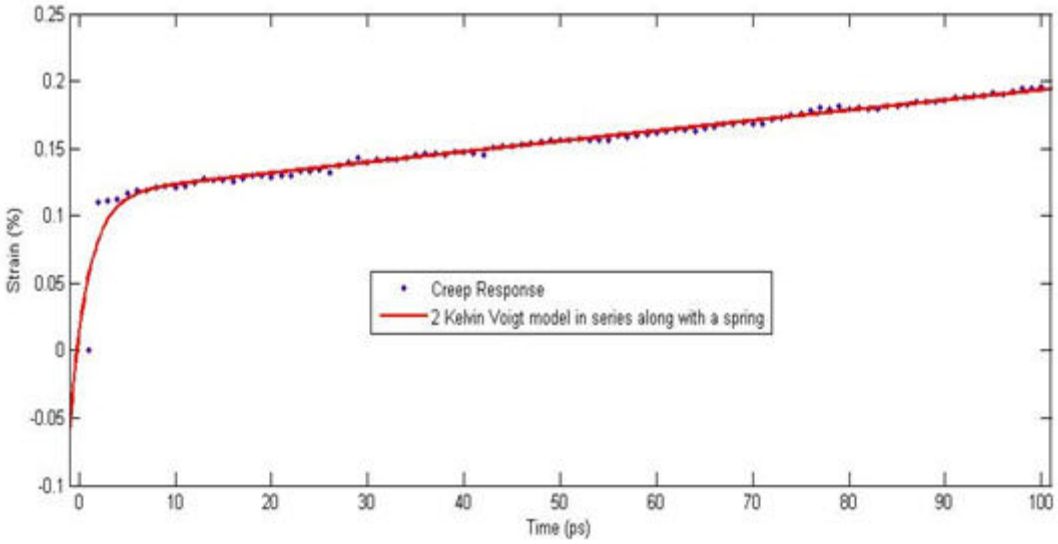


**Figure 71: Fitting of polymer response with two Kelvin Voigt model in series**

In the fit shown above, the elastic constant of the independent spring was kept equal to the one found from the initial elastic response. Even though model with two KV model in parallel with a spring in series fitted nicely to the entire stress-strain region, a careful look in to the parameter values and their confidence interval reveals something else. The 95% confidence interval as found after fitting resulted in having the lower ranges of the parameters in the negative zone defying physics. Naturally this was not a solution.

Careful look into three-parameter linear solid model also gave erroneous results in terms of huge confidence interval which also included zone that is unrealistic. Maxwell model is well known for a fluid model. The spring constant was forced to be around the value estimated in the elastic region. The model could replicate some flow behavior; however it was not able to describe the initial jump in strain due to implementation of step stress.

Kelvin Voigt model gave acceptable fitting results and corresponding 95% bounds on parameters estimated. However since Kelvin Voigt model is better suited for a viscoelastic solid, the flow behavior at higher stress was not well fitted as illustrated in

Figure 72. In all this analysis it is however assumed that the polymer at each step stress behaves closely to what it would have behaved in case it was not in a stressed state. We have analyzed another case later where the final stress was obtained by implementing a step stress to the equilibrated structure of the polymer. In the following (Figure 72 and Figure 73) we have shown the fitting of the six different step stress response using Kelvin Voigt model.

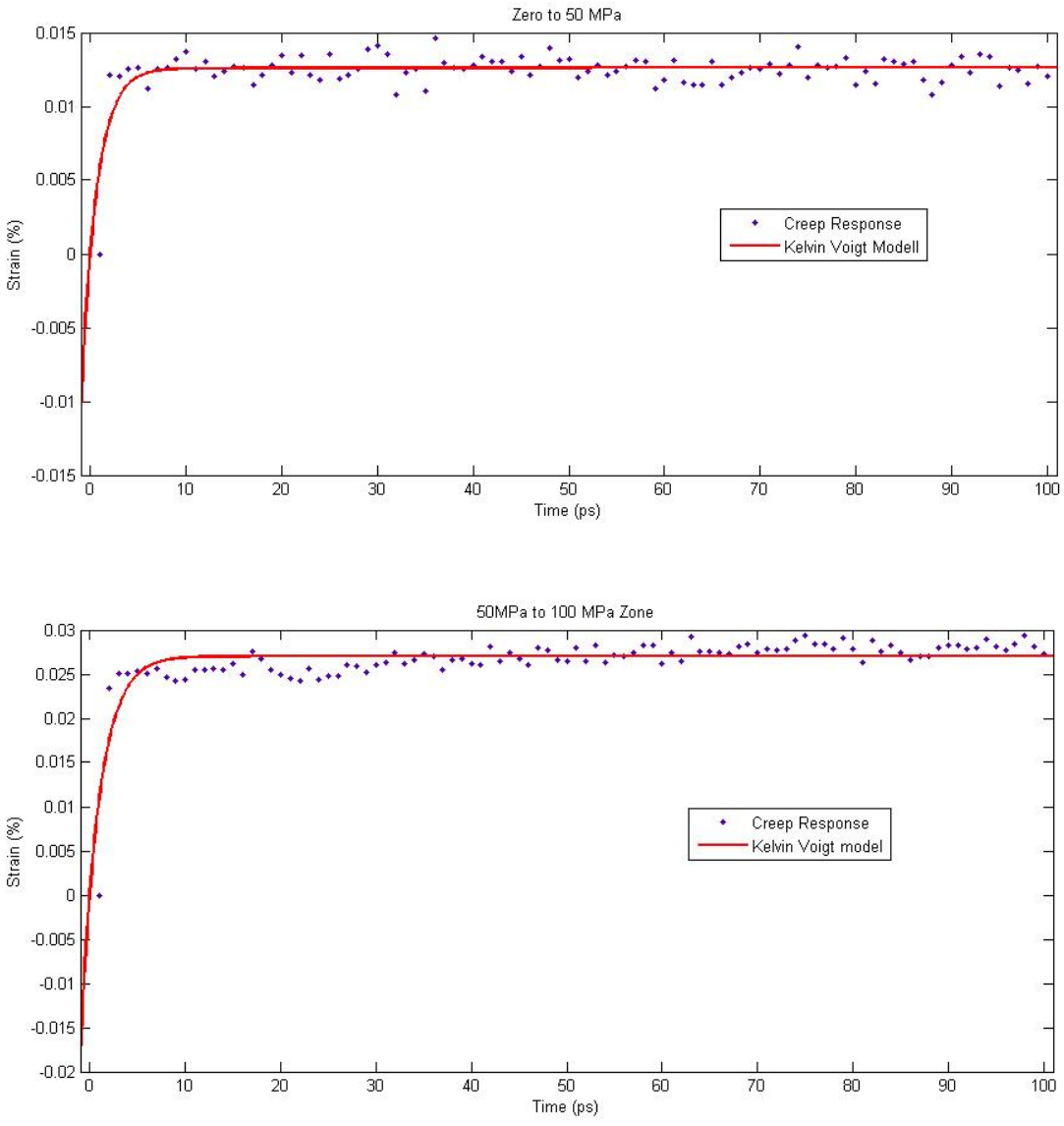


**Figure 72: Polymer response fitted with Kelvin Voigt model for step stress experiment in the elastic zone**

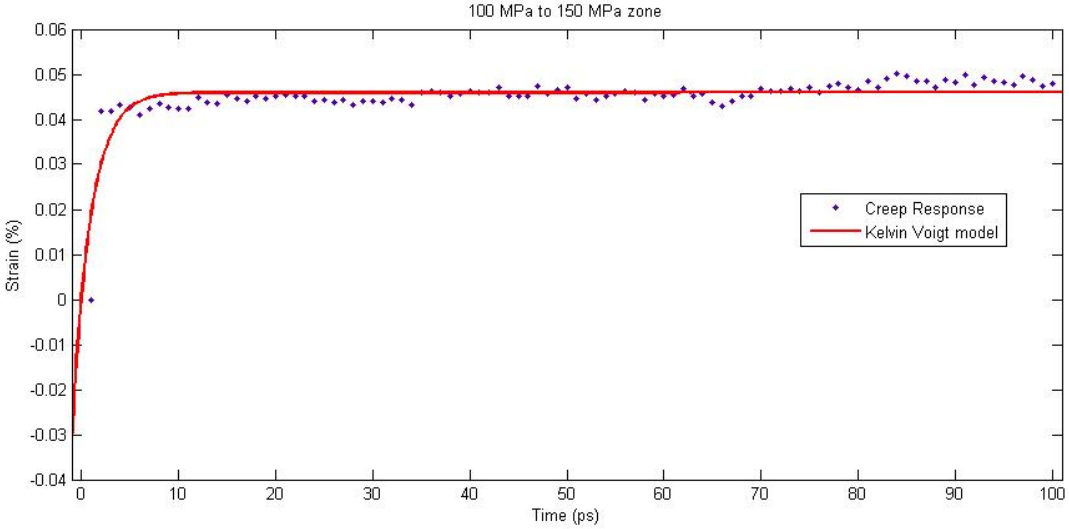


**Figure 72: Continued**

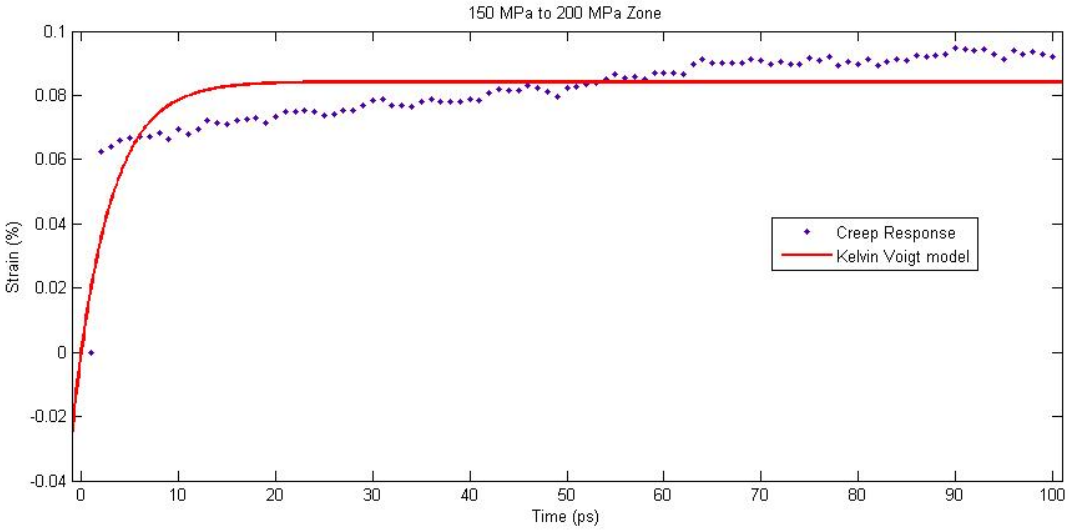


**Figure 73: Polymer response fitted with Kelvin Voigt model for step stress experiment in the plastic zone**

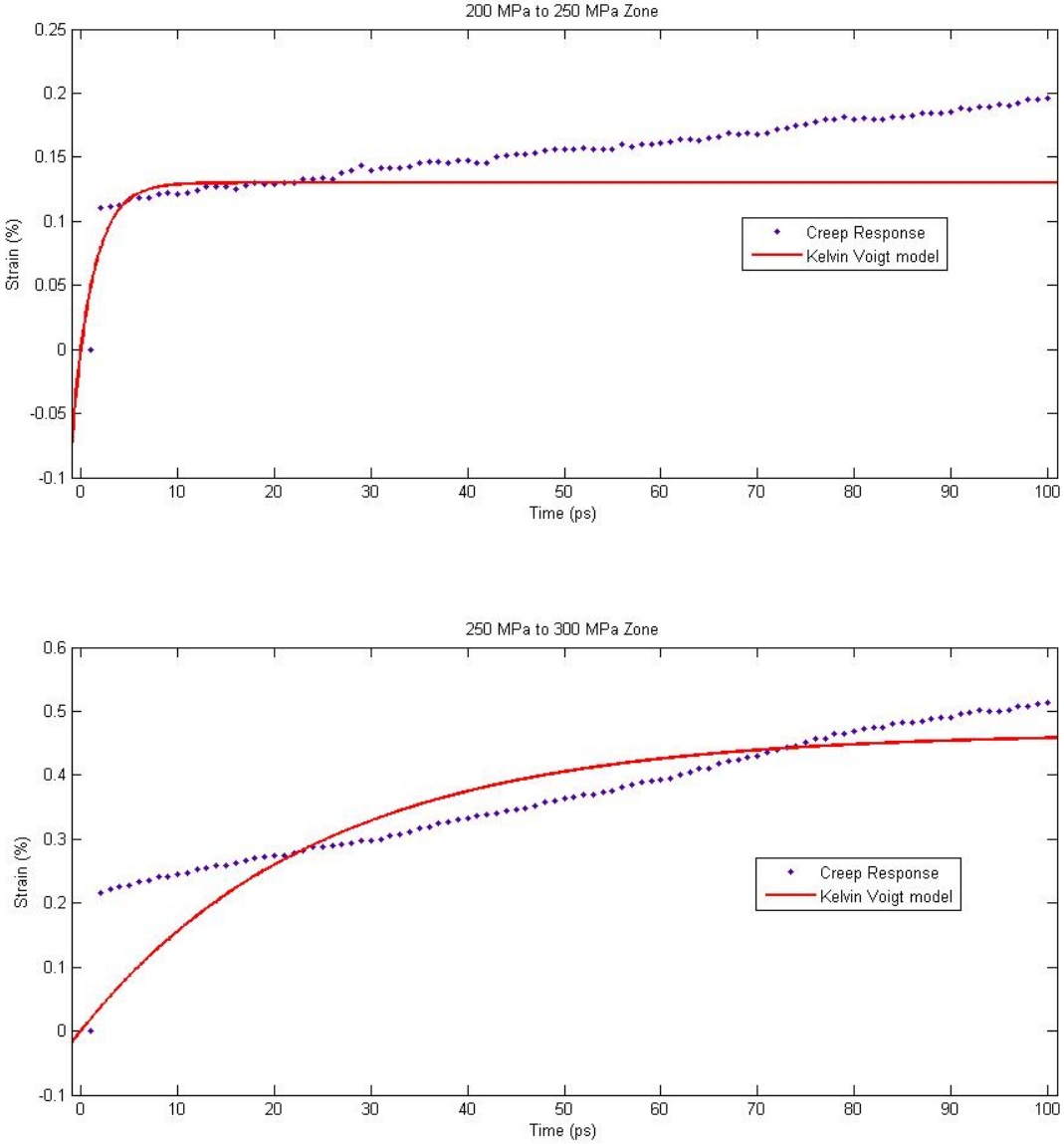


**Figure 73: Continued**

We observe from the figures that the Kelvin Voigt model, being a representative of a viscoelastic solid, can only replicate the elastic response of the polymer. Once the polymer starts showing flow behavior, the model starts deviating from the actual behavior of the polymer. To account for the flow part, the later part was fitted with Maxwell model. Figure 74 gives the fitting of the Maxwell model in the flow region. We can observe that the Maxwell model can well represent the flow behavior of polymer

under high stress values. This was expected due to the inherent fluid like nature of the Maxwell model.

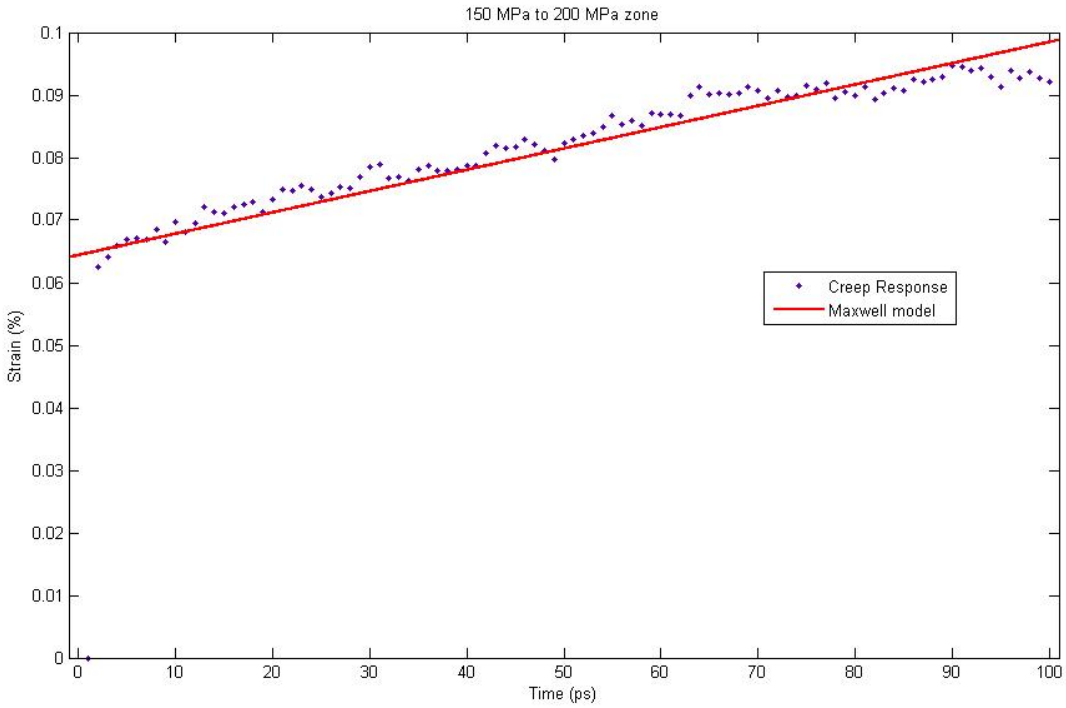


**Figure 74: Use of Maxwell model to fit the flow behavior of the polymer**

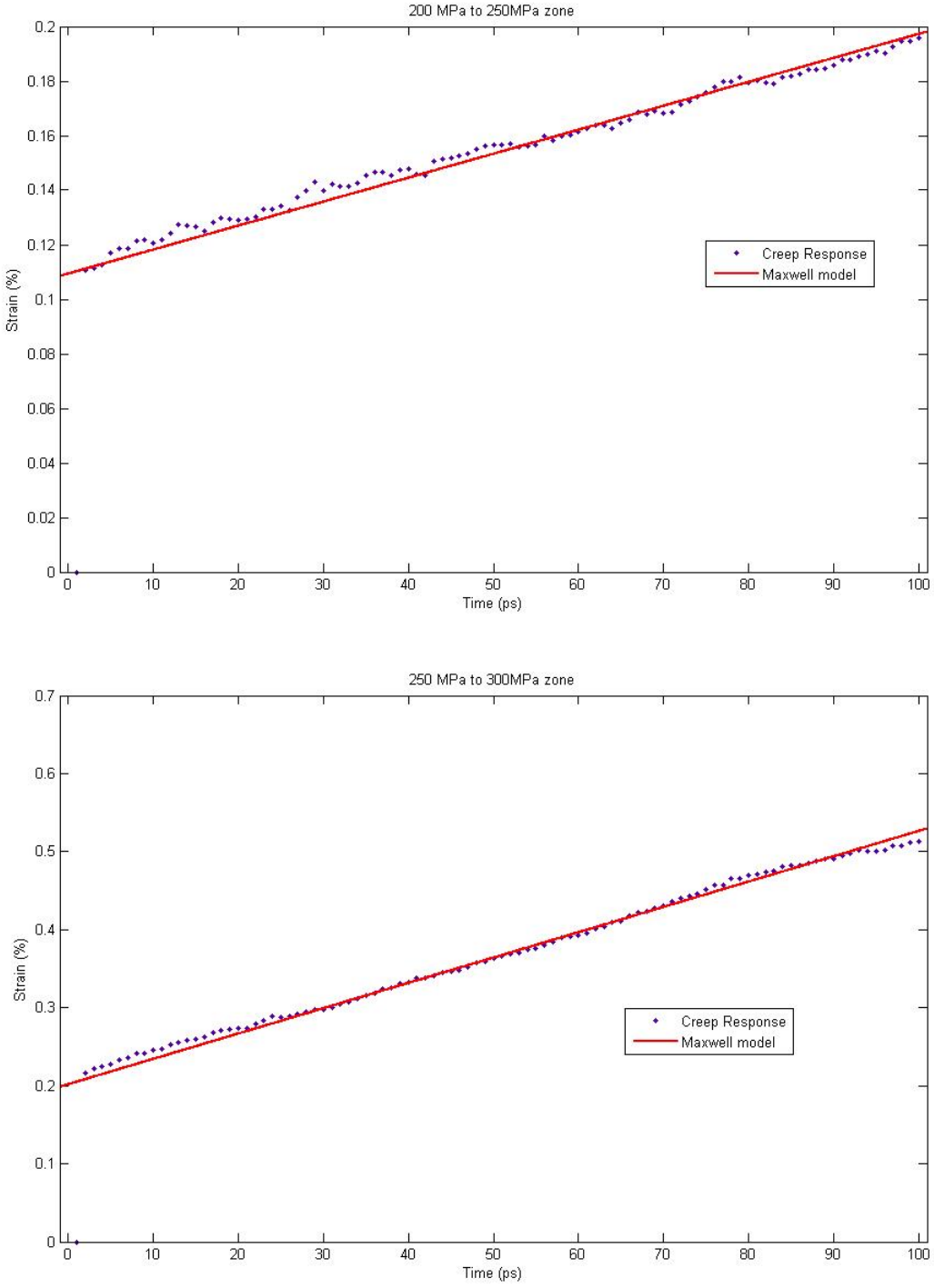


**Figure 74: Continued**

In summary analyzing the mechanical response of the polymer and trying to fit the same in terms of a constitutive model we experience the following:

1. Models with higher number of parameters could fit all the responses; however the estimated values and the corresponding 95% confidence interval didn't make sense at times. For example in some cases, the spring constant was assigned a range consisting of negative value. Additionally the ranges were very high in some cases as compared to the estimated value of the parameter.
2. Simple models were unable to fit the mechanical behavior. Kelvin Voigt model is suited for viscoelastic solid and Maxwell model is suited for Viscoelastic liquid. As a result none of these could address the response in all the regions.
3. Combining Maxwell model and Kelvin Voigt model to a single model to address both responses also didn't do any good. We have not shown that test in here though. In the elastic response region the strain resulting from all but the spring of the Maxwell model are close to zero resulting in un reasonable confidence interval for the estimated parameters.
4. Having separate model for each zone is a better idea. This will be good for fitting the response and having physical sense of the estimated parameters.

Accordingly the mechanical response was divided into two parts. The viscoelastic solid like behavior at small stress and the viscoelastic fluid like behavior at large stress. Observing the above set of figures, the first three responses were modeled with Kelvin Voigt Model and the remaining three were modeled with Maxwell model. The estimated parameters are given in Table 23.

**Table 23: Estimated parameters for constitutive models for viscoelastic response of polymer to application of stress in steps**

| | Spring elastic modulus (GPa) | Viscous constant (Units GPa-ps) | Model |
|---|---|---|---|
| 0 – 50 MPa | 3.97 | 6.42 | Kelvin-Voigt |
| 50 - 100 MPa | 1.85 | 3.58 | Kelvin-Voigt |
| 100 - 150 MPa | 1.09 | 2.08 | Kelvin-Voigt |

**Table 23: Continued**

| | | | |
|---|---|---|---|
| 150 - 200 MPa | 0.78 | 146.6 | Maxwell |
| 200 - 250 MPa | 0.46 | 56.93 | Maxwell |
| 250 - 300 MPa | 0.25 | 15.41 | Maxwell |

As per the above table we have modeled the viscoelastic behavior of the polymer under stress with a spring and a dashpot. The spring and dashpot makes a Kelvin Voigt model and can successfully represent the polymer in the elastic zone. However as the stress value increases, the Kelvin-Voigt model 'collapses' and forms a Maxwell model with the same set of elements. Overall we can term this as a 'collapse model' keeping in mind the physical diagram of the two constitutive models.

In an attempt to make physical meaning out of these we will assume that the spring elastic energy in this model consist of two types of sources, covalent bonding and pair interaction energy. We also assume to make sense out of our model, that these springs are joined in parallel. In other words this means the distribution of stress across this spring varies, but the total sums up to the external stress applied. Accordingly we can convert Table 23 to values consisting two springs instead of one. We can also assume that the spring constant arising from bonded energy will not change much, as oppose to those arising from non-bonded ones. The spring constant arising from bonded energy can be fixed around values obtained from atomistic simulation.

Another set of experiments was carried out where the step stress applied was directly applied to the equilibrated structures. These set of experiments were different than the previous in this sense and reflected the response of the polymer under given step stress from stress free condition. Figure 75 illustrates one such example where polyimide 30_40 was subjected to a step stress of 2000 atmosphere. The fit was performed by three-parameter solid model. Neither of Kelvin Voigt or Maxwell model gave good fitting due to the presence of both solid and fluid like behavior in the data obtained from atomistic simulations of the polymer subjected to 2000 atmospheres.

We observe that for large stresses, stresses under which the polymer starts flowing, the initial response is elastic and similar to what was found before. Afterwards the polymer starts flowing and the final strain seems to attain the value close to the one observed before for similar step stress value from a stressed state. Figure 75 and Figure 76 illustrate the polymer response when step stress is directly applied to the equilibrated structure of the polymer. The tensile stresses applied were 1000, 1500, 2000 and 2500 atmospheres. In each case the polymer was allowed to relax for 100 ps. After trying to fit the polymer response in each case we find as before that to have good fit and to make sense of the estimated parameters none of models tested in our case gave good results for the entire testing range.

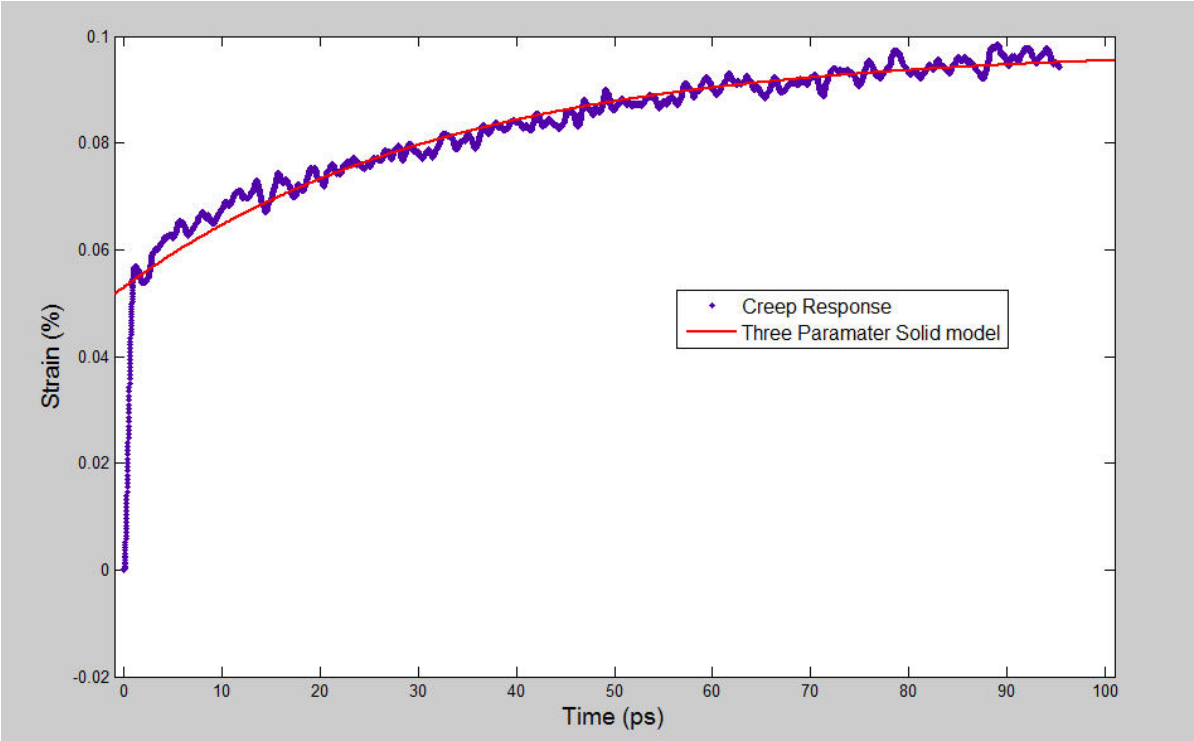


**Figure 75: 3 parameter model in response to 2000 atmosphere step stress**

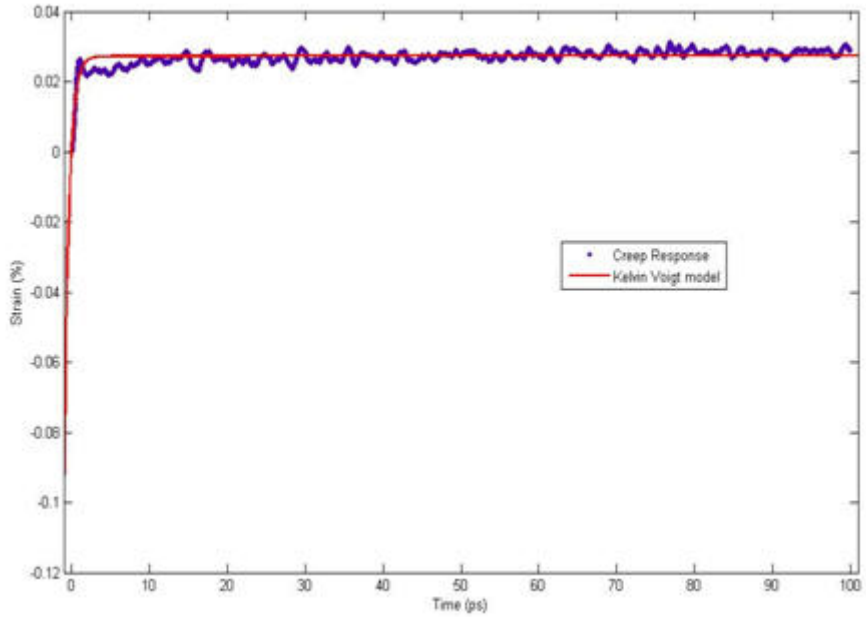


**Figure 76: Kelvin Voigt model in response to 1500 atmosphere step stress**

Unlike earlier case where step stress was applied to the already stressed polymer, here we have applied step stress to the equilibrated structure. Accordingly at higher stresses we observe an elastic response at the very beginning that was missing in the earlier case as the polymer was already in the flow region. Naturally unlike the earlier cases, Maxwell model could not be fitted to any of the cases. The polymer response was fitted with two different basic models, namely Kelvin Voigt model and three-parameter solid model as shown in Figure 77.

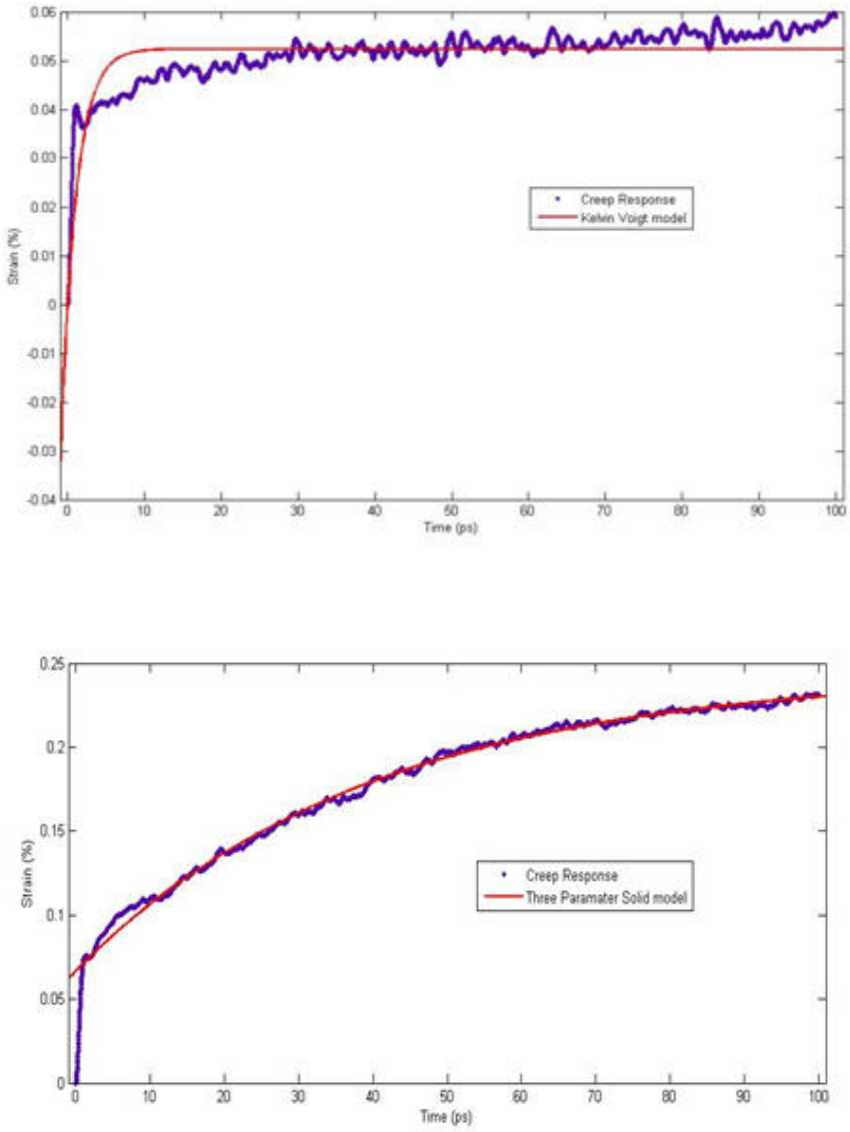


**Figure 77: Constitutive model fitting**

**Table 24: Estimated parameters for constitutive models for viscoelastic response of polymer**

| Applied Stress (MPa) | Spring elastic modulus (GPa) | | Viscous constant (Units GPa-ps) | Model |
|---|---|---|---|---|
| 100 | 3.68 | | 2.37 | Kelvin Voigt |
| 150 | 2.86 | | 5.67 | Kelvin Voigt |
| 150 | 2.75 | 1.78 | 15.34 | Three Parameter |
| 200 | 2.05 | 1.72 | 30.87 | Three Parameter |
| 250 | 1.02 | 2.73 | 29.36 | Three Parameter |

Table 24 gives the values of the fitted parameters. Comparing these values with Table 23 we find that:

1. The elastic spring constant estimated for Kelvin Voigt model in both cases differs a lot. This can be attributed to the fact that in the first case as parameters were estimated for the stretched polymer its stiffness was already less due to the already stretched state. Accordingly it gave lower spring constant even when it behaves like a solid.
2. We also observe a difference in the damping force factor. In the transition we have given fitted values obtained from Kelvin Voigt and Three-parameter solid model.
3. The spring constant value for the KV model coming from the 100 MPa run is very close to that obtained from atomistic simulation (3.68 GPa vs 3.6 GPa). We have also showed earlier that the yield strength of the polyimide is around ~ 125 MPa. Naturally experiments at a higher stress than that will result in lower values of the spring constant as the onset of plastic behavior has already occurred.
4. We also observe that at the transition, the value of the spring constant obtained from Kelvin Voigt model is comparable to that of the first spring constant obtained in case of Three parameter solid model.

These models also gave an estimate of corresponding time constants. From the above set of calculations we also calculated the time constant values as shown in the following Table 25:

**Table 25: Time constant calculation from constitutive models**

| Applied Stress (MPa) | Time Constant (ps) | Model |
|---|---|---|
| 100 | 0.65 | Kelvin Voigt |
| 150 | 2 | Kelvin Voigt |
| 150 | 14 | Three Parameter |
| 200 | 33 | Three Parameter |
| 250 | 40 | Three Parameter |

From the above table we find the following:

1. We observe that in the elastic zone the value of time constant is very low. This is expected as the response of the polymer is very fast in that region.
2. Due to usage of different models the time constant values cannot be compared with each other. As shown for the transition zone the time constant values obtained from different models are very different. The table still shows an increase of time constant value with higher applied stress within each model.

Similar to fitting the tensile stretch response we fitted Figure 78 using constitutive models the compressive stretch response of the polymer. In the following we have examined the same. In this case the polymer was relaxed for 200 ps in each step stress. The polyimide considered here is 10_30 unlike 30_40 in the tensile case. Although the samples are different and the rate is half that of the earlier case we expect that in terms of fitting constitutive models the trend and parameters should not be affected.

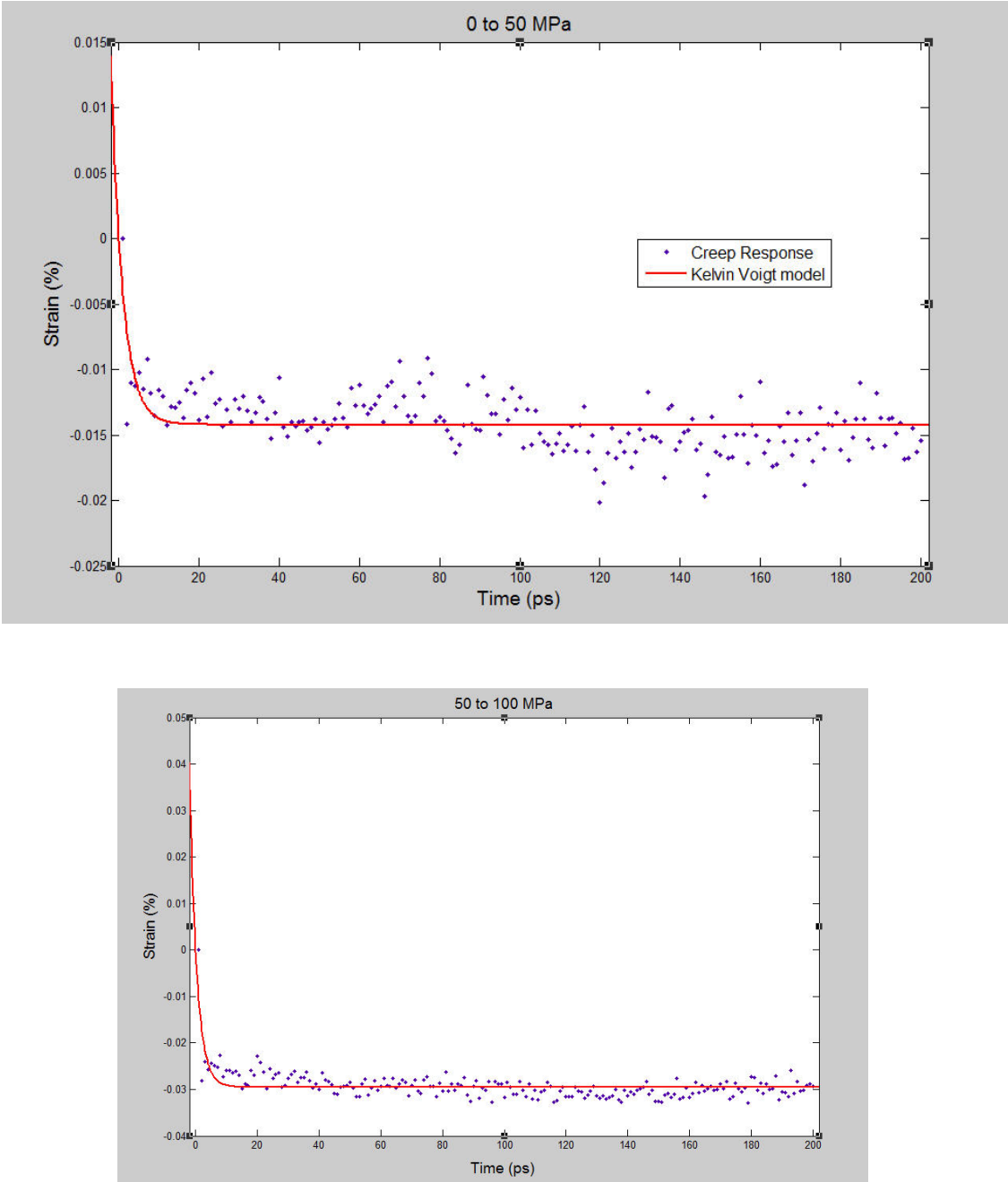


**Figure 78: Fitting Kelvin Voigt model to compressive stress response of polymer**

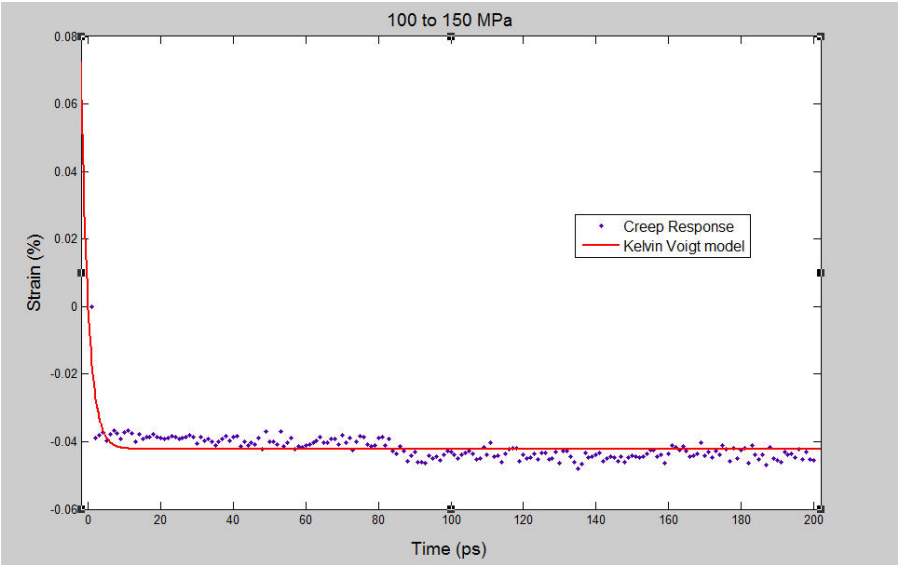


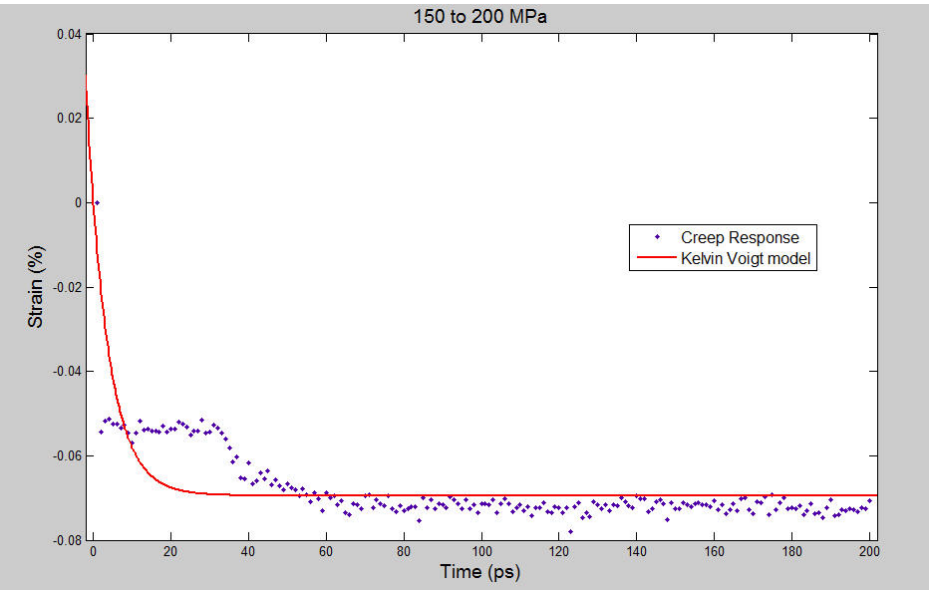


**Figure 78: Continued**

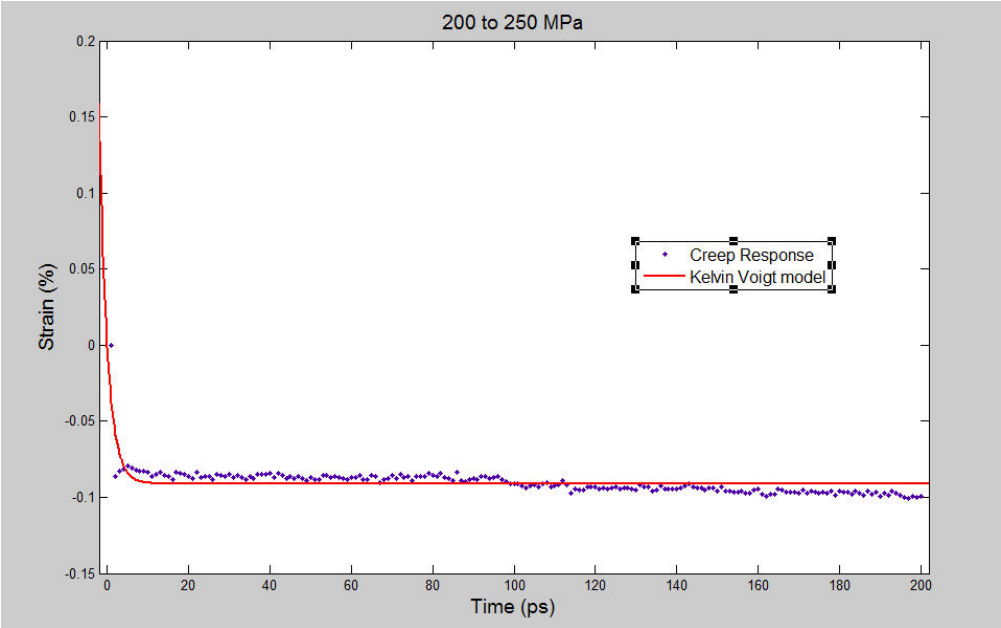


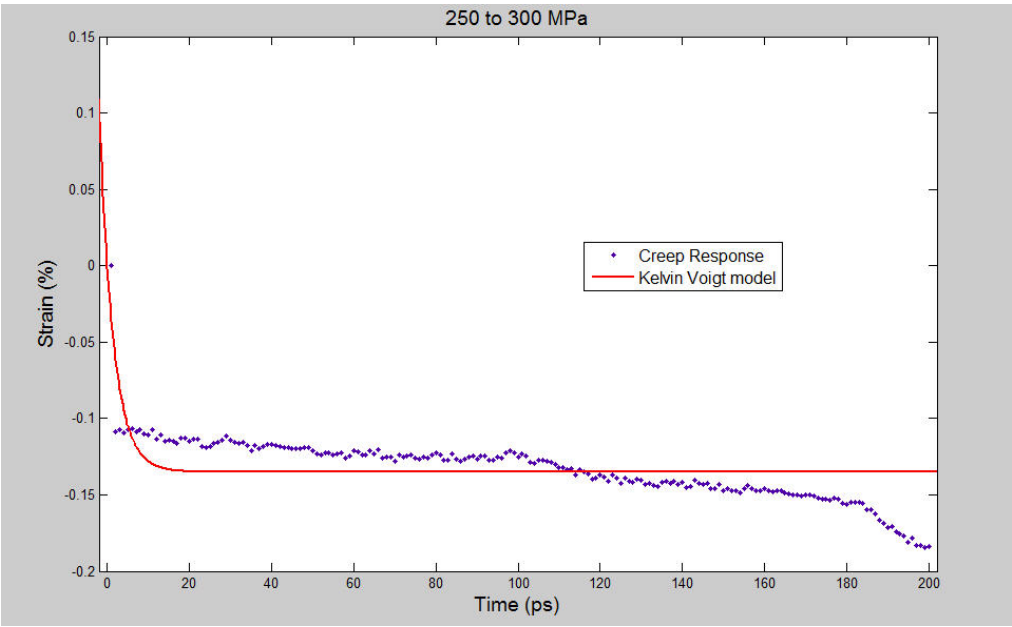


**Figure 78: Continued**

**Table 26: Estimated parameters of constitutive models for compressive experiment**

| | Spring elastic modulus (GPa) | Viscous constant (Units GPa-ps) | Model |
|---|---|---|---|
| 0 – 50 MPa | 3.52 | 10.3 | Kelvin-Voigt |
| 50 - 100 MPa | 1.70 | 3.94 | Kelvin-Voigt |
| 100 - 150 MPa | 1.18 | 2.36 | Kelvin-Voigt |
| 150 - 200 MPa | 0.72 | 4.0 | Kelvin-Voigt |
| 200 - 250 MPa | 0.55 | 1.1 | Kelvin-Voigt |
| 250 - 300 MPa | 0.37 | 1.25 | Kelvin-Voigt |

From Table 26 and Figure 78 we observe the following:

1. In the compressive zone the flow behavior is not so predominant at higher stresses unlike the case tensile stretch.
2. We observe that starting from 100 to 150 MPa in the compressive stress zone there are parts in the strain behavior where there is flow tendency (as shown by an ellipse) for a while. This agrees well with the yield behavior we observed of the polymer in the tensile case. This tendency seems to increase with higher stresses. It may be argued that in response to application of large stress the chains tries to flow in order to adjust. However due to the congestion of the chains resulting from the compressive nature of the stress, getting space becomes difficult. However as stresses get increasing the chains could manage moving in the other directions and eventually setting up a low type behavior as we observe in the 250 to 300 MPa zone.
3. Due to the non-flow nature of the polymer chains in most of the compressive stress zone, Kelvin Voigt model does a good job in fitting the polymer response up to 250 MPa applied stress.
4. Comparing the spring and viscous damping constants obtained from fitting Kelvin-Voigt model in tensile and compressive cases we find similar values of parameters in the elastic response zone of the polymer. In the flow region

designated by stresses higher than 150 MPa the difference in response also makes the difference in fitting constitutive equations.

5. In both cases however we observe decrease in the spring constant value with higher stresses. Responses to these are taken care by the movement of the polymer chains. Initially due entanglement issues the polymer chains could not move much and responds to the perturbation through bond and angle rearrangements.

Similar to application of step stress to the equilibrated structure of the polymer sample, we applied step stress of compressive nature Figure 79 to the polymer sample. In the following we have examined the response of 10_30 polyimide to the above mentioned mechanical experiment. The applied stresses were 1000, 1500, 2000 and 2500 atmospheres. In each case the polymer sample was allowed to relax for 200 ps.

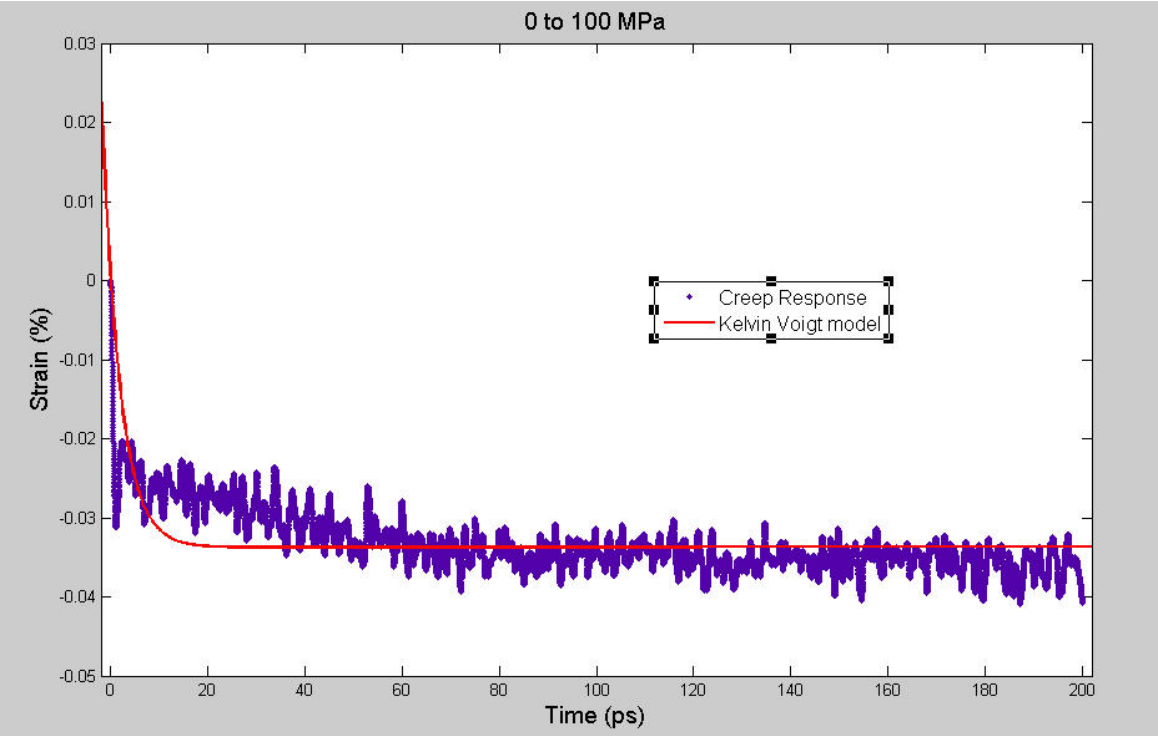


**Figure 79: Kelvin Voigt model fitting**

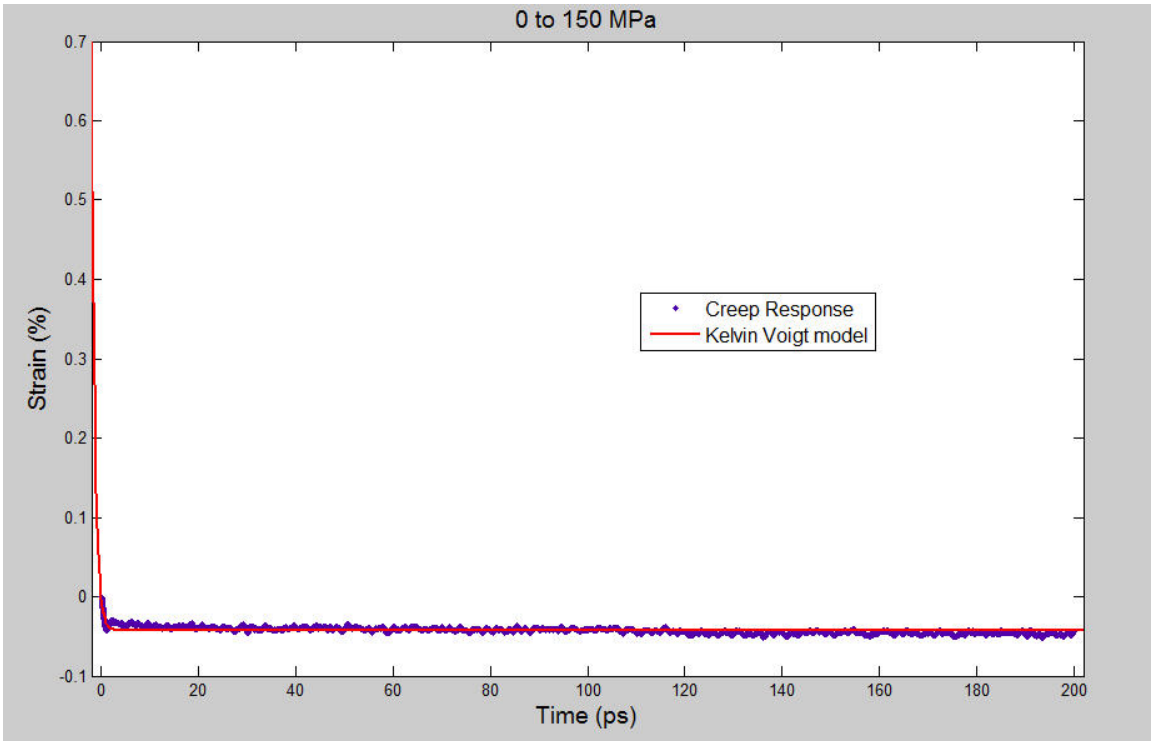


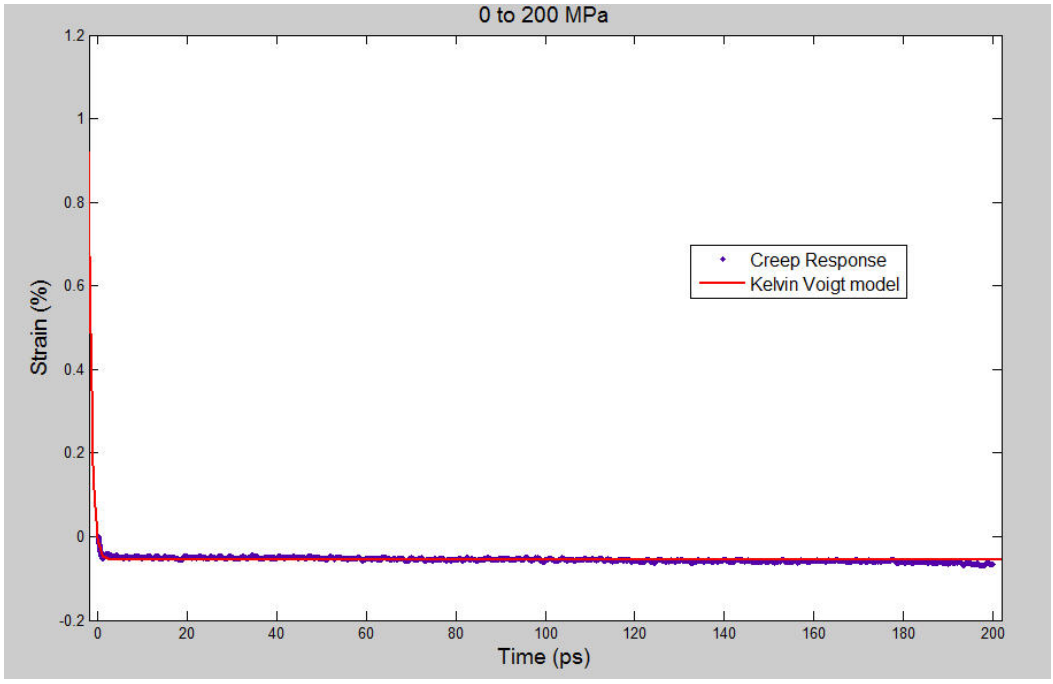


**Figure 79: Continued**

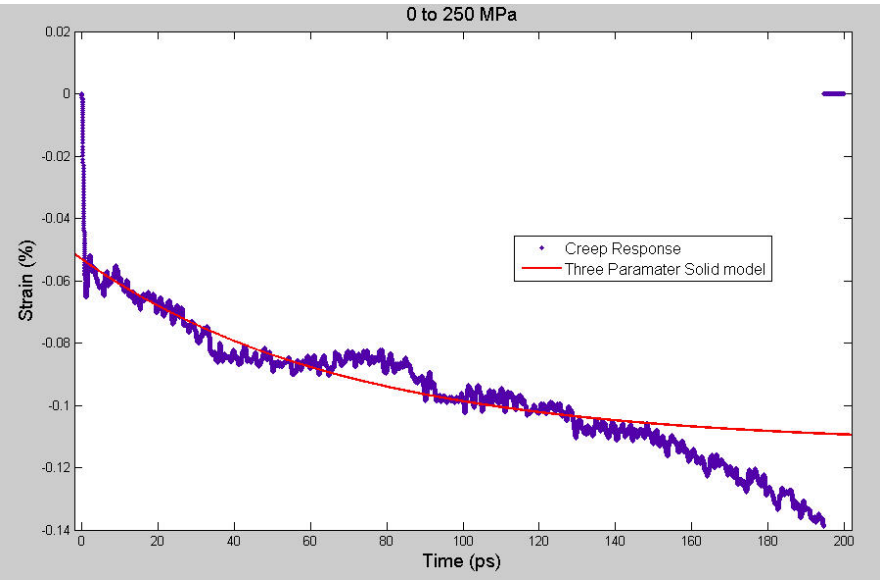


**Figure 79: Continued**

**Table 27: Estimated parameters for compressive step stress to equilibrated structure**

| Applied Stress (MPa) | Spring elastic modulus (GPa) | | Viscous constant (Units GPa-ps) | Model |
|---|---|---|---|---|
| 100 | 2.96 | | 10.92 | Kelvin Voigt |
| 150 | 3.51 | | 2.46 | Kelvin Voigt |
| 200 | 3.60 | | 2.51 | Kelvin Voigt |
| 250 | 2.2 | 2.49 | 80.6 | Three Parameter |

**Table 28: Time constant calculation from Table 26**

| Applied Stress (MPa) | Time Constant (ps) | Model |
|---|---|---|
| 100 | 3.7 | Kelvin Voigt |
| 150 | 0.7 | Kelvin Voigt |
| 200 | 0.7 | Kelvin Voigt |
| 250 | 69 | Three Parameter |

From Table 27, Table 28 and Figure 79 we observe the following:

1. In the compressive stress experiment the Kelvin –Voigt model does a good job for fitting the parameters in the given timeframe for the low-flow behavior of the polymer.
2. Similar to the tensile experiment results we find that the time constants in the elastic zone is very small and increases by a order of magnitude as it enters the flow region.
3. Due to the repulsive van der Waals forces in the compressive zone we observe the spring constant value to be 3.6 GPa (same as found in atomistic case) even at high stress value experiment.
4. However once into the flow region the time constant value in the compressive experiment is bigger than the tensile case (69 ps vs 40 ps). This can be attributed to the fact that there is difficulty in flow and compress of the polymer chains in the compressive experiment, as we have found earlier when analyzing the contour length behavior of the polymer chain.

### 3.4.6 Conclusions

We have applied stress of different nature on a piezoelectric polyimide through the use of molecular dynamics simulation. We could extract the polymer viscoelastic behavior by applying very high stress rate and hence compensated the usual requirement of a long relaxation time to observe the same. We have found that the flow behavior of polymer is a result of both flow of the polymer chains and change in contour length of the polymer chain. A ‘collapse model’ can possibly describe the behavior of a polymer sample in such high stress. By collapse model here we mean a Kelvin – Voigt model collapses to form a Maxwell model at the high stress limit to initiate the flow behavior in an otherwise solid model. However doing experiment in an equilibrated sample showed that Kelvin Voigt model can closely predict the young’s modulus value of the polymer. It should be kept in mind that in the atomistic simulation the chains have the ability to reorient themselves in order to adjust stress and release some of it by expanding or contracting in other directions, an effect which is not taken care by 1 D constitutive

models considered here. We have also found time constant values of the polymer sample from the constitutive models in different region showing very low values in the elastic zone and an order of magnitude higher time constant values in plastic zone.

In conclusion we have showed the 1 D constitutive models can be built based on atomistic simulation results of a polymer sample. Building this type of models gives the reliability due to the source of data being atomistic and gives the accessibility to larger scale phenomena through constitutive models. Also the advantage of having a constitutive model describing the response of a polymer is that the parameters of that model can be used to determine other useful properties of the polymer. Just like we have estimated the time constants of the polymer response at this high stress level, we can also estimate dynamic modulus of the system without actually applying stress of sinusoidal nature.

## 3.5 Application of Step Strain

To look into the mechanical properties in another way, the system was strained axially keeping other two directions fixed. The resulting stress on the polymer sample was calculated and the stress-strain behavior was analyzed. However due to the restrictions imposed on the Poisson ratio ($\upsilon = 0$) this test should lead to generation of higher stress in the sample for a particular strain. Accordingly it is expected that the stress strain curve obtained from this experiment will be steeper in nature. Figure 80 compares the stress-strain behavior obtained from creep and relaxation test for 10_30 polyimide. The time span for both the experiment was same.

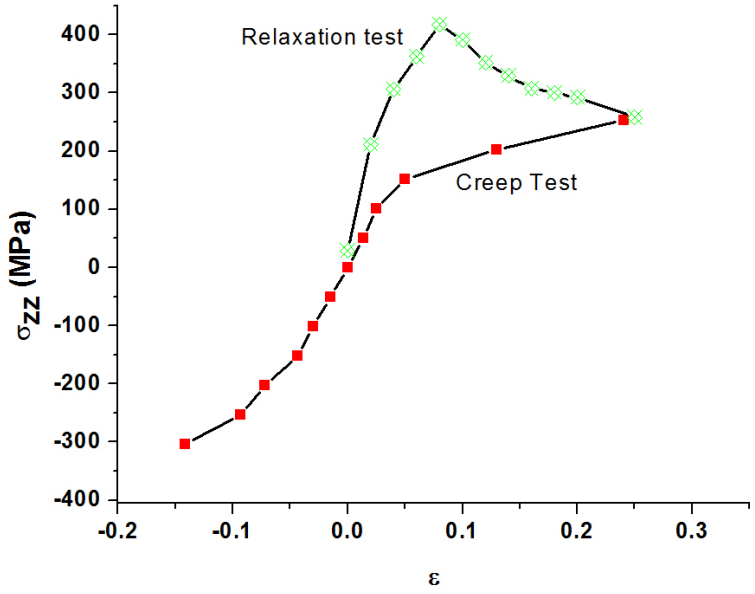


**Figure 80: Comparison of polymer response in creep and relaxation test**

From Figure 80 we observe:

1. The stress-strain curve for relaxation case is steeper. The reason as mentioned before can be attributed to the inability of the polymer to relax in other two directions.
2. We also observe a breaking type behavior, which we missed in our stretch experiment.
3. Finally we observe that the stress value at large strain does converge to values obtained from creep test.

The extra information this experiment provides than the creep test is the values of the off diagonals in the stiffness tensor. Due to the limitation of LAMMPS in the creep test, the system cannot have a shear strain. However in the relaxation test, it is possible to extract the six components of pressure and hence the off diagonal components of the stiffness matrix. For similar reasons we also cannot calculate the shear modulus directly. However we calculated the shear modulus values using isotropic conditions. For an

isotropic material only two independent material constants are needed. Combining the results of these two tests we have found the stiffness tensor of the polymer sample.

In terms of modeling the response of stress from applied step strain, constitutive equations described before is probably more suitable. The primary reason being in the atomistic simulation, part of the stress applied axially could be dissipated through the effect of Poisson ratio. The lateral dimensions were allowed to expand or contract as per need without changing the stress in the three directions. In constitutive model however the whole stress is countered by the presence of any spring and dashpot nature of the polymer.

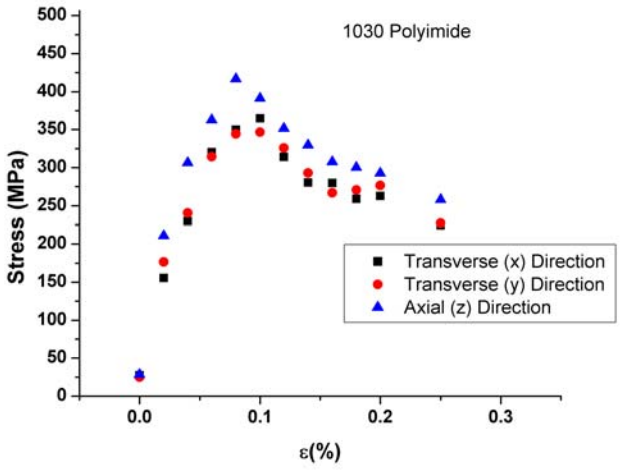


**Figure 81: Polymer response in relaxation test**

## 3.6 Work (Strain) Hardening

Work hardening refers to strengthening of a material through the increase of material's dislocation density. Earlier we have observed the response of a 30_40 polymer sample that was mechanically stretched up to 2500 atmosphere. The polymer sample was equilibrated back to 0 atmospheres condition. The resultant sample was subjected to creep test as before. In other words it was subjected to tensile stress of from 0 to 2500

atmospheres in steps of 500 atmospheres. The sample was allowed to relax for 100 ps in each stress level. Figure 82 displays and compares the response of the two cases. We observe a clear strengthening behavior of the polymer in question.

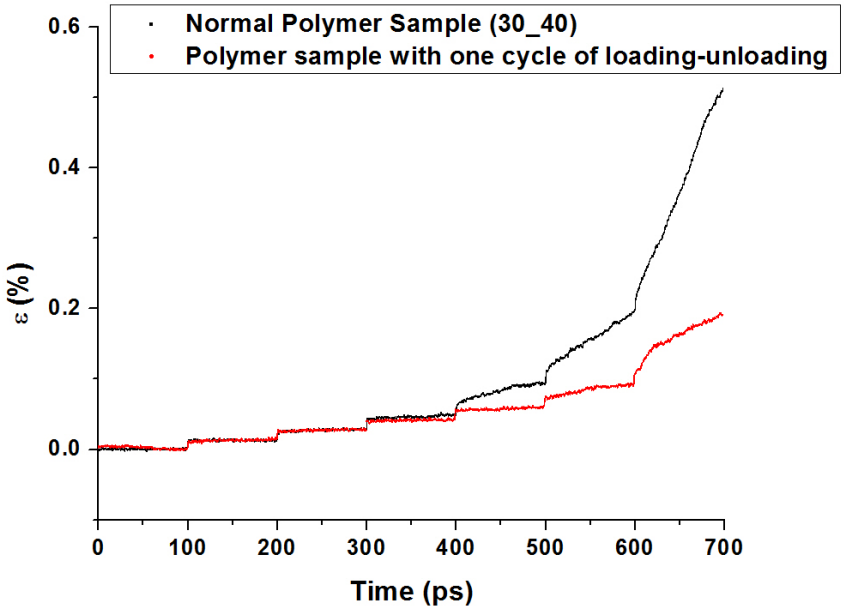


**Figure 82: Strain hardening**

Since the polymer sample in question has gone through one cycle of axial stress annealing, it is expected that there will be changes in chain conformations, alignments entanglement rearrangements and it should behave differently. From figure 82 we observe the following:

1. We can clearly observe the work hardening of the polymer sample.
2. In the elastic region we observe identical response in both cases.
3. The difference in response starts from the flow region.

## 3.7 Dipole Moment – $R_e$ Relation

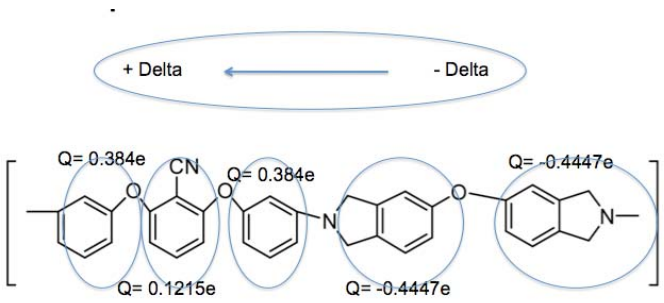


**Figure 83: The basis for dipole moment and end-to-end vector relation**

The approach taken here for calculating dielectric properties of the polymer does not take into account the instantaneous charge transfer among the atoms within the system. Single chain polymers with different length of monomers were built and charges on the atomistic model were calculated using charge equilibrium method. In each case the charges in the middlemost monomer was considered to avoid any side effects. Analyzing the above mentioned different cases final static charges were assigned on the atomistic model. So these charges on respective atoms were fixed throughout the calculation.

In view of the fact just stated above and a careful look into the monomer charge distribution, we get Figure 83. As we observe, there is an implicit division between the concentration of negative and positive charges in the monomer. Accordingly as indicated in figure 83, the dipole moment as a result of the charge distribution will roughly be along the monomer direction. The more rigid the monomer behaves, more linearly related should the dipole moment vector and the polymer direction will be.

The polymer direction when added up results in the end-to-end vector as shown in Figure 84. To investigate the above mentioned hypothesis an isolated monomer was taken and was subjected to isothermal isobaric simulation for 1 ns. The instantaneous end-to-end vector of the monomer was kept track of along with the chain dipole moment. Figure 85 puts the two together in three-dimensional space for comparison. The vector values of both the properties are very different from the bulk behavior. However

the purpose of the calculation is fulfilled. We observe that there is a near linear relationship between the two.

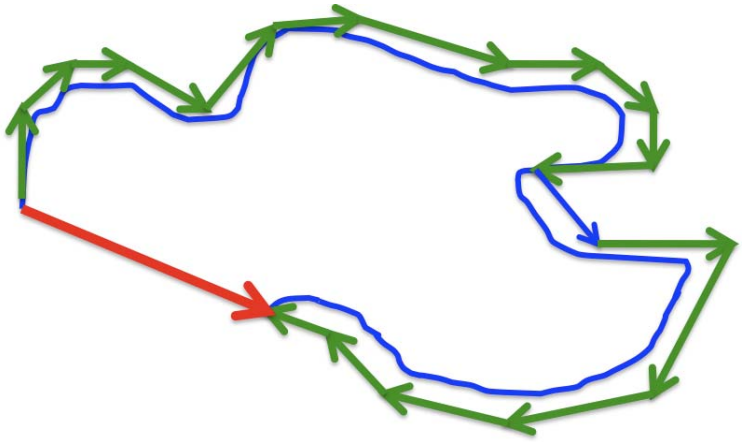

**Figure 84: Cartoon of a typical polymer chain**

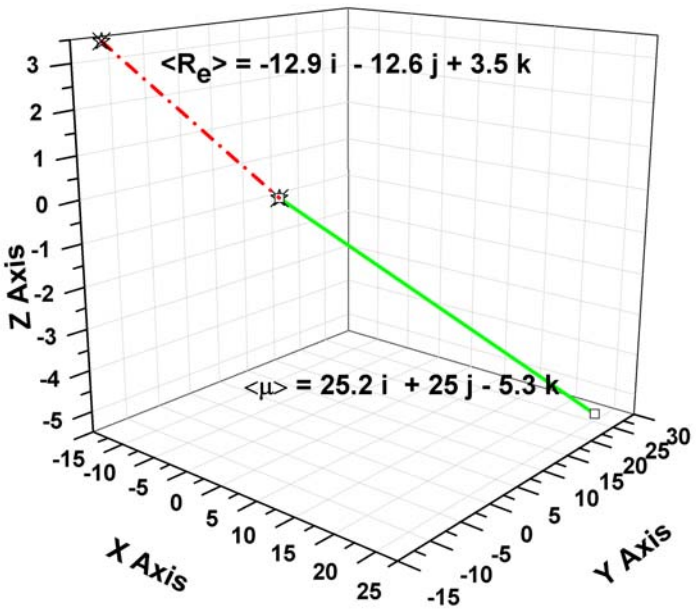


**Figure 85: End-to-end vector and dipole moment of an isolated monomer**

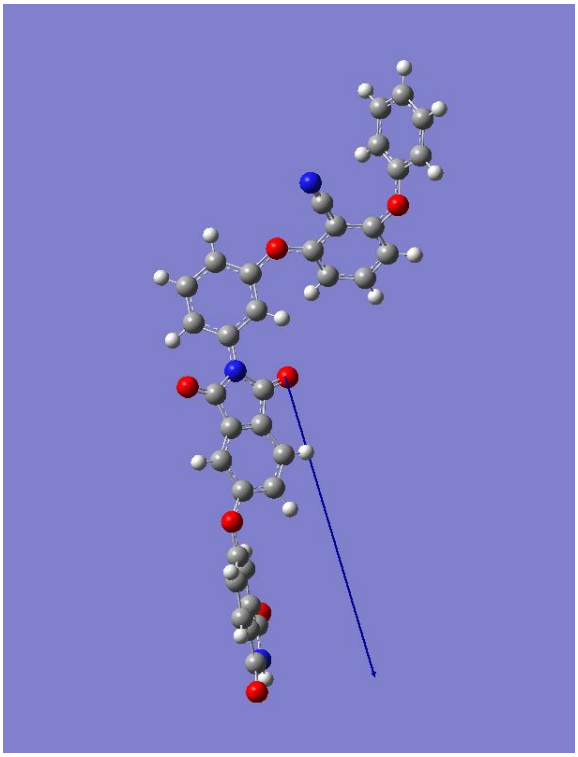

**Figure 86: Dipole moment from DFT calculation**

In addition to using molecular dynamics study we also did single point energy calculation on the minimized structure of the monomer. We have used DFT theory with 6-31 B3LYP as basis set. Figure 86 illustrates the dipole moment vector (shown by arrow) as calculated from first principles. We observe that even though the dipole moment vector does not lie exactly along the end-to-end vector direction; they do intersect at a very small angle.

Backed by these studies the x, y and z component of the end-to-end vector was plotted against corresponding components of the dipole moment. Figure 87 shows the near-linear relationship obtained between end-to-end vector and dipole moment in x direction. Similar relationship was observed for ‘y’ and ‘z’ direction.

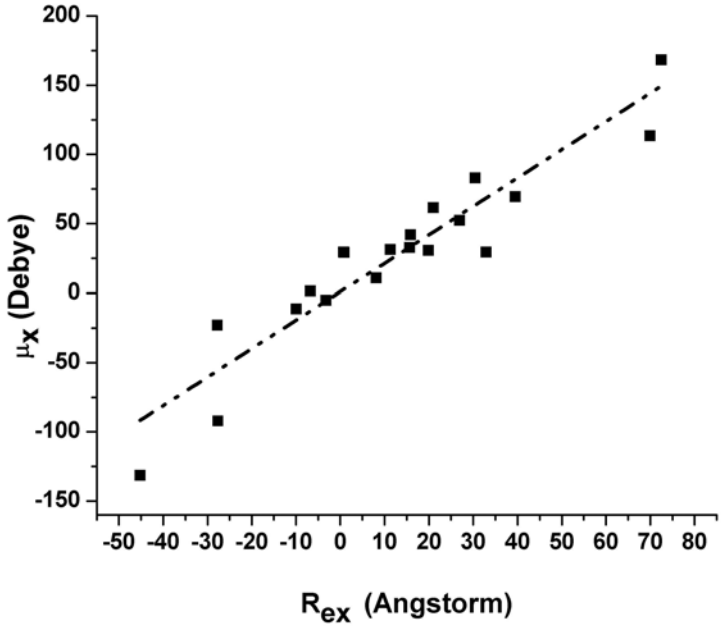


**Figure 87: Near linear relationship between end-to-end vector and dipole moment of a chain**

In a similar fashion based on the above argument we can relate the fluctuation of the two properties. In other words the end-to-end vector fluctuation can be related to the dielectric constant of the polymer sample.

*Response to step stretch:* Earlier we have mentioned about our step stretch experiment. We have looked into the stress response of the polymer in the same section. In this section we have looked into and analyzed the dielectric response of the polymer for the same applied stress. In the absence of electric field the piezoelectric coefficient tensor can be defined as follows:

**Equation 52**

$$P_i = d_{ijk}\sigma_{jk}$$

where

$\sigma_{ij}$ represents stress

$P_k$ represents polarization

$d_{ijk}$ represents piezoelectric coefficient

As per equation 52 we see that piezoelectric tensor has 27 coefficients. The step stretch experiment was done by applying stretch axially. We have not applied shear stress due to the limitation explained before. We must also mention that as earlier we use the advantage of the polymer sample being isotropic and accordingly handle all the three directions.

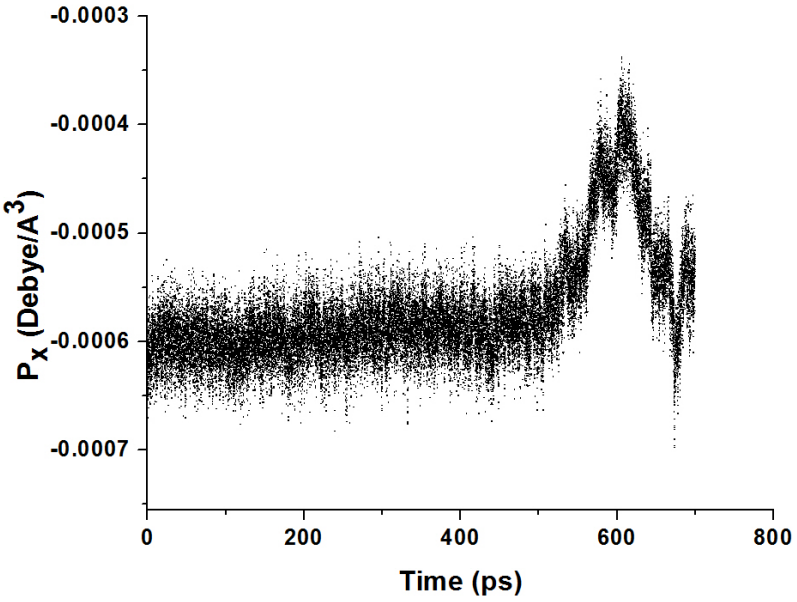


**Figure 88: Instantaneous polarization response to creep test**

Figure 88 illustrates the change in polarization value of the polymer sample in response to step stress in x direction. In presence of no electric field we find that the change in polarization value in the elastic zone is not very prominent. The order of the piezoelectric response of this polymer [47] is in the range of few pC/N. Accordingly the change expected in polarization should be in the order of $10^{-5}$ Debye per $A^3$ per 1000 atmospheres. The fluctuation of the polarization as observed from figure 88 is an order of magnitude higher than that. It appears that the change in polarization happens slowly

through large fluctuations. It can be argued that within the elastic zone under given time frame there is very little permanent rearrangement of atoms to develop a change in polarization value. Since the change is less within the given timeframe there are also no specific trends. Once the polymer enters into the plastic zone, the change in polarization looks drastic. As the polymer enters flow region, due to the space available to the atoms it becomes relatively easier to respond to the higher stress locally with rearrangement of atoms.

We also observe an anomaly in terms of steep changes in polarization values after 400 ps run. This corresponds to step stress of 1500 atmosphere. In other words the anomaly starts showing up once the polymer enters the plastic region.

Looking in to the polarization aspect we find that three variables are involved. Given the nature of the calculation (i.e no charge transfer) we are left with two, namely position of the atoms and volume of the material.

We can formulate a problem to see what would have happened if the changes in atom position due to step stress application was proportional to overall change in volume in that direction. Accordingly we can write for a stress value of $\sigma_{ii}$ the change in $P_i$ can be formulated as:

**Equation 53**

$$P_{i0} - P_i = P_{i0} - \frac{\mu_{i0}(1+\varepsilon_{ii})}{V_0(1+\varepsilon_{ii})(1-\nu\varepsilon_{ii})^2} = P_{i0}\left(1 - \frac{1}{(1-\nu\varepsilon_{ii})^2}\right) = P_{i0}\left(1 - \frac{1}{\left(1-\nu\frac{\sigma_{ii}}{C_{ii}}\right)^2}\right)$$

Assuming the applied stress is within elastic limit (~ 100 MPa), the value of $C_{ii}$ in the order of several GPa and $\nu < 0.5$ we can further approximate the above equation to:

**Equation 54**

$$\Delta P_i = P_{i0}\left(1 - \left(1 + \frac{2\nu\sigma_{ii}}{C_{ii}}\right)\right) = -P_{i0}\left(\frac{2\nu\sigma_{ii}}{C_{ii}}\right) \Rightarrow d_{iii} = -\frac{2\nu P_{i0}}{C_{ii}}$$

Analyzing the above equation we find the following:

1. For an absolute amorphous polymer sample with no residual polarization at equilibrated state, in the absence of charge transfer among atoms, there will be no piezoelectric contribution axially due to translation of the polymer atoms under an applied stress in the axial direction.
2. With a residual polarization in the order of $10^{-3}$ Debye/(Angstorm)$^3$ (as found in our calculation) with a poisson ratio 0.4 (for this polymer) and taking the value of axial stiffness constant as several GPa we have piezoelectric constant in the order of few pC/N which is comparable to experimental values [47]. This implies in modeling piezoelectric polymer the presence of any residual polarization will have axial piezoelectric contribution due to the translation of the polymer atoms in response to axial stretch is in the order of actual piezoelectric response.
3. The deviation from this result indicates the deviation of the polymer behavior from the actual assumption. The deviation relates to the flexible nature of the polymer chains. The presence of entanglement and chain interactions will not allow the polymer chain to behave evenly all throughout the chain. In view of the collective contribution argued before in response to step stress we can also add that the change in contour length also does not happen evenly all along the chain. And that should lead to deviation.

## 3.8 Thermal Properties

The polymer samples were heated from 300 K to 700 K with increment of 100 K. The samples were heated instantaneously and then allowed to relax for 400 ps.

Plotting the density values (Figure 90) of the polymer samples with temperature we find that for smaller samples 6_6, 10_12 and 5_25 the variation of density with temperature is linear. Samples 10_30, 15_40, 20_30, 30_40 and 40_40 however show a change in the rate of density variation with temperature in the range of 450 - 500 K temperature. Figure 90 shows the trend described above. It indicates the presence of a glass transition behavior. Similar values 491 K [23] have been obtained experimentally for

$T_g$ for $(\beta - CN)APB/ODPA$ polyimide. There also seem to have some system size effect as we observe a different trend for systems containing less than 10,000 atoms.

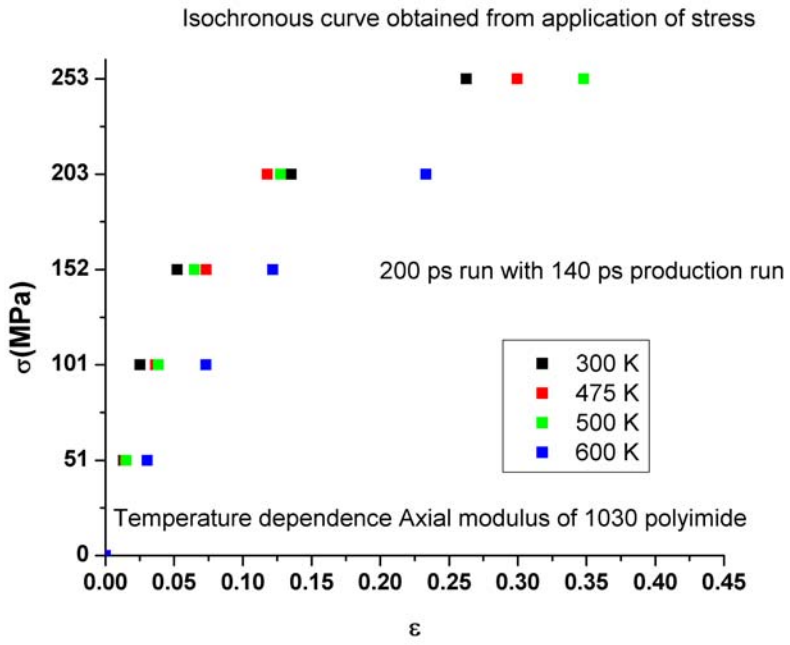


**Figure 89: Softening of polymer young modulus**

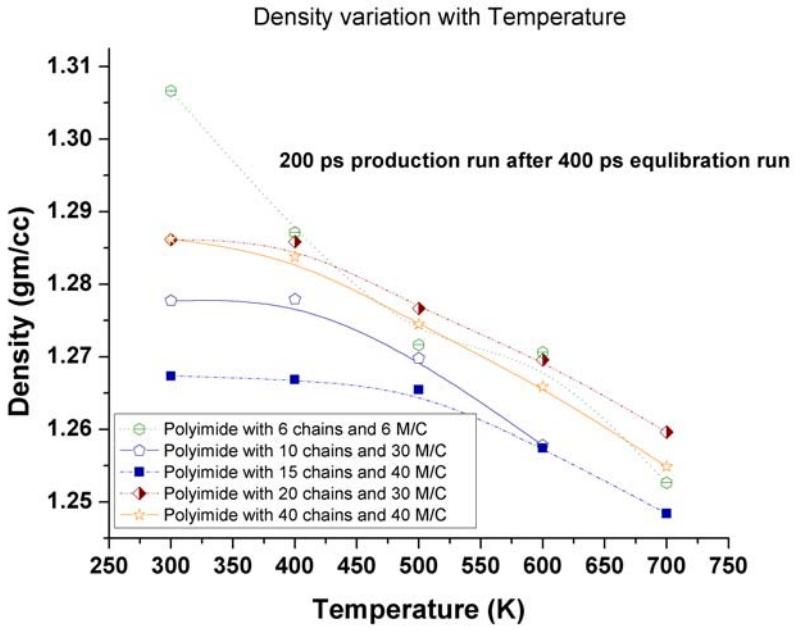


**Figure 90: Effect of temperature on density**

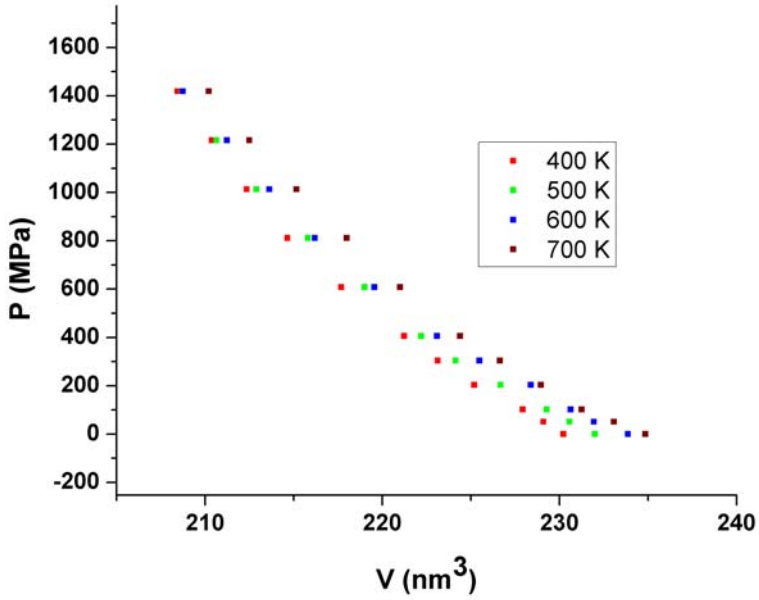


**Figure 91: Equation of state curve**

Observation of figure 89, 90 and 91 tells us the following:

1. The glass transition temperature of the polymer lies somewhere between 450 and 500 K as per figure 90. This agrees reasonably with experimental findings.
2. We do observe a softening of the material in figure 89 for T = 600 K but not for T=500K. It can be argued that since the actual $T_g$ as found in experiments is very close to 500K, simulation at 500 K may not be able to observe it. Simulation with longer runs or temperature little higher than 500K might show a softening behavior to support the glass transition.
3. Smaller system does not show any glass transition behavior as observed in figure 89.
4. The equation of state curve (for 10_30 polymer) does not show explicit softening behavior although careful inspection reveals a change in behavior of curve corresponding to 500 K from 400 K near zero atmospheres.

## 3.9 Conclusions

Piezoelectric polymers with thermal stability at high temperatures are potential candidates for future generation materials. However it is necessary to understand the polymer behavior at the atomistic scale to engineer its properties targeted at desired applications. In line with these requirements we have looked into thermo-mechanical properties of a piezoelectric polyimide through classical molecular dynamics simulation in this section. We have been able to force the polymer out of its elastic zone to plastic zone with application of excess stress and characterized the flow behavior of the polymer as a collective contribution of extension of chain contour length and the flow of the chain itself. We have also observed the strain hardening behavior of the polymer sample through the application of high stress. Application of ramp stress at similar rates allowed us to identify the yield point of the polymer sample. We were able to relate the dipole moment of a chain to the end-to-end vector of it. This enables us to relate the chain dipole moment to other chain characteristics like radius of gyration, persistence length and order parameter through end-to-end vector.

# 4. COARSE GRAINING

## 4.1 Introduction

Polymer needs no introduction. Combined with excellent set of properties, the ease of processing of these materials has enabled them to play a non-trivial role in our daily life. Among others one of the vital and important properties of polymers, which has intrigued researchers over years is its plastic deformation characteristic [137-140]. Plasticity deformations in materials represent the non-reversible change in shape under applied loads. The loads may be static or dynamic. This mechanism is complex in nature and given the potential there is a definite need to understand this phenomena comprehensively in order to come up with future generation materials from polymers. Classical molecular dynamics (MD) is a useful tool in tracking events at the atomistic level of any material. In principle plastic deformations in materials can be studied using classical MD. However MD is inherently limited in length and time scales if no compromises are made at the molecular level details. Unfortunately the timescale at which most of the phenomena occurs in a polymer, due to its slow segmental movements is rather large relative to the timescale accessibility of a typical MD simulation. On the other hand in order to have realistic estimates and reliable conclusions especially for an amorphous polymer, a relatively larger system than what a typical MD simulation can address is desired to generate enough randomness in the model for its isotropic properties. As shown in Figure 92, in order to move a step ahead both in time and length scales in such simulation studies one needs to rely on approaches which are higher up in the ladder of a hierarchical multi-scale modeling approach.

Time scales are dictated by the high frequency modes arising from the intra-molecular bonds forcing one to keep smaller integration time step for classical MD simulation of a system leading to coverage of a smaller domain in phase space with reasonable computational resources. However, approach such as Coarse Grain (CG) representation can eliminate these fast modes of a system. This route has been a useful approach elsewhere[141-148] where the finer details of the system are averaged out in favor

of building a low-resolution model in order to simulate larger size models for longer periods of time.

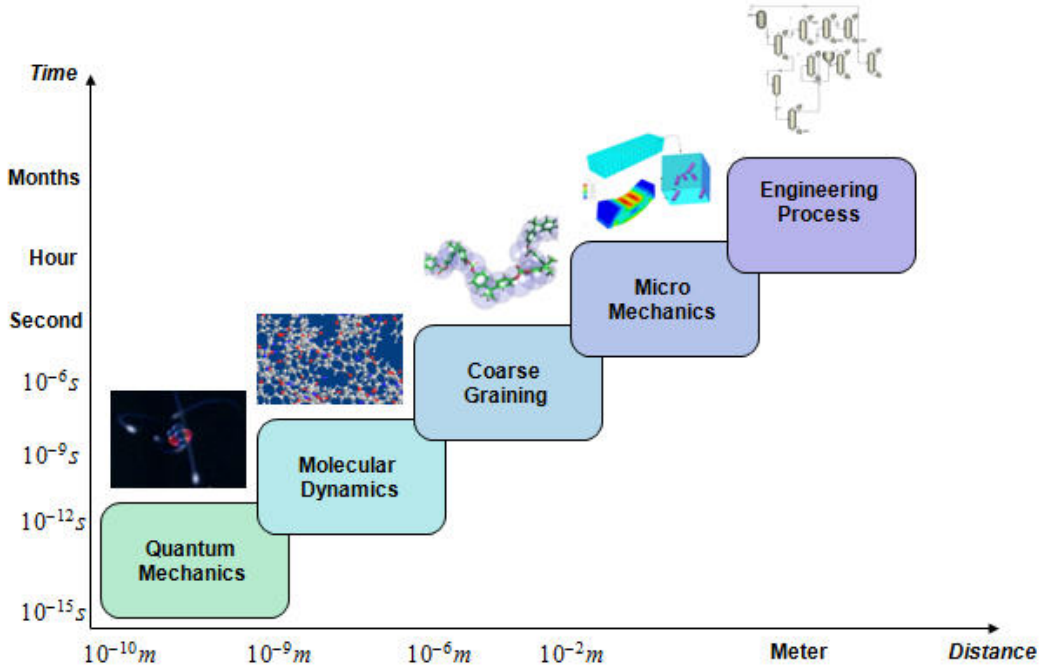


**Figure 92: Multiscale modeling**

We have faced the same problem while studying the elastic and plastic properties of an amorphous, aromatic polyimide substituted with nitrile dipole by molecular dynamics simulation. Motivated by the success of meso-scale modeling in addressing similar limitations, in our present work we have developed coarse graining parameters for a piezoelectric polyimide exclusively based on our atomistic level simulation results and have made an attempt to describe the system in a CG model without losing much material specificity. The reasonable agreement obtained between MD and CG results has motivated us to access larger time and length scale events, which was otherwise very expensive through a regular MD route. Additionally we obtained impressive gain in terms of computing resources. In terms of computational time we observed a gain in the order of hundreds for keeping system size and number of CPU's constant. For data

saving purposes of individual atoms the gain was in the order of tenths, the factor by which the number of atoms was decreased by introducing super atoms.

### 4.1.1 Coarsening

In context of modeling coarsening refers to lump a set of atoms into a single super-atom. Ideally the system built of super atoms is supposed to reproduce the characteristics as closely as possible of the same system when it is treated like all atom model. The advantage of coarse-grained model is exploited in two ways. The most widely use of coarsened model is accessing the larger timescale and length scale phenomena [149-152]. Another use of this approach is to get an equilibrated structure of system faster through mapping and reverse mapping from atomistic to coarsened model [141,153,154]. The building of a coarsened model has no defined approach and hence can be achieved in various ways keeping the objective in mind. Issues that are most important to a researcher are mapping techniques [153,154] and systematic approach in building a coarsened model [144,155,156]. Various methods like dissipative particle dynamics[157-159], Boltzmann inversion technique[154,160], force matching method[161], fitting energy distribution[142,162] has successfully been used. Treating a system as coarsened model has been successfully demonstrated mostly in biological systems [144,147-149,163-167], polymers [143,145,154,168,169] dendrimers [143,170] and liquid state systems [171,172]. Impressive gain in terms of computational resources has also been observed in several cases[142]. However the generation of a coarsened model introduces loss in degrees of freedom in the system and hence raises questions on certain aspects[173]. It must also be noted that coarsening is specific to a system and hence non-transferable among different systems.

### 4.1.2 Super Atom

The first part of the methodology consists of defining the super atoms. Although there is no mathematical equation to solve for such a step and is rather subjective, factors such as problem objective, group of atoms expected to move together, validity of spherical type super atoms assumptions etc. acts as rule of thumb. Based on these the piezoelectric

polyimide system was coarse grained from 62-atoms per monomer, polymer system to a 5-interaction center per monomer, polymer system as illustrated in Figure 93.

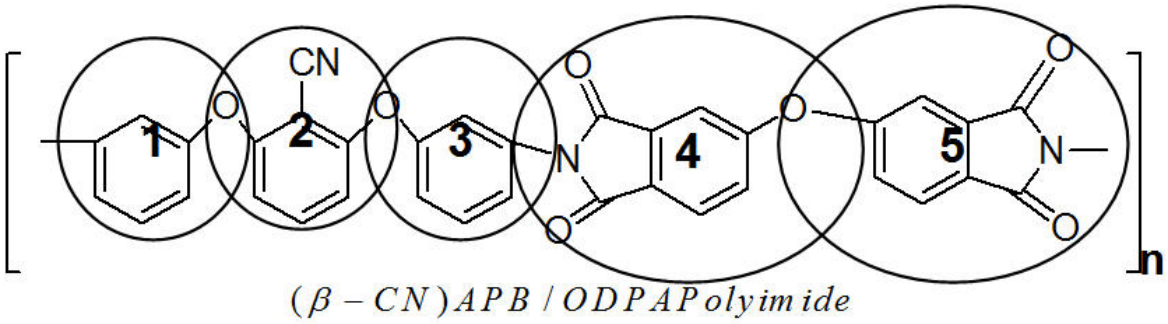


**Figure 93: Coarse graining an atomistic model**

4.1.3 Parameter Estimation

The interactions of this system were described by the following potential energy expression:

**Equation 55**

$$E = E_{bond} + E_{angle} + E_{vdw} + E_{coul}$$

where

$E_{bond}$ =Energy due to bond stretch defined by a harmonic bond stretching function

$E_{angle}$ =Energy due to angle bending defined by a harmonic angle bending function

$E_{vdw}$ =Energy due to Van-der-Waals interaction defined by a Morse function

$E_{coul}$ =Electrostatic energy defined by Coulomb law

Atomistic simulations in canonical ensemble of isolated polymer chains built from 3, 5, 7 and 9 monomers were run for 5ns at 300 K while keeping track of the movement of the center of mass of the set of atoms defining a bead-interaction center for the coarse grain model. The positions of the center of mass obtained from the atomistic

runs were noted and were used to fit to a Gaussian distribution function of the corresponding energy term as follows.

*Bond:* The bond stretching energy was described by a harmonic function and subsequently a cost function was minimized to determine the parameters for the coarse grained model.

**Equation 56**

$E_b = \frac{1}{2} k_b (r - r_0)^2$ Where $k_b$ is the force constant and $r_0$ is the equilibrium bond length

**Equation 57**

$$C_b(k_b, r_0) = \int_0^\infty dr P(r) - \frac{\sqrt{\pi} RT}{k_b} \exp\left(-\frac{E_b}{RT}\right)$$

Figure 94 is an example of one such fit from where parameters are estimated for an equilibrium bond length and force constant between two super atoms.

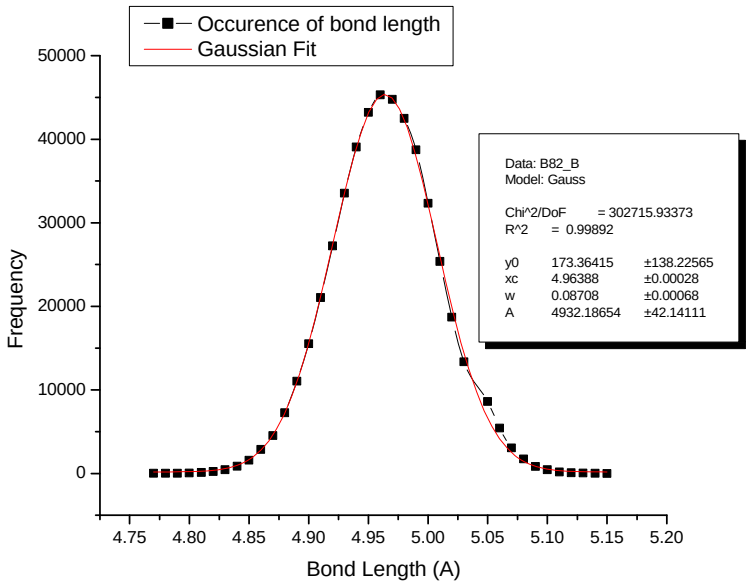


**Figure 94: Bonding parameter estimation**

*Angle:* In a similar way the angle bending energy was also fitted to a Gaussian curve and the corresponding parameters were estimated.

**Equation 58**

$E_a = \frac{1}{2} k_a (\theta - \theta_0)^2$ Where $k_a$ is the force constant and $\theta_0$ is the equilibrium angle

**Equation 59**

$$C_a(k_a, r_0) = \int_0^\infty dr P(r) - \frac{\sqrt{\pi} RT}{k_a} \exp\left(-\frac{E_a}{RT}\right)$$

*Van-der-Waal:* In order to determine the parameters for estimating the van-der-Waal forces, isolated group of atoms defining a bead was taken and its pair interaction energy with self was calculated for varying distance and orientation. The charges on the individual atoms were zeroed out so as to capture only the effect of the van-der-Waals interaction. The average energy obtained with different distance was fitted to a Morse potential to estimate the parameters.

**Equation 60**

$$E_{VDW} = D\left\{\left(e^{-0.5\alpha\left(\frac{r_{ij}}{r_0}-1\right)}\right)^2 - 2\left(e^{-0.5\alpha\left(\frac{r_{ij}}{r_0}-1\right)}\right)\right\}$$

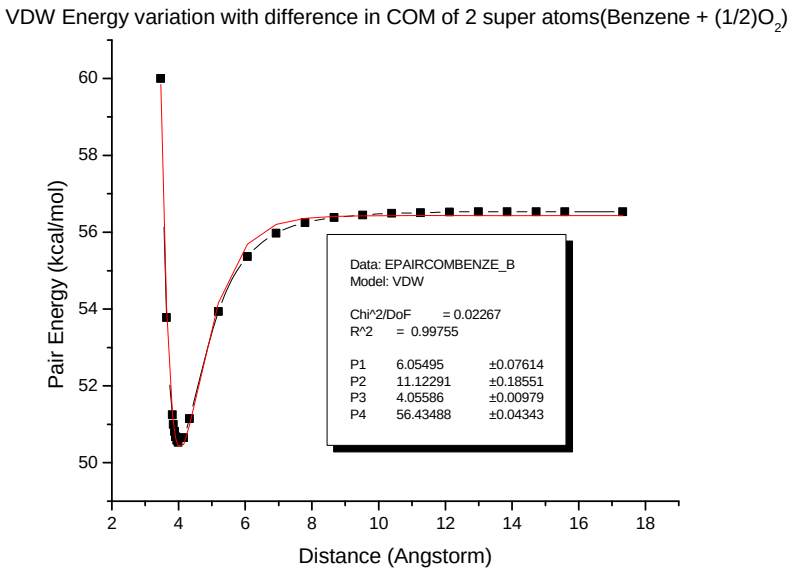


**Figure 95: VDW parameter estimation**

Figure 95 illustrates one such fitting of pair interaction energy in the process of estimation of van- der-Waals parameters. The parameters estimated were taken as initial set of parameters. We will show later that these parameters were further refined in order to meet atomistic density and stiffness of the system. The stiffness properties matched were calculated through molecular mechanics and no effect of temperature was considered.

*Coulombic:* The electrostatic interaction was estimated from monopole interaction. The summation of charges on each set of atoms defining a group was assigned to the bead. Accordingly the electrostatic energy of the system was described by:

**Equation 61**

$$E_{coul} = \sum_{i}^{N} \sum_{j=i}^{N} \frac{q_i q_j}{r}$$

PPPM (Particle-particle-particle-Mesh) method was used to incorporate the effect of long-range interactions. The cut off was set to 14 Angstrom.

*Parameter Refinement:* The parameters obtained in the method mentioned above were taken as an initial estimate of parameters for coarse-grained model. Amorphous system

of the coarse grained model was built using Cerius[2.0], Material Studio[174] and equilibrated by standard procedure[8,9] using CVFF force field in LAMMPS[126,127] with the initial estimate of parameters and primarily density and mechanical properties were compared with atomistic simulation results for further refinement of the parameters. A polymer consisting of 10 chains and 30 monomers per chain was subjected to NPT ensemble run at 300 K and 0 Atmosphere pressure for 2 ns and different properties obtained from coarse grained and atomistic model were compared for further refinement of the parameters. Only the van-der-Waals parameters were varied for updating the parameters as described below. The energy expression for van-der-Waals energy is given by:

**Equation 62**

$$E_{VDW} = D\left\{\left(e^{-0.5\alpha\left(\frac{r_{ij}}{r_0}-1\right)}\right)^2 - 2\left(e^{-0.5\alpha\left(\frac{r_{ij}}{r_0}-1\right)}\right)\right\}$$

where the parameters were adjusted based on criteria as follows:

$\alpha, r_0$ → Density

$D, \alpha, r_0$ → Hardness

A subset of parameters used in the iterative procedure for super-atom 1 and the corresponding system property comparison for atomistic and coarse-grained model are given in Table 29. Parameters for the other super atoms were scaled accordingly from their initial guess.

**Table 29: Parameter estimation for CG model**

| Iterations | D | $\alpha$ | $r_0$ | $\rho$ (gm/cc) | B (GPa) |
|---|---|---|---|---|---|
| Atomistic | NA | NA | NA | 1.28 | 11.87 |
| 1 | 3.89 | 2.3 | 4.82 | 1.27 | 8.08 |
| 2 | 4.345 | 2.3 | 4.82 | 1.28 | 12.20 |

**Table 29: Continued**

| | | | | | |
|---|---|---|---|---|---|
| 3 | 3.89 | 2.5 | 4.72 | 1.37 | 11.60 |
| 4 | 3.89 | 2.7 | 4.72 | 1.36 | 11.79 |
| 5 | 3.89 | 2.7 | 4.82 | 1.26 | 11.36 |

It is noted that the density is more sensitive to $r_0$ while D and $\alpha$ controls hardness of the system mostly. The parameters obtained from iteration number 5 was chosen as the final set of parameters for CG model as both the density and Bulk modulus were within reasonable agreement with the atomistic results. The coefficients for cross interactions were calculated as follows:

**Equation 63**

$$D_{0,ij} = \sqrt{D_{0,i} D_{0,j}}$$

**Equation 64**

$$r_{0,ij} = \sqrt{r_{0,i} r_{0,j}}$$

**Equation 65**

$$\alpha_{0,ij} = \frac{1}{2}\left(\alpha_{0,i} + \alpha_{0,j}\right)$$

4.2 Computational Experiments

The end hydrogen atoms of a polymer chain were absorbed in the super atom they were attached to. The parameters attached to those super atoms were not modified for two reasons. The addition of hydrogen to a super atom should not change the parameters significantly. Additionally super-atoms of such kind were low in numbers (two per polymer chain) with respect to the system considered.

4.2.1 Equilibrium Properties

Using the set of parameters obtained as explained in earlier section, amorphous model consisting of different number of chains and degree of polymerization were built using

Cerius$^{2.0}$ and Materials Studio. The systems were built with an initial low target density and were compressed, annealed and relaxed in NVT ensembles in cycles until it reached little over experimental density. The compressed sample was then relaxed in NPT ensemble to reach a final state.

The success of a coarse grained model depends on how well it can represent the atomistic level phenomena of the system of interest. We have shown the systematic method of estimation of parameters and refinement of the same to match the density and stiffness properties of the polymer sample. The model polymer sample to estimate these parameters used were 10_30 polymer. It was thought to be a decently sized polymer sample with not so expensive requirement in terms of computational resources for doing all the iterations involved in refining the parameters.

To establish confidence in our model it was important to compare other important polymer properties obtained from the CG model with that obtained from the MD model. It was also important to test the validity of the model for bigger systems. In the following sections we will first compare the properties of 1030 polyimide modeled in fully atomistic way with the coarsened representation of the same. Subsequently we have investigated the properties obtained for other coarsened polyimides using the parameters obtained based on 1030 polyimide simulation. Table 30 compares the final set of equilibrium properties for the 1030 polyimide described by CG models and atomistic simulation. We find reasonable agreement between the two models of the polymer sample. Each run was 2ns long of which 400 ps data were considered as equilibration part and the rest as production run.

**Table 30: MD vs. CG: equilibrium properties**

| Polymer | $\rho$ (gm/cc) | | $\sqrt{\left(\langle V^2\rangle - \langle V\rangle^2\right)}$ ($A^3$) | | D (Debye) | | $\varepsilon$ | |
|---|---|---|---|---|---|---|---|---|
| | MD | CG | MD | CG | MD | CG | MD | CG |
| 1030 | 1.28 | 1.26 | 414 | 312 | 1.52 | 1.13 | 3.3 | 1.81 |

The CG model also enabled us to use bigger integration time-step (10 fs as oppose to 1 fs for a fully atomistic model) without sacrificing anything in terms of properties evaluated. Figure 96 gives the frequency distribution of instantaneous volume in NPT ensemble for 500 ps at 300 K of a polymer system consisting of 10 chains and 30 degree of polymerization for each chain for the fully atomistic and coarse-grained model. We observe that the difference in the mean value of the volume is in the order of ~ 1% and the standard deviations for each of the curve are in reasonable agreement with each other.

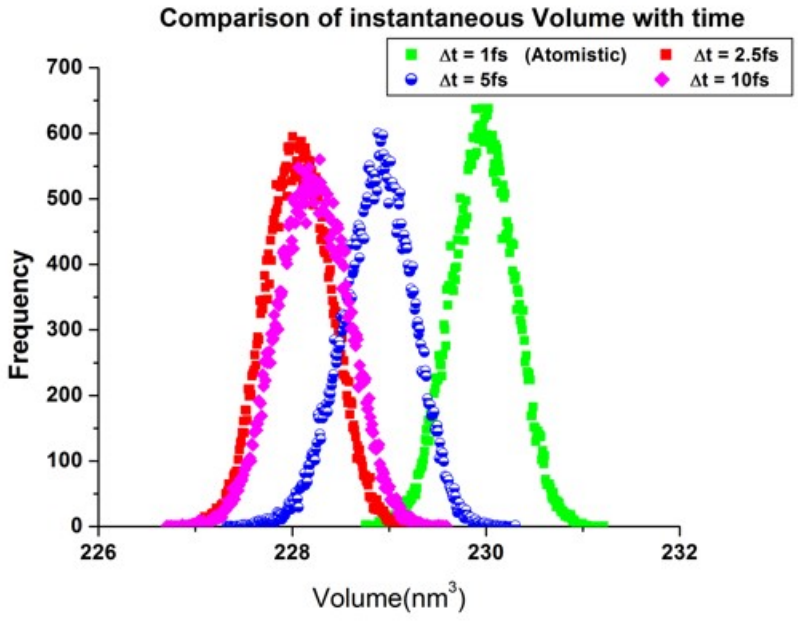


**Figure 96: Frequency distribution of instantaneous volume for 1030 polyimide**

### 4.2.2 Molecular Mechanics

Molecular mechanics was used to calculate the stiffness constants of the models. For finding the bulk modulus, the cell was stretched and compressed using hydrostatic pressure and the second derivative of energy with respect to volume was evaluated to estimate the bulk modulus. To find the shear modulus we have applied tetragonal strain[133] on the system. Due to the amorphous nature of the polymer, the axial elastic constant were calculated from the knowledge of bulk and shear modulus together with the implementation of isotropic condition. The strain in both directions was applied up to 6% in order to keep the polymer within the elastic region. Table 31 compares the values obtained from MD and CG model for 1030 polyimide.

**Table 31: Molecular mechanics results comparison for 10_30 polyimide**

| B | | $C_{11}$ | | $C_{22}$ | | $C_{33}$ | | $C_{44}$ | | $C_{55}$ | | $C_{66}$ | |
|---|---|---|---|---|---|---|---|---|---|---|---|---|---|
| MD | CG | MD | CG | MD | CG | MD | CG | MD | CG | MD | CG | MD | CG |
| 12.2 | 11.35 | 13.65 | 13.54 | 13.64 | 13.72 | 13.64 | 13.38 | 1.085 | 1.64 | 1.08 | 1.78 | 1.08 | 1.52 |

### 4.2.3 Pressure Annealing

We have applied hydrostatic pressure on the polymer sample in steps (as shown in the inset of Figure 97) and later took it off which resulted in a denser system different than the starting one due to the plastic property of the material. Figure 97 compares the result of atomistic and coarse-grained results of such study on a polymer sample (18620 atoms or 1500 beads). We observe that for both loading and unloading curve the atomistic and coarsened model pressure-density characteristic are reasonably matched, except for the fact that the coarsened model seems to be little softer than its corresponding atomistic model.

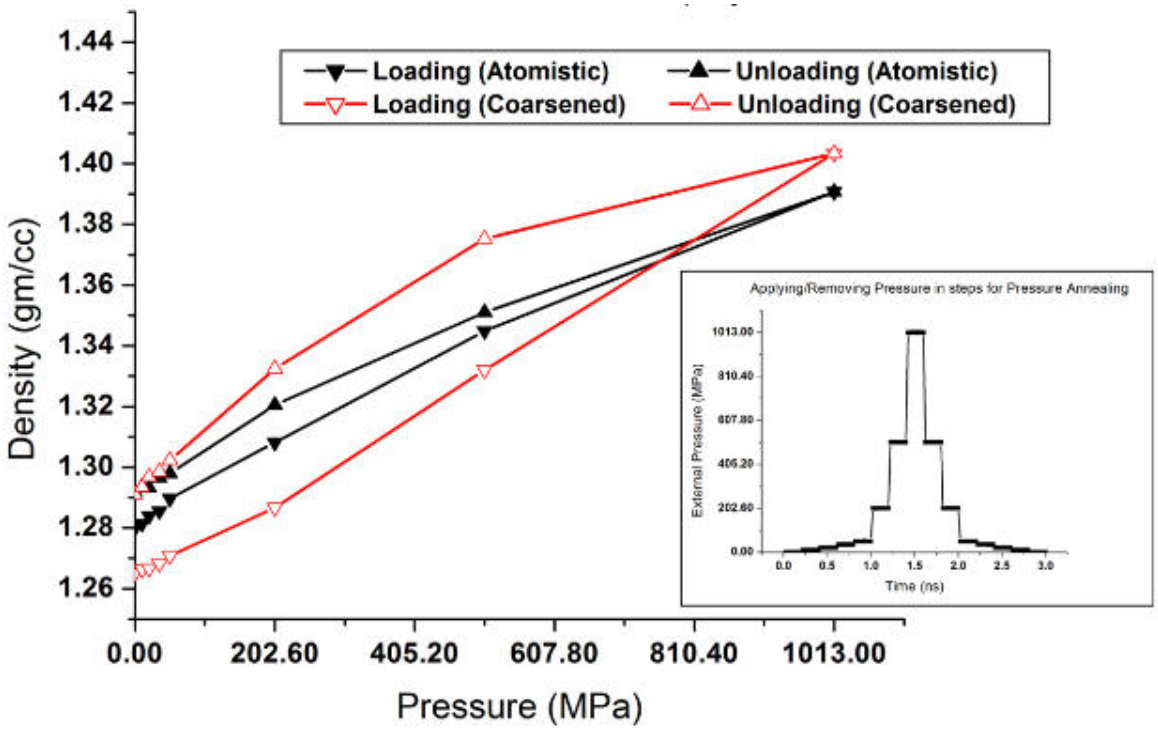


**Figure 97: Pressure annealing comparison: atomistic vs. coarse grain**

### 4.2.4 Chain Properties

Radius of gyration, end-to-end vector, order parameter and persistence length are some of the important parameters for understanding the chain configurations in a polymer system. These microscopic details or the combinations of these are believed to dictate several macroscopic properties of a polymer. We compared similar properties of our CG model to those estimated from our MD model. Table 32 shows a good agreement between average of end-to-end vector and radius of gyration of polymer chains of a 10_30 polyimide estimated via CG and MD simulation.

**Table 32: Chain properties comparison for CG and MD model of the polymer sample**

| | $\mu_{R_e}$ (A) | | $\sigma_{R_e}$ | | $\mu_{R_g}$ (A) | | $\sigma_{R_g}$ | |
|---|---|---|---|---|---|---|---|---|
| | MD | CG | MD | CG | MD | CG | MD | CG |
| 10_30 | 53.18 | 51.77 | 24.47 | 20.17 | 26.03 | 23.19 | 4.13 | 3.99 |

### 4.2.5 Forces on Individual Chains

Forces were calculated for individual chains and compared for both cases as shown in Figure 98. The overlap of the plots demonstrates that in both cases the total force on each of 10 chains fluctuates around the same value. The bigger fluctuation in the coarsened model is because of the softer nature of the same that we have already observed while comparing pressure-annealing response of the two models.

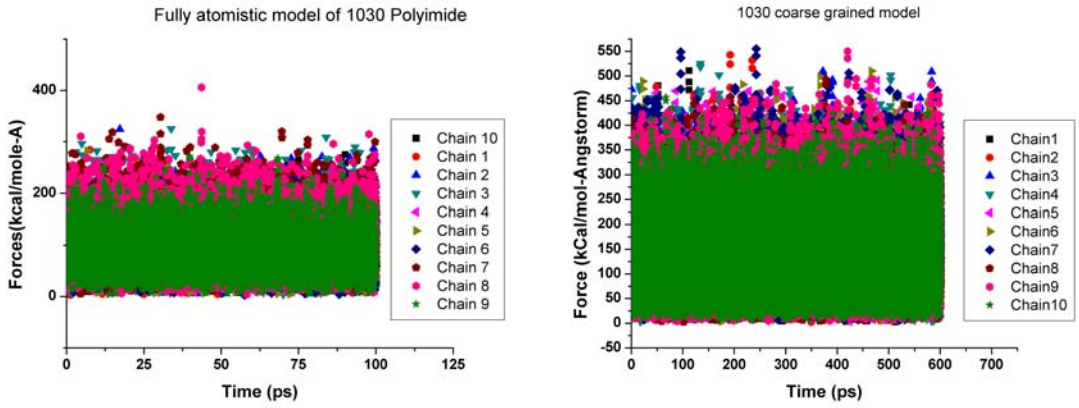


**Figure 98: Comparison of forces on individual chains**

## 4.3 Scaling Up

### 4.3.1 Bulk Properties

In building a coarse grain model, a good match of several bulk properties is a necessary condition as pointed before. A gain of 12 in system size prompted us to start computational experiment with 10_30 polymer sample. Any smaller system mapped

from atomistic sample would have resulted in less than 1000 super-atom system risking the reliability of the results. The smallest sample built hence contained 1500 super-atoms. Systems smaller than this were ruled out for the likely hood of introducing end effects. Polymer samples of 10_30, 20_30, 15_40, 30_40 and 40_40 were built through our coarse graining procedure and parameters. The number of chains and monomer per chain was kept identical to our atomistic simulation for fruitful comparison and analyzing atomistic data and coarse-grained data. In addition to the above mentioned polymer samples we have built 80_60 and 100_60 polymer samples to exploit the advantage offered by the developed coarse-grained method.

Similar to the atomistic model of the polymer sample we have estimated thermo-mechanical properties of the polymer sample from our coarse-grained simulations. The samples were built using similar procedure as used to build same polymer samples for atomistic simulations. Accordingly the samples were built amorphously with very low density in Cerius$^{2.0}$ and Materials Studio and were subjected to compression of the unit cells with application of temperature annealing in cycles. Finally an isothermal-isobaric simulation was carried out to attain the final equilibrated structure of the bead model. Details of the procedure can be found in the section dedicated to equilibration of polymer samples through atomistic simulation.

The average property values along with properties from fluctuation from our coarse grain simulation were calculated as shown in our work of atomistic simulation of $(\beta - CN)APB/ODPA$ polyimide. Table 33 presents bulk properties of our interest of systems equivalent from ~18000 atoms to ~ 372000 atoms.

**Table 33: Bulk property comparison for CG and MD model**

| Sample | Beads Atoms (k) | $\rho$ gm/cc | B GPa | E/ monomer kcal/mol | $C_p$ KJ/ Kg-K | Production ns | Equilibration ns |
|---|---|---|---|---|---|---|---|
| 10_30 | 1.5 (18.62) | 1.26 | 7.78 | -56.74 | 0.24 | 1.5 | 0.5 |
| 20_30 | 3 (37.24) | 1.25 | 3.2 | -56.47 | 1.3 | 0.5 | 0.5 |
| 15_40 | 3 (37.23) | 1.24 | 8.77 | -54.54 | 0.24 | 0.5 | 0.5 |
| 30_40 | 6 (74.460) | 1.26 | 5.82 | -54.8 | 0.66 | 0.5 | 0.5 |
| 40_40 | 8 (99.28) | 1.24 | 2.41 | -54.77 | 1.75 | 0.4 | 0.2 |
| 80_60 | 24 (297.76) | 1.28 | 4.09 | -60.1 | 0.23 | 0.6 | 0.4 |
| 100_60 | 30 (372.2) | 1.27 | 3.15 | -55.82 | 1.07 | 0.5 | 0.5 |

Comparing our results from coarse graining simulation with atomistic simulation of the same polymer samples we observe the following:

1. The average density calculated for various polymer samples before implementation of pressure annealing are in reasonable agreement with the atomistic simulation result of the polymer samples.
2. The volume fluctuation estimating the bulk modulus of the samples gave results in the same order as the atomistic results. However like atomistic simulation results we also found a range in bulk modulus values across samples.
3. The normalized energy values of the polymer samples in general did not vary much across samples unlike our atomistic simulation study where we found an

increase in energy with bigger system size. The absolute values cannot be compared as both simulations have different reference values.

4. The specific heat capacity estimated of the polymer samples was found to be an order of magnitude lower than our atomistic simulation. This is expected. We have found in Table 33 itself that the total energy of the samples is much lower in absolute terms than their atomistic counterpart. The absolute value of the fluctuation of a small number with respect to a large number makes the difference. We will explain the same mathematically by just considering the kinetic energy of the two methods. We know that:

**Equation 66**

$$\langle KE \rangle \alpha N$$

where:

KE = Kinetic Energy

N = Number of Atoms

Since the number of atoms (super-atoms) is different in two methods we can write for $k \approx 12$ :

**Equation 67**

$$\left(\left\langle KE_a^2 \right\rangle - \left\langle K\overline{E}_a \right\rangle^2\right) \alpha \left(\left\langle N_a^2 \right\rangle - \left\langle \overline{N}_a \right\rangle^2\right) = k^2 \left(\left\langle N_{cg}^2 \right\rangle - \left\langle \overline{N}_{cg} \right\rangle^2\right) \text{ As } N_a = kN_{cg}$$

$$\left(\left\langle KE_{cg}^2 \right\rangle - \left\langle K\overline{E}_{cg} \right\rangle^2\right) \alpha \left(\left\langle N_{cg}^2 \right\rangle - \left\langle \overline{N}_{cg} \right\rangle^2\right)$$

This implies that the fluctuation value of the kinetic energy of the atomistic model becomes higher by a factor of $k^2$ through implementation of coarsening technique. Staying with the argument, the order of magnitude difference in specific heat capacity estimated from fluctuation of total energy is inherent in the process of the coarsening the system. However since the volume of the polymer samples is comparable for both the models as it should be, any difference in the fluctuation of the same is due to the dynamics and not due to the loss of degrees of freedom of the system.

Similar to our atomistic simulation analysis we have estimated the normalized dipole moment and dielectric constant of the polymer samples by using the fluctuation of the dipole moment. Like pointed out before in atomistic simulation case, the Kirkwood-Frohlich (KF) method for estimation of dielectric constant is applicable here and hence in Table 34, dielectric constant values calculated from Clausius-Mossotti (CM) equation are not reported.

**Table 34: Comparison of dielectric properties for CG and MD model of polymer**

| Polyimide | Dipole Moment/Monomer (Debye) | | | | Equilibration Run (ns) | Production Run (ns) | Dielectric constant (KF) Method |
|---|---|---|---|---|---|---|---|
| | $\mu_x$ | $\mu_y$ | $\mu_z$ | $\mu$ | | | |
| 10_30 | 0.41 | -0.16 | -1.03 | 1.13 | 0.5 | 1.5 | 1.81 |
| 20_30 | 0.78 | 0.49 | -0.42 | 1.01 | 0.5 | 0.5 | 4.78 |
| 15_40 | 0.46 | 0.89 | -0.47 | 1.10 | 0.2 | 0.4 | 2.32 |
| 30_40 | 0.08 | -0.21 | -0.02 | 0.23 | 0.5 | 0.5 | 2.28 |
| 40_40 | 0.03 | -0.03 | -0.34 | 0.35 | 0.2 | 0.4 | 3.98 |
| 80_60 | -0.19 | -0.02 | -0.2 | 0.28 | 0.4 | 0.6 | 2.45 |
| 100_60 | -0.08 | -0.09 | 0.09 | 0.16 | 0.5 | 0.5 | 3.49 |

Analyzing Table 34 we find the following:

1. There is a reduction of polarization value with bigger system size. This is expected. Generation of higher degree of randomness in the chain orientation with bigger system size leads to such observation. Similar trend was also observed in our work of the atomistic simulation of the same polymer. Ideally for an amorphous polymer the polarization value should go to zero by virtue of being amorphous. The non-zero value of the same hints at the requirement of bigger system or larger time length simulation of the polymer sample to have better statistics.
2. The dielectric constant values are comparable to those obtained from atomistic simulation. The average value estimated in both models is ~ 3.0, although the

MD model shows larger variations. This is a significant outcome backing our coarsened model for dielectric properties. The simple formula for calculating dipole moment allows us to make a comment on atom position dynamics based on this observation. It is natural to expect that the absolute fluctuation of dipole moment is more in case of atomistic simulation than in a coarsened model. This argument naturally leads to an underestimated value of the dielectric constant for the coarsened model. Only in case of atoms moving in phase with each other will the result be in such agreement as observed in this study. This outcome solidifies the foundation of the coarsened model we have developed in this work. Unlike in the case of specific heat calculation, the inherent nature of coarsening did not affect the dielectric properties due to lumping of atoms into super atom.

### 4.3.2 Molecular Mechanics

Molecular mechanics method was implemented on the coarsened samples of different size and the outcomes of estimated elastic constants were compared with its atomistic counterpart. Table 35 illustrates the comparison between the two models of the polymer samples. As observed we find reasonable agreement in estimated elastic constants. The properties estimated for 80_60 and 100_60 polyimide through our CG model did not have it atomistic counterpart due it's requirement of expensive calculation of building the models through classical MD.

**Table 35: Molecular mechanics calculation**

| Polymer | B | | $C_{11}$ | | $C_{22}$ | | $C_{33}$ | | $C_{44}$ | | $C_{55}$ | | $C_{66}$ | |
|---|---|---|---|---|---|---|---|---|---|---|---|---|---|---|
| | MD | CG | MD | CG | MD | CG | MD | CG | MD | CG | MD | CG | MD | CG |
| 2030 | 12.04 | 10.38 | 13.54 | 12.19 | 13.38 | 12.19 | 13.53 | 12.27 | 2.25 | 2.72 | 2.01 | 2.72 | 2.24 | 2.83 |
| 1540 | 10.73 | 9.00 | 12.32 | 10.95 | 12.24 | 10.99 | 12.27 | 10.97 | 2.39 | 2.92 | 2.26 | 2.98 | 2.31 | 2.95 |
| 3040 | 9.79 | 10.85 | 11.20 | 12.80 | 11.04 | 12.89 | 11.19 | 12.90 | 2.12 | 2.93 | 1.88 | 3.06 | 2.10 | 3.08 |
| 4040 | 11.99 | 10.82 | 13.32 | 12.67 | 13.38 | 12.57 | 13.22 | 12.69 | 1.99 | 2.78 | 2.08 | 2.63 | 1.84 | 2.81 |
| 8060 | ? | 12.50 | ? | 14.72 | ? | 14.81 | ? | 14.82 | ? | 3.33 | ? | 3.46 | ? | 3.48 |

### 4.3.3 Chain Properties

Chain dynamics plays a major role in polymer physics. Although our coarsened model of the piezoelectric polymer could describe polymer bulk properties reasonably well, it was also important to inspect polymer properties at the chain level to understand the pros and cons of our model with physical explanation. End-to-end vector, radius of gyration and contour length of the polymer samples as estimated through the CG model simulation has been looked upon in this section.

**Table 36: Chain property comparison**

| | $\mu_{R_e}$ (A) | | $\sigma_{R_e}$ | | $\mu_{R_g}$ (A) | | $\sigma_{R_g}$ | |
|---|---|---|---|---|---|---|---|---|
| | MD | CG | MD | CG | MD | CG | MD | CG |
| 10_30 | 53.18 | 51.77 | 24.47 | 20.17 | 26.03 | 23.19 | 4.13 | 3.99 |
| 20_30 | 49.29 | 58.14 | 22.36 | 27.23 | 22.68 | 31.7 | 3.93 | 11.67 |
| 15_40 | 46.28 | 81.63 | 15.86 | 32.6 | 24.67 | 43.29 | 4.38 | 12.3 |
| 30_40 | 52.15 | 83.95 | 22.94 | 39.83 | 24.98 | 41.47 | 4.46 | 14.63 |
| 40_40 | 55.39 | 83.35 | 18.41 | 46.29 | 26.28 | 40.57 | 4.33 | 17.06 |
| 80_60 | ? | 62.69 | ? | 25.08 | ? | 30.82 | ? | 5.73 |
| 100_60 | ? | 134.84 | ? | 57.78 | ? | 60.05 | ? | 22.70 |

Table 36 illustrates the comparison of end-to-end vector and radius of gyration of the polymer samples as estimated from classical molecular dynamics simulation and coarse-grained model. It also compares the variance of both the properties as obtained from dynamics for a specified period (400 ps) of time. Close inspection of Table 36 shows:

1. The chain properties were to be found in excellent agreement for the model polymer considered in building the CG model from atomistic simulation data. The comparison is also reasonable for the 20_30 polymer case.
2. Continuing from #1 observation, as we move to bigger chain size we find an explicit difference in the chain morphology of the polymer sample. The samples

described by the CG model appear to be more scattered and stretched with respect to their atomistic counterpart. However we also find the there is a contradicting trend in the behavior of the same property of 80_60 and 100_60 polymer. While 80_60 polymer shows the presence of confined polymer chains estimating low values of end-to-end and radius of gyration values, 100_60 polymer values shows otherwise. The lack of atomistic data for those sample sizes does not allow us to draw any firm conclusion about the source of this observation.

3. In all cases however the relation between $R_e$ and $R_g$ is maintained in a way close to as predicted by freely jointed model.

## 4.4 Application of Step Stress

### 4.4.1 Step Stress Test

Axial tensile stress was applied in z direction of the polyimide and the response was noted. The temperature maintained by Nose-Hoover thermostat was 300 K. The initial response of the polyimide in the both the models was elastic, however as expected, as the stress level increased we observed the onset of viscous flow in the polyimide.

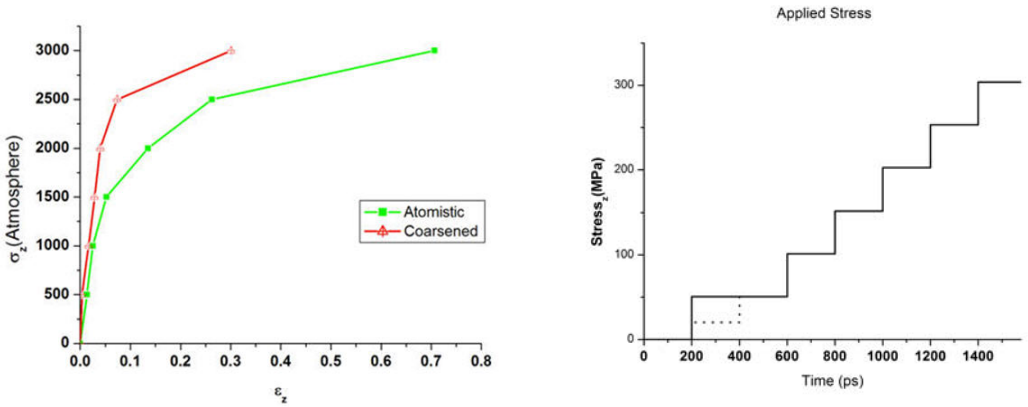


**Figure 99: Response to creep test at multiple stress levels**

Figure 99 and Figure 100 shows that in response to creep test the coarsened model shows little more resistance to stretching resulting in a higher yield strength, however the elastic modulus are very much the same for stress levels almost up-to 1500 atmospheres or roughly 150 MPa. Although stresses were applied up-to 500 MPa, the curve does not incorporate all of those as the characteristics we are interested in are already being captured in a smaller window.

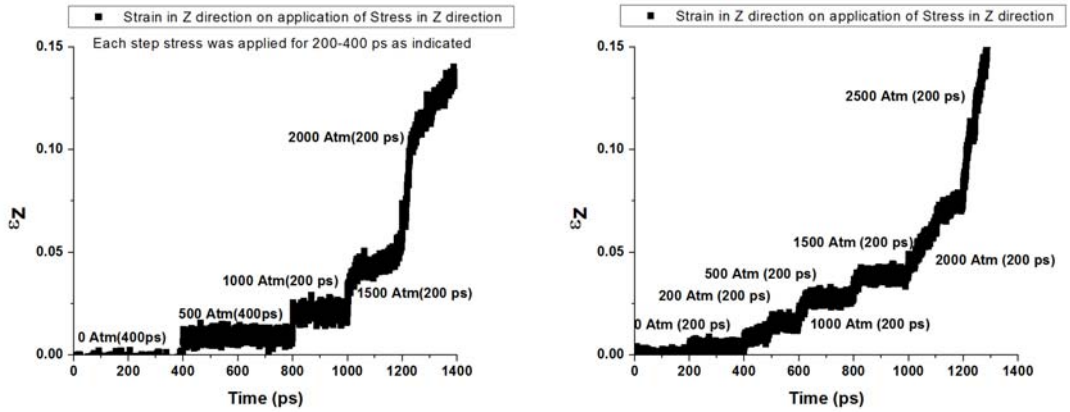


**Figure 100: Instantaneous strain nature comparison**

The only difference in the applied stress profile was that the applied stress of 500 atmospheres was applied for 400 ps for the atomistic case as oppose to the coarsened model where it was subjected to 200 atmospheres for 200 ps and to 500 atmospheres for the rest 200 ps. This however cannot be possibly attributed to the differences in responses. We observe similar trends in instantaneous strains of the two models representing 1030 polyimide. For small stresses almost up-to 100 MPa, there was no inkling of viscous flow that afterwards sets in and the strain rate instead of the strain itself becomes constant at higher applied stresses. It is the very value of stress from where as observed in Figure 99, the identical curves for two model starts deviating from each other indicating a different viscous response.

The response of the polymer sample within the elastic region gave us the estimate of the Young modulus of the sample. Figure 101 represents the response of

polymer samples of different sizes under applied stress. The average value of Young modulus of the polymer samples was estimated to be 5.1 GPa at 300 K and zero atmosphere pressure.

The value of Young modulus estimated for the coarsened model is slightly higher than estimated by atomistic simulation. The observation is in similar lines with Figure 99. It can be argued that in response to the applied stress, due to the absence of rotational degrees of freedom the super-atoms might opt for a higher energetic conformation than its atomistic counterpart. This continues to happen till enough space is available for translational and vibrational movement to be the dominant mode. Once the polymer reaches the plastic region, the coarse-grained model starts flowing faster than its atomistic counterpart. The absence of rotational degrees of freedom forces the chains to flow more than its atomistic counterpart.

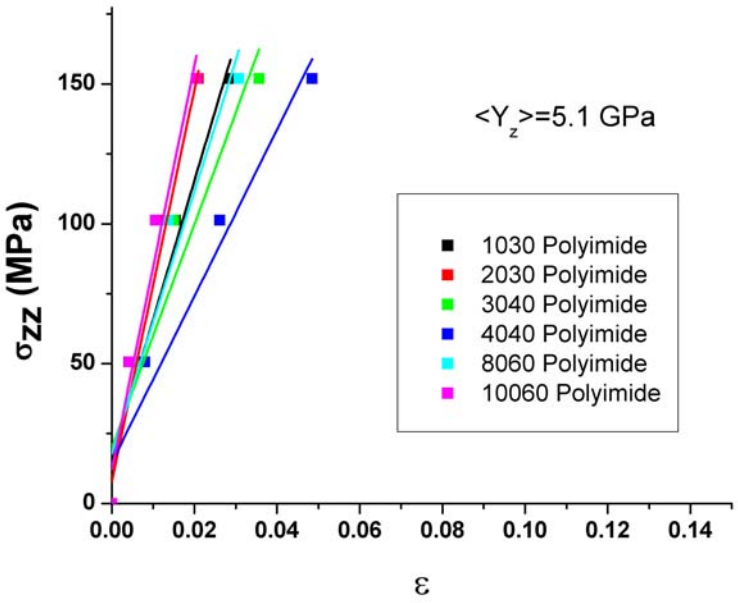


**Figure 101: Estimation of young modulus of polymer samples (CG models)**

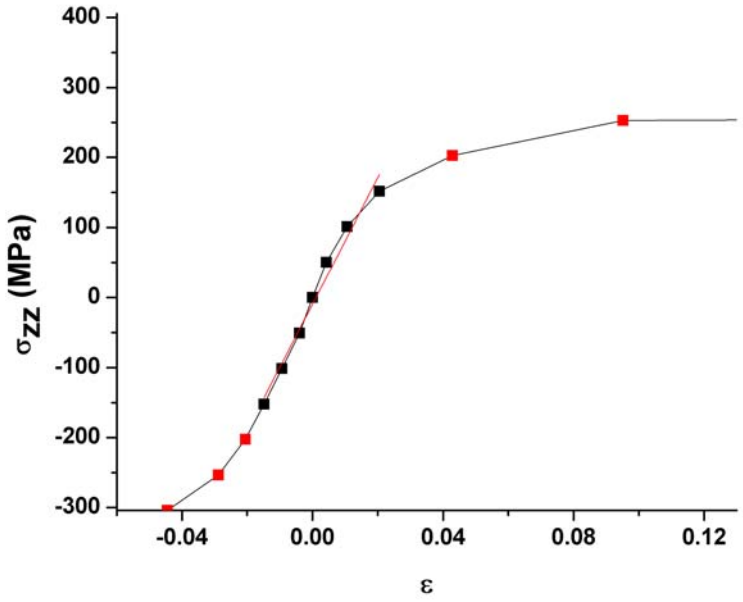


**Figure 102: Average response of coarsened polymer upon application of stress**

We have also applied stress of compressive nature to the polymer sample. Figure 102 illustrates the response of 100_60 polyimide from compressive 3000 atmospheres to tensile 3000 atmospheres in steps of 500 atmospheres with 200 ps relaxation time given at each stress level. Figure 103 compares the response of the polymer samples in terms of instantaneous axial strain the above mentioned cases. The stiffer compressive modulus of the polymer samples is explicit from the figure. The initiation of flow in the polymer happens much before in the tensile case than its compressive counterpart. It is expected and in similar lines to the observations made in case in our classical molecular dynamics study. However, the compressive axial modulus was also found to be much stiffer than its atomistic counterpart. This goes back to the argument presented before on the stiffer nature of the CG model in the initial period of the elastic zone. Since on compression the polymer chains find it difficult to find its way out the strain obtained is much lesser.

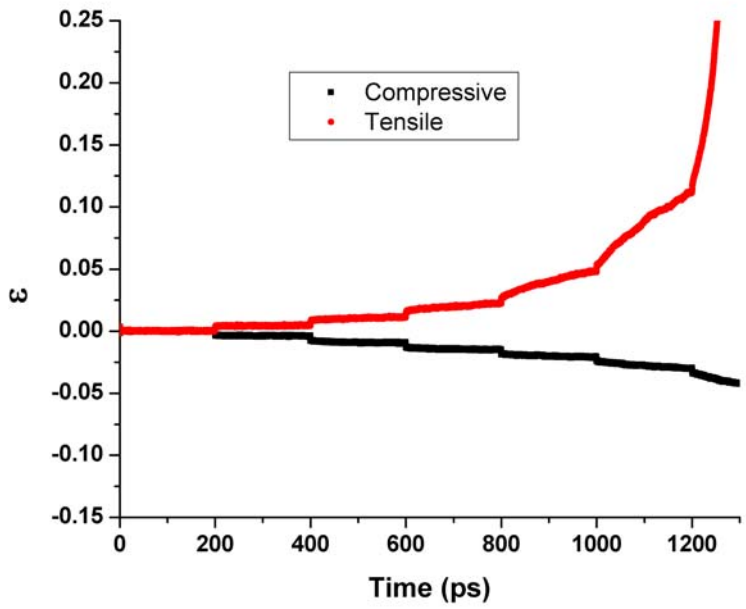


**Figure 103: Instantaneous strain response observed for CG model**

4.4.2 Work Hardening

Increase of dislocation density results in work hardening of a material. We have earlier observed this phenomenon in our atomistic simulation of the polymer sample. The coarsened model of the polymer system namely 100_60 polyimide was subjected to tensile stress up to 2500 atmospheres in steps of 500 atmospheres per 200 ps, as described in our creep test experiment. The stretched sample was then allowed to relax under zero atmosphere pressure. A creep test performed on such a sample showed work hardening of the sample. Figure 104 clearly illustrates the effect of such hardening. We observe identical responses within the elastic region of the polymer sample. Once the sample is out of that zone the stretched polymer sample shows more resistance to the applied stress than the initially built equilibrated sample.

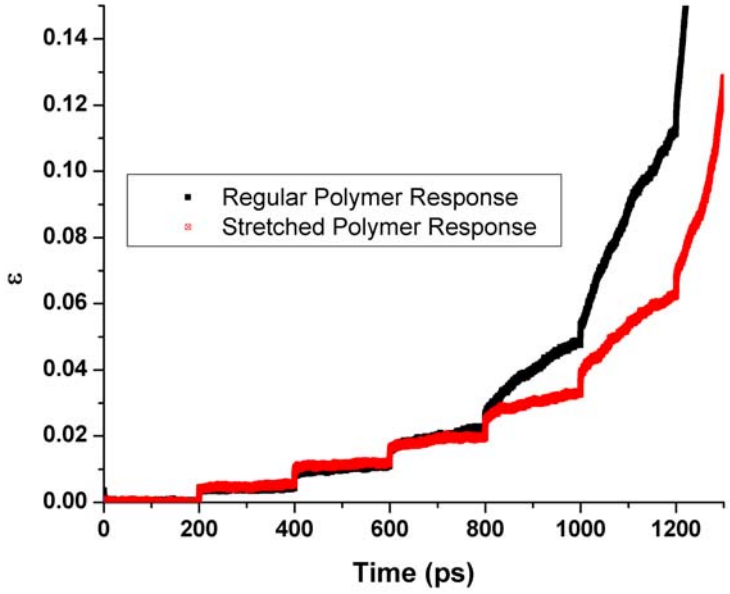


**Figure 104: Work hardening observed in CG model of polymer**

The agreement between the work hardening responses of the polymer samples of MD and CG model also our CG model more valuable and reliable.

4.5 End-to-end Vector and Dipole Moment

The near linear relationship between end-to-end vector and dipole moment of a chain specific to our polymer system was pointed out earlier in our atomistic simulation work. Identical argument led us to plot the three components of dipole moments and end-to-end vector of a coarsened model of a 20_30 polyimide. We have earlier observed that the coarsened model is more prone to fluctuation. Figure 105, 106 and 107 goes well with the argument and the observation with the atomistic simulation case. However the obtained fit was better in the atomistic case (<R-square> ~ 0.9) than the coarsened case (<R-square> ~ 0.7). The relative scatter can be attributed to the ease of movement of rings as super atoms as oppose to the atomistic model of the rings where energies are also spent in rotational movements.

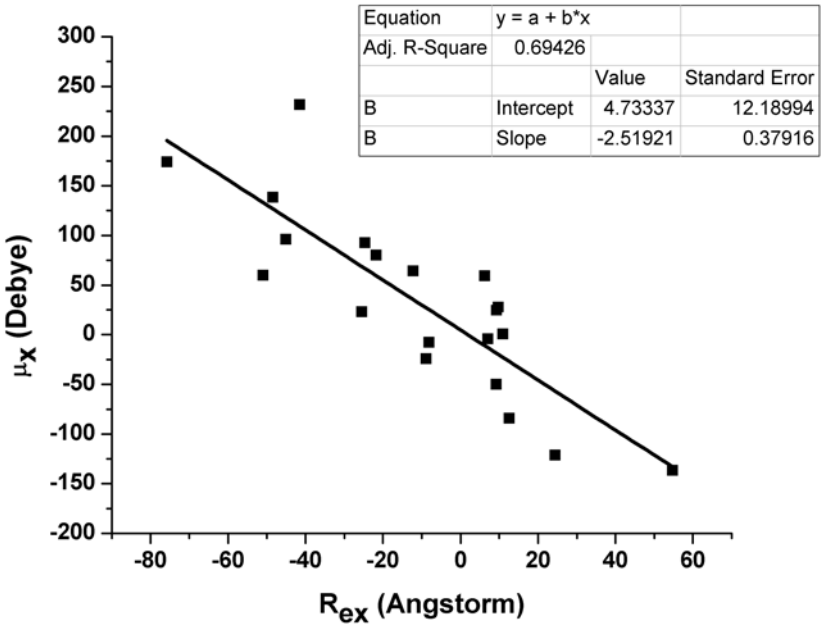


**Figure 105: x direction component relation for end-to-end vector with dipole moment for CG model**

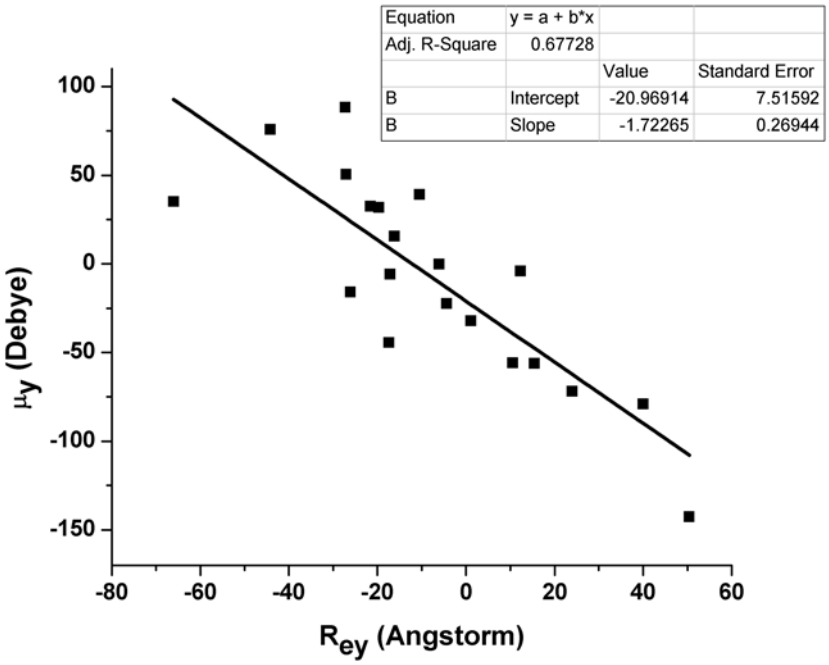


**Figure 106: 'y' direction component relation for end-to-end vector with dipole moment for CG model**

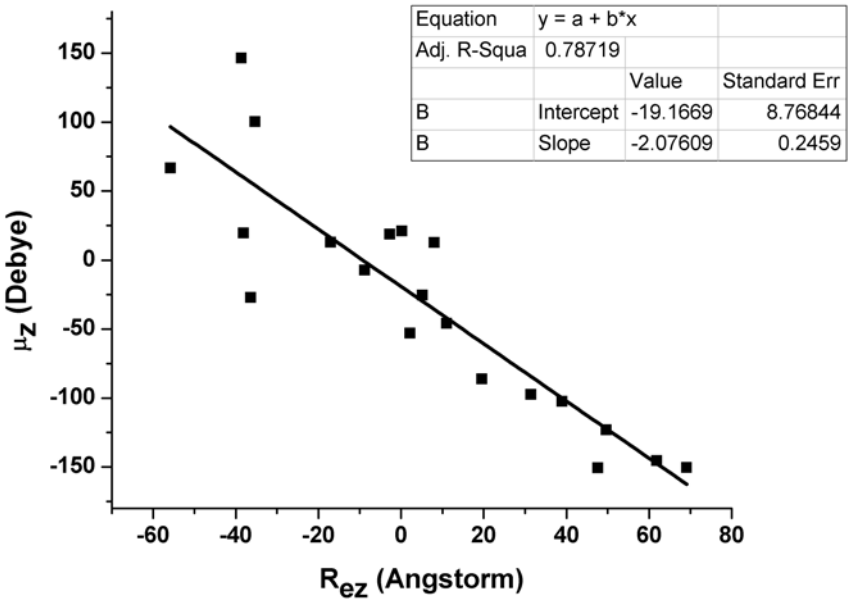


**Figure 107: z direction component relation for end-to-end vector with dipole moment for CG model**

## 4.6 Thermal Properties

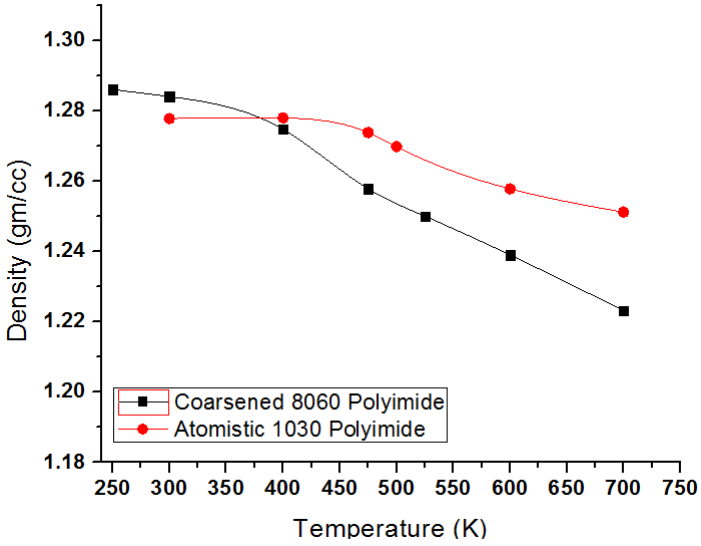


**Figure 108: Temperature dependence of density**

Estimation of thermal properties of the polymer samples described by our CG model was important. This tells us about the domain of our CG model where it is valid. We have earlier shown our study on the polymer thermal properties through classical molecular dynamics simulation. Thus the study performed at the atomistic level helped us to evaluate our model and find possible root causes for discrepancy if any.

Different samples of the polyimide were subjected to thermal expansion up-to 700 K with increment of 100K starting from 300K. Like atomistic case, system consisting of lower number of atoms/super-atoms did not show any indication of change in thermal expansion behavior around the experimental glass transition temperature 496 K[35]. Hence Figure 108 compares thermal expansion behavior of 1030 polyimide in fully atomistic model (18620 atoms) and 8060 polyimide described by coarsened model (24000 super-atoms equivalent to 297600 atoms). We observe that the coarsened model shows little early glass transition like behavior and higher expansion coefficient relative to the fully atomistic model. A typical volumetric thermal expansion coefficient estimated through the CG model for this polymer is in the order of $10^{-4}$ ~$10^{-5}$ /K which goes well with the observation in figure 108 for both cases, for temperatures below glass transition.

## 4.7 Resources Comparison

We observe in Table 37 and its corresponding figure (Figure 109) that the CG model developed shows gain in the order of hundreds in terms of CPU time usage while maintaining reasonable match in property evaluation as shown in previous sections.

**Table 37: CPU time comparison**

| Processors | Time (sec) Atomistic | Time (sec) Coarsened |
|---|---|---|
| 2 | 41943 | 99 |
| 4 | 20804 | 83 |
| 6 | ---- | 66 |

**Table37: Continued**

| | | |
|---|---|---|
| 8 | 10655 | 62 |

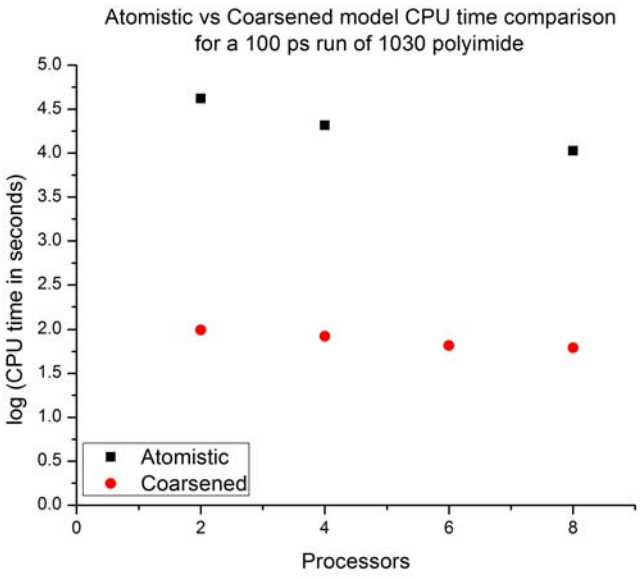


**Figure 109: CPU time comparison in semi log scale**

The apparent reduction in gain for higher number of processors is due to the higher percentage contribution of communication time between processors as oppose to the calculation of the model itself. The disk space saved for saving trajectories is just proportional to the factor by which the number of atoms in the fully atomistic system is reduced to the CG model.

## 4.8 Larger System and Longer Timescale

The systematic coarse graining of our polymer system was done keeping in mind its utility for bigger system and longer timescale simulation. Accordingly a 45 ns simulation was carried out on the 100_60 polymer sample in 300 K temperature and zero atmosphere pressure. Figure 110 and 111 illustrates the instantaneous volume and total energy of the system over this time period. To reduce the number of data points for the purpose of plotting, block average of properties with width of 10 ps was done and

plotted against time. The simulation was carried out on an already equilibrated system of the 100_60 polymer sample.

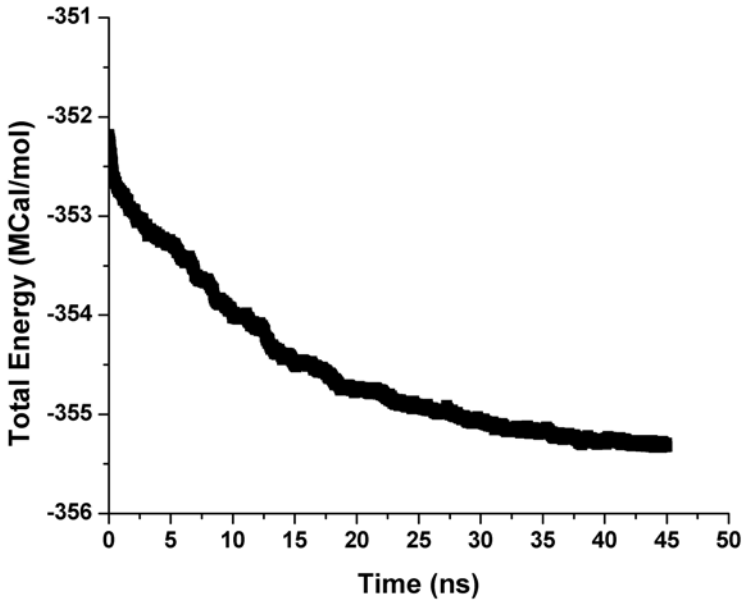


**Figure 110: Instantaneous total energy of 100_60 polymer sample at normal condition**

From figure 110 and 111 we observe that:

1. Even though the polymer sample taken was in equilibrated state, over a period of 45 ns there was a decrease in energy in the order of ~ 1%. This hints at the existence of a driving force to push the system to a favorable structure. The steady decrease in total energy of the sample is not evident within a span of 2 ns, the window that in our work has been used to determine the equilibrated nature of the given sample. Even though the decrease might look like negligible in molecular dynamics scale, in realistic timescale a change in energy in this rate would be sufficient to transit to another structure in the order of microseconds.
2. We observe similar to figure 108 that there is a continuous change in volume making the system less dense. Both the figure indicates that even though the

truncated study on 2 ns window suggest a equilibrated system, changes are still on with the polymer getting relaxed through expansion and reducing the total energy.

3. The observation in this study suggests the slow conformational change of polymer chains in typical MD timescale and backs up the cause for using coarse grain model for the purpose of equilibration of large polymer samples.

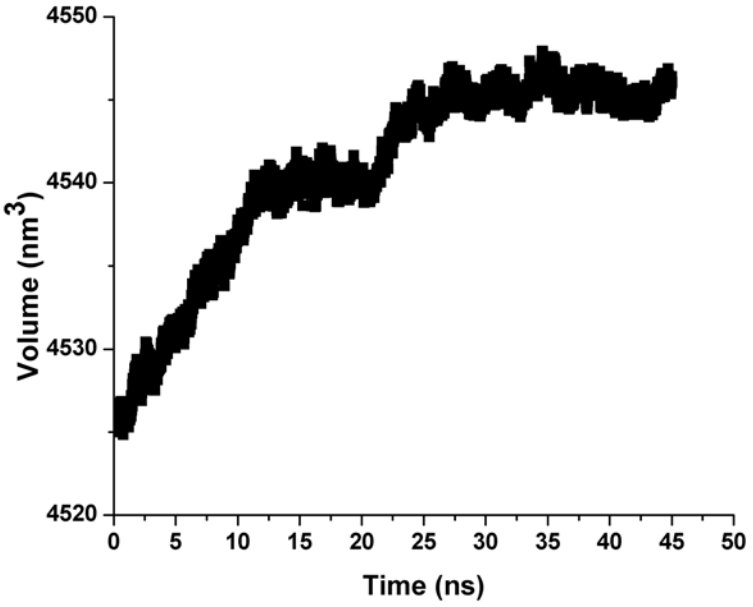


**Figure 111: Instantaneous volume of 100_60 polymer sample at normal condition**

## 4.9 Conclusions

We have showed that the methodology used in generating the coarse-grained model produced data agreeing reasonably with that of the atomistic simulation results. We have compared equilibrium properties, chain properties, mechanical, dielectric and thermal properties.

The coarse grained model shows a stiffer response in the elastic region due to the absence of its rotational degrees of freedom in the model. For similar reason it starts flowing faster than its counterpart once it is forced to enter the plastic zone. We could also show the work hardening behavior of the polymer samples with our CG model.

Dielectric constants estimated were found to be in the same order as obtained from the atomistic simulation. This also establishes the coarsening policy taken for this particular polymer. The chains were also able to show a near linear relationship between their end-to-end vector and dipole moment of each chain.

Inspection of thermal properties shows an early glass transition behavior of the polymer sample for similar reason. Since no energy is expended in rotation of the rings in the CG model, the thermal vibration could set the glass transition earlier than its atomistic counterpart.

To exploit the advantage gained by our CG model we have built a CG model equivalent to ~ 372,000 atoms and have run isothermal-isobaric ensemble for 45 ns. We have observed very slow decay of the total energy in the system. The pattern is not obvious within a window of few nanoseconds.

We obtained a the two orders of magnitude gain in terms of computational time required and an order of magnitude gain in system size through implementation of our coarse grain model. It must also be mentioned that there is an order of magnitude gain in terms of disk space utilization in saving trajectories due to the gain in system size.

In conclusion we have developed a coarsened model of a piezoelectric polyimide that could successfully describe the bulk properties and chain properties of the system. It can also reproduce the viscoelastic response of the sample under huge stress. It has also succeeded in estimating the thermal, mechanical and dielectric properties barring the effect of rotational degrees of freedom. Incorporation of the same through implementation of rigid body dynamics is expected to better the present model. The substantial gain in terms of CPU time and the opportunity to extend the system sizes is encouraging. It is thus possible to reliably access domain not accessible to Molecular dynamics by coarsening a system in the way described in this article.

# 5. NANOCOMPOSITE

## 5.1 Introduction

Polymer nanocomposites refer to a broad range of composite materials with one of the components being polymer acting as the matrix and the other being any material which has at least one dimension in the order of 1 ~ 100 nanometer. Due to unprecedented improvement observed in properties of nanocomposites, research interest in this area has grown exponentially in recent years. The possibility of engineering these materials at the atomistic level targeted towards different advanced applications has made them lucrative to researchers and industry[1,27,49,50]. However due to the lack of detailed understanding of the physics of these materials, finer control of properties at nanoscale has yet not been achieved. As a consequence, development of these materials is still largely empirical. Hence, the available room for improvement in designing these materials along with the demonstrated potential shown by them has identified the importance to understand the structure property relationship of nanocomposites at utmost detail. Thus modeling and simulation has stepped into for better understanding of their behavior at atomistic level to explain and justify the different and fascinating structure property relationship observed.

Of several attractive and complex polymer properties, piezoelectricity of a polymer can be regarded as one of the few observed but valuable property. Naturally the controlled combination of electromechanical property of a polymer with rather well known superior set of carbon nanotube properties is an interesting and useful problem to look at. Only a rational understanding of the interaction of these properties will enable us to design future generation materials in a most efficient and effective way.

In here we have looked into nanocomposites with different filler weight percentage and analyzed its behavior from its response in various experiment. We have also used well-known micromechanics theories for composites and compared those models through our atomistic simulation results.

### 5.1.1 System

In our work we have looked into nanocomposites made from carbon nanotube and an amorphous piezoelectric polymer substituted with nitrile dipole. The polymer termed as $(\beta - CN)APB/ODPA$ polyimide is stiff in nature owing to its rod like structure. The nanotube used as filler in this work is an armchair (10, 10) nanotube. For our study purpose, we have used a unidirectional infinite tube. Accordingly this study serves as a limiting case of dispersion of nanotube in polymer nanocomposite. Furthermore no chemical bonding was considered between the nanotube and the polymer chains. Hence in our study, the only way the nanotube interacts with its neighboring polymer chains is through non-bonded interaction which refers to the combination of van der Waals and columbic interaction. Limited by time and length scale owing to inherent nature of classical molecular dynamics simulation, for reliable conclusion and better statistics we have built eight different nanocomposite samples. Needless to mention more samples would have established higher confidence in the results obtained from our computational experiments sacrificing efficiency in terms of computational resources.

### 5.1.2 Force Field

In order to have reliable outcomes from our classical molecular dynamics simulation runs it was important to describe the components of the Hamiltonian for the heterogeneous system correctly. As an example carbon atoms as part of a polymer chain and carbon atoms in the nanotube interact with their neighboring atoms very differently. Therefore it was necessary to use hybrid potentials for estimating the energy components of the composite system. This ensured a proper way of representation of atom interactions depending upon the system. Likewise harmonic functions were used to describe the polymer angle-bending energy, cosine-squared functions were used to quantify angle-bending energy in carbon nanotube. Though similar differences existed in torsional potential, the torsional energy expression for nanotube was approximated and a single type of function was used. Other than the functions itself the parameters used for carbon-carbon interactions were also very different for nanotube and polyimide. The

nanotube potentials were described by [99]. The polyimide energetic was depicted by CVFF force field. We carried out computational experiment on eight different polymer nanocomposite samples using the above mentioned hybrid force field.

### 5.1.3 Model Building

The nanotubes considered, as mentioned before, were infinite in length. The tubes were bonded across periodic boundaries of the unit cell to account for the same. The approach implemented to build the nanocomposite was the modified version of building amorphous polymer samples[8]. Accordingly a polymer sample with a very low density was built with Cerius$^{2.0}$ or Materials Studio to initiate the process. Unlike in the polymer sample building case, the requirement of building low-density polymer samples at the initial stage served two purposes. Other than help attaining a favorable structure of the polymer sample as its final equilibrated structure through steps, it was also important to have enough space in between polymer chains to conveniently place the nanotube along the desired axial direction.

During the process of equilibration the nanotube was treated as a rigid rod and energies resulting from bond stretching and angle bending were not considered. This was beneficial in terms of computational resources. Additionally this helped to preserve the rod like structure of nanotube as oppose to risking allowing the individual atoms to explore the available abundant space around it at low density structure and resulting in a distorted tube for no physical reason. Once the structure was allowed to relax in isothermal isobaric ensemble similar to pristine polymer building methodology, the rigid rod restriction was removed from nanotube and individual atom dynamics were taken into account. The infinite nature of the nanotube structure with periodic boundary conditions led us to put the nanotube in parallel to one of the axis direction. The approach of compressing the unit cell length in all three directions for polymer samples was modified by barring compression in the nanotube axial direction. This otherwise would have led to distortion of the already equilibrated structure of nanotube. The idea was to drive the polymer chains towards equilibrated structure without disturbing the nanotube structure. Hence all the techniques used in building amorphous polymer

samples were modified in order to selectively apply those only on polymer samples. As the sample became denser and the chains started surrounding the nanotube, the charges at the interface were updated through implementation of charge equilibration technique[120].

The presence of an infinite nanotube in the sample posed other restrictions on the equilibration procedure. Unlike in the polymer sample simulation case, no pressure annealing techniques through application of hydrostatic compressive pressure were used in here. The method ran the risk of deforming the nanotube for its negligible mobility. For identical reason the nanocomposite samples were not compressed to significantly higher density than their estimated experimental densities unlike the polymer sample equilibration methodology. However the initial low built sample went through the same set of temperature annealing within each compression cycle and was followed by isothermal-isobaric (NPT) molecular dynamics simulation to reach to a final equilibrated state. Figure 112 illustrates a sample nanocomposite as viewed in molecular dynamics simulation environment. It must be noted that the perfect circular shape of the nanotube is not expected at the interface as the polymer chains will try to bend it due to its interaction with the same.

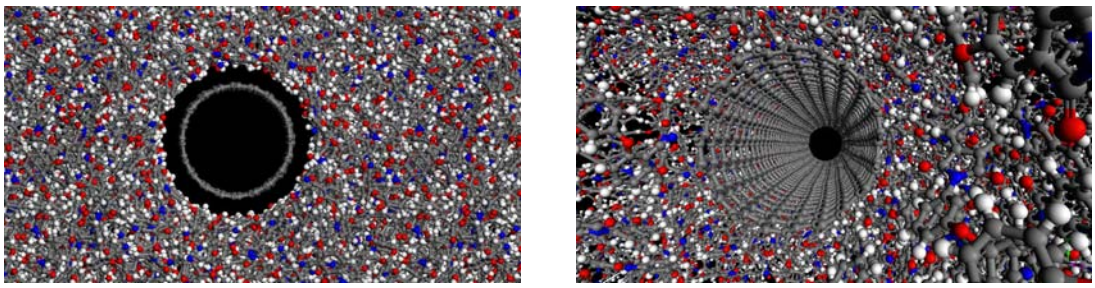

**Figure 112: Nanocomposite in a simulation window**

### 5.1.4 Equilibration

In this work the nanotube weight percentage in the nanocomposite varied from 18.7 % to 2.18 %. As an initial step we built nanocomposite samples made from 6_6 polyimide to

40_40 polyimide as described in section 5.13. Subsequently we relaxed the compressed system in an isothermal-isobaric ensemble. Similar to our observation while investigating properties of pristine polymer, we observe as illustrated in Figure 113 the property values stabilized around a constant value indicating equilibration of the sample. Likewise we find an equilibration run of ~ 20 ps makes the sample good for the production phase.

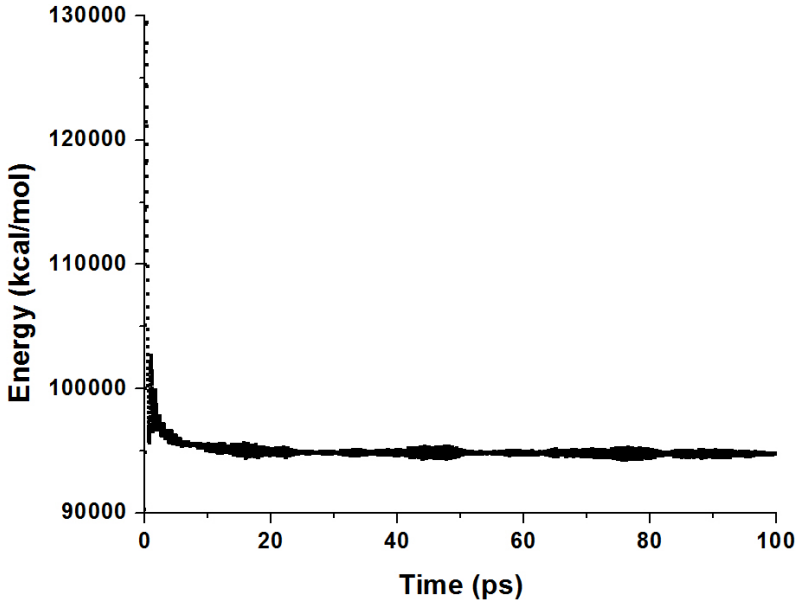


**Figure 113: Equilibration of nanocomposite**

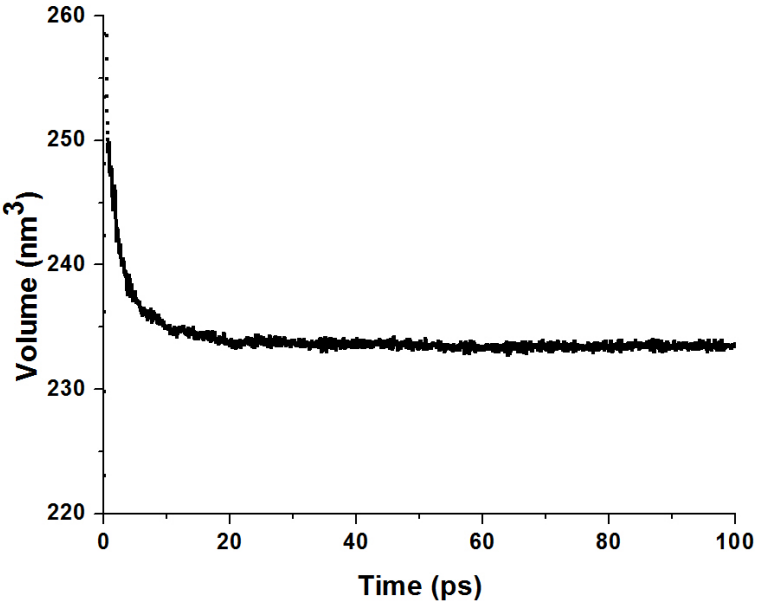


**Figure 113: Continued**

## 5.2 Properties

### 5.2.1 Bulk Properties

Similar to our approach described in section 3.2, the very first step of our study involved the estimation of the bulk properties of the polymer nanocomposite. The production run subsequent to equilibration allowed us to estimate few important properties. This also includes estimating properties based on fluctuation properties. Whether longer runs are needed for a more reliable estimate of fluctuation properties is a different issue all by itself. The mathematical equations used to estimate the different properties are given in section 3.1.4. Other than the variation in number of chains and monomers per chain, the nanocomposite samples also varied in terms of nanotube weight percentage. Naturally this also affected the estimated set of final properties.

**Table 38: Bulk properties as estimated for nanocomposites through atomistic simulation**

| Sample | CNT % (wt) | $\rho$ (gm/cc) | B (GPa) | E/ monomer (kcal/mol) | $C_p$ (KJ/ Kg-K) | Production (ns) | Equilibration (ns) |
|---|---|---|---|---|---|---|---|
| 6_6 | 18.4 | 1.40 | 34.7 | 330 | 3.5 | 1.5 | 0.5 |
| 10_12 | 9.77 | 1.43 | 18.4 | 250 | 2.57 | 1.5 | 0.5 |
| 5_25 | 9.42 | 1.42 | 28.8 | 232 | 3.51 | 1.5 | 0.5 |
| 10_30 | 9.77 | 1.39 | 11.38 | 229 | 1.58 | 1.5 | 0.5 |
| 20_30 | 5.62 | 1.37 | 19.2 | 205 | 2.46 | 1.5 | 0.5 |
| 15_40 | 5.62 | 1.37 | 20 | 395 | 4.05 | 1.5 | 0.5 |
| 30_40 | 2.89 | 1.31 | 3.24 | 243 | 3.93 | 1.5 | 0.5 |
| 40_40 | 2.18 | 1.35 | 7.79 | 244 | 4.00 | 1.5 | 0.5 |

The weight percentage of the nanotube in these nanocomposites varies from 18.7 % to 2.18 % as it moves from 6_6 polymer nanocomposite to 40_40 polymer nanocomposite. From observation of Table 38 we find the following:

1. The density of the polymer nanocomposite is little higher than regular polymer samples although the polymer and the nanotube itself has similar density. This can be attributed more towards modeling approach than the effect of the nanotube. In the process of building the model the model is compressed and then allowed to relax. Due to stiff nature of the composite it might sometimes be difficult to expand as much as required and go to lower density in reasonable amount of simulation time. However as we showed before that the equilibrated sample was considered after inspection of the instantaneous property and volume values.
2. In general there is a tendency of having high bulk modulus values for nanocomposite systems with smaller polymer sample. This is expected as smaller system in our study also means higher weight percentage of carbon nanotube.
3. The normalized energy value per monomer was calculated approximating 62 atoms of nanotube equivalent to one monomer. Apparently the energy goes down with lesser weight percentage of nanotube. However there are exceptions as well. The limited simulation time can be a major reason behind this discrepancy.

4. While the volume fluctuation showed the effect of the nanotube in general, the specific heat capacity does not show any significant and explicit change in the energy fluctuation value due to the presence of the nanotube.

### 5.2.2 Dielectric Properties

By tracking the instantaneous dipole moment of the system we attempted to find any possible effect of carbon nanotube on the dielectric properties of the nanocomposite. Table 39 presents the values estimated from our MD runs.

**Table 39: Dielectric properties estimation for different nanocomposite sample**

| Polyimide | Dipole Moment/Monomer (Debye) | | | | Equilibration Run (ns) | Production Run (ns) | Dielectric constant (KF) Method |
|---|---|---|---|---|---|---|---|
| | $\mu_x$ | $\mu_y$ | $\mu_z$ | $\mu$ | | | |
| 6_6 | 2.08 | 0.28 | -10.1 | 10.3 | 0.5 | 1.5 | 2.05 |
| 10_12 | 0.41 | 0.33 | 4.6 | 4.7 | 0.4 | 1.6 | 2.35 |
| 5_25 | 0.27 | -0.17 | -5.14 | 5.15 | 0.4 | 1.6 | 2.32 |
| 10_30 | 0.02 | -0.23 | 39.8 | 39.8 | 0.4 | 1.6 | 4.4 |
| 20_30 | 0.32 | -0.33 | 0.96 | 1.07 | 0.4 | 1.6 | 2.38 |
| 15_40 | -0.23 | -0.09 | 0.27 | 0.37 | 0.4 | 1.6 | 2.68 |
| 30_40 | 0.16 | 0.04 | 0.84 | 0.85 | 0.4 | 1.6 | 2.59 |
| 40_40 | -0.16 | 0.15 | -0.25 | 0.33 | 0.4 | 1.6 | 2.57 |

The dielectric properties of the eight different nanocomposite samples as estimated from 2ns run as shown above hints to the following:

1. The dielectric constants estimated through KF method, show no significant effect of the presence of nanotube. The difference in the absolute values of the dielectric constant for composite with its pristine counterpart may more likely due to sampling issues rather than any physical reason, as the effect (if any) does not scales as per weight percentage of the carbon nanotube in the composite.
2. The presence of the nanotube destroys the isotropic nature of the polymer sample. Accordingly we expect directional preference of any property

component along the nanotube axial direction (‘z’ direction) of the sample due to possible alignment of the chains along the same direction. However the value of $\mu_z$ in Table 39 in case of 10_30 polyimide apparently seems to be an outlier than physically influenced. The reason can be attributed to the modeling methodology and the way the dipole moment was calculated. The dipole moment, as noted before in the polymer section 3.27, was calculated by summing the product of charge and the absolute position of an individual atom. With high weight percentage of infinite length nanotube present in the system, in the process of equilibration through compressing the sample some chains has a tendency to slide from one periodic box to another leading to higher contribution of dipole moment in that particular direction. Also in presence of nanotube aligned in ‘z’ direction, ‘z’ direction will be the preferred direction for polymer chains to get aligned and thereby increasing the dipole moment.

3. We expect here to observe similar values of dipole moment in ‘x’ and ‘y’ direction. However similar to our atomistic simulation observation owing to limited system size and small simulation window we do not observe the expected.

### 5.2.3 Molecular Mechanics

Molecular mechanics calculation was carried out on the polymer nanocomposite samples obtained after production run. This method estimates mechanical properties of a material at zero K. Accordingly as pointed out in our polymer work this gives an upper estimate of mechanical properties of the sample in concern. The basic idea is to expand the energy of the deformed polymer sample around its equilibrated structure in Taylor series and estimate the second order coefficient. Details can be found in section 3.2.8.

Since our study involved placing carbon nanotube in the ‘z’ direction, we expect to observe the reinforcement effect in the same direction. Accordingly through molecular mechanics we estimated the value of axial modulus (Table 40) along ‘z’ direction for different nanocomposite samples we have built.

**Table 40: Effect of Carbon nanotube on axial modulus**

| Polyimide | Pristine Polymer $C_{33}$ (GPa) | Nanocomposite | |
|---|---|---|---|
| | | % | $C_{33}$ |
| 6_6 | 13.14 | 18.4 | 135 |
| 10_12 | 13.14 | 9.77 | 101 |
| 5_25 | 13.66 | 9.42 | 94.5 |
| 10_30 | 13.64 | 9.77 | 96.3 |
| 20_30 | 13.38 | 5.62 | 65.7 |
| 15_40 | 12.24 | 5.62 | 60.3 |
| 30_40 | 11.04 | 2.89 | 37.5 |
| 40_40 | 13.65 | 2.18 | 40.3 |

Translation of table 40 gave us Figure 114. The figure agrees well with the expectation of reinforcement of the composite in the axial direction and is directly proportional to the weight percentage of the nanotube present in the system.

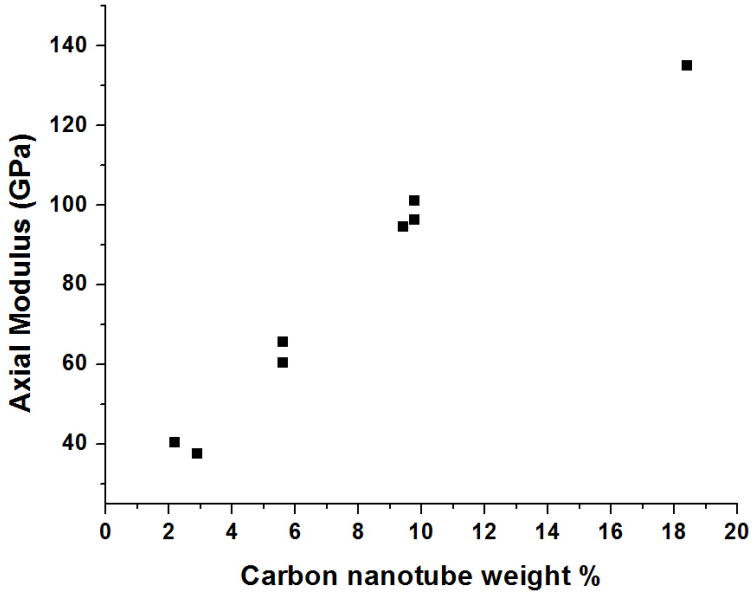


**Figure 114: Reinforcement of nanocomposite with uni-directionally dispersed CNT**

As the plot generated is the result of molecular mechanics calculations, the observed reinforcement effect does not take into account the influence of temperature. As a natural consequence of this we looked into the mechanical properties of the samples at 300 K and zero atmospheres pressure. The difference in the response also serves as an idea about the thermal softening nature of the nanocomposite.

5.3 Effect of Temperature

The stiffness of nanotube in the axial direction can be exploited in nanocomposite. The infinite length ensured the directional stability of the nanotube under all circumstances. This also means that the outcomes of this study pertain to the limiting effect for a perfect unidirectional dispersion of the nanotube in the composite.

Section 5.2 on molecular mechanics has shown the reinforcement effect of nanotube on the polymer. In here we inspect the effect under the influence of temperature. This is done through conventional molecular dynamics simulation in an

isothermal-isobaric (NPT) ensemble. Although we have looked into nanotube weight percentage as high as 18.4, in here we report cases of samples having up to ~ 10% by weight of nanotube. Couple of samples which were also built with ~ 10% nanotube by weight are not included here as the corresponding system sizes were small and consisted of less than 10,000 atoms.

The agglomeration tendency of nanotube with higher weight percentage in a nanocomposite [56] tends to destabilize the system and hence the dynamics described through constraining the mobility of the nanotube in our infinite tube model may not seem to be realistic. However in reality the aspect ratios of nanotubes used as part of composite are high enough (~ 1000) showing limited mobility as well.

Figure 115 illustrates the effect of nanotube on axial modulus of the polymer nanocomposite. We observe the shift in stress strain slope with different weight percentage of nanotube. The figure represents the nanocomposite response under normal condition.

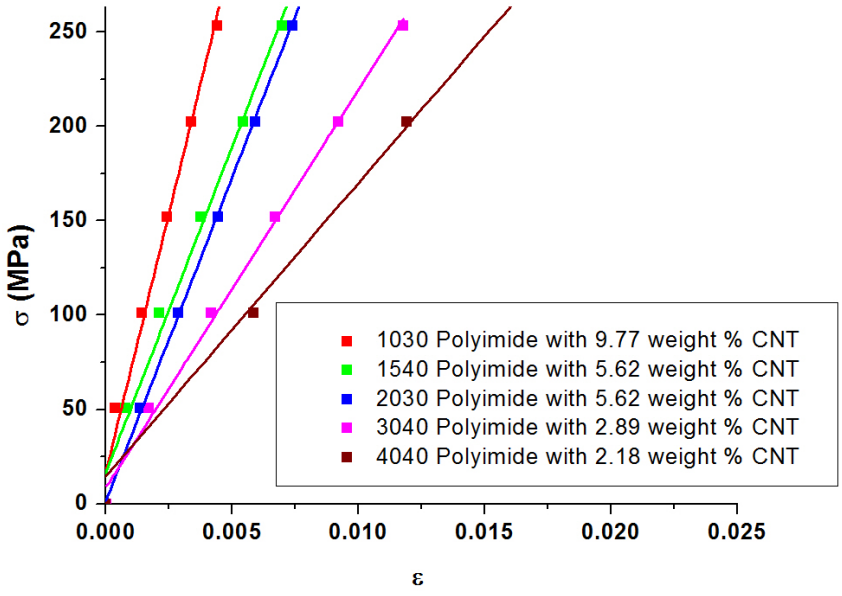


**Figure 115: Axial modulus of nanocomposite**

Analyzing figure 115 we find:

1. The presence of nanotube reinforces the polymer nanocomposite. We clearly observe a strengthening effect proportional to the weight percentage of the nanotube.

2. The presence of nanotube also affects the plastic property of the polymer. We have observed in our polymer simulation study in section 3.4 that the polymer enters the viscous region with a stress level > 150 MPa. However on applying stress along the axial direction of nanotube we do not observe any such response here and the response remains linear. We have later showed in section 5.5 that any stress applied in the perpendicular direction to the nanotube axis does result in response similar to that of a pristine polymer.

Estimation of Young modulus from figure 115 resulted in Table 41

**Table 41: Axial young modulus of reinforced nanocomposites**

| T / CNT (%) | 300 K (MD) |
|---|---|
| 0 | 4 |
| 2.18 | 15.56 |
| 2.89 | 21.12 |
| 5.62 | 34.4 |
| 9.77 | 54.94 |

## 5.4 Micromechanics Models

There is an overwhelming need for modeling of nanocomposite for finer control of their properties suited for advanced applications. The challenge lies in capturing properties of materials at all length scale into a single model. Naturally bridging of molecular level

studies with continuum mechanics is an important part of composite modeling. It is thus important to capture the atomistic level simulation results for design of next generation materials from nanocomposite.

Micromechanics models have been developed for different material property of a composite. In most cases the effective property of the composite is determined by calculating the stress or strain concentration tensor. Some of the widely used methods in determining composite properties through the use of above approach are Mori-Tanaka [175,176] and self-consistent method. Halpin-Tsai [57] is another widely used method that uses a different approach in determining composite properties.

Mori-Tanaka and self-consistent field approach take advantage of the Eshelby solution [177] in determining the concentration tensor. In general these methods use the following equation in evaluating the modulus of the composite consisting of a matrix and a filler material:

**Equation 68**

$$E_C = E_M + c_{CNT}(E_{CNT} - E_M)A_{CNT}$$

where:

$E_C$ = Elastic modulus of the composite

$E_M$ = Elastic modulus of the matrix (Polymer in our study)

$c_{CNT}$ = Volume fraction of carbon nanotube

$A_{CNT}$ = Concentration tensor of carbon nanotube

The difference in estimation of the concentration tensor of the filler material makes the difference in approaches of Mori-Tanaka and self-consistent field theory.

For Mori-Tanaka approach the concentration tensor is calculated as follows:

**Equation 69**

$$A_{CNT} = A_{CNT}^{dil}\left[c_{CNT}I + c_{CNT}A_{CNT}^{dil}\right]$$

where the dilute concentration tensor is calculated by:

**Equation 70**

$$A_{CNT}^{dil} = \left[I + S_{CNT} E_M^{-1} (E_{CNT} - E_M)\right]^{-1}$$

where $S_{CNT}$ represents the Eshelby tensor for carbon nanotube.

In self-consistent field approach the concentration tensor used in equation 68 is estimated as follows:

**Equation 71**

$$A_{CNT} = \left[I + S_{CNT} E_{COMP}^{-1} (E_{CNT} - E_{COMP})\right]^{-1}$$

Comparing equation 71 and 68 we observe that the equations are coupled through the appearance of the unknown modulus of the composite ($E_{COMP}$) in the right hand side of equation 71. Accordingly to solve the same an iterative scheme is used in self-consistent field method.

Details of these methods, derivations, calculation for Eshelby tensor for different filler geometry and the like can be found elsewhere [].

Halpin-Tsai method predicts composite property through a different methodology. It is well known for its theoretical framework in predicting properties of unidirectional composites as a function of a given aspect ratio. Accordingly it is expected to be well suited for our study. The axial modulus predicted by this model is formulated as:

**Equation 72**

$$E_{COMP} = E_{CNT} \upsilon_{CNT} + E_M \upsilon_M$$

where

$E_i$ = Axial modulus of 'i' (i stands for composite, nanotube and polymer matrix)

$\upsilon_i$ = Volume fraction of component 'i' (i stands for carbon nanotube and Polymer matrix)

While Halpin-Tsai model also gives prediction separately for transverse modulus, the model is only valid where the matrix and the filler is firmly bonded [178].

We compared our atomistic simulation result with those predicted by the above mentioned micromechanics theories. We utilized the properties estimated for the pristine polymer and nanotube as input to the micromechanics model for predicting nanocomposite properties and compared the same with our atomistic simulation results for the nanocomposite samples. Figure 116 represents the comparison in graphical terms.

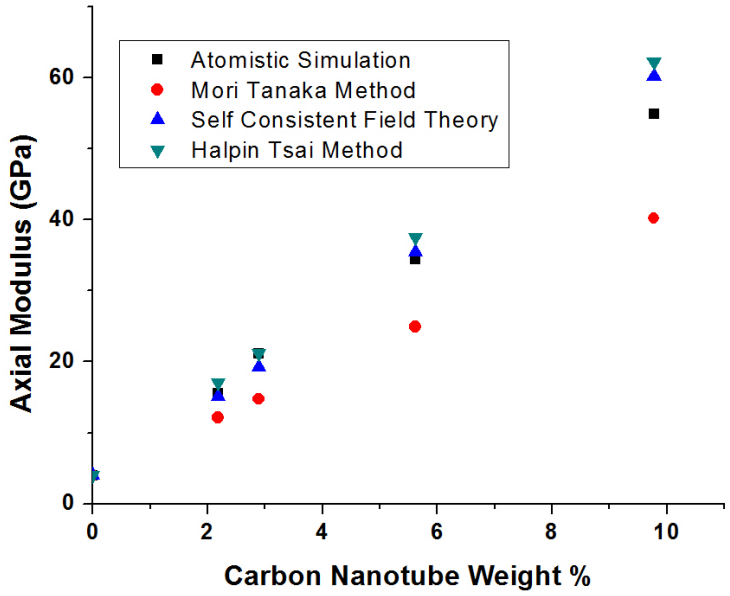


**Figure 116: Comparison of atomistic simulation results of nanocomposite axial modulus to those predicted by few micromechanics model for composites**

Analyzing figure 116 we find that:

1. The atomistic results agree best with self-consistent field theory. It also does agree reasonably with Halpin-Tsai theory than Mori-Tanaka.
2. With higher weight percentage of nanotube, difference seems to build up between atomistic results and micromechanics models. Since the nanotube content in a nanocomposite is usually much lesser the disagreement at the higher weight percentage of nanotube may not be of that importance.

3. The above mentioned micromechanics model uses volume fraction of nanotube as one of the input parameter. Since the nanotube density and the polymer density in our study is similar, replacing volume fraction by weight fraction did not change anything significantly.

Translation of figure 116 results in Table 42:

**Table 42: Comparison of various micromechanics theories with atomistic simulation**

| Theory / CNT (%) | Atomistic | Mori-Tanaka | Self Consistent Field theory | Halpin-Tsai |
|---|---|---|---|---|
| 0 | 4 | 4 | 4 | 4 |
| 2.18 | 15.56 | 12.12 | 15.17 | 16.99 |
| 2.89 | 21.12 | 14.76 | 19.34 | 21.22 |
| 5.62 | 34.4 | 24.89 | 35.51 | 37.49 |
| 9.77 | 54.94 | 40.21 | 60.21 | 62.23 |

5.5 Radial Stretch

We have observed reinforcement effect in the polymer matrix along the nanotube axial direction. This is expected as much of the stress applied is used up in stretching the stiff carbon-carbon bonds of the nanotube. Accordingly we expect that in the radial direction, the composite behavior will be matrix dominated. With the following applied tensile stress profile along the radial direction as shown in Figure 117, Figure 118 represents the polymer response.

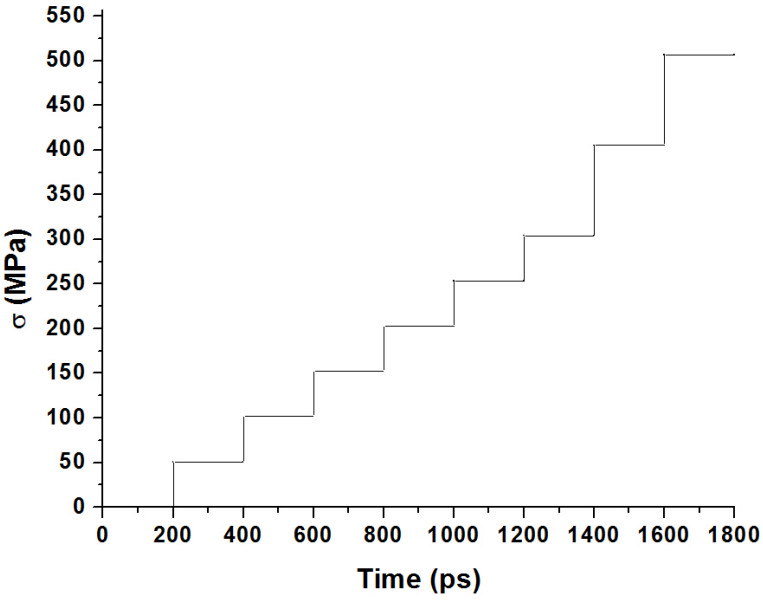


**Figure 117: Stress profile in 'y' direction**

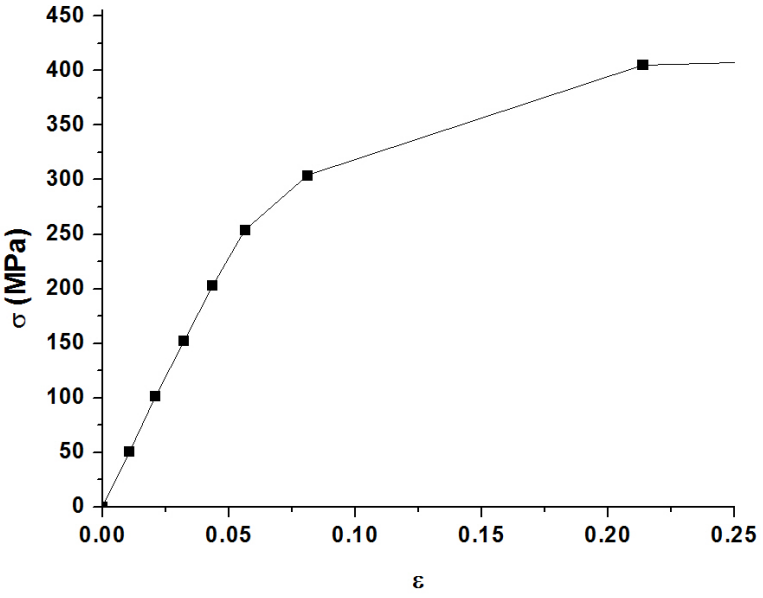


**Figure 118: 40_40 Nanocomposite response to applied stress in nanotube radial direction**

We have observed in section 3.4 that the polymer response changes from elastic to plastic as stress value is increased. Likewise owing to the orthogonal orientation of the applied stress with respect to the nanotube axis we observe similar response from composite as shown in figure 118.

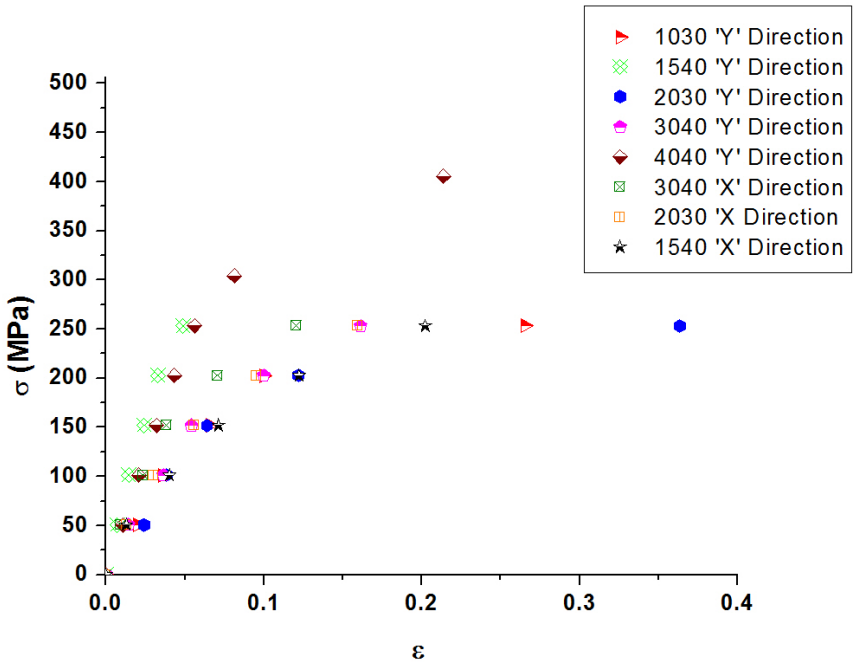


**Figure 119: Response to stress applied perpendicular to nanotube axial direction**

Extending our study to other nanocomposites samples built in this work, we applied radial stress and the response resulted in Figure 119. Again we find the similarity of response between pristine polymer and its nanocomposite sample. Although few cases (4040 and 1540 in 'Y' direction) show strengthening effect by delaying the plastic response (figure 120 and 121), careful observation reveals the absence of the same in its counterpart or the other radial direction (e.g response of 1540 polymer nanocomposite in 'X' and 'Y' direction).

The above mentioned anomaly relates more to the model building and sampling issues than the effect of the nanotube. As we have argued before in pristine nanotube mechanical property analysis in section 2.43, the primary reason for its strength is the carbon-carbon bond and angle strength. Accordingly there is minimal expectation for the nanotube to help nullify any effect of force-applied orthogonal to its axial direction unless it is chemically bonded to any polymer chain. In our study the only interaction of polymer chains with the nanotube is through van der Waals and columbic forces. Figure 120 and 121 helps us to look into the same issue in a convenient way by incorporating the pristine polymer properties into the plot.

Figures 120 and 121 compare the axial modulus, transverse modulus and modulus of pristine polymer for a high (9.77 weight %) and low filler (2.18 weight %) content samples in our study. We find as observed before that the effect on the axial modulus is roughly proportional to the weight percentage of the nanotube in the system. Figure 121 indicates a strengthening effect in the transverse direction by delaying the plastic effect but the observation in figure 120 dealing a nanocomposite with a higher percentage of filler does not agree well with the claim. This again relates to the anomalous observation stated earlier and can be attributed to the modeling and sampling related issue.

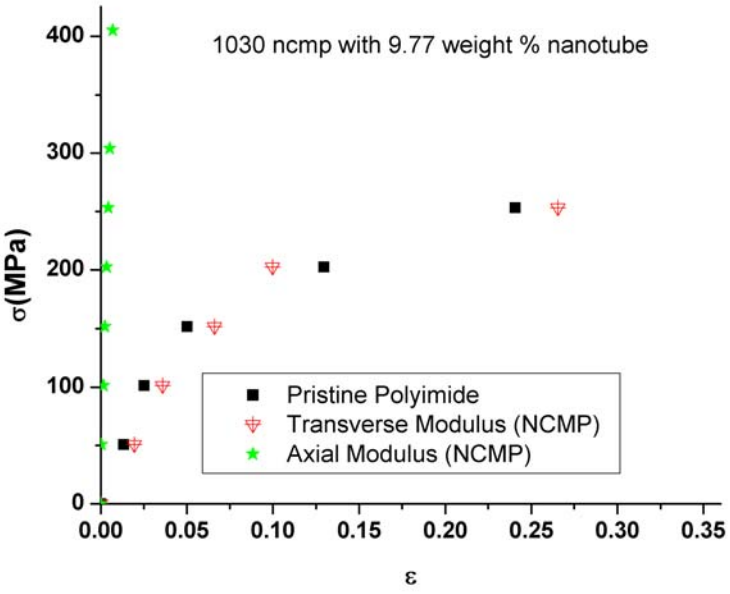


**Figure 120: Comparison of modulus for 10_30 polymer and its nanocomposite**

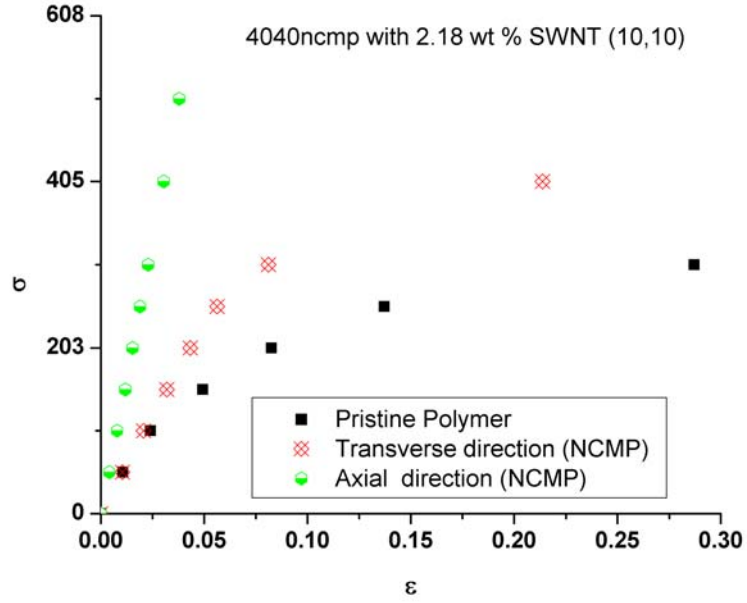


**Figure 121: Comparison of modulus for 40_40 polymer and its nanocomposite**

To look into the chain shape response we calculated the instantaneous values of moment of inertia components of each chain. Upon calculating the normalized principal moment of inertia of all the chains we observe as shown in Figure 122 that chains get stretched in the direction of the applied stress ('y' in this case) and as a consequence the value of the moment of inertia reduces for that direction. However to facilitate such process in presence of the entangled network of the polymer chains, few chains act otherwise. Figure 122 clearly shows that for majority of the chains the normalized $I_{yy}$ reduces barring few chains. On the contrary the values of $I_{xx}$ and $I_{zz}$ increases at a rapid rate as the polymer enters the plastic region indicating the loss of orientation along those directions.

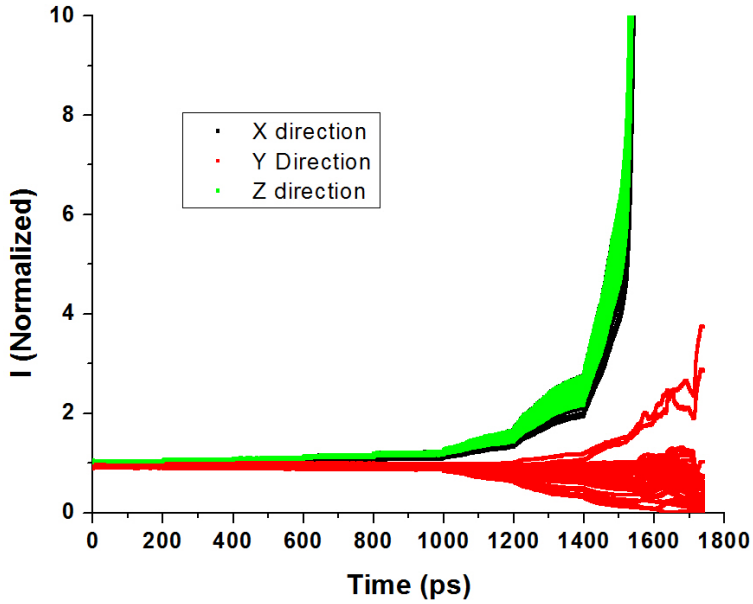


**Figure 122: Moment of inertia analysis for 40_40 nanocomposite with 2.18 weight % SWNT**

In addition to change in shape we have also investigated the effect of applied stress on the chain contour properties. Figure 123 represents the polymer response in

terms of chain contour length. Similar to our observation in section 3.42 (pristine polymer response case), the change in contour length happens in steps prior to its entry in the plastic region. Afterwards the contour length profile in general takes similar shape to the strain of the system. However similar to our observation in analysis of $I_{yy}$, in here we find contour length of few chains starts decreasing as the polymer sample enters the plastic region and increases afterwards.

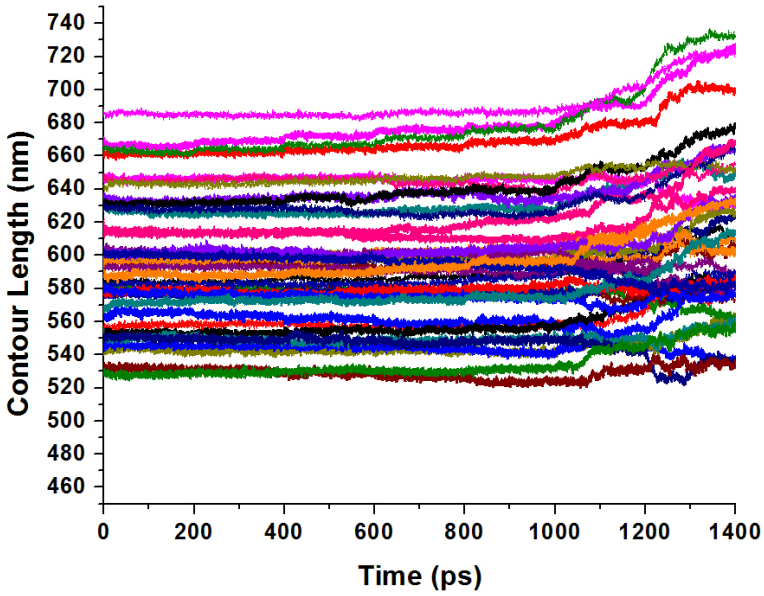


**Figure 123: Change in contour length of 40_40 nanocomposite with 2.18 weight % SWNT**

## 5.6 Thermal Properties

The different nanocomposites built were subjected to heating from 300 K to 700 K with increments of 100 K. Earlier in our study of the thermal properties of pristine polymer sample by atomistic simulation in section 3.8 we have observed presence of glass transition behavior. We expect that the presence of nanotube will resist the glass transition like behavior. Figure 124 shows near linear relation between composite

density reductions with temperature. Contrary to polymer case no glass transition like behavior is observed here.

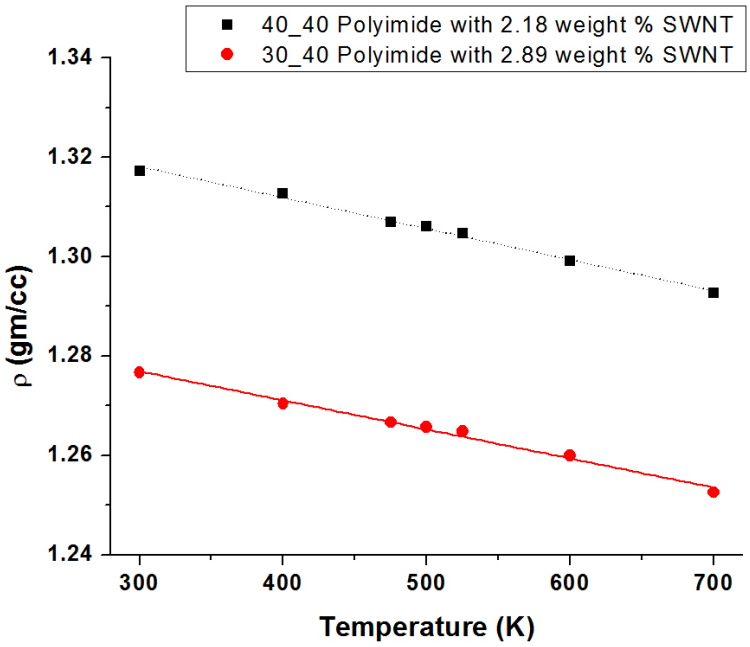


**Figure 124: Thermal expansion of nanocomposite**

## 5.7 Conclusions

In this work we have studied the effect of carbon nanotube on the polymer matrix. We have found that similar to our pristine carbon nanotube study the primary reason for the strengthening effect of a nanocomposite with incorporation of a nanotube is the carbon-carbon bond and angle strength. Accordingly the orientation of the nanotube in the polymer matrix is very important. A perfect axial orientation does result into improving the axial modulus, but in radial direction any strengthening for such a unidirectional composite does not seem possible without any bonding between the two components.

The moment of inertia study indicates the stretching of chains along the applied stress direction. It also indicates the loss of orientation among chains along the perpendicular direction of the applied stress.

We have found that self-consistent field theory predictions are closer to our atomistic simulation findings. While Halpin-Tsai model also does a good job in predicting the strengthening effect in axial direction, Mori-Tanaka model underestimates the same for the given study. The dielectric constant and the specific heat capacity do not seem to have any effect within the given modeling approach. In estimation of thermal properties we have found that presence of nanotube does affect the glass transition behavior. It is expected to increase due to the presence of nanotube in the system. Overall we have investigated the effect of (10, 10) nanotube incorporation along a specific direction in the polymer matrix.

# 6. CONCLUSIONS AND RECOMMENDATIONS

In the present work we have developed and implemented a multi-scale modeling approach in investigating the structure-property relationships for an amorphous aromatic piezoelectric polyimide substituted with nitrile dipole, carbon nanotube and nanocomposites made from these components. We have elucidated structure-property relationships of carbon nanotube and the polyimide sample. We have built a coarse-grained model using atomistic level simulation of the piezoelectric polyimide in an attempt to address larger length and time scale phenomena. We have compared and analyzed atomistic scale simulation results of the nanocomposite with those predicted from micromechanics analysis. We have utilized first principle calculations, classical molecular dynamics, molecular mechanics, coarse graining techniques and micromechanics model to different extent in carrying out the present study.

We have come up with equations for predicting nanotube axial modulus as a function of its diameter and addressed the discrepancies in values and trends observed in the literature. The clear understanding of the diameter-axial modulus relationship for the nanotube also enabled us to select appropriate axial modulus values of nanotube in nanocomposite micromechanics model. Extending our investigation to twist modulus of a nanotube through a novel bond rearrangement scheme, we have been able to show the similarity in twist modulus of zigzag and armchair nanotube of infinite length which is otherwise not valid at the finite limit. The finding was important as it qualitatively relates the change in trend of twist modulus as a function of aspect ratio of the nanotube. Van der Waals force contribution was found to have the least significance in strength of a multi walled nanotube but is capable of changing the shape of the same. The effect of temperature was found to be minimal on nanotube modulus and expansion. We also found minimal effect of Stone Wales defect on nanotube axial modulus. The study on carbon nanotori enabled us to calculate the bending modulus of carbon nanotube.

We extended our approach of characterizing and studying the thermo mechanical properties of carbon nanotube to pristine polymer sample. The estimation of the thermo-

mechanical and dielectric properties of the piezoelectric polymer helped us understand the polymer behavior at the atomistic scale. We could observe the flow behavior of the polymer by forcing the polymer sample out of its elastic zone to plastic zone with application of excess stress. We found the flow behavior of the polymer is a collective contribution of extension of chain contour length and flow of the chain itself. The observed flow behavior of the polymer also relates to its time dependent property. It must also be mentioned that the force field used did not have bond breaking capability. Accordingly the outcomes have not considered such a scenario in application of excess stress. We introduced viscoelastic models in the form of combinations of spring and dash pot and developed models based on our atomistic data to describe the polymer response. The importance of development lies in the fact that these viscoelastic models can be used for predicting polymer response to different form of mechanical perturbation (e.g. dynamical mechanical analysis) to its bulk sample. Our atomistic simulation also showed strain hardening behavior of the polymer sample. The application of tensile stress facilitates the alignment of the chains along the applied stress direction. Upon relaxation to normal condition and reapplying tensile stress in the same direction we observe such event owing to alignment of the chains. We also showed that application of ramp stress at similar rates to our creep test allowed us to identify the onset of flow point of the polymer sample more precisely. Identifying the nature of the charge distribution on the monomer we were able to linearly relate the dipole moment of a chain to the end-to-end vector of the same. In such an instance this simple relationship enables one also to relate the chain dipole moment to other chain characteristics like radius of gyration, persistence length and order parameter through end-to-end vector.

Based on the monomer structure and our objective we developed a methodology in generating the coarse-grained model of the polymer we studied. The model produced data agreeing reasonably with that of the atomistic simulation results. We have compared equilibrium, chain, mechanical, dielectric and thermal properties for the two different models and gained confidence in our model. The difference in the response of the two models at times can be attributed to the absence of its rotational degrees of

freedom in the CG model. For similar reason the polymer sample described by the CG model starts flowing faster than its counterpart once it is forced to enter the plastic zone in the creep test. The developed model also successfully showed the work hardening behavior of the polymer samples similar to our atomistic simulation observation. Dielectric constants estimated were found to be in the same order as obtained from the atomistic simulation. This also established faith in the coarsening policy taken for this particular polymer. The polymer chains were also able to show a near linear relationship between their end-to-end vector and dipole moment of each chain. Inspection of thermal properties showed an early glass transition behavior of the polymer sample. Since no energy is expended in rotation of the rings in the CG model, the thermal vibration could set the glass transition earlier than its atomistic counterpart. To exploit the advantage gained by our CG model we have built a CG model equivalent to ~ 372,000 atoms and could run isothermal-isobaric ensemble for 45 ns with reasonable computational resources. We have observed very slow decay of the total energy in the system. We have obtained a two and a half orders of magnitude gain in terms of computational time required and an order of magnitude gain in system size through implementation of our coarse grain model without sacrificing accuracy. It must also be mentioned that there is an order of magnitude gain in terms of disk space utilization in saving trajectories due to the gain in system size. The model could also reproduce the viscoelastic response of the sample under huge stress. Accordingly the model was robust enough to display the time dependent properties of the polymer. Overall it succeeded in estimating the thermal, mechanical and dielectric properties barring the effect of rotational degrees of freedom. Incorporation of the same through implementation of rigid body dynamics is expected to better represent the model. Thus the developed model showed promises to reliably access domain not accessible to Molecular dynamics by coarsening a system in our approach.

Moving to our nanocomposite system, atomistic simulation was used to study the effect of carbon nanotube on the polymer matrix. We have found that similar to our pristine carbon nanotube study the primary reason for the strengthening effect of a

nanocomposite with incorporation of a nanotube was the carbon-carbon bond and angle strength. Accordingly the orientation of the nanotube in the polymer matrix was found to be very important. A perfect axial orientation does result into improving the axial modulus, but in radial direction any strengthening for such a unidirectional composite does not seem possible without any bonding between the two components. We have also found that the self-consistent field theory prediction resulted closer to our atomistic simulation findings. Comparable agreement in predicting the strengthening effect with the Halpin-Tsai model is observed, however, Mori-Tanaka model was found to underestimate strengthening. The dielectric constant did not seem to show any significant change upon incorporation of nanotubes to polymer matrix. Similarly we don't observe any changes in specific heat capacity of the system due to the incorporation of the nanotubes. Through our simulations we have found that the presence of nanotube does affect the glass transition behavior. The reason may be attributed to the fact that the presence of nanotube makes the sample stiffer overall. This is expected to lead to slower movement of the polymer chains. Accordingly, we expect a delayed glass transition both in terms of time and temperature owing to the presence of nanotube. Similar phenomena have been observed in experiments. Overall we have investigated the effect of nanotube incorporation in a specific direction in the polymer matrix. The effect of nanotube in the radial direction appeared to be minimal because of the absence of any chemical bond at the interface. The composite response was similar to that of the pristine polymer and no significant strengthening effect was observed.

In order to extend our multi scale modeling approach, one can build a hybrid model (Figure 125) consisting of atomistic details at the interface and a coarse grain polymer model representing the rest of the matrix. This model will have the advantage of having detailed information at the interface, while maintaining a large system with lower nanotube concentrations, and hence enabling simulations to extend structure-property estimations to realistic limits.

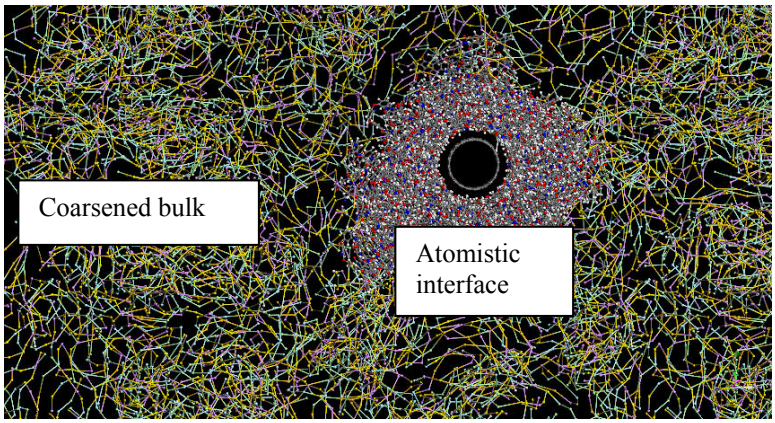


**Figure 125: Hybrid model: a possibility**

One of the main challenges is in describing the interaction potentials at the transition zone. The development of the non-bonded interaction parameters between a super-atom and a regular atom will require a rigorous approach. The presence of an atomistic domain in hybrid models leads back to the use of a smaller time step in MD simulations. However, a multiple time step algorithm may be employed, still, to keep the advantage of the larger integration steps resulted from the Coarse Grain model developed here.

Our study of atomistic simulations of polymer samples and their use with viscoelasticity models can also be extended. The viscoelastic models used here represent one-dimensional response of a material. A three dimensional extension of this model may have the potential to accommodate important non-axial material parameters like Poisson ratio and shear modulus. The challenges will lie in relating the polymer physical property to those of the estimated parameters for the viscoelastic model. Similar models can also be built for carbon nanotubes with inclusion of a spring representing the stiff nature of nanotubes. Capturing the relation between micro-structural change in the polymer and the macro scale response of the material in the viscoelastic models would be beneficial. The models built from atomistic data in that way can help predict polymer and composite response for larger time scales and length scales. It can also be used to predict response of materials for different types of loading mechanism (e.g. dynamical mechanical test). Since our coarse grain model has proven to be successful in predicting

mechanical properties using significantly lesser amount of computational resources relative to its full atomistic MD counterpart, CG model can also be used in estimating response at longer timescales with lower loading rates. This, in turn, can be utilized as input to viscoelastic models.

To further exploit the advantage of coarse grain models development of a force field based on generalized super-atoms might be a good idea. This will eliminate arduous task of Coarse Grain Force Field parameter optimization for each specific system from scratch. The development of a specific CG model force field may then be converted merely into parameter refinement based on reproducing specific system characteristics. However, coming up with a set of widely used generic super-atoms and associated force field parameters would be another challenge.

As pointed out before the coarse grain model developed in this work have not incorporated the rotational dynamics of the super atoms. This does not affect the average of vector properties (e.g. dipole moment), as these cancels out due to rotations of rings over time. However rotational dynamics is expected to contribute in system dynamics while studying glass transition and yield behavior of the polymer system. Accordingly incorporation of rotational dynamics through usage of rigid body dynamics is expected to help develop a better and sophisticated coarse grain model of the polymer system.

Since the present work dealt with both static and time dependent properties through a multi scale modeling approach, it adds value to existing methodologies of modeling nanocomposite. Overall in this work we have developed a computational paradigm to help designing nano-materials with target static (mechanical, thermal, electrical) and dynamic (e.g. yield stress upon loading) properties. Accordingly we believe that this work outlines a systematic approach for modeling and characterizing nanocomposite and its constituents.

# REFERENCES


1. Zeng, Q. H.; Yu, A. B.; Lu, G. Q. Prog Polym Sci 2008, 33(2), 191-269.
2. Feynman, R. P. Annual Meeting of American Physical Society, CalTech, Pasadena, 1959.
3. Alder, B. J.; Wainwright, T. E. J Chem Phys 1957, 27(5), 1208-1209.
4. Rahman, A. Physical Review A-General Physics 1964, 136(2A), A405.
5. Metropolis, N.; Rosenbluth, A. W.; Rosenbluth, M. N.; Teller, A. H.; Teller, E. J Chem Phys 1953, 21(6), 1087 - 1092.
6. Mayo, S. L.; Olafson, B. D.; Goddard, W. A. J Phys Chem 1990, 94, 8897 - 8909.
7. Hagler, A. T.; Huler, E.; Lifson, S. Journal of the American Chemical Society 1974, 96(17), 5319-5327.
8. Sane, S. B.; Cagin, T.; Knauss, W. G.; Goddard, W. A. Journal of Computer-Aided Materials Design 2001, 8, 87-106.
9. Fan, C. F.; Cagin, T.; Chen, Z. M. Macromolecules 1994, 27, 2383 - 2391.
10. Bhowmika, R.; Katti, K. S. Polymer 2007, 48(2), 664 - 674.
11. Frenkel, D.; Smit, B. Understanding Molecular Simulation: From Algorithms to Applications(Computational Science Series, Vol 1); Academic Press, San Diego, 2001.
12. Allen, M. P.; Tildesley, D. J. Computer Simulation of Liquids; Oxford University Press, New York, 1989.
13. Hill, T. L. An Introduction to Statistical Thermodynamics; Dover Publications, New York, 1987.
14. Chandler, D. Introduction to Modern Statistical Mechanics; Oxford University Press, New York, 1987.
15. McQuarrie, D. A. Statistical Mechanics, Viva Books, New Delhi, 2000.
16. Ryckaert, J. P.; Ciccotti, G.; Berendsen, H. J. C. Journal of Computational Physics 1977, 23(3), 327-341.

17. The Australian Concise Oxford Dictionary; Melbourne Oxford University Press, 1987.
18. Wikipedia, www.wikipedia.com, (Accessed May 2005)
19. Katzir, S. Archive for History of Exact Sciences 2003, 57(1), 61-91.
20. Alford, J. T.; Landis, B. A.; Mintmire, J. W. Int J Quantum Chem 2005, 105(6), 767-771.
21. Wang, Z. L.; Song, J. H. Science 2006, 312(5771), 242-246.
22. Sumanth, B.; Dissertation, Texas A&M University, 2008.
23. Park, C.; Ounaies, Z.; Wise, K. E.; Harrison, J. S. Polymer 2004, 45(16), 5417-5425.
24. Ounaies, Z.; Young, J. A.; Simpson, J. O.; Farmer, B. L. Materials Research Society Fall Meeting, Boston, Massachusetts, December 2 - 6 1996.
25. Ounaies, Z.; Young, J. A.; Harrison, J. S.; NASA Langley research center, Hampton, 1999.
26. Miyagawa, H.; Misra, M.; Mohanty, A. K. J Nanosci Nanotechnol 2005, 5, 1593 - 1615.
27. Gilman, J. W.; Kashiwagi, T.; Lichtenhan, J. D. Sampe Journal 1997, 33(4), 40-46.
28. Messersmith, P. B.; Giannelis, E. P. Chemistry of Materials 1994, 6(10), 1719 - 1725.
29. Yano, K.; Usuki, A.; Okada, A.; Kurauchi, T.; Kamigaito, O. Journal of Polymer Science Part A: Polymer Chemistry 1993, 31(10), 2493 - 2498.
30. Iijima. Nature 1991, 354(6348), 56 - 58.
31. Bacon. Journal Of Applied Physics 1960, 31(2), 283 - 290.
32. Iijima, S.; Ichihashi, T. Nature 1993, 364(6439), 737 - 737.
33. Bethune, D. s.; Kiang, C. h.; Devries, M. s.; Gorman, G.; Savoy, R.; Vazquez, J.; Beyers, R. Nature 1993, 363(6430), 605 - 607.
34. Bessonov, M. I.; Koton, M. M.; Kudryavtsev, V. V.; Laius, L. A. Polyimides - Thermally Stable Polymers; Plenum Publishing Corporation: New York, 1987.

35. Young, J. A.; Farmer, B. L.; Hinkley, J. A. Polymer 1999, 40(10), 2787-2795.
36. Wong, C. P., Ed. Polymers for Electronic & Photonic Application; Academic Press, San Diego, 1992.
37. Kawai, H. Japanese Journal of Applied Physics 1969, 8(7), 975-&.
38. Scheinbeim, J. I.; Chung, K. T. Journal of Applied Physics 1981, 52(10), 5983-5987.
39. Scheinbeim, J. I.; Chung, K. T.; Pae, K. D.; Newman, B. A. Bulletin of the American Physical Society 1981, 26(3), 365-365.
40. Chung, K. T.; Newman, B. A.; Pae, K. D.; Scheinbeim, J. I. Bulletin of the American Physical Society 1981, 26(3), 261-261.
41. Sen, A.; Scheinbeim, J. I.; Newman, B. A. Journal of Applied Physics 1984, 56(9), 2433-2439.
42. Newman, B. A.; Chen, P.; Pae, K. D.; Scheinbeim, J. I. Journal of Applied Physics 1980, 51(10), 5161-5164.
43. Scheinbeim, J. I. Journal of Applied Physics 1981, 52(10), 5939-5942.
44. Mathur, S. C.; Scheinbeim, J. I.; Newman, B. A. Journal of Applied Physics 1984, 56(9), 2419-2425.
45. Dargaville, T. R.; Celina, M.; Chaplya, P. M. J Polym Sci Pt B-Polym Phys 2005, 43(11), 1310-1320.
46. Park, C.; Ounaies, Z.; SU, J.; Jr, J. G. S.; Harrison, J. S.; NASA Langley Research Center, Hampton, 1999.
47. Simpson, J.; Ounaies, Z.; Fay, C. Materials Research Society 1996 Fall Meeting, Boston, 1996.
48. Hilczer, B.; Malecki, J. Electrets (Studies in Electrical and Electronic Engineering), 1986.
49. Ajayan, P. M.; Schadler, L. S.; Braun, P. V. Nanocomposite science and Technology; Wiley, San Francisco, 2003.
50. Thostenson, E. T.; Li, C. Y.; Chou, T. W. Compos Sci Technol 2005, 65(3 - 4), 491 - 516.

51. Frankland, S. J. V.; Harik, V. M.; Odegard, G. M.; Brenner, D. W.; Gates, T. S. Compos Sci Technol 2003, 63(11), 1655-1661.
52. McLachlan, D. S.; Chiteme, C.; Park, C.; Wise, K. E.; Lowther, S. E.; Lillehei, P. T.; Siochi, E. J.; Harrison, J. S. J Polym Sci Pt B-Polym Phys 2005, 43(22), 3273-3287.
53. Peeterbroeck, S.; Alexandre, M.; Nagy, J. B.; Moreau, N.; Destree, A.; Monteverde, F.; Rulmont, A.; Jerome, R.; Dubois, P. Macromolecular Symposia 2005, 221, 115-126.
54. Park, C.; Crooks, R. E.; Siochi, E. J.; Harrison, J. S.; Evans, N.; Kenik, E. Nanotechnology 2003, 14(9), L11-L14.
55. Ounaies, Z.; Park, C.; Wise, K. E.; Siochi, E. J.; Harrison, J. S. Compos Sci Technol 2003, 63(11), 1637-1646.
56. Park, C.; Ounaies, Z.; Watson, K. A.; Crooks, R. E.; Smith, J.; Lowther, S. E.; Connell, J. W.; Siochi, E. J.; Harrison, J. S.; Clair, T. L. S. Chem Phys Lett 2002, 364(3-4), 303-308.
57. Halpin, J. C.; Kardos, J. L. Polym Eng Sci 1976, 16(5), 344-352.
58. Yakobson, B. I.; Brabec, C. J.; Bernholc, J. Physical Review Letters 1996, 76(14), 2511-2514.
59. Cornwell, C. F.; Wille, L. T. Solid State Communications 1997, 101(8), 555 - 558.
60. Lu, J. P. Physical Review Letters 1997, 79(7), 1297-1300.
61. Gao, G.; Cagin, T.; III, W. A. G. Nanotechnology 1998, 9, 184 - 191.
62. Salvetat, J. P.; Briggs, G. A. D.; Bonard, J. M.; Bacsa, R. R.; Kulik, A. J.; Stockli, T.; Burnham, N. A.; Forro, L. Physical Review Letters 1999, 82(5), 944-947.
63. Zhou, G.; Duan, W. H.; Gu, B. L. Chem Phys Lett 2001, 333(5), 344-349.
64. Treacy, M. M. J.; Ebbesen, T. W.; Gibson, J. M. Nature 1996, 381(6584), 678-680.

65. Krishnan, A.; Dujardin, E.; Ebbesen, T. W.; Yianilos, P. N.; Treacy, M. M. J. Physical Review B 1998, 58(20), 14013-14019.
66. Enomoto, K.; Kitakata, S.; Yasuhara, T.; Ohtake, N.; Kuzumaki, T.; Mitsuda, Y. Appl Phys Lett 2006, 88(15).
67. Van Lier, G.; Van Alsenoy, C.; Van Doren, V.; Geerlings, P. Chem Phys Lett 2000, 326(1-2), 181-185.
68. Popov, V. N.; Van Doren, V. E.; Balkanski, M. Physical Review B 2000, 61(4), 3078-3084.
69. Chang, T. C.; Gao, H. J. J Mech Phys Solids 2003, 51(6), 1059-1074.
70. Sanchez-Portal, D.; Artacho, E.; Soler, J. M.; Rubio, A.; Ordejon, P. Physical Review B 1999, 59(19), 12678-12688.
71. Reich, S.; Thomsen, C.; Ordejon, P. Physical Review B 2002, 65(15).
72. Xiao, J. R.; Gama, B. A.; Gillespie, J. W. Int J Solids Struct 2005, 42(11-12), 3075-3092.
73. Cai, J.; Bie, R. F.; Tan, X. M.; Lu, C. Physica B 2004, 344(1-4), 99-102.
74. Lourie, O.; Wagner, H. D. J Mater Res 1998, 13(9), 2418-2422.
75. Pop, E.; Mann, D.; Wang, Q.; Goodson, K.; Dai, H. J. Nano Lett 2006, 6(1), 96-100.
76. Che, J. W.; Cagin, T.; Goddard, W. A. Nanotechnology 2000, 11(2), 65-69.
77. Berber, S.; Kwon, Y. K.; Tomanek, D. Physical Review Letters 2000, 84(20), 4613-4616.
78. Klemens, P. Proceedings of 26th International Thermal Conductivity Conference, Cambridge, MA, 6-8 August 2001.
79. Shen, S.; Atluri, S. N. Cmc-Computers Materials & Continua 2004, 1(1), 59-90.
80. Lu, J. P. J Phys Chem Solids 1997, 58(11), 1649-1652.
81. Xie, G. Q.; Han, X.; Long, S. Y. Cmc-Computers Materials & Continua 2007, 6(1), 1-11.
82. Xie, G. Q.; Long, S. Y. Cmc-Computers Materials & Continua 2006, 4(1), 11-20.

83. Theodosiou, T. C.; Saravanos, D. A. Cmes-Computer Modeling in Engineering & Sciences 2007, 19(2), 121-134.
84. Yu, M. F.; Files, B. S.; Arepalli, S.; Ruoff, R. S. Physical Review Letters 2000, 84(24), 5552-5555.
85. Wong, E. W.; Sheehan, P. E.; Lieber, C. M. Science 1997, 277(5334), 1971-1975.
86. Falvo, M. R.; Clary, G.; Helser, A.; Paulson, S.; Taylor, R. M.; Chi, V.; Brooks, F. P.; Washburn, S.; Superfine, R. Microsc microanal 1998, 4(5), 504-512.
87. Thostenson, E. T.; Ren, Z. F.; Chou, T. W. Compos Sci Technol 2001, 61(13), 1899-1912.
88. Yakobson, B. I.; Avouris, P. In Carbon Nanotubes: Synthesis, Structure, Properties, and Applications; Dresselhaus, G.; Dresselhaus, M. S.; Avouris, P., Eds.; Springer, New York, 2001, p 447.
89. Dong, Q.; Gregory, J. W.; Wing Kam, L.; Min-Feng, Y.; Rodney, S. R. Applied Mechanics Reviews 2002, 55(6), 495-533.
90. Srivastava, D.; Wei, C.; KyeongjaeCho. Applied Mechanics Reviews 2003, 56(2), 215 - 230.
91. Dresselhaus, M. S.; Dresselhaus, G.; Jorio, A. Ann Rev Mater Res 2004, 34, 247-278.
92. Ashrafi, B.; Hubert, P. Compos Sci Technol 2006, 66(3-4), 387-396.
93. Hohenberg, P.; Kohn, W. Phys Rev 1964, 136(3B), 864A.
94. Kohn, W.; Sham, L. J. Phys Rev 1965, 140(4A), 1133B.
95. Payne, M. C.; Teter, M. P.; Allan, D. C.; Arias, T. A.; Joannopoulos, J. D. Rev Mod Phys 1992, 64, 1045.
96. Kresse, G.; Joubert, J. Phys Rev B 1999, 59(3), 1758-1775.
97. Perdew, J. P.; Burke, K.; Ernzerhof, M. Phys Rev Lett 1996, 77, 3865.
98. Monkhorst, H. J.; Paack, J. D. Phys Rev B 1976, 13, 5188.
99. Cagin, T.; Gao, G.; Goddard, W. A. Turkish Journal of Physics 2006, 30, 221-229.

100. Robertson, D. H.; Brenner, D. W.; Mintmire, J. W. Physical Review B 1992, 45(21), 12592-12595.
101. Dresselhaus, M. S.; Dresselhaus, G.; Avouris, P., Eds. Topics in Applied Physics; Springer-Verlag GmbH, Heidelberg, 2001.
102. Chandra, N.; Namilae, S.; Shet, C. Physical Review B 2004, 69(9).
103. Tu, Z. C.; Ou-Yang, Z. Physical Review B 2002, 65(23).
104. Ruoff, R. S.; Tersoff, J.; Lorents, D. C.; Subramoney, S.; Chan, B. Nature 1993, 364(6437), 514-516.
105. Wang, Y.; Wang, X. X.; Ni, X. G. Model Simul Mater Sci Eng 2004, 12(6), 1099-1107.
106. Falvo, M. R.; Clary, G. J.; Taylor, R. M.; Chi, V.; Brooks, F. P.; Washburn, S.; Superfine, R. Nature 1997, 389(6651), 582-584.
107. Brenner, D. W.; Shenderova, O. A.; Areshkin, D. A.; Schall, J. D.; Frankland, S. J. V. Cmes-Computer Modeling in Engineering & Sciences 2002, 3(5), 643-673.
108. Huhtala, M.; Kuronen, A.; Kaski, K. Computer Physics Communications 2002, 147(1-2), 91-96.
109. Huhtala, M.; Kuronen, A.; Kaski, K. Computer Physics Communications 2002, 146(1), 30-37.
110. Liu, P.; Zhang, Y. W.; Lu, C. Journal of Applied Physics 2005, 98(11).
111. Liu, P.; Zhang, Y. W.; Lu, C. Physical Review B 2005, 72(11).
112. Maniwa, Y.; Fujiwara, R.; Kira, H.; Tou, H.; Kataura, H.; Suzuki, S.; Achiba, Y.; Nishibori, E.; Takata, M.; Sakata, M.; Fujiwara, A.; Suematsu, H. Physical Review B 2001, 64(24), 3.
113. Li, C. Y.; Chou, T. W. Physical Review B 2005, 71(23), 6.
114. Xie, X. L.; Mai, Y. W.; Zhou, X. P. Mater Sci Eng R-Rep 2005, 49(4), 89-112.
115. Stone, A. J.; Wales, D. J. Chem Phys Lett 1986, 128(5-6), 501-503.
116. Lu, Q.; Bhattacharya, B. Nanotechnology 2005, 16(4), 555 - 566.
117. Zhou, L. G.; San-Qiang, S. Appl Phys Lett 2003, 83(6), 1222-1224.

118. S. Tchouikov; Nishioka, T.; Fujimoto, T. Cmc-Computers Materials & Continua 2005, 1(2), 191-204.
119. Nasdala, L.; Ernst, G.; Lengnick, M.; Rothert, H. Cmes-Computer Modeling in Engineering & Sciences 2005, 7, 293-304.
120. Rappe, A. K.; Goddard, W. A. Journal of Physical Chemistry 1991, 95(8), 3358-3363.
121. Hofmann, D.; Fritz, L.; Ulbrich, J.; Schepers, C.; Bohning, M. Macromolecular Theory and Simulation 2000, 9(6), 293-327.
122. Kremer, K.; Grest, G. S. J Chem Phys 1990, 92(8), 5057 - 5086.
123. Fan, C. F.; Hsu, S. L. Macromolecules 1992, 25(1), 266 - 270.
124. Nye, J.F.; Physical properties of Crystal, Oxford University Press, New York, 1969.
125. Nielsen, L. E.; Landel, R. F. Mechanical properties of polymers and composites, CRC Press, Boca Raton, 1993.
126. Plimpton, S. Journal of Computational Physics 1995, 117(1), 1-19.
127. Plimpton, S. J.; Pollock, R.; Stevens, M. Proc of the Eighth SIAM Conference on Parallel Processing for Scientific Computing, Minneapolis, MN, 1997.
128. Hoover, W. G. Phys Rev A 1986, 34(3), 2499-2500.
129. Hoover, W. G. Phys Rev A 1985, 31(3), 1695-1697.
130. Melchionna, S.; Ciccotti, G.; Holian, B. L. Molecular Physics 1993, 78(3), 533-544.
131. Sun, H.; Mumby, S. J.; Maple, J. R.; Hagler, A. T. Journal of the American Chemical Society 1994, 116(7), 2978-2987.
132. Neumann, M. Molecular Physics 1983, 50(4), 841-858.
133. Uludogan, M.; Cagin, T.; Strachan, A.; Goddard, W. A. Journal of Computer-Aided Materials Design 2002, 8(2-3), 193-202.
134. Fuller, F. B. Proceedings of the National Academy of Sciences of the United States of America 1971, 68(4), 815-&.

135. Edvinsson, T.; Arteca, G. A.; Elvingson, C. Journal of Chemical Information and Computer Sciences 2003, 43(1), 126-133.
136. Doi, M.; Edwards, S. F. The Theory of Polymer Dynamics; Clarendon Press, Oxford, 1994.
137. Kausch, H. H.; Michler, G. H. In Intrinsic Molecular Mobility and Toughness of Polymers I; Springer-Verlag : Berlin, 2005, p 1-33.
138. Monnerie, L.; Halary, J. L.; Kausch, H. H. In Intrinsic Molecular Mobility and Toughness of Polymers I; Springer-Verlag : Berlin, 2005, p 215-364.
139. Oleinik, E. F. Polymer Science Series C 2003, 45, 17-117.
140. Stachurski, Z. H. J Ind Eng Chem 2005, 11(6), 773-796.
141. Baschnagel, J.; Binder, K.; Doruker, P.; Gusev, A. A.; Hahn, O.; Kremer, K.; Mattice, W. L.; Muller-Plathe, F.; Murat, M.; Paul, W.; Santos, S.; Suter, U. W.; Tries, V. In Advances in Polymer Science: Viscoelasticity, Atomistic Models, Statistical Chemistry; Springer-Verlag : Berlin, 2000, p 41-156.
142. Molinero, V.; Goddard, W. A. J Phys Chem B 2004, 108(4), 1414-1427.
143. Cagin, T.; Wang, G. F.; Martin, R.; Zamanakos, G.; Vaidehi, N.; Mainz, D. T.; Goddard, W. A. Computational and Theoretical Polymer Science 2001, 11(5), 345-356.
144. Zhou, J.; Thorpe, I. F.; Izvekov, S.; Voth, G. A. Biophysical Journal 2007, 92(12), 4289-4303.
145. Tschop, W.; Kremer, K.; Batoulis, J.; Burger, T.; Hahn, O. Acta Polym 1998, 49(2-3), 61-74.
146. Srinivas, G.; Klein, M. L. Molecular Physics 2004, 102(9-10), 883-889.
147. Izvekov, S.; Voth, G. A. J Phys Chem B 2005, 109(7), 2469-2473.
148. Ensing, B.; Nielsen, S. O.; Moore, P. B.; Klein, M. L. Abstr Pap Am Chem Soc 2005, 229, U771-U771.
149. Ayton, G. S.; Voth, G. A. Biophysical Journal 2004, 87(5), 3299-3311.
150. Molinero, V.; Cagin, T.; Goddard, W. A. J Phys Chem A 2004, 108(17), 3699-3712.

151. Kremer, K.; Muller-Plathe, F. Mol Simul 2002, 28(8-9), 729-750.
152. Tozzini, V. Curr Opin Struct Biol 2005, 15(2), 144-150.
153. Santangelo, G.; Di Matteo, A.; Muller-Plathe, F.; Milano, G. J Phys Chem B 2007, 111(11), 2765-2773.
154. Milano, G.; Muller-Plathe, F. J Phys Chem B 2005, 109(39), 18609-18619.
155. Izvekov, S.; Violi, A.; Voth, G. A. J Phys Chem B 2005, 109(36), 17019-17024.
156. Liu, P.; Izvekov, S.; Voth, G. A. Biophysical Journal 2007, 566A-566A.
157. Groot, R. D.; Warren, P. B. J Chem Phys 1997, 107(11), 4423-4435.
158. Ortiz, V.; Nielsen, S. O.; Discher, D. E.; Klein, M. L.; Lipowsky, R.; Shillcock, J. J Phys Chem B 2005, 109(37), 17708-17714.
159. McGrother, S.; Ming, L. Y.; Goldbeck-Wood, G. In Mesoscale Phenomena in Fluid Systems; Amer Chemical Soc: Washington, 2003, p 227-241.
160. Reith, D.; Putz, M.; Muller-Plathe, F. J Comput Chem 2003, 24(13), 1624-1636.
161. Hone, T. D.; Izvekov, S.; Voth, G. A. J Chem Phys 2005, 122(5), 7.
162. Molinero, V.; Cagin, T.; Goddard, W. A. Chem Phys Lett 2003, 377(3-4), 469-474.
163. Ensing, B.; Nielsen, S. O.; Moore, P. B.; Klein, M. L. Abstr Pap Am Chem Soc 2004, 228, U221-U221.
164. Srinivas, G.; Lopez, C. F.; Klein, M. L. Abstr Pap Am Chem Soc 2004, 228, U221-U221.
165. Saiz, L.; Klein, M. L. Accounts of Chemical Research 2002, 35(6), 482-489.
166. Nanda, H.; Krueger, S.; Curtis, J. E. Biophysical Journal 2007, 572A-572A.
167. Chang, R.; Ayton, G. S.; Voth, G. A. J Chem Phys 2005, 122(24), 12.
168. Srinivas, G.; Discher, D. E.; Klein, M. L. Nat Mater 2004, 3(9), 638-644.
169. Abrams, C. F.; Delle Site, L.; Kremer, K. Multiscale Computer Simulations for Polymeric Materials in Bulk and Near Surfaces; Physics and Astronomy, 2002.
170. Maiti, P. K.; Li, Y.; Çağın, T.; Goddard, W. A. Macromolecules 2007, Submitted.

171. Wang, Y. T.; Izvekov, S.; Yan, T. Y.; Voth, G. A. J Phys Chem B 2006, 110(8), 3564-3575.
172. Izvekov, S.; Voth, G. A. J Chem Phys 2005, 123(13), 13.
173. Louis, A. A. J Phys-Condes Matter 2002, 14(40), 9187-9206.
174. Accelrys, www.accelrys.com, (Accessed July 2007).
175. Mori, T.; Tanaka, K. Acta Metallurgica 1973, 21(5), 571-574.
176. Tandon, G. P.; Weng, G. J. Polym Compos 1984, 5(4), 327-333.
177. Seidel, G. D.; Lagoudas, D. C. Mech Mater 2006, 38(8-10), 884-907.
178. Yung, K. C.; Wang, J.; Yue, T. M. J Reinf Plast Compos 2006, 25(8), 847-861.

# VITA


Name: Arnab Chakrabarty

Address: New Green Park, Sonarpur Road, West Bengal,
Kolkata - 700103, India

Email Address: arnabc@gmail.com


Education: B.Tech., Chemical Engineering, IIT Kharagpur, 2001
M.S., Chemical Engineering, Texas A&M University, 2004
Ph.D., Chemical Engineering, Texas A&M University, 2008